Gamma ray Cerenkov telescope image analysis

Holder, Jamie

Gamma Ray Cerenkov Telescope Image Analysis

by Jamie Holder, B. Sc.

A thesis submitted to the University of Durham in accordance with the regulations for admittance to the degree of Doctor of Philosophy

Department of Physics

University of Durham

April, 1997

Gamma Ray Cerenkov Telescope Image Analysis

by Jamie Holder, B.Sc. **Ph. D. Thesis, University of Durham, 1997**

ABSTRACT

The subject of this thesis is ground based gamma ray astronomy using the imaging atmospheric Cerenkov technique. The first two chapters are introductory, and describe the field of gamma ray astronomy, the generation of extensive air showers in the atmosphere and the Cerenkov radiation they induce. Chapter three describes the atmospheric Cerenkov telescope, including the development of the imaging technique for background discrimination. The characteristics of the three University of Durham atmospheric Cerenkov telescopes and the processing and calibration of their data products are outlined. Chapter four is concerned with periodic sources of gamma ray emission and includes a review of candidate sources and time series analysis techniques. An analysis of the Mark 3 telescope SMC X-1 database is presented. An upper limit of 1.2×10^{-11} cm^{-2} s^{-1} above a cosmic ray threshold of 1 TeV is determined for the guard ring analysis of Mark 3 data. For an analysis of medium resolution Mark 3 imaging data, the upper limit is 2×10^{-10} cm^{-2} s^{-1} above a cosmic ray threshold of 500 GeV. Chapter five introduces a new method for the parameterisation of Cerenkov images of extensive air showers recorded by atmospheric Cerenkov telescopes. This method, involving the optimization of a bivariate Gaussian fit to the image, is shown to be significantly better than the standard moment based parameterisation using simulated images. In Chapter six, both of these methods are employed in an attempt to enhance the signal to noise ratio for observations of the pulsar PSR 1706-44 made with the Mark 6 telescope and some evidence for steady emission is seen. The implied fluxes are $(2.6 \pm 0.3 \pm 0.1)\times10^{-11}$ cm^{-2} s^{-1} above 420 GeV for the bivariate Gaussian analysis and $(1.7 \pm 0.4 \pm 0.2)\times10^{-11}$ cm^{-2} s^{-1} above 500 GeV for the moment analysis.

CONTENTS

PREFACE

All of the work described in this thesis has been associated with the atmospheric Cerenkov telescopes in operation at the University of Durham Gamma Ray Observatory in Narrabri, New South Wales, Australia. The author participated in the collection of data using these instruments for a total of five dark moon periods. During a further three dark moon periods, he was involved with the construction and testing of the new Mark 6 telescope.

In Durham, the author has been involved in the routine pre-processing of telescope data, and in the development of computer software for calibration and analysis purposes. He has also performed Monte Carlo simulations of the development of extensive air showers in order to help understand the telescope response to their Cerenkov images. A full re-analysis of the Durham Mark 3 telescope SMC X-1 database has been made. Observations of the pulsar PSR1706-44 made with the Mark 6 telescope high resolution camera have also been analysed and a novel method for the parameterisation of these data developed.

None of the material presented in this thesis has been submitted previously for admittance to a degree in this or any other university, except where due reference is made.

ACKNOWLEDGEMENTS

I would like to express my gratitude to all those who have helped with my work in Durham.

Professors D. Bloor and B. Tanner are thanked for the provision of the facilities of the Department of Physics and the Particle Physics and Astronomy Research Council (formerly the Science and Engineering Research Council) for their financial support.

I would also like to thank my supervisor, Dr Keith Orford, for his help and ideas throughout my course.

Finally, thanks to all the members of the Durham gamma ray astronomy group and everyone I have been privileged to meet and work with in Durham and Australia.

CHAPTER ONE - GAMMA RAY ASTRONOMY

1.1 Introduction

The presence of a flux of ionising radiation at the Earth's surface was first inferred by Rutherford and Cooke (1903) from observations of the discharge time of a gold leaf electroscope. The rate of discharge was seen to decrease when the electroscope was shielded with metal. This radiation was assumed to be terrestrial in origin until balloon experiments (eg. Goeckel, 1910; Hess, 1911) showed that the flux of radiation decreased only up to an altitude of 1 km. Above this, the flux steadily increased. This result led to the conclusion that the radiation was extra-terrestrial in origin and hence the term "cosmic radiation". These cosmic rays are now known to consist of a wide variety of highly energetic particles. The energy density of cosmic rays within the galaxy is approximately the same as that of starlight photons, of the turbulent gas motion in the interstellar medium and of galactic magnetic fields (Longair, 1994; Toller, 1990); however, full details of their origin remain unknown.

The vast majority of the cosmic ray flux is composed of charged particles. Over interstellar distances, these particles are deflected by the galactic magnetic fields. By the time they reach the Earth, all information about the direction of their origin has been lost. The neutral component of the cosmic radiation, consisting of neutrinos, neutrons and gamma rays, retains its directional information and is therefore of great astrophysical significance. Neutrinos have an extremely small cross-section for interaction with matter and thus are difficult to detect, except in the rare circumstance of a nearby supernova explosion. Neutrons have too short a lifetime to provide significant flux over large distances. For example, a neutron generated at the galactic centre, ~ 7 kpc distant, would require an energy of ~ 1 EeV were it to survive to the earth without decaying. Gamma rays, conversely, are easily detected and can travel for intergalactic distances without interacting. Also, they are

destroyed rather than scattered by interactions and so any observed gamma ray has travelled directly from its source. The study of gamma rays can therefore provide valuable information about cosmic ray sources. It also enables us to explore the processes which occur in very high energy environments.

1.2 VHE Gamma Ray Production

Gamma rays are often defined as photons of energy greater than 0.511 MeV (the rest mass of the electron, m_e). There are four processes which can result in the emission of gamma rays: transitions between nuclear energy levels, the annihilation of particles with antiparticles, the decays of elementary particles and the acceleration of charged particles. Very high energy (VHE) gamma ray astronomy is the subject of this thesis and is concerned with gamma rays of energy greater than those detectable by satellite experiments, from approximately 0.03 to 50 TeV. In this VHE band, the latter two processes dominate.

1.2.1 Elementary particle decay

Gamma ray emission by particle decay arises principally from the decay of the very short-lived neutral pion. These are produced during collisions between high energy nucleons:

$$p + p \rightarrow p + p + \pi^0$$

The resulting pion then decays into two gamma rays, each of energy $\varepsilon_0 = 68$ MeV in the pion's rest frame (Fig. 1.1).

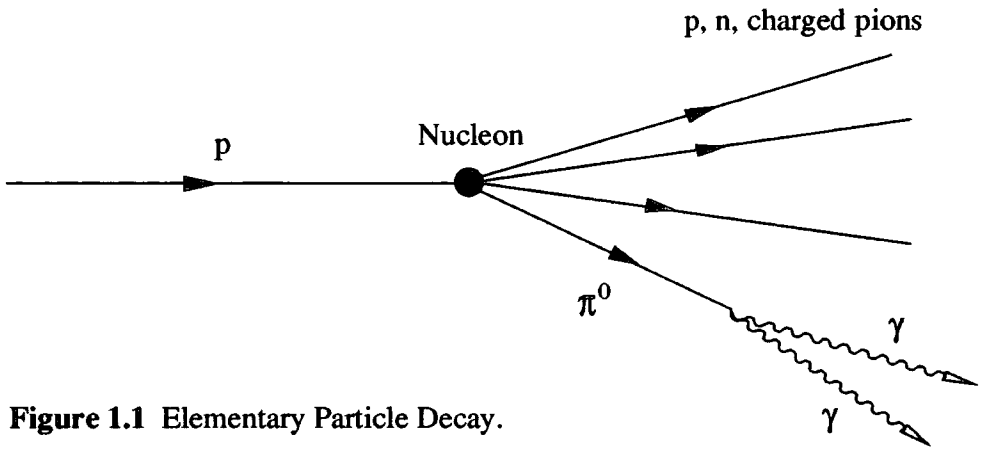

Figure 1.1 Elementary Particle Decay.

In the observer's rest frame, the gamma ray energies range between

$$\varepsilon_0 \left[\frac{(1-\beta)}{(1+\beta)}\right]^{\frac{1}{2}} \quad \text{and} \quad \varepsilon_0 \left[\frac{(1+\beta)}{(1-\beta)}\right]^{\frac{1}{2}}$$

where the initial pion velocity was βc. The resulting gamma ray spectrum has a peak at ε_0.

Less common pion production mechanisms include the annihilation of nucleons with antinucleons, resulting in a sharply peaked gamma ray energy spectrum as the pion is created at rest in the centre of mass frame. Photo-pion production occurs in collisions between very high energy ($>10^{20}$ eV) protons and photons of the 2.7 K cosmic microwave background. The low flux of sufficiently energetic protons limits the importance of this process, except when considering the origin of the highest energy cosmic rays.

1.2.2 Acceleration of Charged Particles

The power radiated during the acceleration of a charged particle in an electromagnetic field is inversely proportional to the square of the particle's mass. As a result of this, electron acceleration dominates gamma ray production in the systems described below.

1.2.2.1 Synchrotron Emission

Synchrotron emission occurs when an electron encounters a transverse magnetic field. The electron is forced to move in a helix around the direction of the field and this acceleration causes it to radiate. In the case of a relativistic electron, the emitted radiation is concentrated about the direction of motion of the particle (Figure 1.2). The photons produced in synchrotron emission are several orders of magnitude lower in energy than the radiating electron. The presence of synchrotron radiation is therefore most useful in identifying regions in which relativistic electrons exist which may produce gamma rays by other mechanisms.

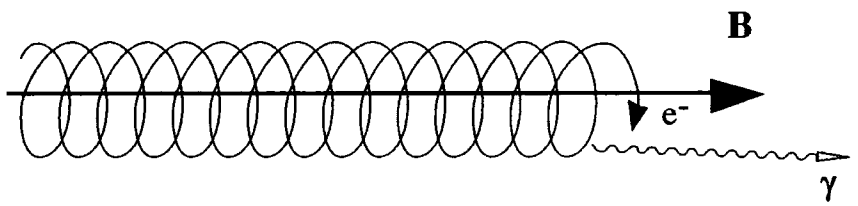

Figure 1.2 Synchrotron Emission.

1.2.2.2 Curvature Radiation

This method of gamma ray production was proposed by Sturrock (1971) in order to explain the gamma ray emission from pulsars. Charged particles moving close to a neutron star are constrained to travel along the magnetic field lines, any motion across the lines being quickly damped by synchrotron radiation. Following the curved path of the field lines causes the particles to radiate photons of energies approaching their own (Figure 1.3). In order to generate gamma rays by this process, a magnetic field of at least 10^{12} Gauss is required.

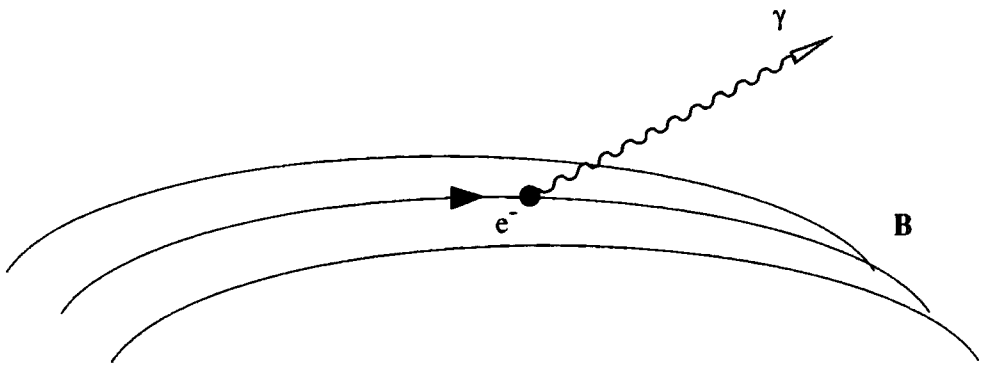

Figure 1.3 Curvature Radiation

1.2.2.3 Bremsstrahlung

When an electron encounters the electrostatic field of another charged particle, it is accelerated and emits a photon (Figure 1.4). The energy of the radiation depends upon the deflection of the electron and has a maximum almost equal to the kinetic energy of the electron. A feature of relativistic bremsstrahlung in astrophysical processes is that a power law distribution of electron energies results in an intensity spectrum for gamma rays of the same form (e.g. Longair, 1992).

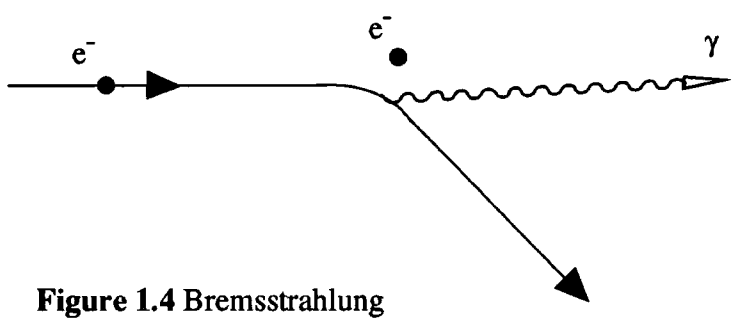

Figure 1.4 Bremsstrahlung

1.2.2.4 The Inverse Compton Effect

A very efficient process for the generation of gamma rays is the interaction of relativistic electrons with lower energy photons (Figure 1.5). A photon of energy E_{ph} which encounters a relativistic electron with energy $E_e = \gamma m_e c^2$ will typically emerge with an energy $E'_{ph} = {}^4/_3\gamma^2 E_{ph}$ (Lang, 1986). For an electron of velocity v, the Lorentz factor, $\gamma = (1 - v^2/c^2)^{-1/2}$.

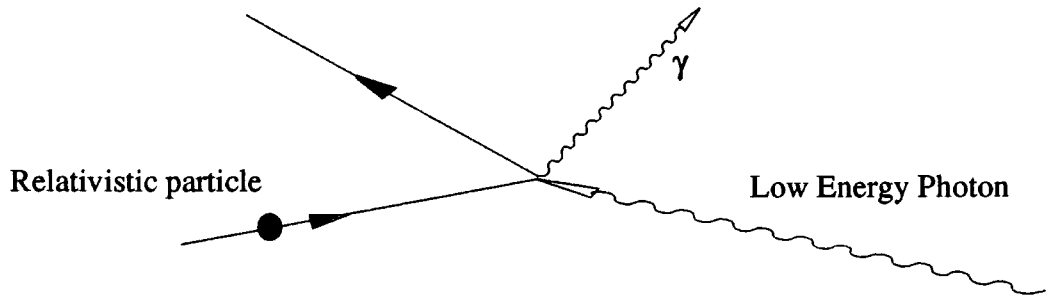

Figure 1.5 Inverse Compton Effect

In the interstellar medium, photons are provided by starlight or the microwave background. In discrete sources, they may be produced at higher energies as the result of synchrotron emission.

1.3 VHE Gamma Ray Absorption

The principle mode of absorption for TeV gamma rays in regions of low matter density is via photon - photon pair production. When the product of the energy of two colliding photons is greater than $(m_e c^2)^2$:

$$\gamma + \gamma \rightarrow e^+ + e^-$$

Gamma rays of energy greater than 10 TeV may interact with photons of the ubiquitous microwave background (Gould & Schréder, 1966; Jelley, 1966). This process may attenuate the emission from galactic sources of gamma rays with energies in excess of 50 TeV (Fig. 1.6). Below 50 TeV, absorption is caused by pair production with background infrared and starlight photons. The interaction length of this mechanism is such that it is unimportant for galactic objects.

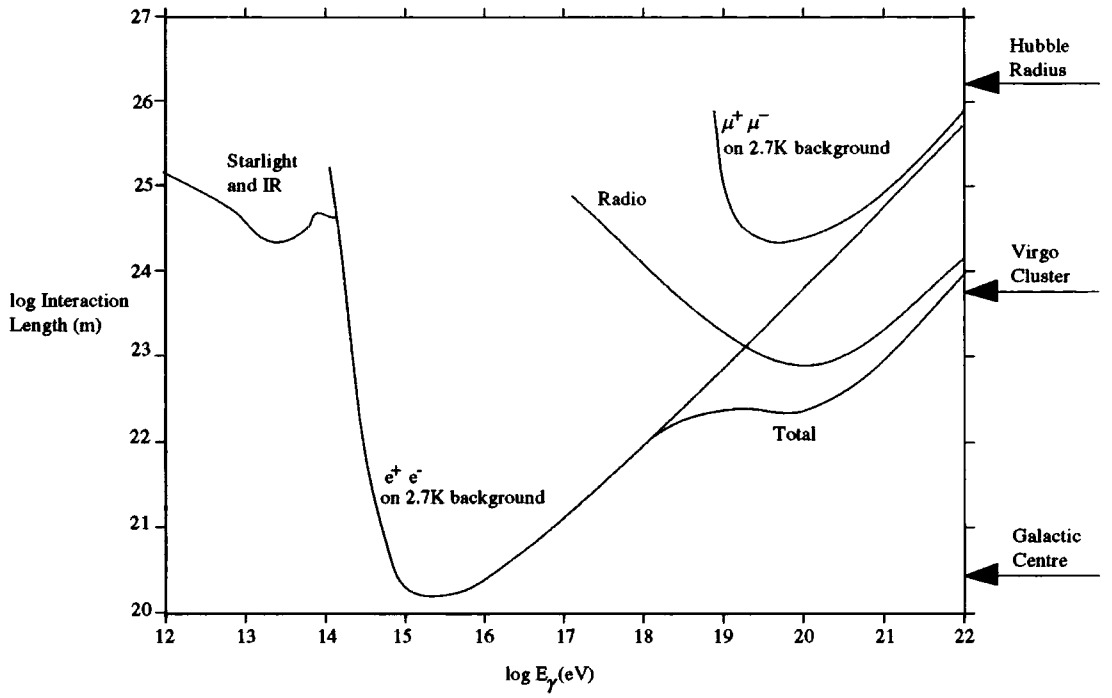

Figure 1.6 Mean free path for a gamma ray against the various background photon fields as a function of energy. (After Ramana Murthy and Wolfendale, 1986)

It has been proposed (Stecker, et al. 1992) that the absorption of TeV gamma rays by the infrared background over intergalactic distances may be useful as a means of measuring the strength of the background. This is discussed in more detail in section 6.2.2.

Pair production may also occur within the electrostatic field of a nucleus, provided that the incident photon has energy > 2 $m_e c^2$. While this has little effect upon gamma rays in free space, it becomes important in regions of high matter density and may lead to absorption of photons close to their source.

Finally, in the very strong (~10^{12} Gauss) magnetic field of a neutron star gamma rays, produced by the curvature radiation process, may interact with virtual photons of the field via pair production.

1.4 Detection Techniques

The vast energy range (0.511 MeV to 100 EeV) covered by gamma ray astronomy has led to the development of a wide variety of instruments for use in their detection. The gamma ray emission from many of the sources which are typically observed follows a steep power law spectrum. Figure 1.7 is the differential spectrum of the unpulsed emission from the Crab nebula and illustrates the rapid decrease in photon flux over the energy range 10 MeV to 10 TeV. The gamma ray spectrum can be divided into a series of regimes based around the detection techniques employed. These are discussed in the following section.

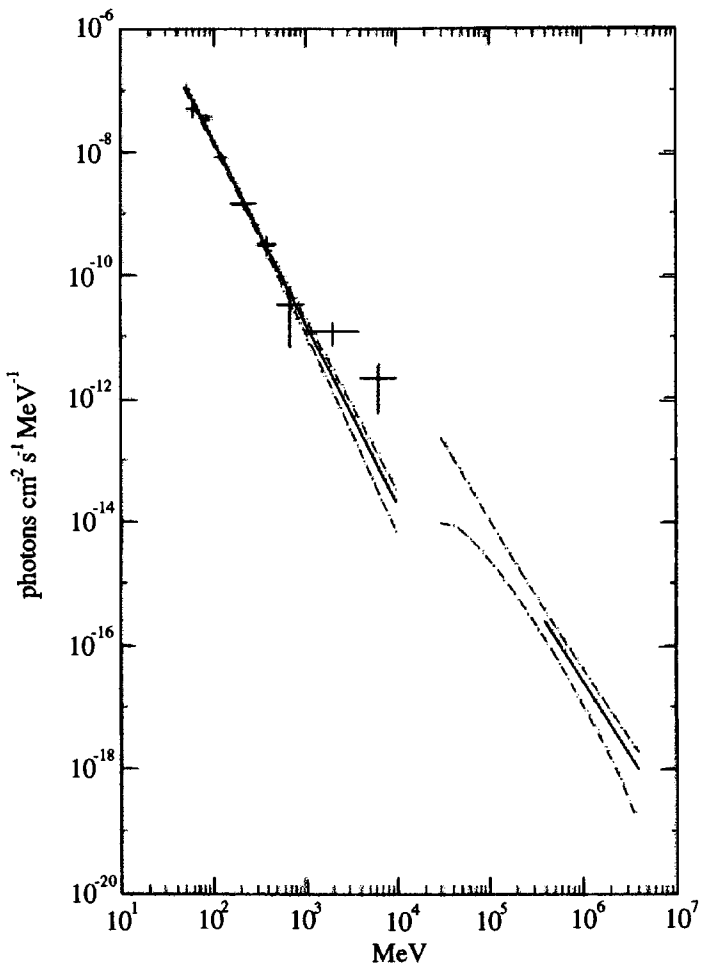

Figure 1.7 Differential spectrum of the unpulsed emission from the Crab nebula (from Nolan, et al. 1993).

1.4.1 Low to High Energy

At energies below 30 GeV, the Earth's atmosphere acts as an effective shield against gamma rays which necessitates the use of high altitude balloon or satellite experiments.

The Compton Gamma Ray Observatory (CGRO) is the second of NASA's "Great Observatories" and was launched in 1992. It carries four of the most sensitive gamma ray detectors developed, a description of which demonstrates some of the techniques in use for observing low to high energy gamma rays.

(i) Oriented Scintillation Spectroscopy Experiment (OSSE)(Fig. 1.8).

This consists of four NaI(Tl) - CsI(Na) scintillation detectors with a collimated field of view of $3.8° \times 11.4°$ full width at half maximum. It operates over the 0.5 to 10 MeV range and provides spectroscopy with an energy resolution of approximately 6%. Both the source and a background region can be monitored simultaneously, or more than one source can be observed.

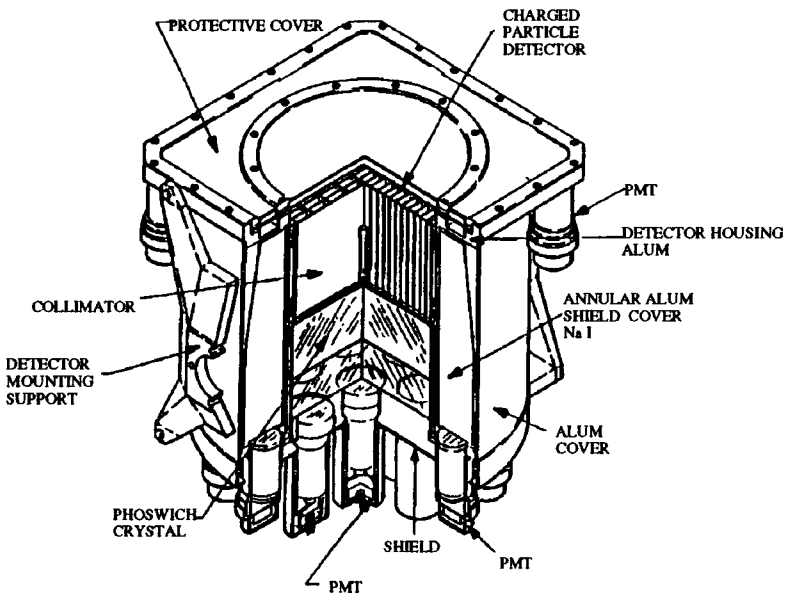

Figure 1.8 An OSSE detector (from Cameron, et al. 1992)

(ii) Burst and Transient Source Experiment (BATSE) (Fig. 1.9).

This comprises four pairs of uncollimated NaI(Tl) scintillation detectors at

each corner of the satellite which give full sky coverage. Each pair is made up of a large area (2025 cm^2) detector with an energy range of 30 - 1900 keV and a smaller (127 cm^2) detector to provide energy measurements in the 15 keV to 110 MeV range. From the relative signal strength in the four large detectors the location of a gamma ray signal can be estimated. BATSE's primary mission has been the observation of gamma ray bursts.

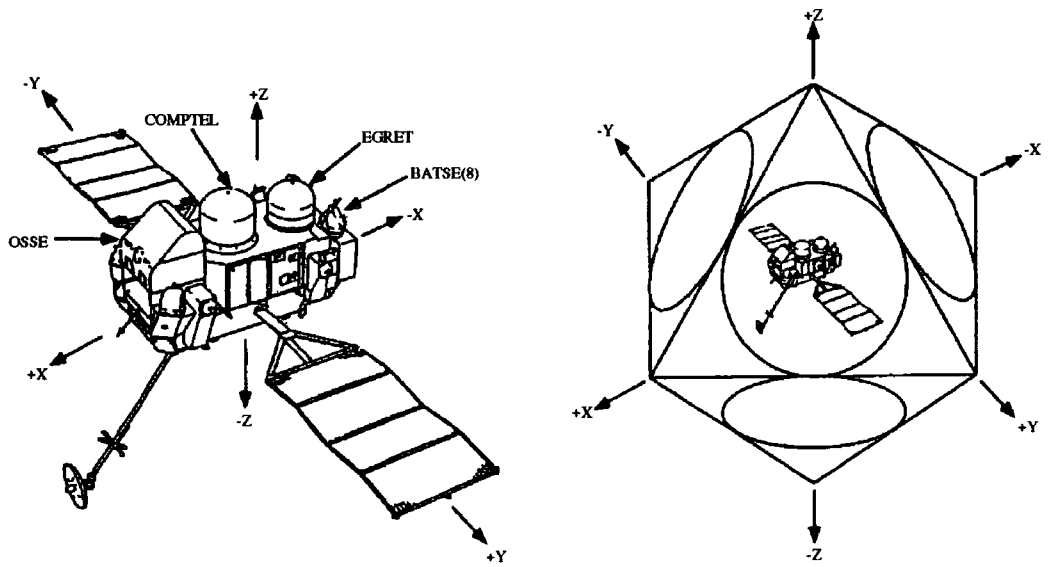

GAMMA RAY OBSERVATORY BATSE DETECTOR ASPECT

Figure 1.9 The location and aspect of the BATSE detectors (from Fishman, et al. 1992)

(iii) Compton Telescope (COMPTEL) (Fig. 1.10).

In the 0.8 to 30 MeV energy range, Compton scattering is an important interaction mechanism. Imaging compton telescopes make use of this interaction to detect gamma ray sources with an angular resolution of one to two degrees. An incoming photon undergoes compton scattering in the first layer of scintillator (D1) and is (ideally) completely absorbed in the second layer (D2). Knowing the energy deposited in each layer allows the Compton scatter angle to be calculated and combining this with the position of the photon in each layer defines a circle on the sky. The superposition of these circles reveals the presence of any point source of

gamma rays. COMPTEL also provides spectral information with a resolution of 10%.

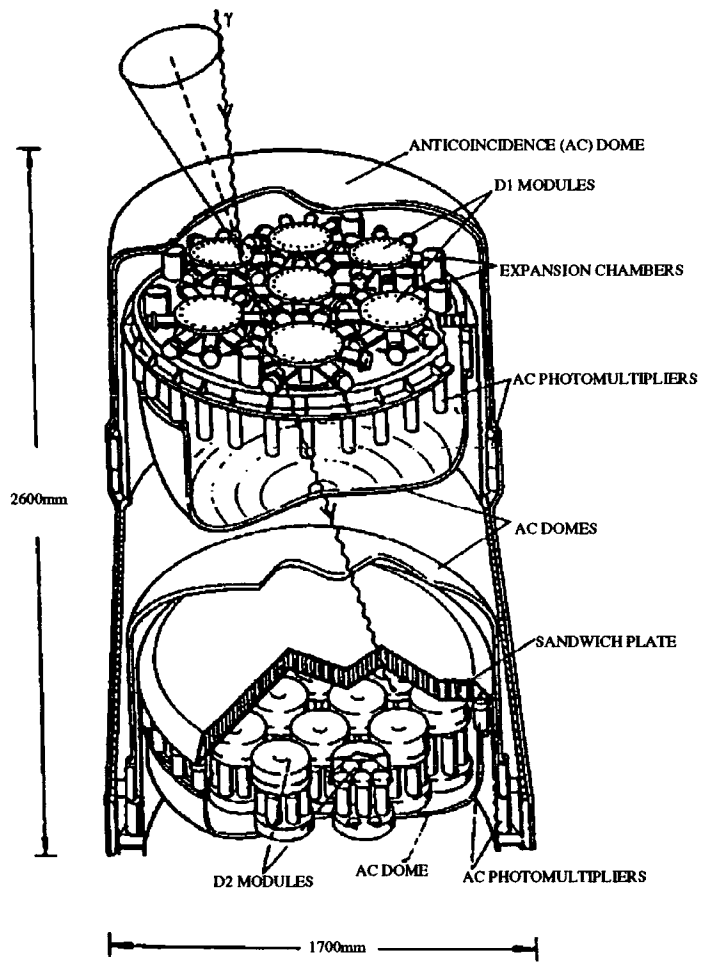

Figure 1.10 COMPTEL (from den Herder, et al. 1992)

(iv) Energetic Gamma Ray Experiment (EGRET) (Fig. 1.11).

At higher energies (above 20 MeV) photons interact almost exclusively via pair production. A spark chamber experiment, such as EGRET, uses this fact to detect and determine the origin of high energy gamma rays. An incoming photon passes through the anti-coincidence shield and enters the spark chamber where it interacts with a tantalum foil to produce an electron positron pair. The cells of the spark chamber are at high voltage such that the passage of a charged particle ionises the gas within them and causes a spark. The position of the sparks follows the track of the charged particles and enables the arrival direction of the incoming photon to be calculated. Energy measurements are made by a scintillation detector below the spark

chamber. EGRET has a 40° field of view and provides an angular resolution of 5 to 10 arcminutes as well as a spectral resolution of 22%.

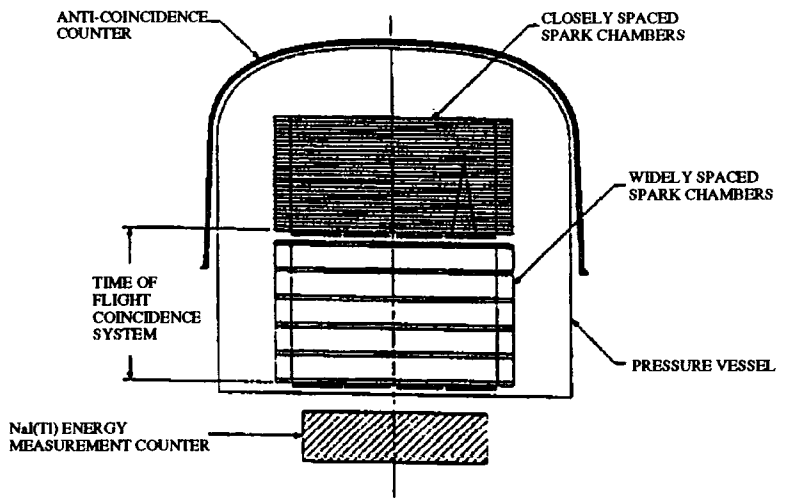

Figure 1.11 EGRET (from Hartman, et al. 1992)

1.4.2 Very High Energy

Above 30 GeV the gamma ray flux becomes negligible for small area satellite-borne detectors. The air cerenkov technique is used to detect the cerenkov radiation from cosmic ray initiated electromagnetic cascades in the atmosphere and has a much larger effective collection area. This technique is described fully in Chapter three.

1.4.3 Ultra High Energy

The remainder of the gamma ray spectrum, from 50 TeV and above , is accessible to ground based scintillator arrays. At these high energies, the particle cascades resulting from an incoming cosmic ray maximize close enough to ground level at mountain altitudes to be detected directly by scintillation detectors. Given sufficient resolution, it is possible to estimate the shower core location and the energy and arrival direction of the primary cosmic ray. Any excess point sources can then be ascribed to a celestial source of neutral particles, probably gamma rays. A typical

array, such as the Tibet II air shower array (Fig. 1.12) consists of 200 scintillation detectors spread over 10^5 m^2.

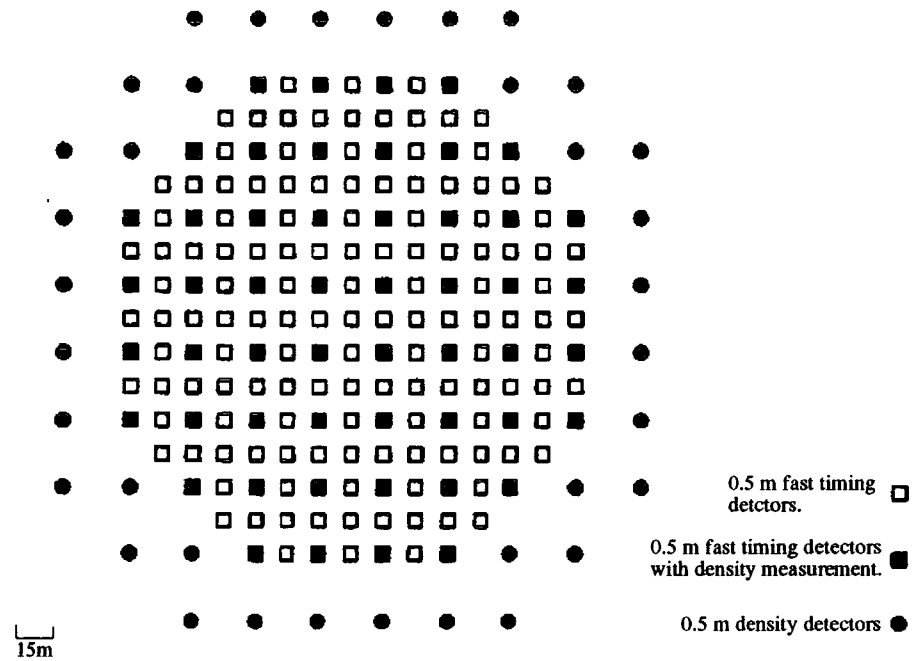

Figure 1.12 Tibet II Air Shower Array (from Amenomori, et al. 1995)

1.5 Summary

The gamma ray region of the electromagnetic spectrum was the last to be exploited as an astronomical window. The subject of this thesis is very high energy (VHE) gamma ray astronomy using the imaging atmospheric Cerenkov technique. Observations made with the EGRET instrument have particular relevance to VHE gamma ray astronomy as they are adjacent in energy range, with the highest energy EGRET photons separated from the lowest energy VHE photons by approximately an order of magnitude.

The most important results from EGRET have been summarised by Fichtel (1996). Over fifty active galactic nuclei have now been detected. These sources have been associated with blazars which are flat spectrum radio loud galaxies. They can

exhibit extreme variability on a timescale of weeks to months. An extrapolation of the typical power law spectra of these sources implies that many of them should be detectable at VHE energies, although emission from the more distant sources would be attenuated by pair production on the extragalactic infra-red background (section 6.2.2). Pulsed gamma rays from seven pulsars have also been observed, again with smooth power law spectra whose extrapolation to TeV energies lies above the flux sensitivity of atmospheric Cerenkov telescopes in some cases. The observation of these sources at TeV energies, whether with positive or negative results, is extremely important for determining the gamma ray production mechanisms involved and the nature of the relativistic particles from which they originate.

There are forty unidentified EGRET sources at low galactic latitudes and associations between some of these and supernova remnants have been suggested by Sturner and Dermer (1995). Supernova remnants are strong candidates as the sources of cosmic ray nuclei and the unambiguous detection of TeV emission from the decay of neutral pions formed in collisions between high energy hadrons would provide significant evidence in support of this theory. In addition, the greater angular resolution of the imaging atmospheric Cerenkov technique may allow mapping of the supernova remnant and reveal where in the remnant the emission is strongest.

In summary, the aim of VHE astronomy is to explore the sites of gamma ray production in order to determine the nature of the source, the type of relativistic particle which produces the photons and the particle acceleration mechanisms involved. This information may in turn enable us to determine finally the source of the cosmic rays. The success of the EGRET experiment has provided a guide for VHE observations which may help fulfil these aims.

CHAPTER TWO - CERENKOV RADIATION FROM EXTENSIVE AIR SHOWERS

2.1 Introduction

As mentioned in Chapter one, VHE gamma rays can be detected by the Cerenkov radiation they cause the atmosphere to emit. This is produced by the electromagnetic cascades which result when a VHE photon interacts in the atmosphere. This chapter includes a description of the development of the extensive air showers (EAS) initiated by both nucleons and photons. The mechanism by which Cerenkov radiation is produced and the implications of this upon Cerenkov emission from charged particles in the atmosphere are also discussed. Finally, the characteristic differences in Cerenkov emission between air showers with nucleon and photon primaries and some of the methods by which gamma ray initiated showers may be recognised are examined.

2.2 Extensive Air Showers

The EGRET experiment on board the CGRO is the largest spark chamber ever operated on a satellite and has an effective area of approximately 1000 cm^2. The flux of gamma rays from a typical source becomes negligible for this detector above an energy of 30 GeV. Extensive air showers are generated when a high energy cosmic ray particle interacts with the Earth's atmosphere. The height of the atmosphere allows the products of such air showers to spread laterally, resulting in much larger effective collection areas for detectors at ground level. The composition and temporal and spatial spread of the shower are dependent upon the nature of the primary particle. In principle, this allows the detection of gamma ray initiated showers over the prevalent background of those with hadronic primaries, which are ~ 1000 times more numerous in the VHE range.

2.2.1 Nucleon Initiated EAS

A cosmic ray nucleus comprised of N nucleons will interact with an interaction length λ_N in the atmosphere, where

$$\lambda_N \approx \frac{Am_p}{\sigma_{N_{air}}}$$

and

$$\sigma_{N_{air}} = \pi R_0^2 (14.5^{1/3} + N^{1/3} - \delta)$$

with R_0 = 1.47fm, δ = 1.12, A = 14.5 (the average atomic mass number for a molecule in air) and m_p is the mass of the proton (Westfall, et al. 1979).This interaction length is longest for a single proton primary (90 gcm^{-2} for a 1 TeV proton), in which case the energy dependence of the interaction length becomes important.

The air shower begins with a process known as pionisation. This is the result of collisions between the incident cosmic ray and nucleons in the atmosphere. Approximately half of the primary energy of the incoming particle is lost in the initial collision during which pions and some kaons are produced. The charged pions, kaons and other nuclear fragments which have not decayed then go on to interact with other nuclei and produce further hadrons. Pion interactions differ from nucleon interactions in that all of the energy of the pion is lost. This nucleonic cascade continues until the energy of the constituent particles is below the threshold for pion production (about 1 GeV), at which point they decay or are brought to rest by ionisation losses.

If the primary particle is a heavy cosmic ray nucleus then the shower will develop more rapidly. The simplest model for the interactions of a cosmic ray nucleus is the superposition model (de Beer, et al. 1966). If the nucleus has a primary energy E_p and an atomic mass A, then the resultant shower is considered to be a

superposition of A showers, each of energy E_p/A. This method tends to overestimate the rate of development of the shower and underestimate the fluctuations in the cascade.

The three pion types are produced in approximately equal numbers. The charged pions may decay via:

$$\pi^+ \rightarrow \mu^+ + \nu_\mu$$

$$\pi^- \rightarrow \mu^- + \bar{\nu}_\mu$$

with a half-life of 2.6×10^{-8} or interact further. Obviously, the higher energy pions with extended lifetimes due to time dilation are less likely to decay. The four kaon species produced at approximately one tenth the rate of the pions can also interact further or decay, producing pions, muons and electrons.

The neutral pion decays very rapidly into two photons which initiate an electromagnetic cascade similar to that observed in a shower with a gamma ray primary (see section 2.2.2).

$$\pi^0 \rightarrow \gamma + \gamma$$

The muon component of the shower is produced mainly in the decay of charged pions produced in the nucleonic cascade, although photopion interactions, kaon decays and pair production ($\gamma \rightarrow \mu^+ + \mu^-$) also contribute. Muons have a very small cross section for nuclear interactions and lose energy at the rate of 2MeV/gcm^{-2} by ionisation. They may also decay via:

$$\mu^+ \rightarrow e^+ + \nu_e + \bar{\nu}_\mu$$

$$\mu^- \rightarrow e^- + \bar{\nu}_e + \nu_\mu$$

with a lifetime of 2.2×10^{-6} s, the resultant electrons contributing in a small way to the electromagnetic component of the shower. A muon with a Lorentz factor >20 will live long enough to reach ground level if vertically incident. Muons are produced

high up in the atmosphere by pions with transverse momenta ~ 0.5 GeV. This results in a wide lateral spreading of the muons as the shower develops. For muons with an energy E_μ > 1GeV, the lateral distribution at sea level as a function of the total number of shower particles, N, and the radius from the shower core, r, is given by (Greisen, 1960):

$$\rho_\mu(r) \approx 18 \left(\frac{N}{10^6}\right)^{0.75} r^{-0.75} \left(1 + \frac{r}{320}\right)^{-2.5}$$

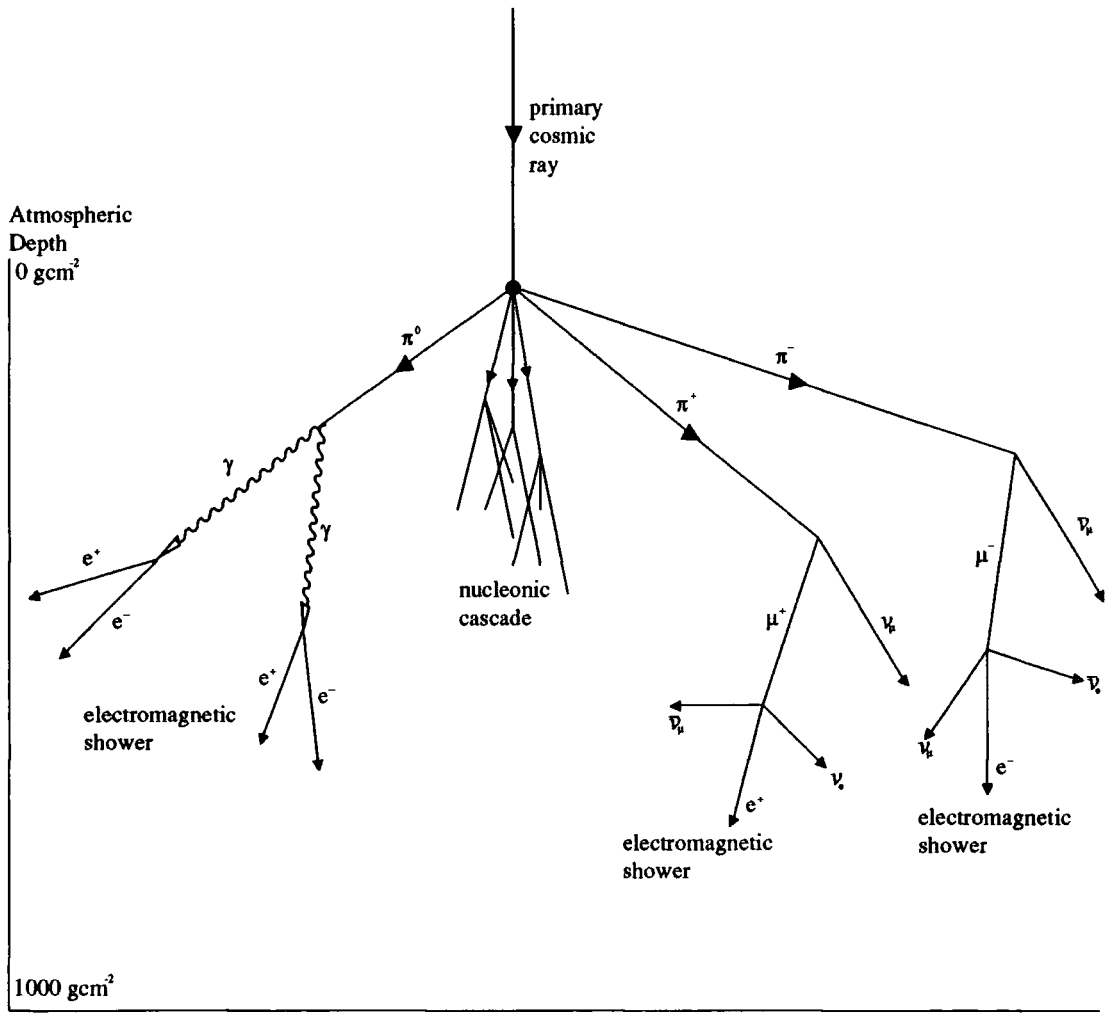

Figure 2.1 A schematic diagram of a nucleon initiated EAS (from Longair, 1992).

2.2.2 Gamma Ray Initiated EAS

A gamma ray photon in the atmosphere will produce an electron positron pair in the electrostatic field of a nucleus ($\gamma \rightarrow e^+ + e^-$). Photonuclear interactions may also occur, resulting in the production of pions and kaons, but the probability of this relative to electron positron pair production is only ~ 2.8×10^{-3}. This results in an air shower which is principally electromagnetic in nature, with the electrons and positrons producing further photons via bremsstrahlung with an interaction length of 37 g cm^{-2}. At TeV energies, approximately 0.1% of the cosmic ray background is composed of high energy electrons (Nishimura, 1994). These will initiate an electromagnetic cascade in the atmosphere which is essentially the same as that caused by a photon primary, the first interaction being Bremsstrahlung and not pair production.

A highly simplified model which reproduces the main features of an electromagnetic cascade is reviewed by Allan (1971). The interaction length for Bremsstrahlung, X_0, is approximately the same as the radiation length for pair production and so the probability of interaction is half at some distance, X_R, given by:

$$e^{\frac{-X_R}{X_0}} = 0.5$$

If we then further approximate that the energy is equally split in each interaction then the average energy of each particle and photon after n interactions is:

$$\langle E \rangle = \frac{E_0}{2^n}$$

where E_0 is the energy of the gamma ray primary. This results in a shower composed of electrons, positrons and photons in equal numbers, shown schematically in figure 2.2.

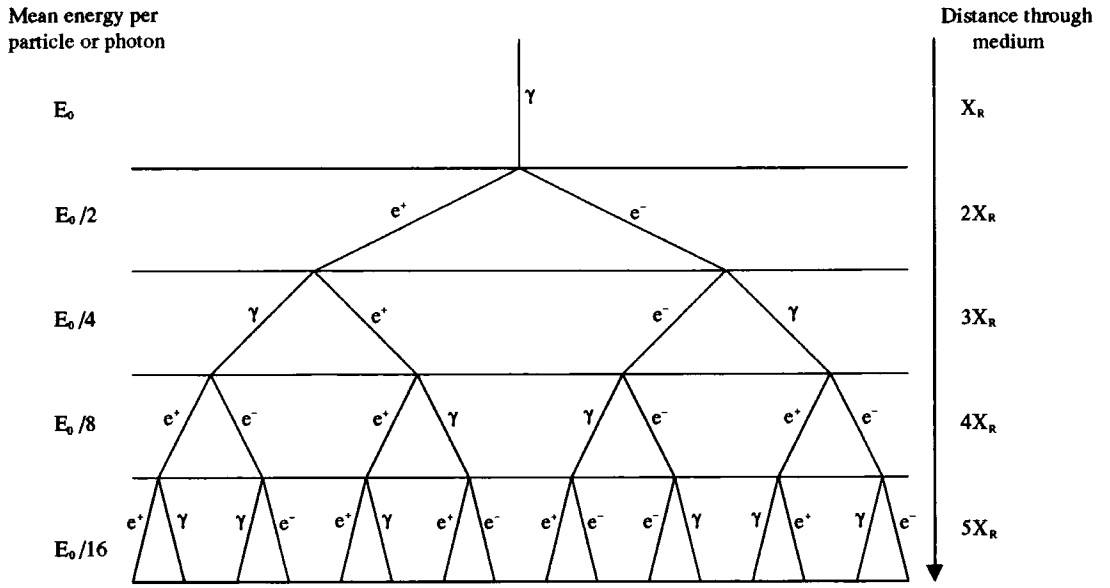

Figure 2.2 A simple model for a photon initiated EAS (from Longair, 1992)

The number of photons and particles in the shower continues to double after each interaction length until the average energy of each drops below the critical energy for air, $E_c \sim 80$ MeV. At this point, ionisation losses become more important than bremsstrahlung for the particles (Fig. 2.3). The cross-section for pair production from the photons also falls until compton scattering and photoelectric absorption dominate (Fig. 2.4). At shower maximum, the total number of particles is:

$$N \sim \frac{E_0}{E_c}$$

and the atmospheric depth is given by:

$$X_{max} \sim X_0 \ln\left(\frac{E_0}{E_c}\right)$$

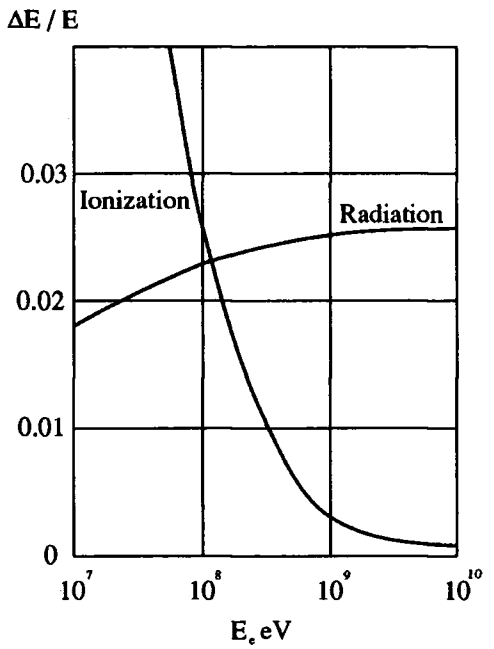

Figure 2.3 Energy loss of electrons through ionization or radiation as a function of energy (Rossi, 1964)

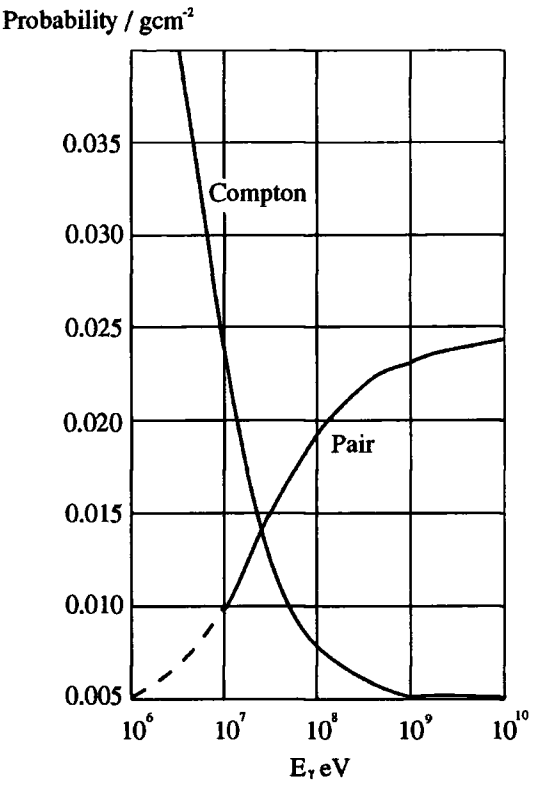

Figure 2.4 The probability of a photon undergoing Compton scattering or pair production in air (Rossi, 1964)

More complete models take account of the ionisation losses and longitudinal dispersion during the growth of the cascade and thus predict fewer particles at shower maximum.The lateral spread of the electromagnetic shower is determined almost entirely by multiple Coulomb scattering of the electrons and positrons (section 2.4.3).

2.3 Cerenkov Radiation

2.3.1 The Cerenkov Effect

The Cerenkov effect was first observed by scientists working with radioactive material as a faint blue light emitted from transparent substances close to a radioactive source. A remarkably accurate classical prediction of this effect was given by Heaviside (1892) and investigations into the nature of the radiation were

first performed by Mallet (1926), but it was not until the experiments of Cerenkov (eg. Cerenkov, 1937) and the subsequent theoretical treatment by Frank and Tamm (1937) that the phenomenon was given a quantum mechanical explanation.

The following qualitative description of the Cerenkov effect is based upon that given by Jelley (1958). When a charged particle passes through a dielectric medium, it induces a polarization in the atoms surrounding it. These polarized atoms are symmetrical, both axially and azimuthally, about the charged particle and so cause no resultant field at a distant point. If the particle is moving with a velocity close to the phase velocity of light within the dielectric then the axial symmetry is lost (Fig 2.5).

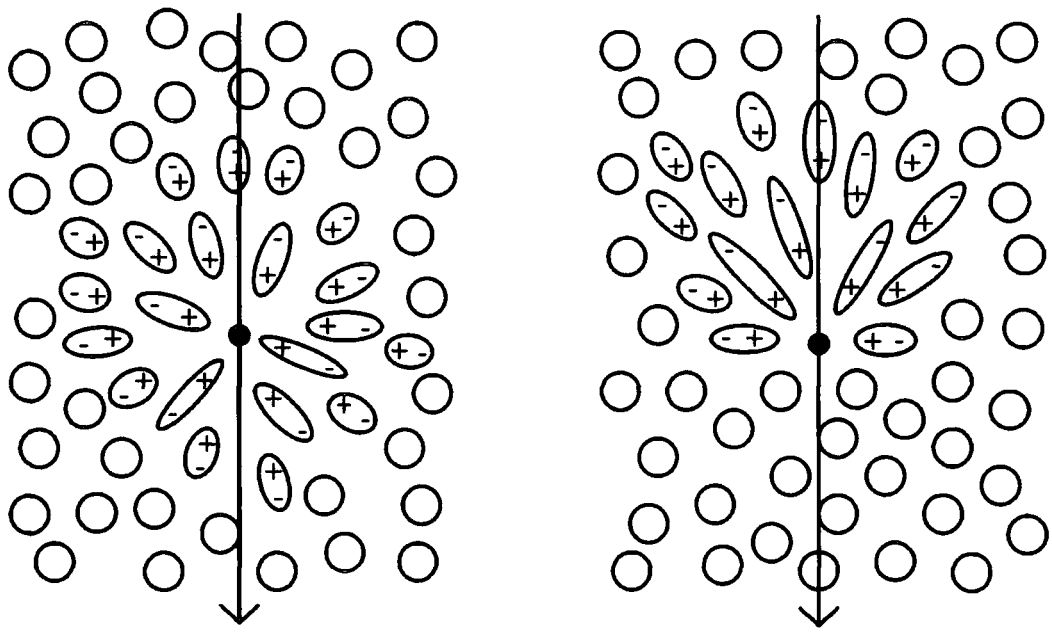

Figure 2.5 The polarization of atoms in a dielectric for a slow moving (left) and fast moving (right) charged particle.

This results in a pulse of radiation from each element along the path of the particle. Generally, this radiation will interfere destructively and will not be observed at a distance; however, if the particle moves faster than the phase velocity of light then the radiation can constructively interfere in certain directions as illustrated in Figure 2.6.

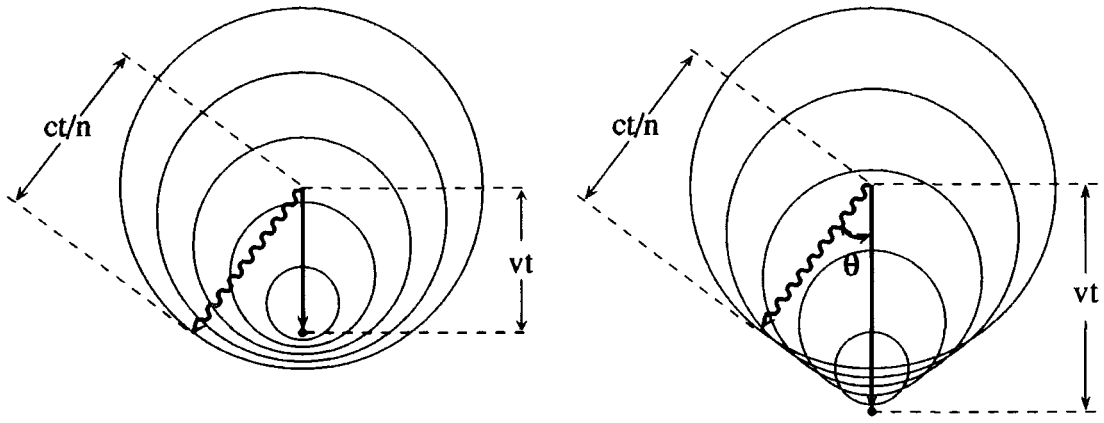

v = 0.8c/n v =1.25c/n

Figure 2.6 Huygen's constructions for charged particles of different velocities.

If the velocity of the particle, $v = \beta c$, then in a time t the particle moves a distance = $t\beta c$. The distance travelled by the radiation in the same time = tc/n, where n is the refractive index of the medium. From this we can derive the angle θ at which the radiation is observed:

$$\cos \theta = \frac{1}{\beta n}$$

The light from each element in the medium is produced in the form of a cone. This conical effect is somewhat analogous to the shock wave produced by a projectile moving faster than the speed of sound in air.

Cerenkov radiation will be produced only when the particle velocity is above $v = \beta_{min} c$, where $\beta_{min} = 1/n$. At this velocity, the Cerenkov radiation is emitted at an angle $\theta = 0$. The maximum angle of emission θ_{max} occurs when $\beta = 1$, therefore:

$$\theta_{max} = \cos^{-1}\left(\frac{1}{n}\right)$$

The conditions for Cerenkov radiation cannot be met if the real part of the refractive index is less than one. In air, this constrains the spectrum of the radiation to wavelengths of ultraviolet and longer.

2.3.2 Cerenkov Radiation in the Atmosphere

The refractive index for all gases is always close to unity, and for air at standard temperature and pressure (s.t.p.) n = 1.00028. Using:

$$\cos \theta_{max} = \frac{1}{n}$$

and writing $n = 1 + \eta$ where η is very small, we obtain:

$$\theta_{max} \sim \sqrt{2\eta}$$

To determine the threshold energy E_T for production of Cerenkov radiation in air we can write $\beta(1+\eta) = 1$ which gives the relation:

$$E_T = m_0c^2 \left(\frac{1}{\sqrt{2\eta}} - 1 \right)$$

The majority of the Cerenkov light from EAS is produced by electrons (Boley, 1964), due to their average energy and number spectra. For electrons in air at s.t.p., $\theta_{max} \sim 1.3°$ and $E_T = 21$ MeV. It is also possible to estimate the photon yield, N, per unit path length, dx, using the expression derived by Frank and Tamm (1937):

$$\frac{dN}{dx} = 2\pi\alpha \left(\frac{1}{\lambda_1} - \frac{1}{\lambda_2} \right) \sin^2\theta_{max}$$

where α is the fine structure constant = 1/137 and λ_1 and λ_2 are the boundaries of the wavelength range of the emission. Approximating $\sin \theta_{max}$ as θ_{max} and assuming a wavelength range of 350 nm to 500 nm gives:

$$\frac{dN}{dx} \approx 390\ \theta_{max} \approx 780\ \eta$$

which at s.t.p. corresponds to 0.2 photons per cm.

The refractive index of the atmosphere is proportional to its density and hence pressure and temperature. Since the atmospheric pressure varies approximately

exponentially with height h above sea level, we can write:

$$\eta = \eta_0 e^{\frac{h}{h_0}}$$

where $\eta_0 = 0.00028$ and the scale height of the atmosphere, $h_0 = 7.1$km. The relationship between refractive index and density implies similar correlations with the properties of the Cerenkov emission, such that:

$$E_T \propto \frac{1}{\sqrt{\rho}}$$

$$\frac{dN}{dx} \propto \rho$$

$$\theta \propto \sqrt{\rho}$$

These relationships are illustrated in Figure 2.7. At shower maximum for an air shower initiated by a gamma ray of energy 1 TeV, the atmospheric depth is ~ 300 gcm^{-2} and the average particle energy is ~ 80 MeV. This produces radiation with a Cerenkov angle ~ 0.65° at the rate of ~ 0.07 photons cm^{-1} particle^{-1}.

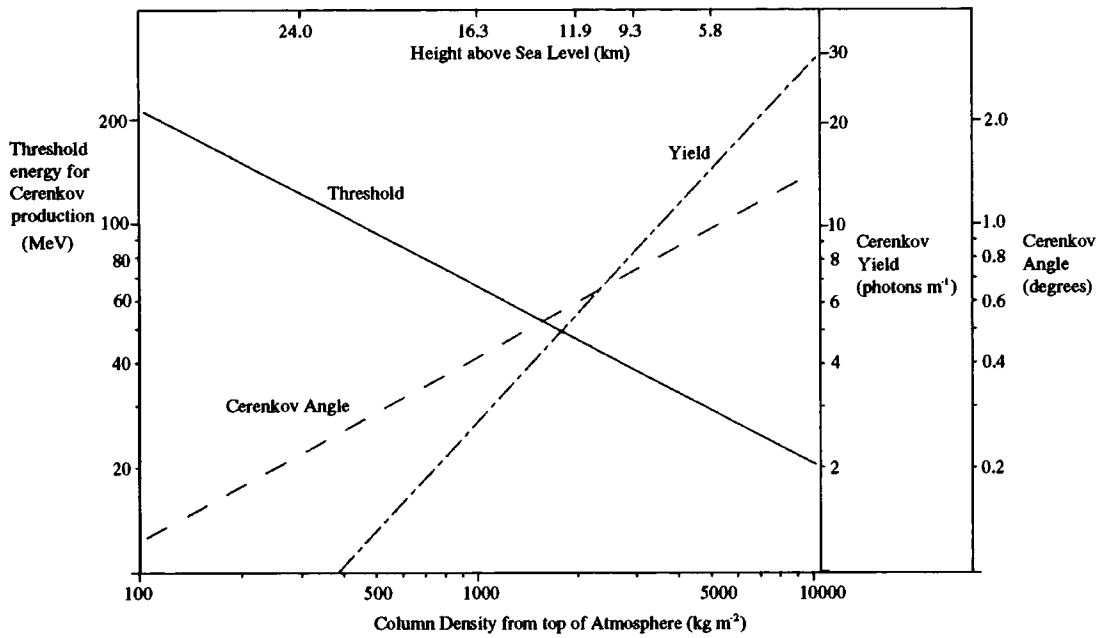

Figure 2.7 The variation with atmospheric depth of different properties of the Cerenkov radiation (from Ramanamurthy and Wolfendale, 1986).

The nature of the Cerenkov flash is therefore dependent upon the development of the EAS. The maximum intensity of Cerenkov production occurs when the number of particles in the cascade is greatest, i.e. when the average particle energy is at E_c, the 80 MeV critical energy discussed in section 2.2.2. Once emitted, the radiation can be attenuated by Rayleigh scattering, aerosol scattering and ozone absorption, with approximately half of the emitted photons surviving to ground level.

2.4 Differences in Cerenkov Emission from Nucleon and Photon Initiated EAS

2.4.1 The Cerenkov Image of EAS

Figure 2.8 illustrates some of the differences between a typical photon and proton initiated EAS. Of immediate note is the much greater width of the proton shower, due to the production of pions with large transverse momenta in strong interactions. The Cerenkov light produced by either type of shower forms an image in

the shape of a column in the sky which is aligned with the arrival direction of the primary particle. In the case of the photon initiated shower, half of the Cerenkov light is emitted within 21m of the shower axis and at a median altitude of 8km for vertically incident showers. For the proton induced shower the same proportion of light is emitted 500m closer to the ground and within 70m of the shower axis (Hillas, 1996), making the proton shower image appear much broader to an observer at ground level. The measurement and parameterisation of this image allows the identification of photon initiated showers. The imaging technique of gamma ray signal enhancement is discussed in greater detail in Chapter three.

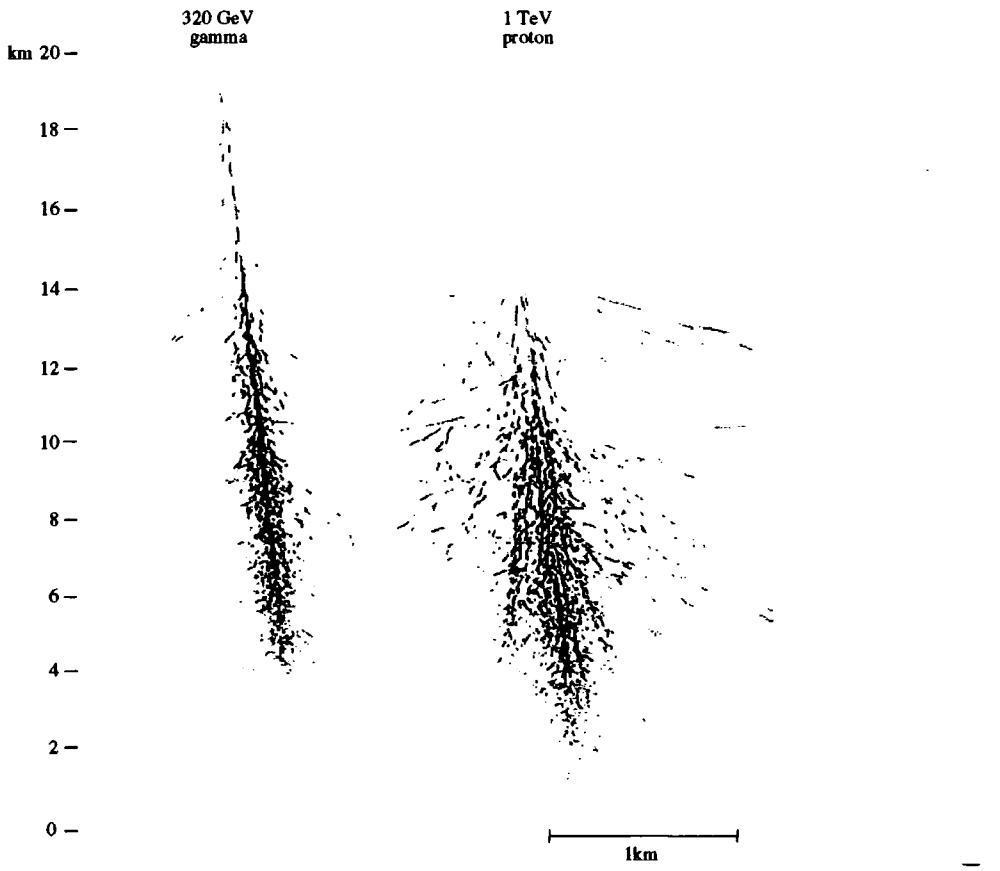

Figure 2.8 Simulation of the development of gamma ray and proton initiated EAS. The lateral scale is exaggerated by a factor of five and the picture is thinned down by showing each particle track as a sparsely dashed line (from Hillas 1996).

2.4.2 The Temporal Spread of Cerenkov Photons

The arrival times of Cerenkov photons at ground level can be used in two ways to discriminate between photon and nucleon initiated showers. In the first

method the Cerenkov light is sampled at a number of points on the ground, enabling the angle of the shower front and hence the arrival direction of the primary particle to be derived. The Durham group used this method of wavefront sampling to observe the Crab Pulsar for a total of 34 hours in 1981. They observed two significant bursts of emission pulsed at the period seen at other wavelengths and lasting 15 minutes each (Gibson, et al. 1982). Further observations during 1982-83 showed evidence for weak persistent emission in 103 hours of exposure with the arrival direction of the pulsed flux being clustered around the source position (Dowthwaite, et al. 1984).

Pulse shape discrimination methods involve sampling the Cerenkov wavefront at a single point and examining the structure of the signal time profile. Showers with nucleonic primaries are expected to show more features in their pulse profile than those with photon primaries as their greater lateral spread and less uniform distribution of shower particles leads to the Cerenkov light emitted being detected after travelling a range of path lengths. The penetrating muon component of nucleon initiated EAS will emit Cerenkov light closer to ground level which is received before the majority of the pulse. Tumer, et al (1990) report the detection of gamma ray emission from the Crab Nebula with a significance of 4.2 σ after rejecting 95% of showers on the basis of a manual analysis of their pulse shapes. More recently, Roberts (1993) has attempted to parameterise the pulse profile in terms of its rise-time, fall-time, pulse maximum and full width at half maximum. This method would appear to be less subjective and less susceptible to electronic or sky noise effects.

2.4.3 The Cerenkov Light Pool on the Ground

The differences described above between the development of nucleon and gamma ray initiated EAS lead to differences in the distribution of the Cerenkov light at ground level. The exponential nature of the atmosphere results in many interaction lengths being traversed in a short space of time. This produces a thin disc of

secondary particles, the lateral extent of which is defined by the opening angles of the interactions and by multiple Coulomb scattering.

Gamma rays, with an interaction length of 37 gcm^{-2}, initiate an electromagnetic cascade high up in the atmosphere. This leads to a Cerenkov light pool on the ground of approximately 150 m radius. The distribution of light across the pool is essentially flat; however, there is a region of increased photon density around the circumference of the pool known as the Cerenkov shoulder (eg. Hillas, 1996). As the density of the atmosphere increases, so too does the angle of Cerenkov emission, causing a focussing effect at large radii (Fig. 2.9).

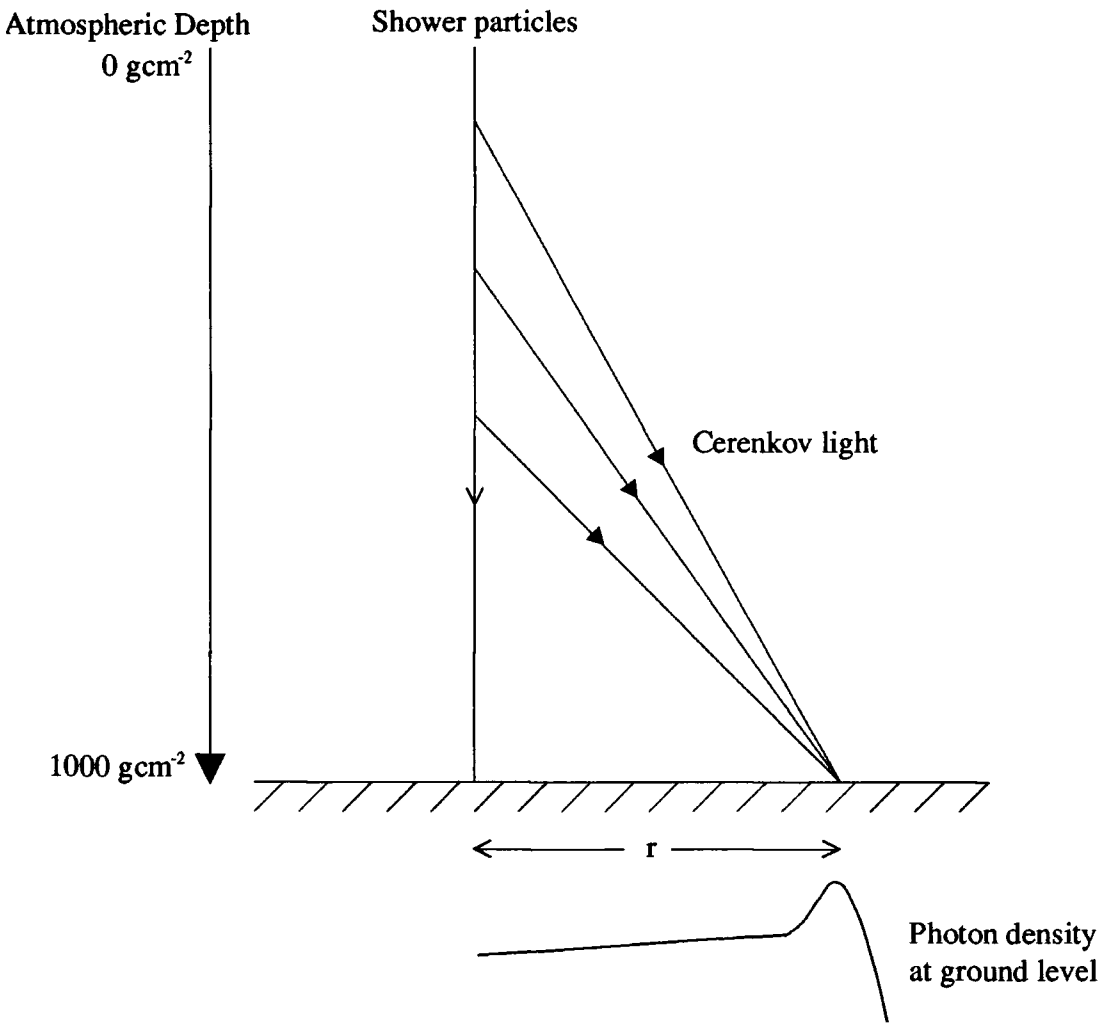

Figure 2.9 Focussing of Cerenkov light due to changing angle of emission.

At shower maximum the focussing is less effective due to multiple Coulomb

scattering of the low energy electrons.The effect of multiple Coulomb scattering is given by (Gaisser, 1990):

$$\langle \delta\theta^2 \rangle = \left(\frac{E_s}{E} \right)^2 \delta t$$

where $E_s \sim 21$ MeV and δt is the distance travelled in gcm^{-2}. For electrons of energy E = 100 MeV, $\langle \delta\theta \rangle_{RMS} \sim 12°$. Beyond the shoulder, the photon density falls off rapidly as $1 / r^2$

Nucleon initiated EAS typically begin much lower in the atmosphere as the interaction length for a VHE proton in the atmosphere is ~ 100 gcm^{-2}. This results in a Cerenkov light distribution on the ground which is sharply peaked about the shower core. In addition to this, other peaks are caused by electromagnetic cascades initiated by pions produced with large transverse momenta in the nuclear interactions. The penetrating muon component of the shower also generates Cerenkov radiation from lower in the atmosphere, giving rise to intense local peaks of emission.

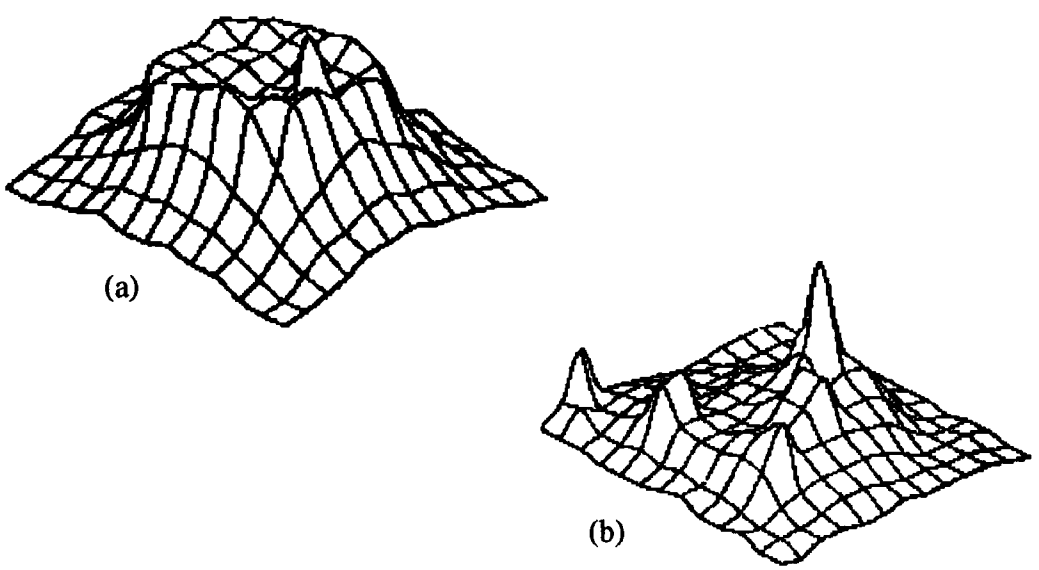

Figure 2.10 Simulations of the Cerenkov photon densities on the ground from EAS initiated by a) 320 GeV gamma ray b) 1TeV nucleon, both vertically incident. The shower axis is at the centre of each figure and the grid spacing is 50 m (from Hillas and Patterson 1987).

2.4.4 The Ultra-Violet Component of the Cerenkov Light

The Cerenkov light produced by an EAS undergoes absorption in the atmosphere. Attenuation of the UV component of the light is greater than at other wavelengths due primarily to ozone absorption. It has been suggested (e.g. Fegan, 1992) that the penetrating muon component of nucleon induced EAS may produce UV light at low altitudes which will not be so effectively absorbed as light emitted by other shower particles higher up in the atmosphere. This could lead to spectral differences between the detected Cerenkov light from gamma ray and nucleon initiated EAS. Monte Carlo simulations by Hillas (1996) suggest that these differences are small for a detector at an altitude of 2.3 km. It is possible that the differences may be more pronounced for a detector at sea level.

2.4.5 The Polarization of the Cerenkov Light

The final feature to consider is the intrinsic polarization of the Cerenkov radiation from air showers. If all of the emitting particles were travelling along the shower axis, the resulting radiation would be polarized along the direction of the shower axis. In practice, the direction of motion of each particle in the shower can vary widely from the shower direction but the expected differences in polarization between gamma ray and nucleon initiated EAS are modest (Fig. 2.11) and difficult to measure (Hillas, 1996).

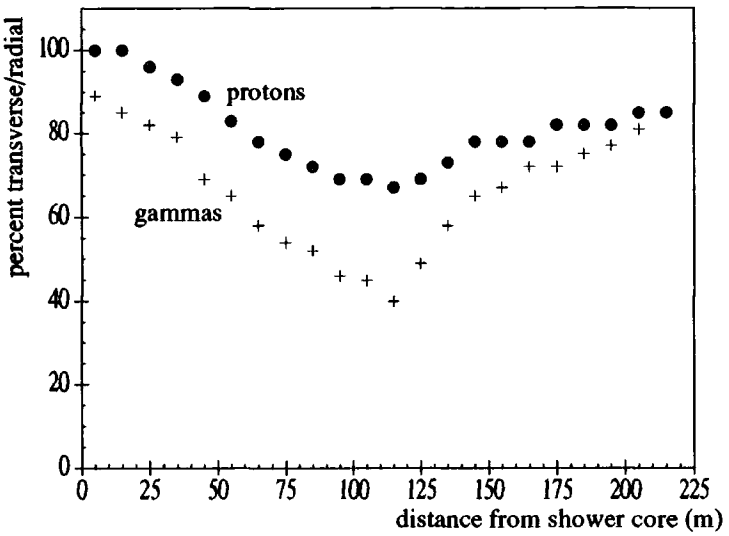

Figure 2.11 Polarization of Cerenkov light (from Hillas, 1996).

2.5 Summary

In this chapter the development of extensive air showers and the characteristics of the atmospheric Cerenkov radiation they produce has been discussed. These characteristics define the specifications of an instrument for gamma ray detection using the atmospheric Cerenkov light flash. A large flux collector of reasonable optical quality on a steerable mount is required to collect as many Cerenkov photons as possible. This light must be focussed on to a high gain detector with a response time ~ 1ns, which is sensitive over the relevant wavelength range (~ 300 to 500 nm). The signal recorded in the detector must be observable over the detector response to background sky light. Finally, the system must be designed to have some discriminatory power between the EAS induced by nucleon or gamma ray primaries.

There are three basic systems currently in use: single dish telescopes, coincidence telescopes and stereo systems. Single dish telescopes are simple to engineer and allow a large mirror area on a single mount; however, the detector gain

must be kept reasonably low to prevent false sky noise triggers and they will also record the Cerenkov light produced by penetrating muons close to the telescope. Coincidence telescopes have more than one flux collector in close proximity and require the detectors from each flux collector to trigger simultaneously for a Cerenkov event to be recorded. This allows the detector gain to be increased without swamping the system with false sky noise triggers. Furthermore, spatial coincidence requirements limit the number of penetrating muon triggers. Coincidence telescopes are more complex to engineer than single dish systems and the total mirror area is split between each of the flux collectors. Stereo systems also use more than one flux collector but these are widely spaced to provide parallax which permits the three-dimensional reconstruction of the Cerenkov light distribution in space and hence better gamma ray selection capabilities. The requirement that a shower be observed by widely spaced detectors reduces the effective collection area for each individual detector and these systems are also costly to construct.

The design of an atmospheric Cerenkov telescope is discussed in more detail in the next chapter, with particular emphasis on the coincidence telescopes used by the University of Durham gamma ray astronomy group.

CHAPTER THREE - THE ATMOSPHERIC CERENKOV TELESCOPE

3.1 Introduction

Extensive air showers and the Cerenkov radiation caused by them have been discussed in Chapter two. This chapter deals with the methods for detecting this Cerenkov radiation at ground level and how this can be used for gamma ray astronomy. The basic elements of an atmospheric Cerenkov detector are examined, followed by a summary of their application and the current status of ground based gamma ray astronomy. A description of the three telescopes operated by the University of Durham is given, as well as the calibration methods and routine data processing necessary to interpret their observations.

3.2 The Generic Atmospheric Cerenkov Telescope

All atmospheric Cerenkov telescopes (ACT's) consist of three principal components: the steerable optical system, which collects the flux of Cerenkov photons, the detector package and the data acquisition system. The contributing factors which influence the design of these components are examined in this section.

3.2.1 The Steerable Optical System

Unlike other telescopes, the collection area for the photon flux for an ACT is defined not by mirror size, but by the size of the Cerenkov light pool on the ground. This being the case, the choice of mirror area is influenced by the need to collect as many photons as possible in order to lower the telescope's detection threshold and by engineering considerations.

The scale of the Cerenkov image of an EAS as seen by an ACT is ~ 1° and the scale of meaningful structure within the image is ~ 0.2° (Weekes, 1988). Mirror

quality is therefore less important than in other optical systems. The shape of the reflector is also not critical, although the use of a paraboloid removes on-axis spherical aberrations and ensures the isochronous arrival of light at the detector. This improves the efficiency of the telescope triggering system by giving maximum illumination of the detector within its response time. Off-axis aberration in the form of coma is still present but can be reduced at the expense of isochronous performance and on-axis image quality.

The choice of mirror surface is dictated by the spectrum of the Cerenkov emission. The differential spectrum is proportional to λ^{-2} with atmospheric absorption due to ozone cutting the spectrum off at approximately 300 nm (Jelley, 1967). The surface chosen for the University of Durham ACT's is anodised aluminium. This material has a specular reflectivity of ~ 80%, peaking at a wavelength of 400 nm. The mirrors are vacuum formed to the required shape and consist of a thin reflective surface bonded to an aluminium honeycomb backing which is plated with a thicker aluminium sheet (Fig. 3.1). A full description of the mirror manufacturing process is given by Dickinson (1995).

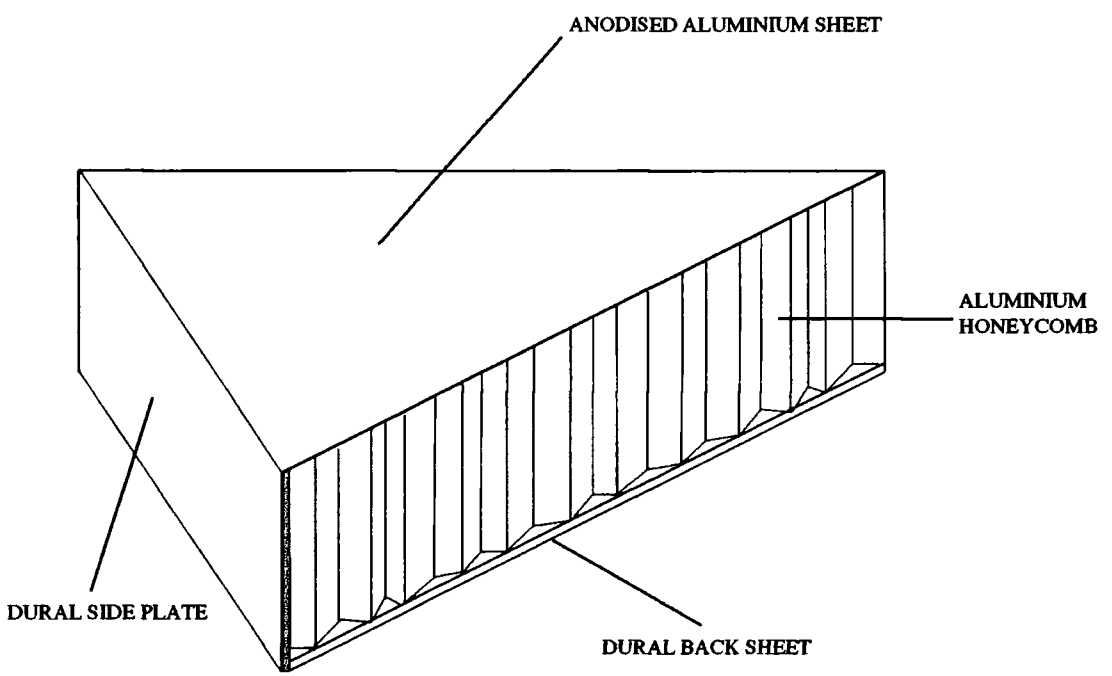

Figure 3.1 Cross-section of a Durham telescope mirror segment.

Financial and engineering considerations dictate that most large ACT's are steered by an alt-azimuth mount and not equatorial. Observations can be performed in three operational modes. Drift scanning entails setting the detector attitude at a constant zenith and azimuth angle and allowing the candidate source to transit across the field of view. An equal angular region either side of the source is observed to provide a background for comparison. In tracking mode, the candidate source position is maintained at the centre of the telescope field of view to provide the maximum on source exposure time but no background. This technique is most useful when searching for pulsed emission from a source.

The chopping mode provides a control background by displacing the telescope pointing away from the source direction and has been exploited in two slightly different ways. In the first method, the source is observed for two minutes, followed by a background region alternately two degrees right and left of the candidate source position (Bowden, et al. 1992a). This method minimizes the effects of large scale changes in sky brightness throughout the observation but results in a changing background field as the region of sky viewed appears to rotate around the source. The second method involves tracking a source region for a longer period of time (normally fifteen minutes for Durham observations) and then steering the telescope back to track the same region again after the candidate source has passed. The second scan then provides the background for the first. This method reduces the time spent steering the telescope between source and background regions but may be subject to count rate changes caused by changing sky conditions. This effect can be minimized by keeping the on source/off source cycles shorter than the typical time scale for atmospheric changes, subject to a minimum of $\sim$ 10 minutes to ensure the off source region does not overlap the on source.

3.2.2 The Light Detector Package

As described in section 2.3.3, the Cerenkov image from an EAS is formed by

a thin disc of particles moving at approximately the velocity of light in vacuum. This results in a very brief (~ 2 ns) pulse of light at ground level, with photon densities of ~ 0.1 photons m^{-2} GeV^{-1} for gamma ray initiated cascades, which can be detected over the background of night sky light. What is required then, is for a detector with a very fast response time, sensitive over a suitable spectral range and with high gain and photon detection efficiency. The photomultiplier tube (PMT) is ideal for this application, having a rise time ~ 2 ns, a gain of 10^3 - 10^8 and a spectral response which can be defined by the choice of window and cathode material (Fig. 3.2). The quantum efficiency of a PMT describes its photon to photoelectron conversion efficiency and is of the order of 25%.

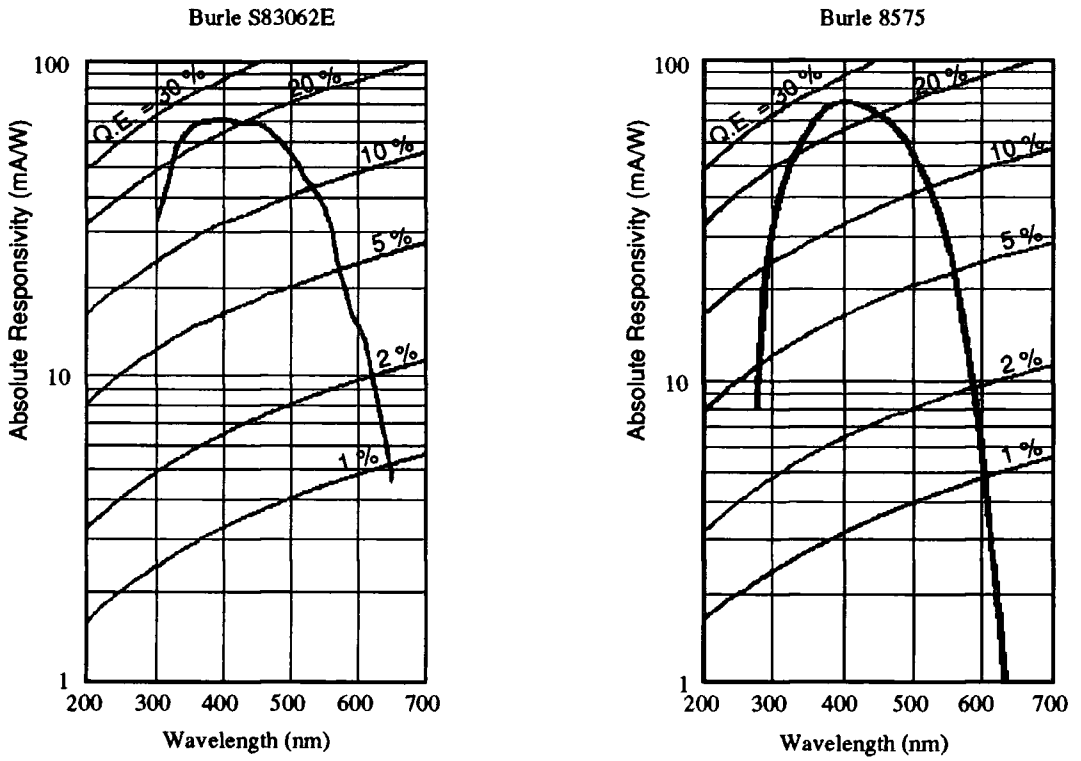

Figure 3.2 Spectral response characteristics for two different types of PMT.

PMT's in atmospheric Cerenkov telescopes usually operate in a state of photoelectron "pile-up", in which more than one background photoelectron is recorded per resolution time per detector. In this mode of operation, the background light is observed as a D.C. offset in the PMT output. The ability of the detector to resolve the Cerenkov pulse is then limited only by the noise fluctuations of the

background.

Following Weekes (1988), the standard deviation in the number of photoelectrons due to the noise fluctuations, N, is given by:

$$N \propto \sqrt{A\varepsilon\tau\Omega\phi}$$

where A is the mirror area, ε, the PMT quantum efficiency, τ, the integration time, Ω, the solid angle subtended by the PMT and ϕ, the night sky background flux. As the recorded Cerenkov signal, $S \propto A\varepsilon$, then the signal to noise ratio varies as:

$$\frac{S}{N} \propto \sqrt{\frac{A\varepsilon}{\tau\Omega\phi}}$$

and the minimum detectable signal is proportional to the inverse of this function.

An improvement in the signal to noise ratio and associated decrease in detector threshold can be achieved by the use of coincidence techniques. Here, the signals from more than one mirror/detector system are required to exceed a discrimination threshold within a narrow time interval for an event to be recorded. The rate, R, at which the coincidence requirement is fulfilled by chance is given by:

$$R = C!\, n^C\, t^{(C-1)}$$

where C is the number of PMT's in coincidence, n is the count rate of each PMT and t is the coincidence gate width. Maintaining a low rate of chance coincidences is necessary to improve the signal to noise ratio. As more detectors are added to the coincidence criterion the gain, and hence detection efficiency for true Cerenkov signals, can be increased for a constant chance coincidence rate. The University of Durham telescopes operate with a three-fold spatial coincidence requirement, which has been shown to provide 85% of the maximum detector efficiency (Brazier, 1991) while remaining cost effective and mechanically feasible. Coincidence techniques also remove background events caused by the passage of local muons through the

transparent window material of PMT's in the detector.

The size of the detector package is determined by the required field of view and the associated sky noise acceptance. The Durham telescopes have a field of view of ~ 3° in diameter which collects the majority of the light produced by an EAS.

3.2.3 Electronics and Data Acquisition

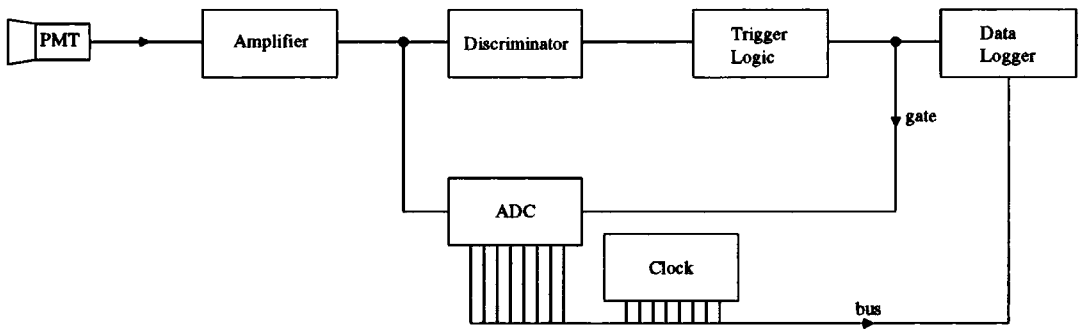

Figure 3.3 A schematic representation of the Data Acquisition system for an ACT

The essential elements of the data acquisition system for an ACT are shown in Figure 3.3. The signal from the PMT is amplified and passed through a discriminator. If the peak voltage of the pulse exceeds a preset discrimination level then the signal has "triggered" and a logic pulse is output to indicate this to the trigger logic unit. The trigger logic unit is used to decide if all of the trigger conditions are met. In the case of the Durham telescopes, the trigger conditions are satisfied if a trigger pulse is received from corresponding PMT's in the other two detector packages within the coincidence gate time, t ~ 10 ns. For single mirror systems, the trigger logic may require a coincident trigger from any two PMT's within the detector package.

When the trigger conditions are met, a gate is opened to the analogue to digital converter (ADC) and the integrated analogue pulse from each PMT is recorded in the form of digital bits by the data logger, along with a time stamp and any other information about the event. The integration time,τ , should be matched to

the duration of the Cerenkov pulse and be as short as possible to reduce the amount of integrated background noise.

3.3 The Development of the Atmospheric Cerenkov Technique

3.3.1 Early History

The possibility of a Cerenkov component in light from the night sky was first considered by Blackett (1948). He estimated its contribution to the total night sky flux to be ~ 10^{-4}. The detection of such a small fraction is infeasible as it is much smaller than fluctuations in the mean background light.

Galbraith and Jelley (1953) realised that the very large number of charged particles in an EAS might produce a detectable pulse of Cerenkov light. Their early experiments consisted of a small (25cm diameter) parabolic mirror with a PMT at the focus connected to an amplifier, pulse height discriminator and oscilloscope. They detected showers in coincidence with a particle detector array.

Morrison (1958) was the first to propose a search for sources of extra-terrestrial gamma rays and Cocconi (1960) predicted a flux of TeV photons from the Crab nebula 1000 times more intense than the background flux of nucleons. Predictions such as these led to the first searches for celestial point sources using ACT's. Two groups, one in Ireland and another in the USSR were particularly active and performed drift scan observations on various radio sources such as supernova remnants, quasars and magnetic variables (Chudakov, et al. 1962, Fruin, et al. 1964). These observations failed to confirm the optimistic predictions and by the late 1970's there were still no reliably detectable sources.

3.3.2 The Imaging Technique for VHE Gamma Ray Astronomy

Photographs of the Cerenkov image of EAS were produced by Hill and Porter (1961) using an image intensifier device. It was quickly realised that the

information available in the image might provide some means of gamma ray signal enhancement (Porter and Long, 1963) but technical problems and the high energy threshold ($\geqslant 10^{15}$ eV) of the experiment precluded further development. Simulations based on analytical models of cascade development also suggested that the differences between the images produced by gamma ray and nucleon initiated EAS would be small (e.g. Zatsepin, 1965).

Weekes and Turver (1977) were the first to suggest the use of a large array of PMT's at the telescope focus. They envisaged a system with a large (3.5°) field of view which would allow the monitoring of an on-source and off-source region of sky simultaneously. The selection of images with a centre close to the centre of the field of view would then provide a gamma ray rich sample. This methodology has been exploited by the Durham telescopes via the use of a "guard ring". In this technique, a central on-source PMT is surrounded by a ring of off-source PMT's separated by a suitable angular distance (~ 2°). Events which trigger the telescope can then be classified into three groups: those which trigger the on-source detector alone, those which trigger only guard ring channels and those with a trigger in both (Fig 3.4). By selecting only those events which trigger the on-source channel alone, ~ 60% of the background of nucleon initiated shower images are rejected. Nearly all of the gamma ray events are retained, thus improving the signal to noise ratio by a factor of 2 to 3.

The obvious limitation to this technique is that the signal to noise ratio cannot be improved beyond the ratio of gamma ray to nucleon events as viewed by the central PMT. As well as this, the steeply decreasing energy spectrum of cosmic rays results in many of the Cerenkov images being detected at a level just over the threshold of a given channel. In the case of the on-source channel, this type of event may well have a reasonably large component of its image within the field of view of a guard ring PMT, indicative of an off-source nucleon event. Because of this, selection of single channel on-source triggers leads to a bias towards faint flashes of any origin. This problem increases for observations made at large zenith angles where the

Cerenkov image decreases in size due to the greater distance of the maximum development of the shower from the telescope.

The problem of faint flashes can be solved by a further selection process. The signal below the triggering threshold for the off-axis tubes is recorded for each event. We then demand that this signal must be less than some preset level relative to the central tube in order for the event to be accepted. With this criterion, all events are treated in the same manner regardless of the total signal size, the only limit to the technique being set by the inherent PMT noise. A typical guard ring analysis of data from an ACT is presented in Chapter 4.

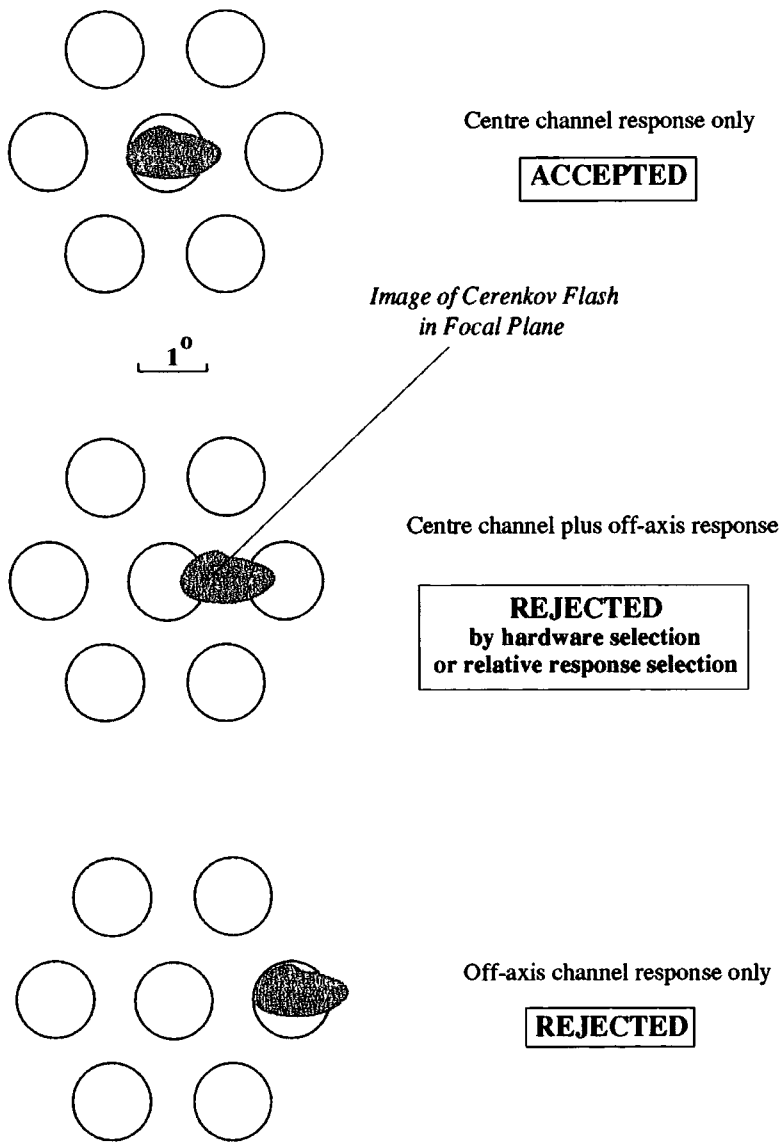

Figure 3.4 Illustration of the guard ring technique for background rejection

In the 1980's, the rapid growth of computing power and the application of "Monte Carlo" techniques allowed much more accurate simulations of the Cerenkov light from EAS to be made. The most influential of these was by Hillas (1985) and based upon the response of the 37 element PMT camera of the Whipple Observatory ACT. As the shower images are approximately elliptical, Hillas parameterised the images he produced using standard moment fitting procedures (Fig. 3.5). The parameters are described in Table 3.1.

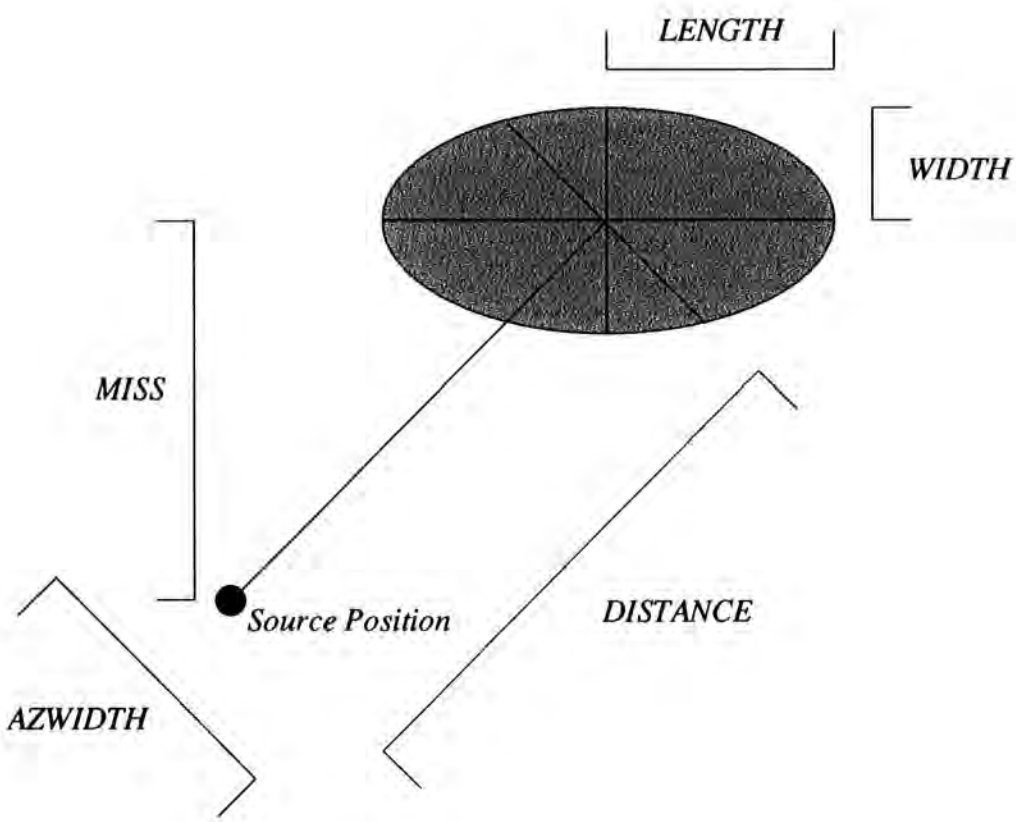

Figure 3.5 The Hillas parameters

Table 3.1: The Hillas parameters

WIDTH	The RMS length of the semi-minor axis of the image. *Width* is sensitive to the lateral spread of the shower.
LENGTH	The RMS length of the semi-major axis of the image. *Length* is sensitive to the longitudinal development of the shower.
MISS	The perpendicular distance between the major axis and the centre of the field of view. The *miss* parameter is a measure of image orientation and as such is sensitive to the arrival direction of the primary particle.
DISTANCE	The distance from the centre of the field of view to the centroid of the image.
AZWIDTH	An abbreviation of azimuthal width and defined as the RMS width of the image perpendicular to a line joining the centre of the field of view and the image centroid. The *azwidth* parameter is dependent upon both the width and the orientation of the image and will be smallest for narrow images pointing to the centre of the field of view.
FRAC(2)	The ratio of the two largest tube signals to the total tube signal.

Some additional derived parameters have developed since the original publication, most notably *ALPHA* = $\sin^{-1}$(*MISS/DISTANCE*). This is the angle between the major axis of the image and the radius drawn from the centre of the camera through the centre of the image.

Applying this parameterisation to simulated images of EAS revealed significant differences between gamma ray and nucleon initiated showers. These differences can be understood qualitatively as follows. The nucleon initiated showers have a larger average lateral spread than the gamma rays, producing broader images. Also, if the axes of the showers are aligned parallel with the optic axis of the detector then the major axes of the images will point towards the centre of the field of view.

This will be the case for gamma ray showers originating from the source position, but not for the isotropic background of nucleon initiated EAS. An example of a simulated gamma ray and proton initiated shower as parameterised in an imaging camera are shown in Figure 3.6. Rejecting events on the basis of the Hillas parameters can therefore be used to enhance a gamma ray signal, with *azwidth* being the best single discriminant. A quality factor, Q, is used to quantify the efficiency of a set of cuts and is defined by:

$$Q = \frac{\eta^{\gamma}}{\sqrt{\eta^{N}}}$$

where η^{γ} and η^{N} are the fractions of gamma ray and nucleon events retained by the cuts, respectively (Fegan, 1992).

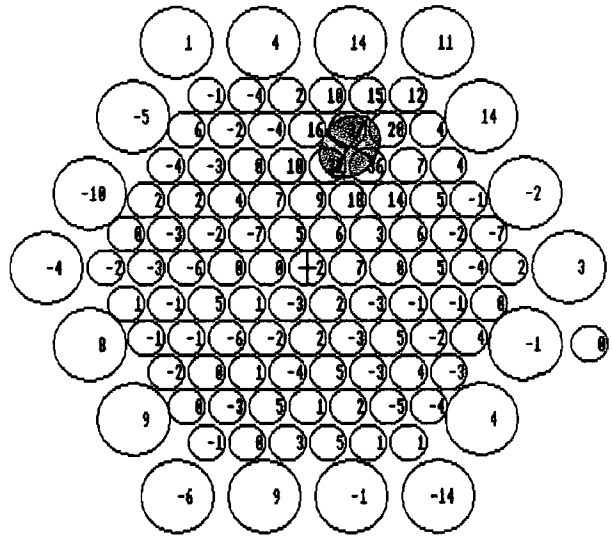

Gamma Ray

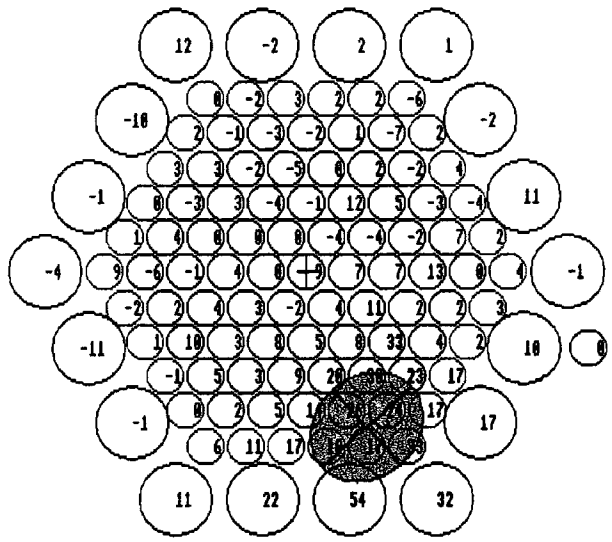

Proton

Figure 3.6 Examples of a simulated gamma ray and proton image.

The value of the imaging technique has been demonstrated on observations of the Crab nebula (Weekes, et al. 1989) taken in the chop mode. Using an azwidth cut value determined by the simulations to reject ~ 99% of the nucleon event background, an excess of events from the on-source region was seen in 82 hours of on-source data, significant at the 9σ level. This was the most significant detection of a VHE gamma ray source at the time and, unlike many of the other detections, the

flux appeared to be constant over a timescale of years.

3.3.3 Recent Developments in the Field

Developments over the last decade have proceeded in two main directions: improved background rejection and lower energy threshold for the detection of gamma ray EAS images. The Whipple Observatory detection of the Crab nebula using the imaging technique has resulted in the development of a number of imaging ACT's worldwide. These systems tend to have more pixels and therefore higher resolution than the original Whipple camera in order to provide more accurate measurements of the image parameters and hence improve the background rejection. A summary of some current imaging systems and their characteristics is given in Table 3.2.

Table 3.2: Summary of some current imaging systems

Name	Pixels	Resolution	Mirror Area
Durham Mk6 (Chadwick et al. 1995b)	109	0.24°	~120 m^2, 3 dish
Whipple 10m (Fegan, 1996)	109	0.23°	~70 m^2, 1 dish
HEGRA CT1 (Rauterberg et al. 1995)	127	0.24°	~5 m^2, 1 dish
BIGRAT (Patterson et al. 1995)	37	0.25°	~38 m^2, 3 dish
CANGAROO 3.8m (Kifune et al.1993)	220	0.12°	~12 m^2, 1 dish

Systems are currently under construction with > 500 pixel detectors (eg. Lamb, 1995).

Further improvements in background rejection have been achieved by the use of multiparameter cuts. The current Whipple Observatory "Supercuts" recipe is estimated to reject ~ 99.7% of the nucleonic background showers whilst retaining ~ 50% of the gamma rays (Fegan, 1996). The cut values used have been optimized using data from observations of the Crab nebula. Various different parameter cutting

approaches have been investigated, such as neural networks (Reynolds, 1991), singular value decomposition (Danaher, et al. 1993), genetic algorithms (Lang, 1995) and cluster analysis techniques (Fegan, 1996) with varying degrees of success.

The other major effort has been in reducing the energy threshold of ACT's for gamma ray images. Turver and Weekes (1978) predicted that the ratio between the Cerenkov light produced by gamma ray and proton showers would dramatically increase below a primary energy of 1 TeV from a value of ~ 2 to ~ 14 at 100 GeV (Fig. 3.7). It is also desirable to lower the threshold in order to explore the region of the electromagnetic spectrum between EGRET energies and current ACT's (~ 30 - 300 GeV). The simplest way to accomplish a reduction in threshold is with an increase in mirror area; however, this is costly and logistically difficult. The other option is to increase the gain of the detector package. This can be achieved, whilst maintaining a reasonable rate of events caused by random noise fluctuations, by the use of more sophisticated trigger logic. Spatial correlation between pixels in a single detector can be exploited, for example, by requiring that a certain number of pixels within the detector must trigger and that they must be adjacent. Detectors other than the PMT are also being considered. Solid state devices such as the avalanche photo-diode have a quantum efficiency ~ 3 times higher than that of PMT's (Lorenz, 1993). These detectors are not practical for ACT's as yet, the major problem being the suppression of noise.

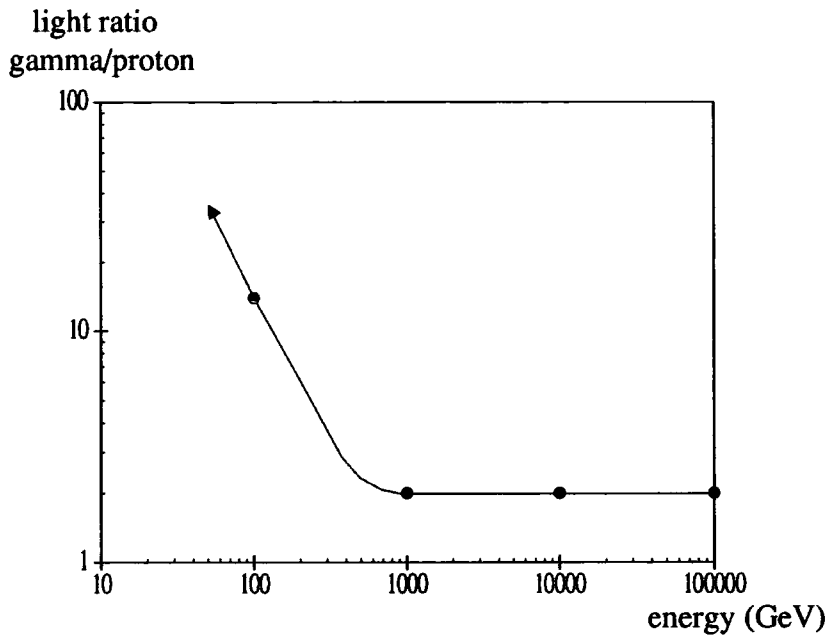

Figure 3.7 Cerenkov photon yield ratios for gamma ray and proton showers of the same energy at 100 m from the shower core (after Turver and Weekes, 1978).

The operation of more than one ACT at the same observing site can produce improvements in both background rejection and energy threshold. A simplistic analysis of the improvement in quality factor obtained by using two telescopes (a "stereo" system) gives the combined quality factor (Thornton, et al. 1995):

$$Q_{12} = Q_1\left(\frac{\eta^{\gamma}}{\sqrt{\eta^{N}}}\right)(f\ Q_2)$$

where Q_1 and Q_2 are the quality factors of each telescope, η^{γ} and η^{N} the fraction of gamma ray and nucleon events, respectively, observed by both telescopes. The factor f is less than unity to indicate the existence of correlations between the image parameters derived by each telescope. An alternative approach to a simple combination of the information provided by each telescope about the image parameters is to define new parameters which exploit the correlations between the images seen in each telescope. These correlations will tend to be stronger for the more uniform gamma shower images. This type of analysis is discussed in section 3.4.4

The stereo technique can be used to reduce the energy threshold for gamma rays if the telescopes are operated in a hardware coincidence mode. This is essentially the same as the coincidence techniques which have been described in section 3.2.2. As more telescopes are added to the coincidence, the probability of noise fluctuations producing a chance coincidence falls and so the detectors can be operated with a higher gain and hence a lower threshold. Low thresholds are best achieved by placing the telescopes as close together as possible such that their collection areas overlap completely. High background rejection can be obtained by widely separated telescopes which view the showers from different angles (Chadwick, et al. 1996, Kohnle, et al. 1996). Any stereoscopic system will represent a compromise between these variables.

The current status of any field of astronomy is best illustrated by its source catalogue. Table 3.3 presents those sources which are considered most credible. This is the catalogue presented by Weekes (1996) with the addition of the active galactic nucleus (AGN) Markarian 501. The recent report of emission from this source (Catanese, et al. 1995a), significant at the 8.4 σ level warrants its inclusion in the catalogue.

Table 3.3: TeV source catalogue

Source	Nature	Detections	Variable	Periodic
Crab Nebula	SNR	Whipple, Sandia, Crimea, ASGAT, HEGRA, Themis., CANGAROO	No	No
PSR1706-44	SNR	CANGAROO	No	No
Vela X-1	X-Ray Binary	Durham, Potchefstroom	Yes	Yes
AE Aqr	CV	Durham, Potchefstroom	Yes	Yes
Mkn 421	AGN	Whipple, HEGRA	Yes	No
Mkn 501	AGN	Whipple	Yes	No

It can be seen that there are a variety of different objects of interest in the TeV gamma ray sky. AGN, Supernova remnants (SNR), cataclysmic variables (CV) and X-ray binaries feature in the table above and transient emission has been reported from other examples of these as well as from isolated pulsars (see Weekes, 1988 for an earlier catalogue). While some of these earlier, less significant detections may have been statistical fluctuations, others may simply prove to be highly variable in nature and further observations with more sensitive telescopes will clarify their status as sources.

3.4 The Durham Instruments

The three ACT's of the Durham VHE Gamma Ray Observatory are located at the Bohena settlement near Narrabri, New South Wales, Australia, latitude 30° 28' 20.6" south, longitude 149° 39' 36.5" east at an altitude of 260 m above sea level. The site was chosen as the southern skies contain the majority of X-ray binaries, the galactic centre and the large and small Magellanic clouds, all of which are of astrophysical interest. It was previously occupied by the University of Sydney giant

air shower array (SUGAR) and so fulfilled the logistical requirements.

3.4.1 The Site Facilities

A plan view of the site is shown in Figure 3.8. The Mark 3 and Mark 5 telescope were the original stereo pair and are situated 100 m apart along an east/west line. The Mark 4 telescope has now been decommissioned. The Mark 6 was added in 1995 and is approximately 20 m from the Mark 3, such that it may also form a stereo pair with the Mark 5. Each telescope has its own local control room constructed out of shipping containers. A further container is used as a general control room, known as the "annex", from which the operation of all three telescopes may be monitored.

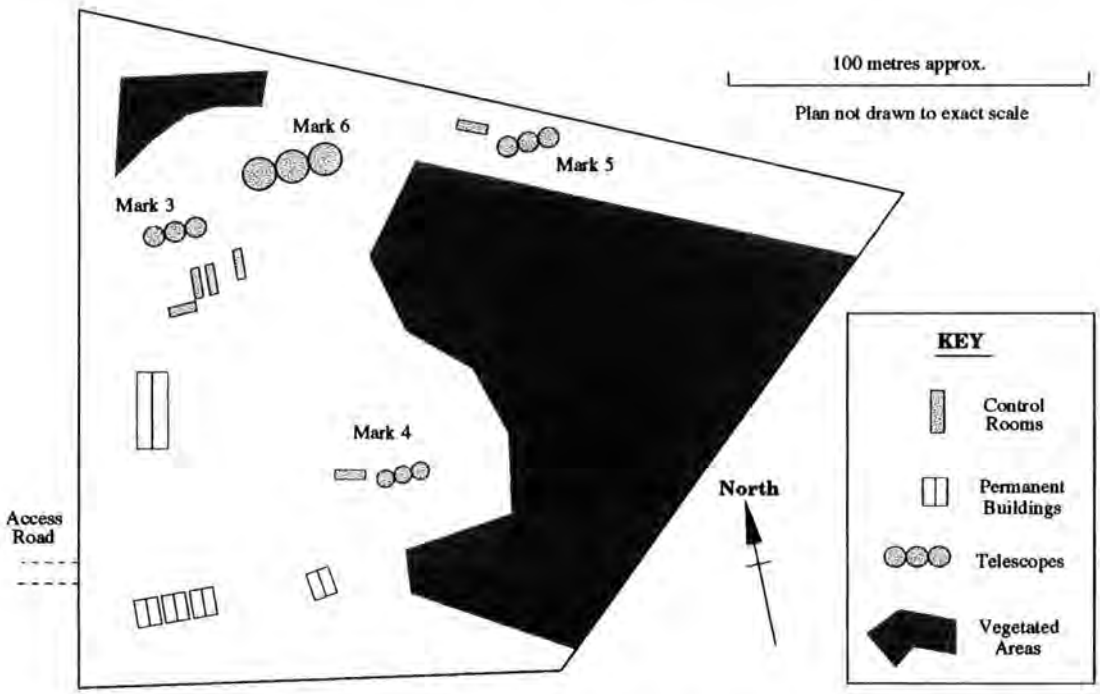

Figure 3.8 A plan view of the facilities at the Bohena site.

To help with the operation of the telescopes, there is a sitewide computer network. Each telescope has its own local area network (LAN) and all computers are linked via a wide area network (WAN). A feature common to all of the telescopes is the performance monitoring system. This runs on an Archimedes microcomputer installed in each of the local control rooms and is used to display and record

environmental conditions, steering information, coincidence rates and instantaneous values of the anode current and noise trigger rate for every PMT. The same information is also displayed on remote monitors installed in the annex such that the observer may be aware of any irregularities in the operation of any of the telescopes.

Accurate timekeeping is obviously of great importance when periodic analysis of millisecond pulsar signals is required. Timing information for each of the three telescopes is provided by a Rubidium atomic oscillator housed in the Mark 3 control room. This Efratom model FRK-L Rb oscillator provides a 10 MHz output signal which is used to time stamp events to μs accuracy. The oscillator is provided with a battery back-up power supply, sufficient to cover a 10 day mains failure. The Rb clock was first synchronised to an off-air radio time signal in January of 1987 and its constant drift rate has been measured regularly since. Initially this was by comparison with an Australian timing standard radio signal but this was replaced in April 1992 by a Global Positioning Satellite (GPS) system installed in a PC. An oscillator which loses its power and is restarted is prone to drift at a different rate and so such interruptions are avoided. Drift rate since the latest restart has been 0.05287 ± 0.00005 ms day^{-1} (Dickinson, 1995). Figure 3.9 illustrates the remarkable stability of this drift rate relative to the value of UT (Universal Time) received from the GPS system.

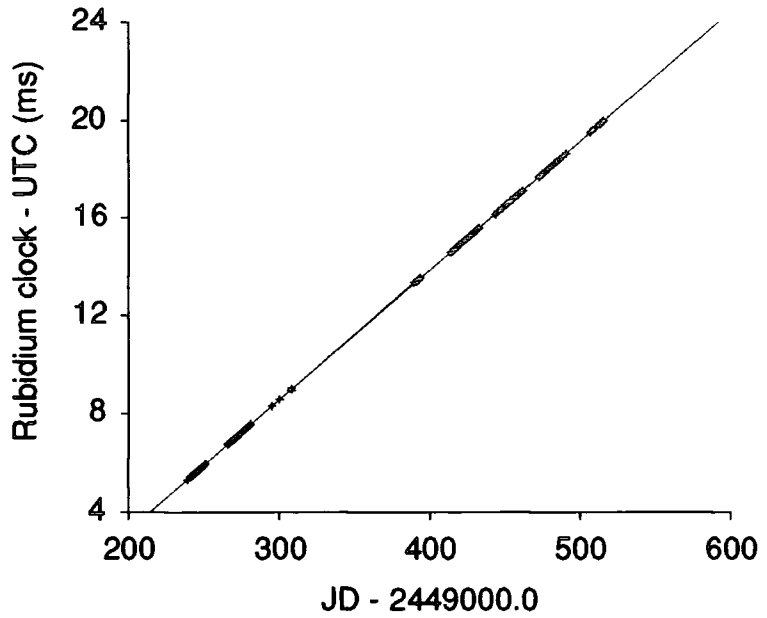

Figure 3.9 The drift of the Rubidium clock delay measured relative to GPS.

The site is manned for ~ 10 dark moon periods every year, a typical observing trip being three weeks long. The weather is generally excellent except during midsummer when lightning storms can cause serious problems. During the colder months, condensation and ice may form on the mirrors as they are radiatively coupled with the cold night sky. The adverse effect of condensation on the reflectivity of the mirrors is removed by spraying the mirrors every night prior to the observations with a high quality wetting agent. This prevents droplet formation for up to 12 hours and gives mirror performance equal to that on dew free nights. Ice formation is a more difficult problem but may be solved in the future by positioning fans around the flux collectors to circulate the air. The nearest town is over 20 km distant and so light pollution is not a problem. The total duty cycle of the telescopes is estimated to be ~ 10%.

3.4.2 The Mark 3 Telescope

The Mark 3 was constructed in Durham and moved to Narrabri in 1986. It has undergone various upgrades to the mirrors and detector packages during its

operation. The following sections describe the principle characteristics of the telescope.

3.4.2.1 The Mirrors

In the telescope's original form, all three of the flux collectors were tessellated structures, the left and right collectors being composed of 43 mirrors and the centre collector of 44. Each individual mirror was 60 cm in diameter and each flux collector had a diameter of 4 m and a focal length of 2.45 m. The effective mirror area was 11 m^2 for each collector. The mirrors were constructed out of aluminium using the technique outlined in section 3.2.1. There has been no noticeable change in reflectivity due to mirror degradation over the ten year lifetime of the experiment.

For the three-fold coincidence technique to be effective, it is important that the optic axes of the three flux collectors are parallel. This was accomplished by directing the telescope at a second magnitude star and examining the anode currents of the on-axis PMT's. The position at which the anode currents were maximum was noted relative to the image of the star viewed by an analogue video camera mounted on the telescope superstructure. Adjustments were made by manipulating the structure supporting the detector packages.

In April 1993 the central flux collector was replaced by a new collector of the type developed for the Mark 5 telescope. The consists of 12 mirror segments, each of which represents a 30° sector of a composite parabolic flux collector. The mirrors were aligned using a system of parallel laser beams to simulate a point source at infinity (Dickinson, 1995). The width of the point spread function at full width half maximum (FWHM) is ~ 2.5 cm. This flux collector has a focal ratio of approximately 1.0, with a mirror diameter of 3.5 m and focal length of 3.32 m. It is surrounded by baffles in order to reduce background light which increases the noise in the PMT's.

3.4.2.2 The Telescope Mount and Steering

The telescope is mounted on an alt-azimuth platform which was developed from a Royal Navy surplus gun mount. It is driven by a D.C. servo motor with an output torque of 20 Nm and integral gear box, giving a maximum slew rate of ~ $1° s^{-1}$ which can be reached from rest within ~ 10 s. The position of the telescope is measured to within 5 arc minutes using 12 bit shaft encoders. The encoders were calibrated by noting the measured positions of a number of widely separated stars and solving for the angular offsets in altitude and azimuth. The offset of the telescope's axis from local vertical is allowed for in the tracking software as an offset in geographical location. The tracking software is the same for all three telescopes and runs on a BBC microcomputer. The target position and measured shaft encoder position is recorded for each event in the data stream. In 1994 a CCD camera was mounted on the telescope superstructure to provide a continuous steering monitor. The operation of this is described in section 3.5.3

3.4.2.3 The Detector Packages

Each of the three detector packages initially consisted of four PM tubes. A central channel was surrounded by three guard ring tubes set 2° off-axis and spaced at 120° intervals. A further three tubes were added later to give coverage at 60° intervals. The tubes chosen were 2" diameter RCA 8575's after tests in the laboratory and in earlier experiments showed their stability and noise rate were acceptable (Chadwick, 1987). In March 1991 the off-axis tubes were moved in to a distance of 1.5° from the central channel after simulations suggested that this would increase the efficiency of the guard ring background rejection. The 46 mm photocathode size suggests a field of view for each tube of 1.1° FWHM at a focal length of 2.45 m; however, this has been directly measured as 0.9° FWHM by noting the anode current variation in a tube as a star is allowed to transit across its field of view. Each tube was operated in three-fold coincidence with the corresponding tubes in the other detector

packages, giving seven coincidence channels. The tubes were held in watertight containers, shielded magnetically and electrostatically using μ-metal shields and mounted in cylindrical plastic holders on the focal plane. In order to maintain gain stability in the face of changing sky brightness a green LED was installed at the face of each tube and the brightness of this was varied in response to the PMT's measured anode current. This "hardware padding" technique provides gain stability at the expense of a lower energy threshold.

At the same time that the central flux collector was upgraded, all three detector packages were replaced to take advantage of the improvement in the optical system and to form a compatible telescope to be used as one of a stereo pair with the newly constructed Mark 5. The new detectors consisted of 7 hexagonally close-packed triggering tubes for the left and right collectors and a 31 tube medium resolution imaging camera in the centre. The left and right tubes were 1.5" Burle C7151Q's which are smaller than the RCA 8575's and are somewhat noisier for the same gain. These were chosen as the focal ratio of the left and right collectors is such that the field of view of the triggering packages would have been larger than that for the Mark 5 and larger than the Mark 3 central imaging camera if the 2" RCA 8575's had been retained. This field of view compatibility has recently been sacrificed with the replacement of the 1.5" Burle tubes by hexagonal Philips XP3422 PMT's which have a photocathode minimum size of 56 mm across the flats. The noise/gain characteristics of these tubes has been shown to be very good (Dickinson, 1995) and their hexagonal shape removes much of the dead area between tubes.

The medium resolution imaging camera contains tubes of two different sizes. The inner 19 are 1" diameter Burle S83062E tubes, hexagonally close-packed, with a tube pitch of 3 cm. These cover a field of view of 2.5°, sufficient to contain the majority of the Cerenkov image of an EAS, with a resolution of 0.5°. Surrounding these in a circular ring are twelve 1.5" Burle C7151Q tubes, designed to provide intensity information on the extremities of images whose centroids are close to the

edge of the camera. The coincidence requirement is for corresponding tubes in the left and right detectors, and any one of the 19 one inch camera tubes to have exceeded the discriminator threshold within the coincidence gate time. The camera is shielded with light baffles which reduce the background light seen by the PMT's.

Since the installation of the central camera, hardware padding LED's have not been used in an effort to minimize the energy threshold of the telescope. The smaller pixels of the imaging camera accept less sky noise and with more accurate calibration techniques and increased image information their application has been unnecessary.

Each of the three detector packages has recently been upgraded by the addition of light gathering cones. These are reflective funnels which have a circular aperture at the face of the tube and a hexagonal aperture to the dish with a width equal to the pitch of the tubes. In the case of the circular 1" camera tubes, the circular aperture is designed to be the same size as the photocathode. For the hexagonal tubes, this aperture is somewhat smaller than the photocathode in order to focus the light onto the central area of the photocathode where the bandwidth of the tubes has been measured to be the fastest (I. Roberts, private communication). The addition of these cones has increased the counting rate of the telescope by ~ 20%.

The three detector packages in their current configuration are shown in Figure 3.10, along with a photograph of the Mark 3 telescope, complete with baffles around the central collector.

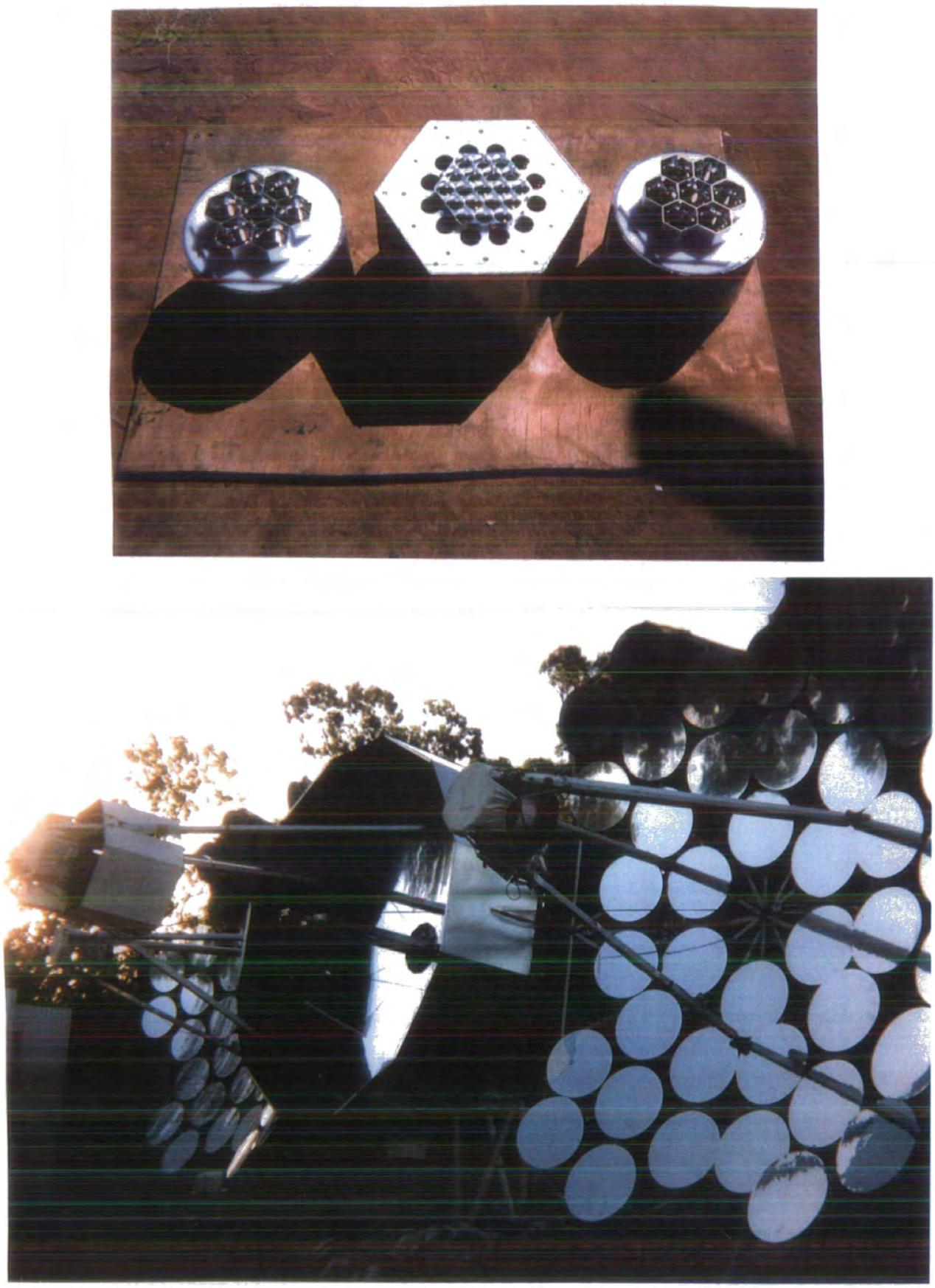

Figure 3.10 The Mark 3 telescope and its detector packages.

3.4.2.4 Data Acquisition and Electronics

The high voltage required for the operation of the PMT's is provided by a multi-channel LeCroy HV4032A E.H.T. unit. Each tube signal is passed to an electronics unit which isolates the D.C. component of the analogue output of the PMT's. The anode current of each PMT is compared with a reference current. The measured difference is used to provide the feedback which was used to drive the hardware padding LED's. The anode current is now passed to an analogue to digital converter (ADC) and fed to the telescope monitoring system.

At the input to the AGC the PMT signal is A.C. coupled to an amplifier. The A.C. component of the signal is magnified by a factor of 10 by a LeCroy 612A amplifier unit. This signal is then passed to a voltage discriminator and to a charge to time converter (QT unit). If the signal exceeds a preset peak discriminator voltage (usually 50mV), a logical output is generated and passed to the three-fold coincidence trigger logic unit. If the three signals within a coincidence channel each generate a logical output from the discriminator within a coincidence gate time ~ 10 ns then the coincidence channel has triggered and a gate is opened to the QT units. The QT units are LeCroy model 2249 ADC's which digitise the integrated charge of the PMT signals within a 30 ns gate time. The outputs of the QT units are then scaled and fed to the data logger. A coincidence register records which of the coincidence channels have fired for each event.

The data logging is performed by a Motorola 68000 based microcomputer developed by the Durham University Microprocessor Centre coupled to a CAMAC based electronics system. The most important consideration for a data logger in this application is system dead time. Consequently, the software is interrupt driven with a rank of priorities headed by control signals, followed by data collection. With one megabyte of RAM buffer, the dead time of the system is 350 μs. Within this dead time, the arrival times alone of a further 16 events can be stored for recording with a dead time of 6 μs.

Each fully recorded event consists of the arrival time to μs accuracy, the integrated charge from each of the PMT's, the output of the coincidence register, the target and measured position of the telescope in zenith and azimuth, the output from the tracker CCD camera (section 3.5.3) and the instantaneous anode current for selected PMT's. The events are stored on magnetic tape for transport back to Durham.

3.4.3 The Mark 5 Telescope

The Mark 5 telescope was constructed in 1992. It was designed primarily as a prototype for the Mark 6 telescope and as one element of a Mark 3/Mark 5 stereo pair.

3.4.3.1 The Mirrors

The three principal flux collectors of the Mark 5 telescope are composite mirrors constructed of twelve 30° segments, parabolic in shape with a diameter of 3.50 m and a focal length of 3.32 m, identical to the current Mark 3 central dish. As with the Mark 3, a system of parallel laser beams were used to align the segments. An image of a star as seen by the Mark 5 central mirror is shown in Figure 3.11. The detector package supports were constructed such that the centre of the package is vertically above the centre of the collector, making the optic axes parallel. This alignment was checked by examining the anode current response of PMT's to a bright star. All three mirrors are surrounded by light baffles.

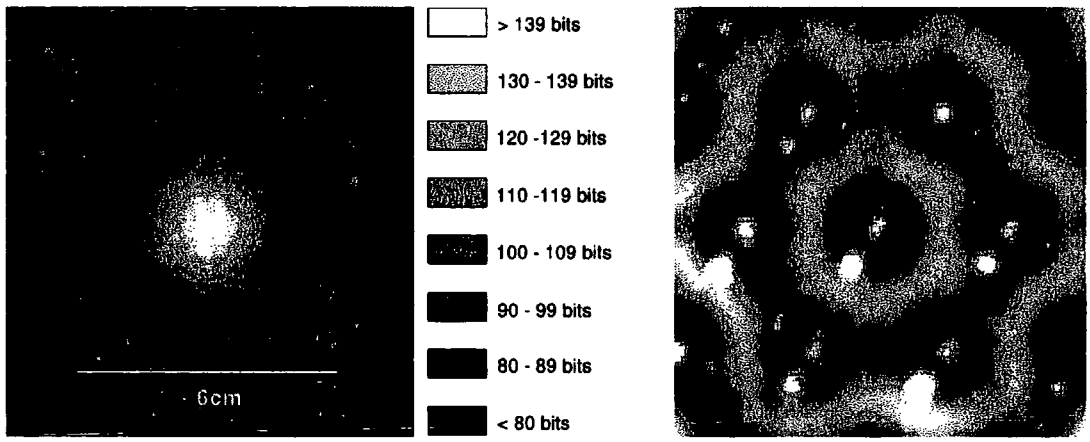

Figure 3.11 (a) A CCD exposure of a star image focussed on to a plain white target at the focal plane of the central dish . (b) A CCD image of the centre of the PMT assembly at the focal plane on the same scale.

The Mark 5 also has a fourth flux collector, of area 6 m^2, mounted above the other three. At the prime focus of this is a large (12.5 cm diameter) PMT viewing an aperture ~ 2°. This system is designed as a Cerenkov pulse time profile experiment of the type discussed in section 2.4.2.

3.4.3.2 The Telescope Mount and Steering

Unlike the Mark 3 telescope, the mount for the Mark 5 was designed and purpose built for this application. The telescope is driven azimuthally through ~ 350° by a D.C. servo motor on a gear ring of 27" diameter and between 0° and 90° zenith angle by a similar motor on a gear quadrant of 18" radius. Absolute position information, sensed by 12 bit shaft encoders to within 5 arc minutes, and data from a CCD camera mounted on the frame of the telescope are recorded in each event as with the Mark 3. The steering is controlled by a BBC microcomputer. Figure 3.12 shows the various elements of the motor control system and the feedback between them.

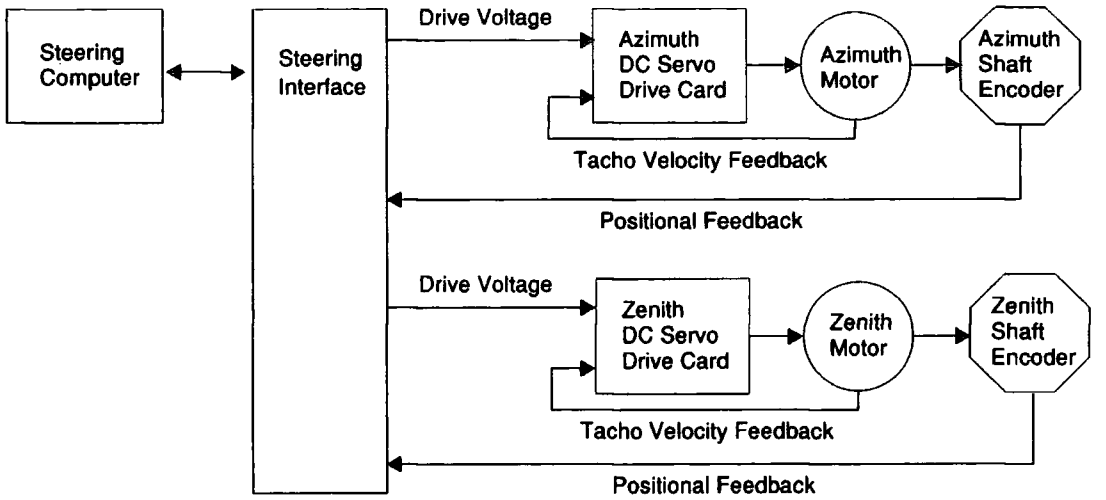

Figure 3.12 A schematic diagram of the motor control system.

3.4.3.3 The Detector Packages

In their present state, the three detector packages are identical in every way to the current detectors of the Mark 3. The tubes are magnetically shielded by a cylinder of μ-metal and electrically insulated by a plastic heat-shrink material. The left and right detector packages were initially constructed of seven 2" Burle 8575's but these tubes have since been replaced by the hexagonal Philips XP3422. Light collecting cones have recently been installed on the left and right hexagonal tubes and on the 1" tubes of the camera, increasing the count rate by ~ 20% and lowering the telescope energy threshold. The field of view of the left and right packages is smaller for the Mark 5 than the Mark 3 as the focal ratio of the left and right collectors is larger. For the Mark 5, the left and right tubes overlap the 1" triggering tubes of the camera, as shown in Figure 3.13.

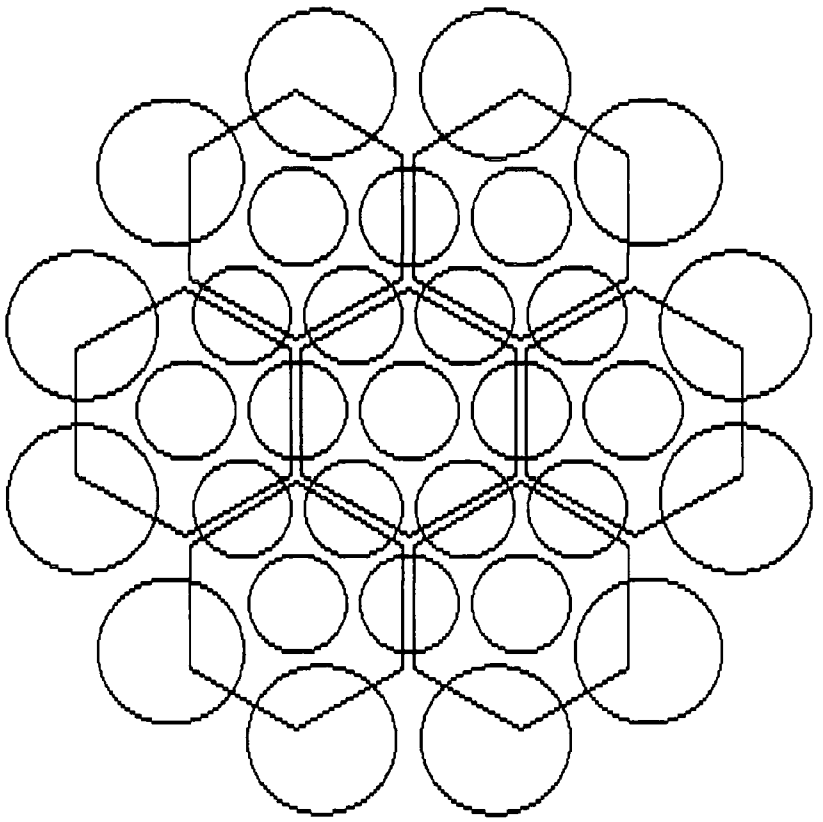

Figure 3.13 Superposition of the left/right detectors and the camera triggering channels of the Mark 5 telescope.

As with the Mark 3, the event trigger is provided by a coincidence between corresponding left and right tubes and any one of the 19 one inch camera tubes. All three detector packages are shielded from background light by baffles. Figure 3.14 shows a picture of the Mark 5 telescope and its detectors in their current form. The flux collector for the pulse timing experiment can be clearly seen mounted above the main mirrors.

Figure 3.14 The Mark 5 telescope and its detector packages.

3.4.3.4 Data Acquisition and Electronics

The high voltage for the PMT's is provided by a CAEN E.H.T. unit. The signal path is identical to that of the current Mark 3 system (section 3.4.2.4).

Increases in processing speed, decrease in price and ease of use made commercial microcomputers an attractive alternative to a 68000 based Mark 3 type logger. The logging is performed by an Archimedes microcomputer which runs an interrupt driven logging program and communicates with the CAMAC electronics via CAMAC interfaces. The system has a dead time of 1 - 2 ms which could be decreased by upgrading the processor should the need arise. The event structure is identical to the Mark 3 and the events are recorded directly on to the hard disk of the logger computer. Once the observation is complete, the data are transferred over ethernet to a large (4 Gb) hard disk in the annex control room and then copied to DAT tape for transport back to Durham.

3.4.4 The Mark 3 / Mark 5 Stereo Pair

When both the Mark 3 and Mark 5 telescopes are operating and observing the same source, a subset of the Cerenkov flashes will be recorded by both telescopes. This subset can be identified by the times of arrival of the flashes at each ACT. Approximately 45% of the events recorded by each telescope at the zenith are stereo events. Correlations between the lower moments of the images recorded by each medium resolution camera have been exploited in three ways (Chadwick, et al. 1996).

The height of Cerenkov light maximum, H_c, is derived from the intersection of lines (or the distance of closest approach of skew lines) drawn through the centroids of the images. Longitudinal and transverse fluctuations in nucleon initiated EAS result in the height of maximum of the light for these showers being less well defined than for gamma ray EAS.

D_{miss} is a parameter which describes the separation between the centroid of

the image measured in one telescope and a predicted centroid position derived from the image in the second telescope, assuming the primary was a gamma ray. This separation should be small for events which are initiated by gamma rays.

For a gamma ray initiated cascade, simulations predict small fluctuations in the azimuthal development of the shower, correlation between the impact parameter (the distance of the telescope from the shower core) and the position of the image centroid and a continuous and predictable lateral intensity distribution of light across the shower front. Given these characteristics, a value of the energy of the primary photon can be estimated reasonably accurately. More importantly, the value of this estimate derived by different telescopes should agree closely if the cascade primary was a gamma ray. This gives rise to the third parameter, R_{ep}, which is the ratio of the two estimates of primary energy.

These parameters have been successfully applied to enhance the gamma ray signal in a 4200 s burst of emission from the cataclysmic variable AE Aquarii (Chadwick, et al. 1995a).

3.4.5 The Mark 6 Telescope

The Mark 6 Telescope was constructed at the Bohena site in June 1994. Alignment of the flux collectors and commissioning of the electronics took a further two - three months. The Mark 6 is the most ambitious project attempted by the Durham group, having twice the linear dimension of the Mark 5. Its properties are described in the following sections.

3.4.5.1 The Mirrors

The technique for the construction of the mirrors for the Mark 6 was essentially the same as that for the Mark 5; however, each mirror covers only a 15° sector of the paraboloid. The composite flux collectors each have a focal length of ~7.2 m and a diameter of ~7 m giving a total mirror area of ~120 m^2 which is four

times that of the Mark 5 and represents an approximate halving of the energy threshold. This large collecting area enables the image of a bright star to be observed visually when a target board is placed at the focal point. The optic axes could therefore be aligned initially by eye. This alignment was then checked by examining PMT anode currents.

The flux collectors were focussed using the same laser alignment system as used for the Mark 5 (Dickinson, 1995). The laser system was at the limit of its utility for this application and it is possible that re-alignment using a different technique may improve the image quality. A recent measurement of the point spread function of the central collector is shown in Figure 3.15. An upgrade to the telescope was made between July and November 1995, when the telescope superstructure was covered with an opaque light shielding material. This performs the same function as the Mark 5 light baffles by reducing the background light.

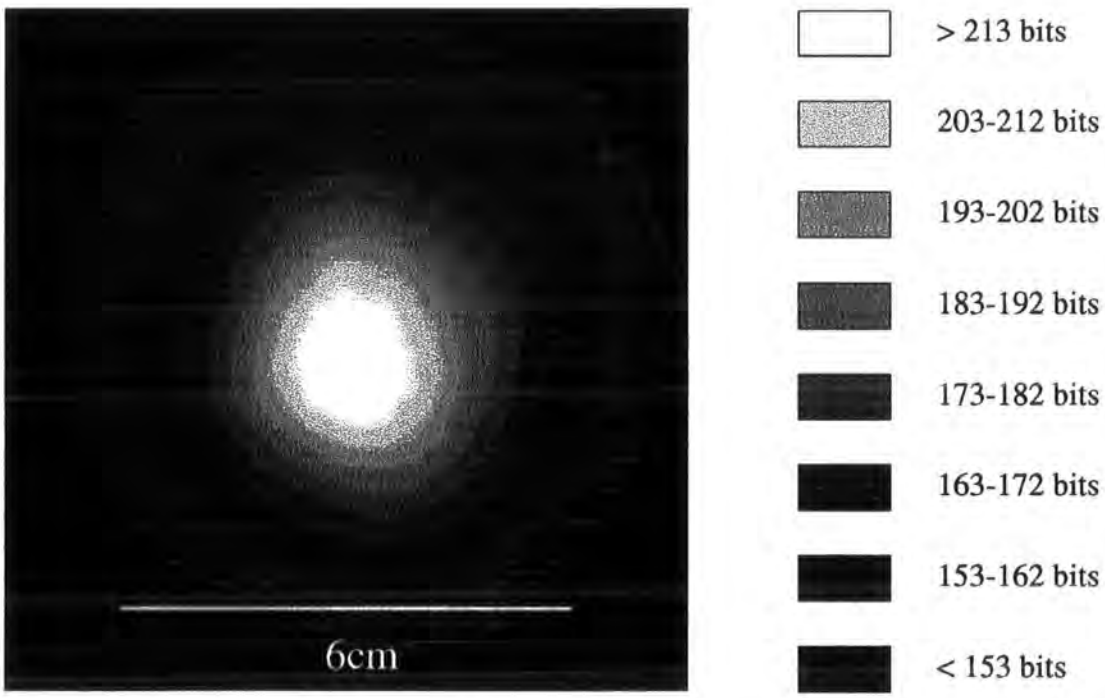

Figure 3.15 A CCD exposure of a star image at the focal plane of the Mark 6 telescope central flux collector.

3.4.5.2 The Telescope Mount and Steering

The Mark 6 mount and drive system is essentially the same as that for the Mark 5 but with some compensations for its much larger moment of inertia. The 5' diameter steel plate on which the telescope rotates in azimuth is 25% larger than the Mark 5 turntable, although the gear ring remains the same with a diameter of 27". The zenith gear quadrant is also larger than for the Mark 5, having a radius of 24". Both the zenith and the azimuth D.C. motors are more powerful for the Mark 6 and can deliver a maximum torque of 75Nm. Initial problems with the azimuth drive have been solved with the addition of a torque limiter which allows slippage under potentially damaging loading, thus protecting the azimuth drive shaft. The telescope can be safely operated in ~ 5 knots of wind and can be moved to a safely anchored parking position under much worse conditions. Wind has not proved to be a serious limitation to observations as nights with high wind tend to produce unstable sky conditions.

The steering software runs on the same type of BBC microcomputer as for the other two telescopes and the target position is updated with the same 12 bit, 5 arcminute accuracy. The actual position of the Mark 6 is sensed to within about 1 arcminute by 14 bit shaft encoders and this information is stored in each event. along with information from a frame-mounted CCD camera.

3.4.5.3 The Detector Packages

The Mark 6 was designed to have a low energy threshold and efficient background rejection capabilities, requiring a greater photon flux and more detailed image information. The use of larger flux collectors increases the photon flux, whereas an imaging camera with finer resolution provides better image information. The central detector package is a high resolution, 109 element camera consisting of 91 hexagonally close-packed one inch PMT's surrounded by a guard ring of 18 two inch diameter Burle 8575 PMT's. The 1" tubes have a pitch of 3cm giving a pixel

resolution of 0.24° and a total aperture for high resolution imaging of 2.64° across opposite vertices. The 2" guard ring tubes are not involved in the coincidence trigger and exist to provide extra information on images which fall close to the edge of the camera.

The left and right triggering packages each contain 19 hexagonal Philips XP3422 tubes. These are close-packed and overlap the same field of view as the 1" camera tubes. The triggering requirement for the Mark 6 is somewhat more sophisticated than for the other two telescopes. To trigger efficiently on gamma ray initiated EAS it is desirable for the triggering element to match the characteristic size of a gamma ray image which is ~ 0.5°. The aperture of the 1" camera tubes is less than half of this and so the following four-fold trigger scheme has been devised. For an event to register, two adjacent tubes from a cluster of seven 1" camera tubes must trigger along with the corresponding tubes in the left and right detectors within the coincidence gate time ~ 10 ns. This is illustrated in Figure 3.16.

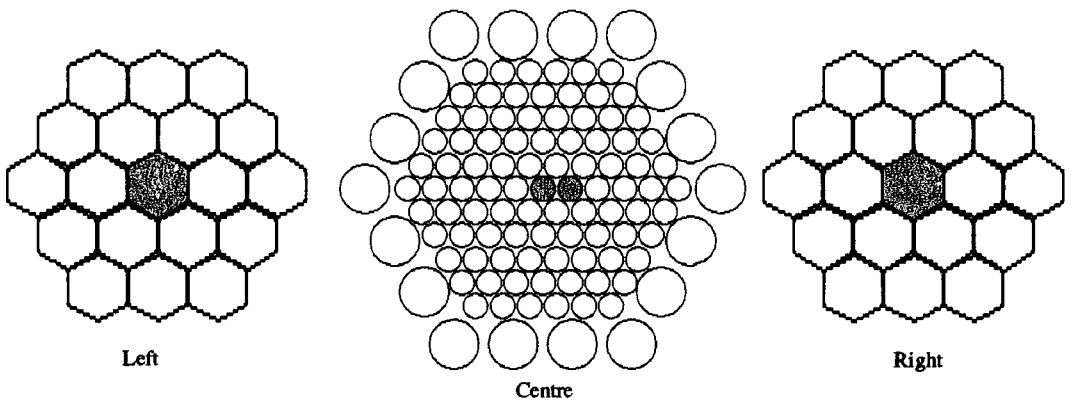

Figure 3.16 The Mark 6 telescope trigger condition: three-fold spatial coincidence between two adjacent central detector PMT's and the corresponding left and right tubes.

Light collecting cones have been fitted to the left and right collectors to focus light on to the centre of the PMT face in order to improve the bandwidth of their response and to the 1" camera tubes to minimize the dead area. The detectors are partially shielded by small light baffles (Fig 3.17).

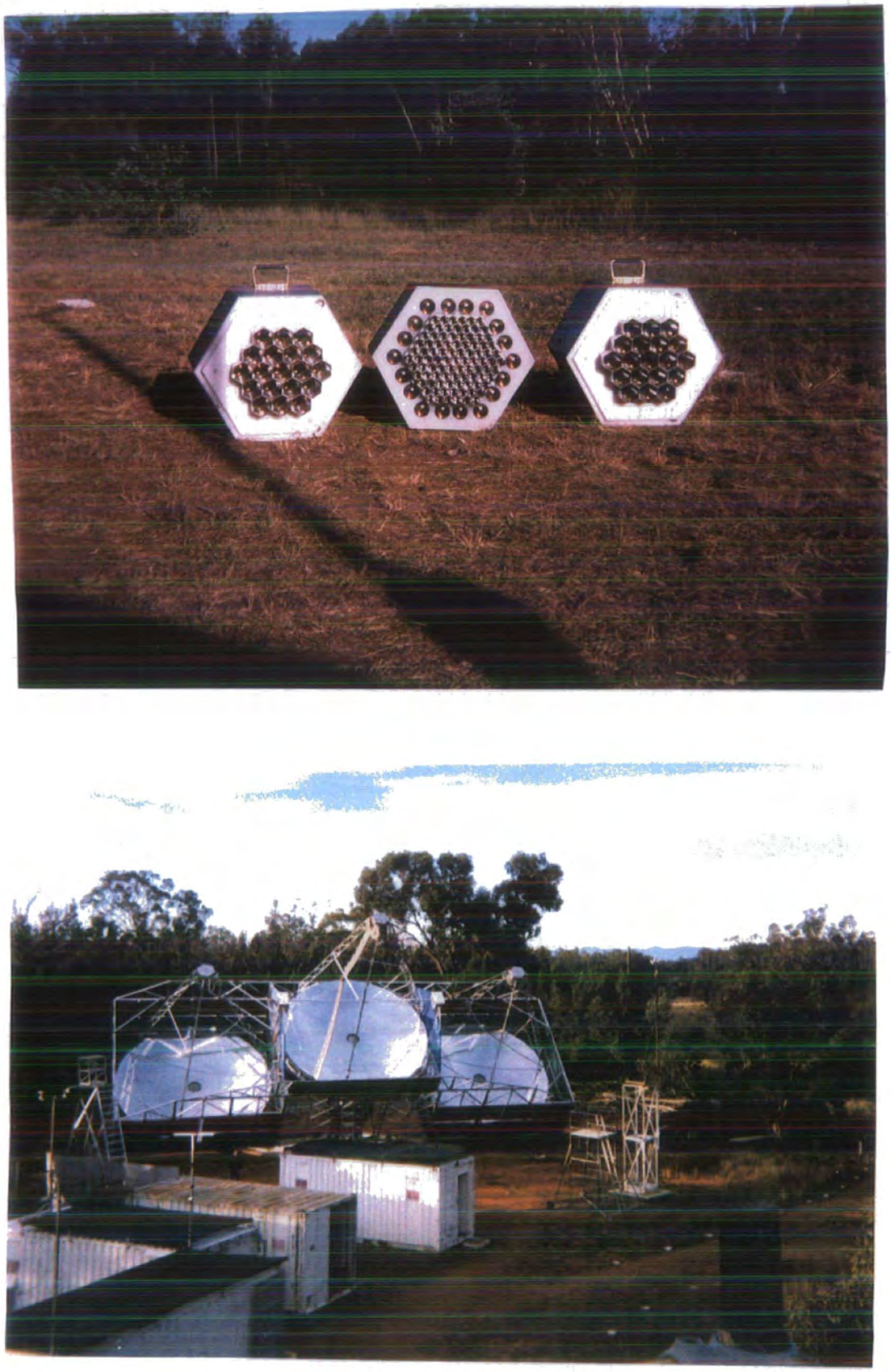

Figure 3.17 The Mark 6 telescope and its detector packages.

3.4.5.4 Data Acquisition and Electronics

The PMT high voltage in the Mark 6 is provided by a number of commercial E.H.T. units. The signal path is essentially the same as for the other two telescopes but with 19 coincidence channels as opposed to 7. The control and logging electronics are shown schematically in Figure 3.18.

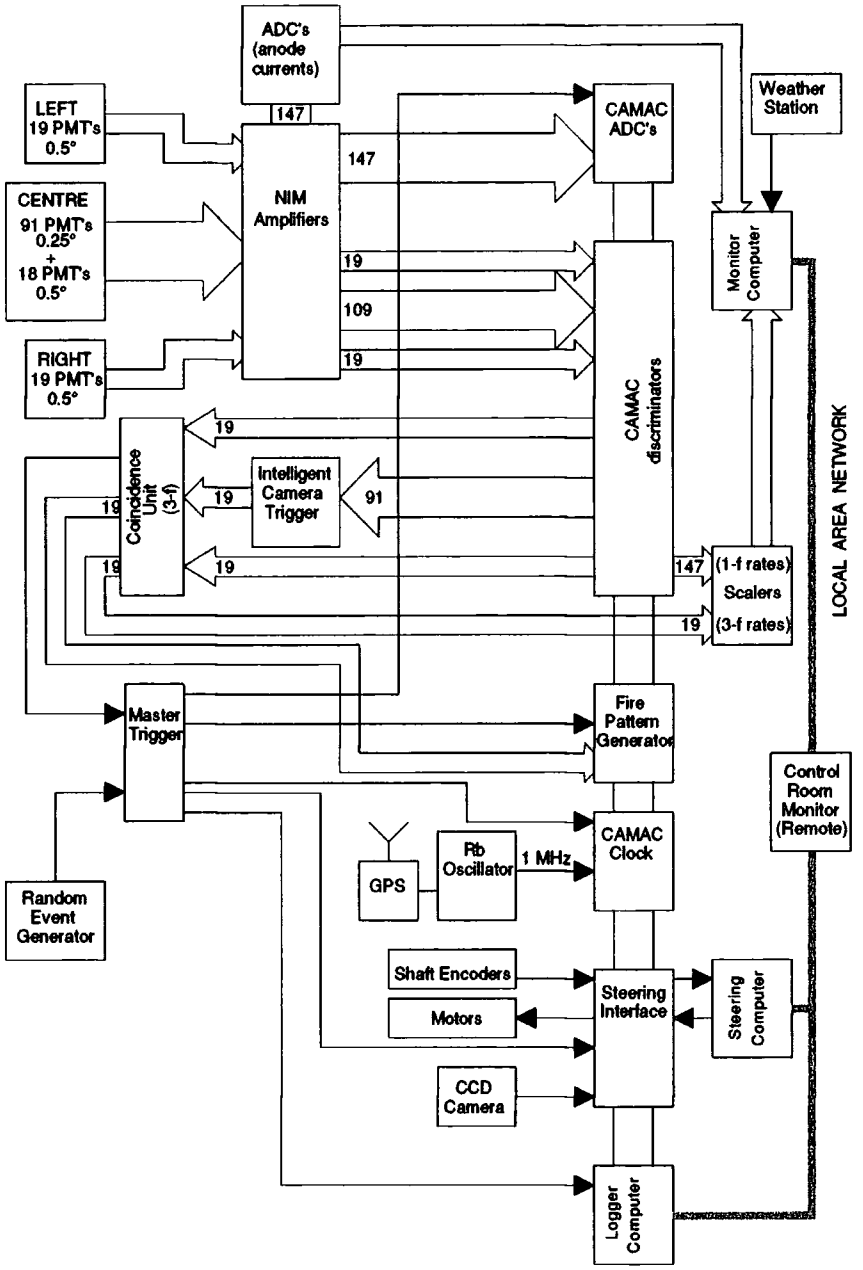

Figure 3.18 Schematic diagram of the Mark 6 control and logging electronics

The data logging and storage for the Mark 6 telescope is performed in the same way as for the Mark 5, using an Archimedes microcomputer with a dead time of ~ 2 ms. The event records have the same format as those for the Mark 3 and are ~ 0.5 Kbytes long.

3.4.6 Energy Thresholds of the Three Telescopes

Estimating the energy threshold for the detection of gamma rays of an ACT is a notoriously difficult problem. The approach of the Durham group has been to scale the threshold based upon the measured counting rate for cosmic rays, with reference to an original measurement using a small telescope array (e.g. Chadwick, 1987). This technique has been used in this thesis to derive the energy threshold for cosmic rays quoted for the Mark 3 telescope in Chapter four.

A more sophisticated method has been adopted for the Mark 6 telescope. The cosmic ray trigger rate for an ACT is given by:

$$R \sim \eta A_{coll} \Omega \int_{E_{min}}^{E_{max}} f(E)dE$$

where η is the triggering efficiency, Ω is the field of view and A_{coll} is the collection area of the telescope, defined by the size of the Cerenkov light pool. The differential cosmic ray flux, $f(E)dE = 1.7 \times E^{-2.7}$ s^{-1} cm^{-2} sr^{-1} GeV^{-1} (Gaisser, 1990). Monte Carlo simulations of the photon yield from cosmic ray EAS have been generated using the MOCCA program (Hillas, 1982). 40000 cosmic rays were generated from a circular field of view 2° in radius and out to a maximum impact parameter of 250 m^2. The simulations were performed for a telescope inclined at 20° to the zenith. These have then been presented to a model of the Mark 6 telescope. By altering the discriminator thresholds of the telescope model, it is possible to match the trigger rate for the simulations to the measured counting rate.

This model can now be applied to Monte Carlo simulations of gamma ray

EAS in order to give some idea of the expected threshold energy for detection of photons. 50000 gamma ray showers were generated with energies ranging from 100 to 10^5 GeV for a source with a power law spectrum with a differential index of -2.4. This is the same as the measured value of the differential index for the spectrum of the Crab nebula in the VHE range (Vacanti, et al. 1991). The effective area for an ACT depends upon the gamma ray energy, the Cerenkov light pool size and the triggering probability. Figure 3.19 shows the effective area for the Mark 6 telescope as a function of energy for gamma rays from a point source. One way of defining the energy threshold of an ACT for gamma ray detection is the energy at which the differential gamma ray flux is maximum (e.g. Aharonian, et al. 1995). This is illustrated in Figure 3.20, which predicts a threshold energy for gamma rays of ~ 300 GeV.

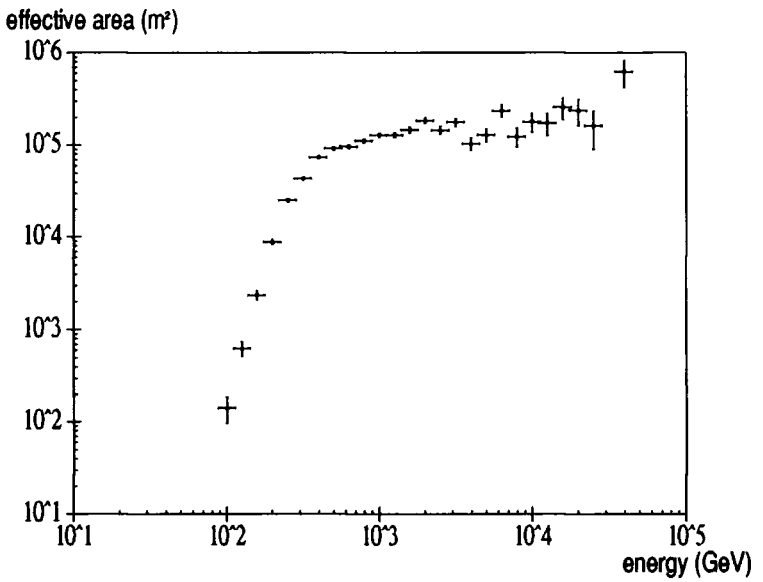

Figure 3.19 Effective area for gamma ray detection of the Mark 6 telescope as a function of primary energy.

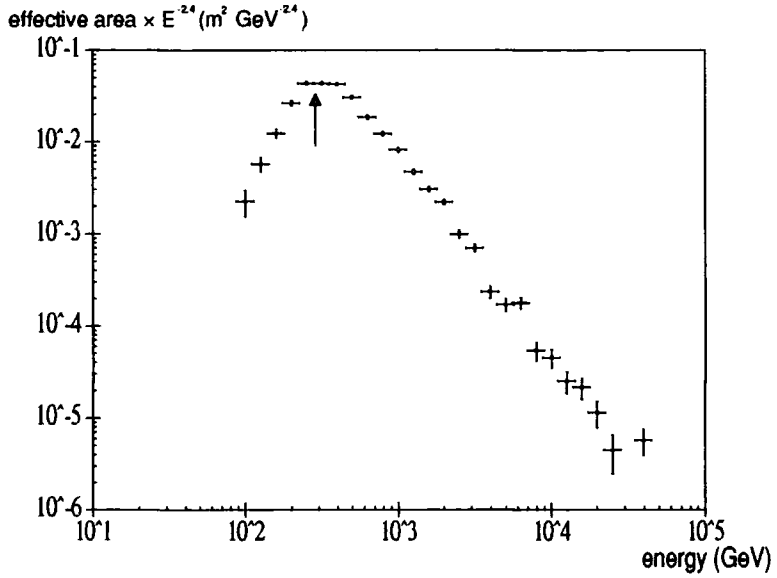

Figure 3.20 Definition of the energy threshold for gamma rays. The source differential spectrum is assumed to be -2.4. The threshold energy is defined to be the the energy of the maximum differential flux and is approximately 300 GeV.

There are many potential sources of error in this estimate of the energy threshold. The accuracy of the simulations can only be confirmed by comparison between real and simulated hadron shower images. This comparison is made in Chapter five and some important differences are seen between the two. The spectral index, trigger conditions, and mirror reflectivity also introduce uncertainties. The systematic error in the energy threshold is conservatively estimated as ± 100 GeV. The average effective collection area which is used for the calculation of fluxes and flux limits is given by the mean effective area above the threshold energy. This is ~ 1.5×10^5 m^2.

It is important to note that the values derived here are the threshold energy and mean effective area assuming 100% gamma ray retention. Any background discrimination will also reject a fraction of the gamma ray signal, altering the energy threshold and effective area for gamma ray detection. This is discussed further in section 6.4.4.

3.5 Data Preparation

Prior to any form of analysis the data recorded by the Durham telescopes must undergo various formatting and calibration procedures. The calibration techniques have become more rigorous in recent years as the need for accurate Cerenkov image measurements has increased. This section describes the methods currently in use.

3.5.1 Formatting

The logging microcomputers of each of the telescopes record the time, QT values and steering information for each event as the data are received from the CAMAC electronics. The format of the records is designed to minimize the logging time such that the system dead time is small. The first step in the data preparation, once all of the data have been transferred from magnetic tape to a hard disc drive in Durham, is to translate each event into a FORTRAN record format. The formatted events have a more logical structure (Table 3.4) which is compatible with the analysis software.

Table 3.4: Formatted event structure for the three telescopes.

Item	Length in Mk3	Length in Mk5	Length in Mk6
Seconds	4	4	4
Microseconds	4	4	4
Spare bytes	3	3	3
Fire pattern	1	1	1
Telescope flag	1	1	1
Chop mode flag	1	1	1
Azimuth position	2	2	2
Zenith position	2	2	2
Azimuth drive volts	1	1	1
Zenith drive volts	1	1	1
Drive error signal	1	1	1
Azimuth target	2	2	2
Zenith target	2	2	2
PMT QT bytes	90	90	294
Anode currents	2	x	x
Timing dish info	x	34	x
Raw CCD bytes	6	6	6
CCD Azimuth	4	4	4
CCD Zenith	4	4	4
Dead time	4	4	4
Event number	4	4	4
CCD source X-offset	4	4	4
CCD source Y-offset	4	4	4

3.5.2 PMT Calibration

In order to produce an accurate picture of the distribution of Cerenkov light across the field of view, the relative response characteristics of each PMT in the detector packages must be measured. The three elements involved in this calibration procedure are addressed in this section.

3.5.2.1 PMT Pedestal Offsets

For a PMT which views little or no Cerenkov light in a given event, it is possible that statistical sky noise fluctuations may produce a negative output signal. In order for these negative responses to be measured, the QT units which record the integrated PMT signals are provided with an artificial positive DC offset. These offsets, known as the pedestals, must be measured and deducted from the recorded QT values of each PMT when the camera images are analysed.

The pedestal values can be measured by artificially triggering the telescopes to record an event using a random pulse generator. These random events, devoid of any Cerenkov light, can then be used to produce the distribution of measured signals for each PMT. The pedestal value is then the mean value of this distribution (Fig 3.21). Random events are recorded throughout each observation at a rate of 50 min^{-1} and their event records are flagged by the coincidence register for easy identification and removal during calibration.

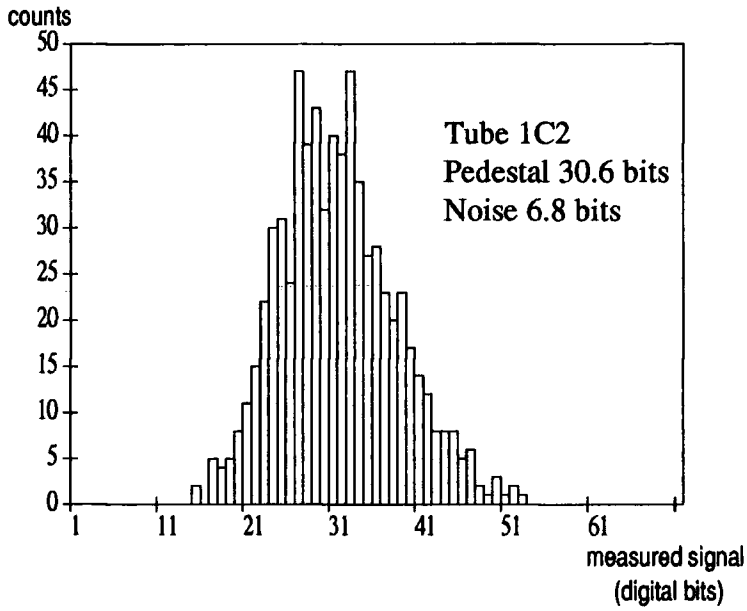

Figure 3.21 The pulse height distribution of 15 minutes of random triggers for a typical tube. The pedestal is the mean of the distribution and the noise is the standard deviation.

If random events are unavailable for any reason, a backup system has been developed. This uses the information recorded by the coincidence register in each event about which coincidence channels were triggered (the "fire pattern"). If a tube within the camera is located far enough away from the triggered channels, it may be considered to contain no Cerenkov light. Tube responses under this condition can then be used to build up the distribution of PMT signals and the pedestal calculated in a similar way to the random triggers. This technique is less effective for tubes near to the centre of the camera, where some fraction of the Cerenkov image almost

inevitably falls. A correction factor for these tubes has been derived empirically by comparison with the results from randomly triggered signal distributions.

3.5.2.2 PMT Sky Noise Response

Standard methods of image parameterisation involve calculating the first and second moments of the PMT signals in the camera and using these to fit an ellipse to the image (section 3.3.2 and section 5.2). For this method to be robust, it is necessary to ignore noise dominated tubes far removed from the image centre. Some measure of the sky noise response of each PMT is therefore required in order to define a threshold, below which tube signals are not used. The random events can be used for this part of the calibration also, with the tube noise response being given by the standard deviation of the distribution of PMT signals (Fig 3.21). As with the pedestals, if random events are not present a slightly less accurate measure of sky noise can be obtained by using tubes not involved in the triggered channels of Cerenkov events.

3.5.2.3 PMT Relative Gains

The gain of a PMT is dependent upon the high voltage used to accelerate electrons through its dynode chain. The voltages on the tubes in the camera of an ACT are set such that the gains are similar for each and give a "flat-field" response to Cerenkov flashes. More accurate flat-fielding is achieved by measuring the relative tube gains during an observation and normalising the recorded QT signals to account for any differences.

The relative gain measurements can be made in several different ways. Initially, a plastic scintillator impregnated with the radioactive isotope Americium 241 was used to generate a light pulse with a known, constant average intensity. This light source was then presented to each PMT in the detector in turn and the distribution of recorded signals used to estimate the relative tube gains. This system

suffered from the fact that only a fraction of the photocathode area was illuminated and the tube responses were critically dependent upon the exact location of the light source. This method of calibration was also very time consuming and could only be performed once for each telescope during each three week dark period.

A great improvement in the relative gain calibrations has been the provision of a light source which illuminates all of the PMT's in the detector packages uniformly at the same time. A pulsed nitrogen laser is used to produce a 3 ns flash of UV light which excites a block of plastic scintillator, causing it to emit blue light. This blue flash is then piped by optic fibre to the centre of each of the three flux collectors where an opal diffuser is used to spread the light and ensure uniform illumination of the detectors. The flashes are large enough to trigger the telescope and the relative tube responses for these triggers can be used to determine the gain normalization factors required to flat-field the detector. There is only one laser available at the observatory and this is used twice per month to calibrate the Mark 3 and Mark 5 telescopes prior to an observing run. For the Mark 6, the laser is mounted on the telescope during each run and provides an average of 50 flashes per minute throughout the observation. These flashes are identified during calibration by examining the response of a PMT mounted on the side of the camera and shielded such that it views the laser flash but not the flux collector. Any event containing a signal in this tube greater than five times its sky noise response is picked out as a laser induced event.

The laser calibration technique has also allowed the development of a back-up system based upon the response of the detectors to the cosmic ray images. Over the course of an observation, if we assume that there are no biases due to an uneven triggering response over the detector package, the PMT's should be subject to a uniform average illumination from the Cerenkov images of the isotropic cosmic rays. Using a technique based upon that suggested by Punch (1993), the integral distribution of signals for each PMT is collected for all events. The number of QT

bits over which the integral distribution falls from the 30% to the 5% level is then used as the value to be equalised by the gain factors (Fig 3.22).

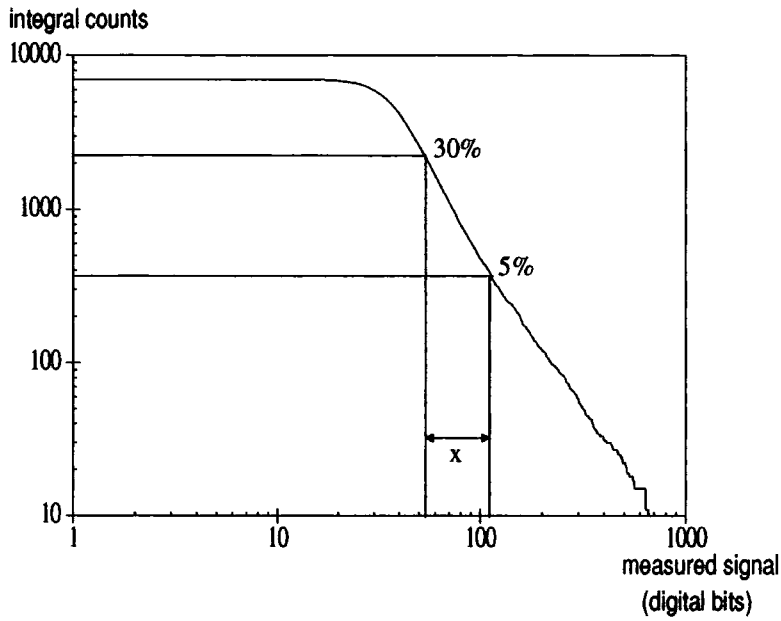

Figure 3.22 Gain calibration using the cosmic ray beam. Gain factors are calculated such that the value "x" indicated in the integral pulse height distribution is normalized between each PMT.

This region of the spectrum is chosen so as to avoid the smaller flashes where triggering biases become important. In addition to this, results from the laser calibration system are used to provide an extra normalization factor between each ring of PMT's in the detector package. This method is used to provide gain calibration for the Mark 3 and Mark 5 telescopes throughout their observations. An improvement to this method which is less effected by variations in the number of small triggers may be to use fixed rate levels other than the percentage criteria. A comparison of the results from the three different gain measurement techniques is given in Figure 3.23, which shows good correlation between the laser and cosmic ray methods.

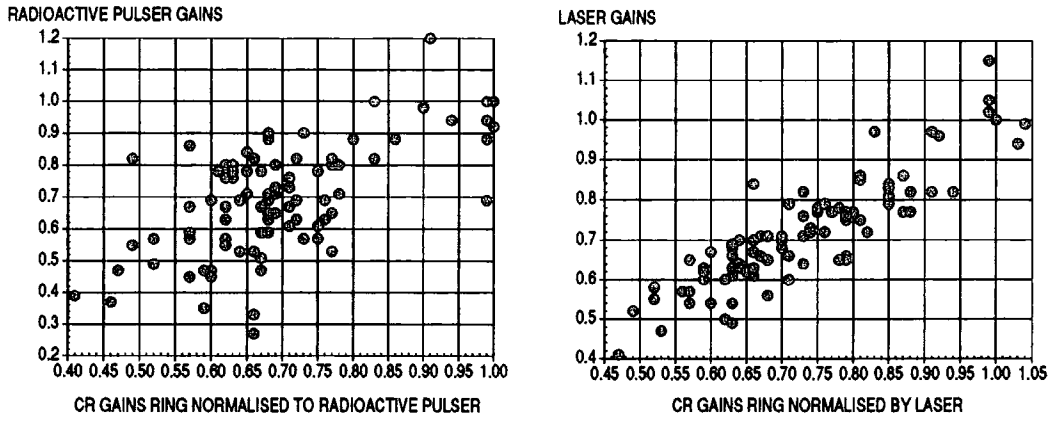

Figure 3.23 A comparison of PMT gains calculated using the cosmic ray beam with those calculated using the radioactive light pulser and the laser.

3.5.3 The CCD Star Tracking System

The Mark 3 and Mark 5 telescopes have imaging cameras with 0.5° PMT pixels and shaft encoder resolution ~ 0.09° while the Mark 6 has 0.24° PMT pixels and shaft encoder resolution of ~ 0.02°. The shaft encoders therefore measure the telescope positions with enough resolution to specify the source position in the field of view accurately. What is not known, however, are the absolute offsets in the encoder positions relative to the celestial sphere. These offsets vary with time and with telescope attitude and can be as large as 0.2° for some pointing directions. In the past, the offsets have been kept to a minimum by monitoring the positions of 12 widely spaced stars with an analogue camera aligned with the optic axis of the telescope. If the steering appeared inaccurate, constants in the steering software were altered to compensate.

The development of inexpensive astronomical CCD cameras has led to a much improved system. All of the Durham telescopes are now equipped with an astronomical CCD camera for the purpose of tracking stars in the field of view. The CCD chip and control package are model SBIG ST4 and view an f/1.4, 50mm lens. The chip itself has an area of 2.54 mm^2 divided into 165x192 rectangular pixels, giving a field of view ~ 2° and 1 arcminute resolution. In order to provide useful

tracking information, the camera must be aligned with the optic axis of the telescope. This is achieved by maximizing the anode current of the central camera PMT on a bright star and noting the position of the star in the CCD camera frame.

At the beginning of every observation, a CCD camera full frame picture is recorded. The exposure time for this picture is ~ 5 s and stars of 8th magnitude can be resolved. This is then compared to a database of stars in order to check the orientation of the chip with respect to the celestial sphere. Throughout the observation, the CCD camera outputs the position of the current brightest pixel in its field of view. The x, y coordinates of this position, the brightness of the pixel, the exposure time (~1s), and the time the exposure was taken are added to each event record. The exposure time is kept to a minimum to allow rapid update of the position and stars of ~ 7th magnitude can be tracked with reasonable consistency. During the pre-processing of the data, the position of the brightest pixel is compared with the expected position of stars within the CCD camera field of view. As the prediction of the star's position relies on the time of the event, it is important that the CCD corrections are applied prior to the barycentring of the data. The deviation of the brightest pixel from the expected position is then used to calculate the shaft encoder offsets. The shaft encoder measurements with these offsets removed can then be used to reliably locate the actual candidate source position within the field of view. Each formatted event contains the x,y coordinates of the true source location in the field of view and Cerenkov images are then parameterised relative to this position. Figure 3.24 shows a typical CCD camera frame with the brightest pixel records for an observation added.

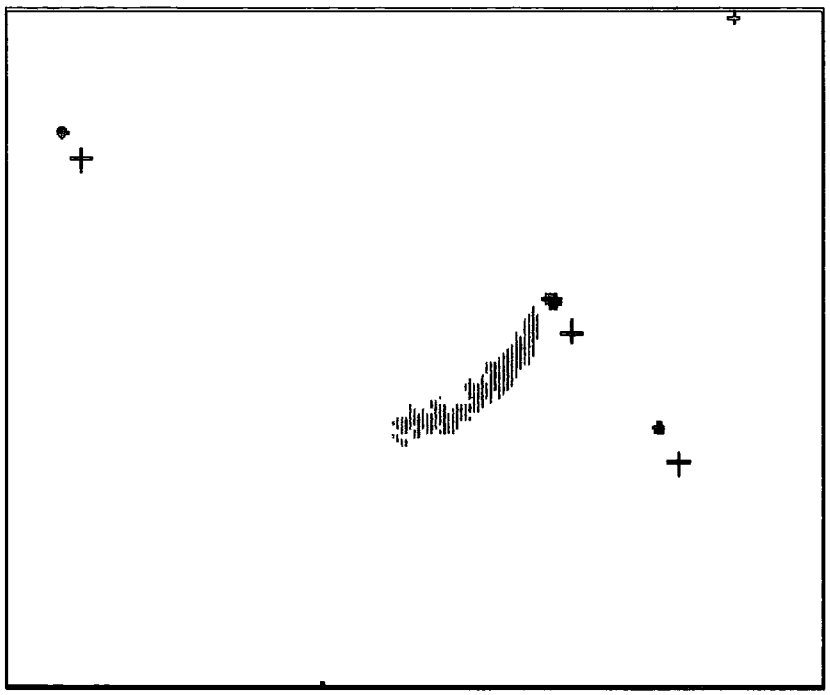

Figure 3.24 The CCD camera frame for an observation of Vela X-1. The circles represent stars in the initial, full frame exposure. Crosses indicate the predicted star positions at the start of the observation. The shaded arc shows the movement of the brightest pixel throughout the run.

CHAPTER 4 - A SEARCH FOR PERIODIC EMISSION OF TeV GAMMA RAYS

4.1 Introduction

The techniques of time series analysis have often been used to search for periodic sources of VHE gamma rays (for reviews see e.g. Chadwick, et al. 1990; Moskalenko, 1995; Weekes, 1988). This chapter deals with the mechanisms by which TeV emission with a characteristic time profile may be produced and the types of source in which this emission may occur. Some of the methods used in searching data for evidence of periodicity are reviewed. These methods are then applied to observations of the high mass X-ray binary system SMC X-1.

Two forms of background discrimination are used in an attempt to enhance the ratio of gamma ray to nucleon initiated events in the data. The guard ring rejection technique is applied to the 1986 - 1991 Mark 3 telescope data and medium resolution image discrimination is used on observations made after the Mark 3 telescope upgrade in 1993.

4.2 Sources of Periodic Emission: Pulsars and X-Ray Binary Systems

Some of the most interesting astrophysical phenomena are associated with objects whose emission is in some way periodic. In addition to this, the existence of a pulsed source with a known frequency for emission at other wavelengths allows the possibility of gamma ray flux measurements significantly below those attainable for steady sources. Radio pulsars have been strong candidates for VHE investigations since their discovery in 1967 (Hewish, et al. 1968) as their non-thermal continuum emission is indicative of relativistic charged particles which may produce TeV photons. X-ray satellites, such as UHURU, provided the first evidence for a new class of objects consisting of a close binary pair of stars where one of the stars is a compact

object (a neutron star, black hole, or white dwarf). These X-ray binary systems have become some of the most intensively studied candidates for VHE gamma ray emission.

4.2.1 Formation of Compact Object Systems

When a star has exhausted its supply of nuclear fuel it may collapse rapidly under gravity, causing a supernova explosion which sheds the stellar envelope. The state of the stellar remnant is determined by its initial mass. Stars with a mass less than $\sim 7M_{\odot}$ form a white dwarf star with a mass less than $\sim 1.4M_{\odot}$ and a radius $\sim 10^7$ m. Stars of mass greater than $\sim 9M_{\odot}$ are likely to form a neutron star in which the majority of protons and electrons have combined to form neutrons via:

$$p + e^- \rightarrow n + \nu$$

and further gravitational collapse is prevented by the neutron degeneracy pressure. Neutron stars have a mass ~ 1.4 to $3M_{\odot}$ and a radius of ~ 10^4 m. Those with a mass much greater than this will form black holes. Both neutron stars and white dwarves initially have a strong magnetic field associated with them as the magnetic flux lines of the progenitor star are "frozen in" to the almost perfectly conducting remnant when it forms. The field strength is determined by the original magnetic field and the size of the compact object. Typical values are ~ 10^{12} Gauss for neutron stars and ~ 10^6 Gauss for white dwarf stars (e.g. Mészáros, 1992).

Gamma ray production from these objects, by any of the mechanisms discussed in Chapter one, requires the presence of relativistic particles. Young neutron stars rotate very rapidly, with a period of tens of milliseconds, due to the angular momentum which is conserved after the collapse of the progenitor star. Energy may be transferred to the acceleration of particles by a decrease in the rotational energy of the pulsar. Alternatively, if the compact object exists in a close binary system, its emission may be powered by the energy released during the

accretion of matter from the companion star on to the compact object. The mechanisms by which particles may be accelerated up to energies great enough to produce TeV gamma rays are discussed in section 4.2.4.

4.2.2 Isolated Pulsars

Pulsars were discovered as radio sources in 1967 (Hewish, et al. 1968). They are characterised by their emission of extremely regular pulsed radiation, with periods varying between 0.001 s and 5 s. They are believed to be neutron stars whose beamed emission crosses the line of sight as the neutron star spins. This is supported by the fact that the pulse period for most pulsars is decreasing, implying that some of their rotational energy is being radiated away. Only seven pulsars have been detected by the CGRO satellite in the gamma ray region. They are the Crab pulsar (Nolan, et al. 1993), the Vela pulsar (Kanbach, et al. 1994), Geminga (Bertsch, et al. 1992), PSR1706-44 (Thompson, et al. 1992), PSR1055-52 (Fierro, et al. 1993), PSR1951+32 (Ramanamurthy, et al. 1995), and PSR 0656+14 (Ramanamurthy, et al. 1996). Of these, all exhibit pulsed emission and only Geminga has no radio emission.

In the TeV region, there have been reports of pulsed emission from the Crab (e.g. Gibson, et al. 1982, Bhat, et al. 1986, Dowthwaite, et al. 1984), Vela (Grindlay, et al. 1975, Bhat, et al. 1985) and Geminga (Bowden, C.C.G, et al. 1993) pulsars. With the advent of high resolution imaging techniques for ground based gamma ray astronomy highly significant detections of a steady flux of TeV photons from the direction of the Crab pulsar (Weekes, et al. 1989) and PSR1706-44 (Kifune, et al. 1995) have been made. The Crab pulsar data show no evidence for pulsed emission (Gillanders, et al. 1995) and although full results of the time series analysis of the PSR1706-44 observations are yet to be reported, it is unlikely that a major portion of the detected flux is pulsed.

4.2.3 X-Ray Binary Systems

The accretion driven systems can be further subdivided in to three main classes: high mass X-ray binaries, low mass X-ray binaries and cataclysmic variables. High mass X-ray binary systems are associated with young, population I stars. They consist of a massive OB supergiant star and a compact object, usually a neutron star, and have a high X-ray luminosity ~ 10^{37} erg s^{-1} (e.g. Rappaport & Joss, 1983). Matter is transferred from the supergiant to the compact object through a strong stellar wind which ejects ~ 10^{-4} $M_\odot$ per year (Bondi & Hoyle, 1944; Davidson & Ostriker, 1973). The X-ray luminosity is given by the rate at which the accreting material is losing gravitational potential energy, with the maximum luminosity from accretion being given by the Eddington luminosity, L_{ED}. This occurs when the gravitational forces on the accreting material are balanced by the outward radiation pressure. For spherically symmetric accretion:

$$L_{ED} = \frac{4\pi G M m_p c}{\sigma_T} = 1.26 \times 10^{38}\left(\frac{M}{M_\odot}\right)$$

where M is the mass of the compact object, m_p is the proton mass and σ_T is the Thompson cross-section. If the accretion flow is not symmetric and falls only on to a small region of the star surface then the Eddington limit will be correspondingly smaller. A small accretion disc may form due to the small angular momentum of the stellar wind, but the optical emission from these systems is dominated by the supergiant itself. X-ray emission from the neutron star shows eclipses as it is obscured by the supergiant. The X-rays are often pulsed as the compact object's strong magnetic field directs the accreting matter on to the magnetic poles which are displaced from the spin axis. The X-ray emission is then only seen when a pole is orientated towards the observer, giving a 'lighthouse' effect (Pringle & Rees, 1972). A sub-class of high mass X-ray binaries have rapidly rotating Be type stars as the companion to the compact object. The X-ray emission from these objects is often produced in periodic outbursts as the compact object passes through an equatorial

ring of matter ejected from the larger star (e.g. Charles & Seward, 1995). Figure 4.1 illustrates the standard model of a high mass X-ray binary system.

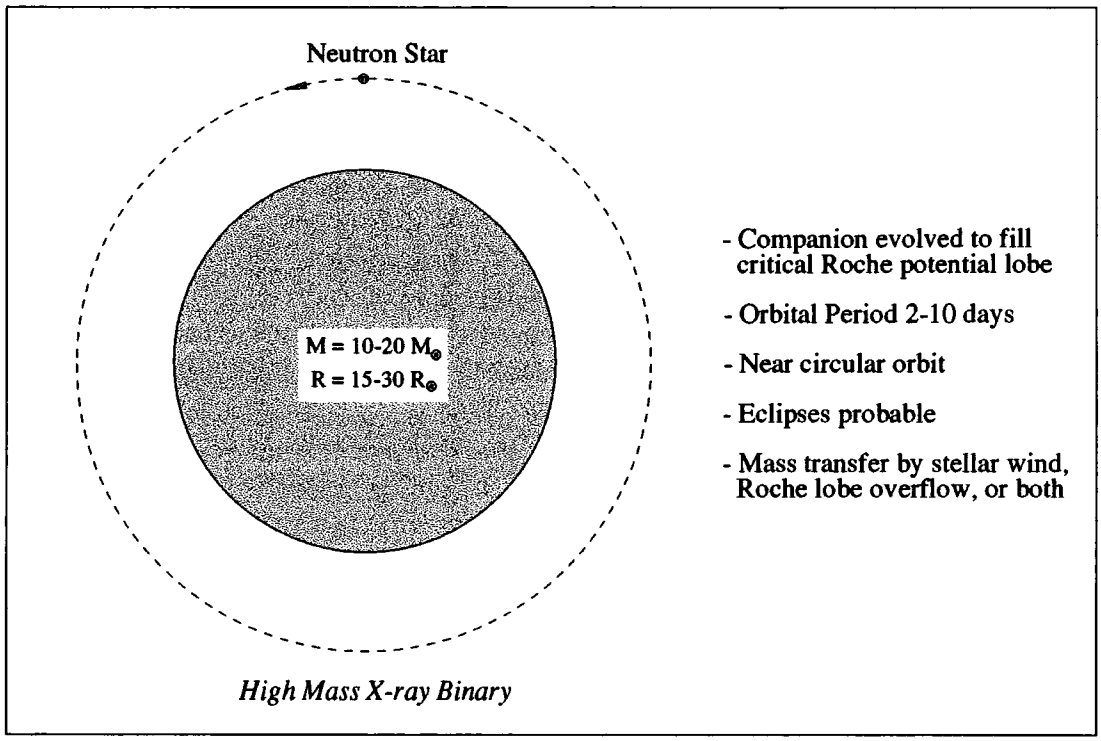

Figure 4.1 The standard model of a high mass X-ray binary system (after van den Heuvel, 1983)

Low mass X-ray binary systems are generally associated with older, population II stars and are characterized by faint optical emission and unpulsed steady X-ray emission of a slightly lower luminosity than that of high mass systems, but with occasional bursts. They are believed to consist of a cool, late-type star less massive than the sun which has filled its Roche lobe and is transferring matter on to a neutron star through the inner Lagrangian point (e.g. van den Heuvel, 1983). This matter carries a large angular momentum which causes the formation of a large accretion disc around the compact object which may sometimes be observed optically. The X-ray emission from the neutron star is basically unpulsed as the magnetic fields associated with these older objects have significantly decayed, although quasi-periodic oscillations (QPO's) are sometimes seen due to interactions between the accretion disc and the remnant magnetic field (van der Klis, 1988).

Bursts of X-rays are produced by unstable thermonuclear burning of He on the surface of the neutron star. The configuration of a typical low mass X-ray binary system is shown in Figure 4.2.

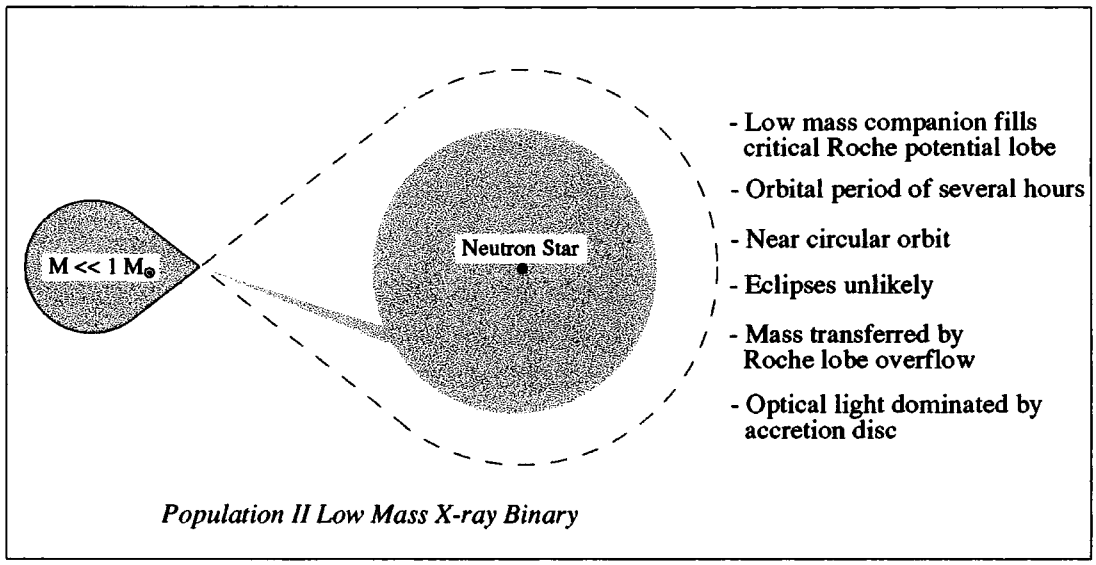

Figure 4.2 The standard model of a low mass X-ray binary system (after van den Heuvel, 1983)

Cataclysmic variable systems are intrinsically less luminous in X-rays than the other X-ray binaries, producing ~ 10^{31} erg s^{-1} at soft X-ray energies. They have been known for some time to produce optical outbursts (e.g. Liebert, 1980) and, in some cases, pulsed optical emission. These systems are believed to be similar in configuration to the low mass X-ray binaries, but with the compact object being a white dwarf and not a neutron star. The optical outbursts are explained by an increase in the rate of mass transfer from the companion star, or by a change in the structure of the accretion disc. The pulsed optical emission is likely to be from accretion hot spots on the surface of a magnetised white dwarf at the magnetic poles.

X-ray binary systems were popular TeV pulsed source candidates in the 1980's and many detections of varying significance have been reported. Reviews of these have been presented by Chadwick, et al. (1990) and Weekes, (1988). The most convincing detections are associated with the X-ray binaries Cyg X-3, Her X-1, 4U0115+63, Cen X-3 and Vela X-1 (Chadwick, et al. 1990 and references therein)

and the cataclysmic variable AE Aquarii (Chadwick, et al. 1995a, Bowden, et al. 1992, Meintjies, et al. 1992 and 1994).

4.2.4 Particle Acceleration Mechanisms

Many different source models have been proposed for the compact object systems described; however, each model must employ some form of particle accelerator. The various mechanisms by which charged particles may be accelerated up to energies high enough to generate TeV photons are reviewed in this section.

4.2.4.1 Dynamo Mechanism

An ordered magnetic field **B**, such as that associated with a neutron star spinning with a velocity **v**, will induce an electric field $\mathbf{E}_i = \mathbf{v} \times \mathbf{B}$. In the presence of a conducting plasma, the net field is reduced to zero, that is, $\mathbf{E} + (\mathbf{v} \times \mathbf{B}) = 0$. However, if there is a region of vacuum, a potential drop may develop through which particles can be accelerated.

4.2.4.2 Plasma Turbulence (Second Order Fermi Acceleration)

This method was proposed as a means of cosmic ray acceleration in interstellar space by Fermi in 1949. He supposed a situation in which charged particles are reflected from "magnetic mirrors" associated with irregularities in the galactic magnetic fields. The probability of a head on collision, by which the particle gains energy, is marginally greater than that of a tail end collision, where energy is lost. Over a series of collisions, the particle gains energy with the average gain per collision, ΔE, being given by (Longair, 1994):

$$\frac{\Delta E}{E} \sim \frac{8}{3}\left(\frac{V}{c}\right)^2$$

where V is the velocity of the magnetic irregularity. Particles accelerated by this mechanism will naturally be produced with a power law distribution.

Collisions with interstellar clouds, which Fermi initially proposed may be responsible for this type of acceleration, are too infrequent to increase the energy of charged particles at a reasonable rate to account for the observed cosmic ray spectrum. In addition, the effect of ionisation losses on the particles as they are accelerated means that particles must be injected into the acceleration region with an energy greater than the maximum energy loss rate (see Fig 4.3). The process may be important, however, in small-scale regions of turbulent plasma such as occur in accreting systems.

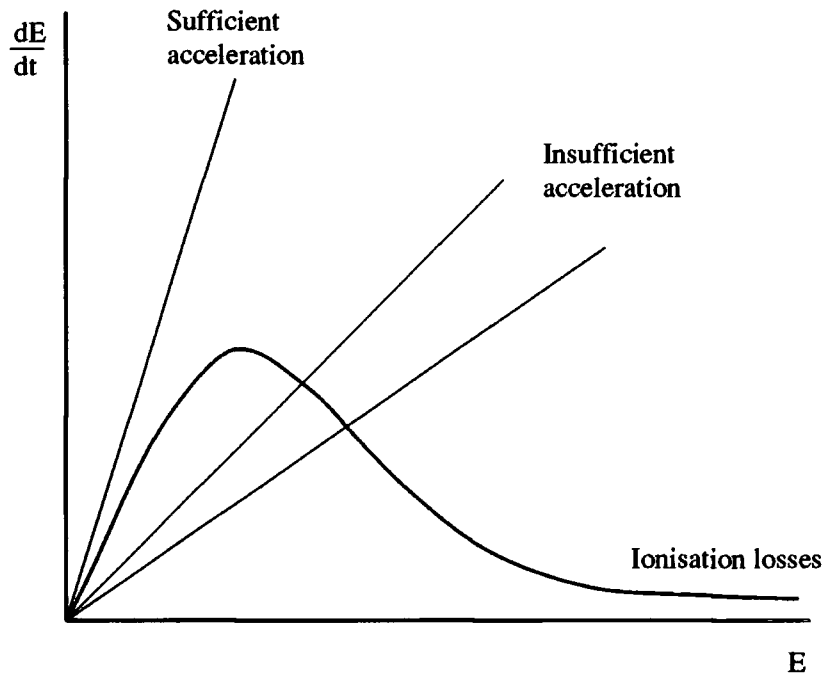

Figure 4.3 The effect of ionisation losses on particle acceleration by the second order Fermi mechanism. (after Longair, 1994)

4.2.4.3 First Order Fermi Acceleration

In the second order Fermi mechanism, energy gain by the particle $\propto (V/c)^2$ as the particle loses energy to tail end collisions. If a system whereby only head on collisions occur could exist, then $\Delta E \propto (V/c)$, and the process becomes much more efficient (Fermi, 1954). Such a situation occurs in the region of a collisionless shock in a plasma, when the shock front is moving with a velocity greater than the Alfvén speed in the medium (e.g. Bell, 1978). If a flux of high energy particles is present

either side of the shock front, they will be scattered through the shock in both directions as they reflect from magnetic irregularities and turbulent plasma. These particles will gain energy upon each crossing of the shock front, in either direction. This process has been reviewed by Drury (1983).

4.2.4.4 Magnetic Reconnection

In a highly conducting ionized plasma environment, any magnetic flux is "frozen" such that bulk motions in the plasma can cause shearing and twisting of the magnetic field lines. If oppositely directed field lines are brought close together, a neutral current sheet will form between them and reconnection of the field lines occurs (see Fig 4.4).The resulting induced electric fields along the neutral sheet can then cause particle acceleration.

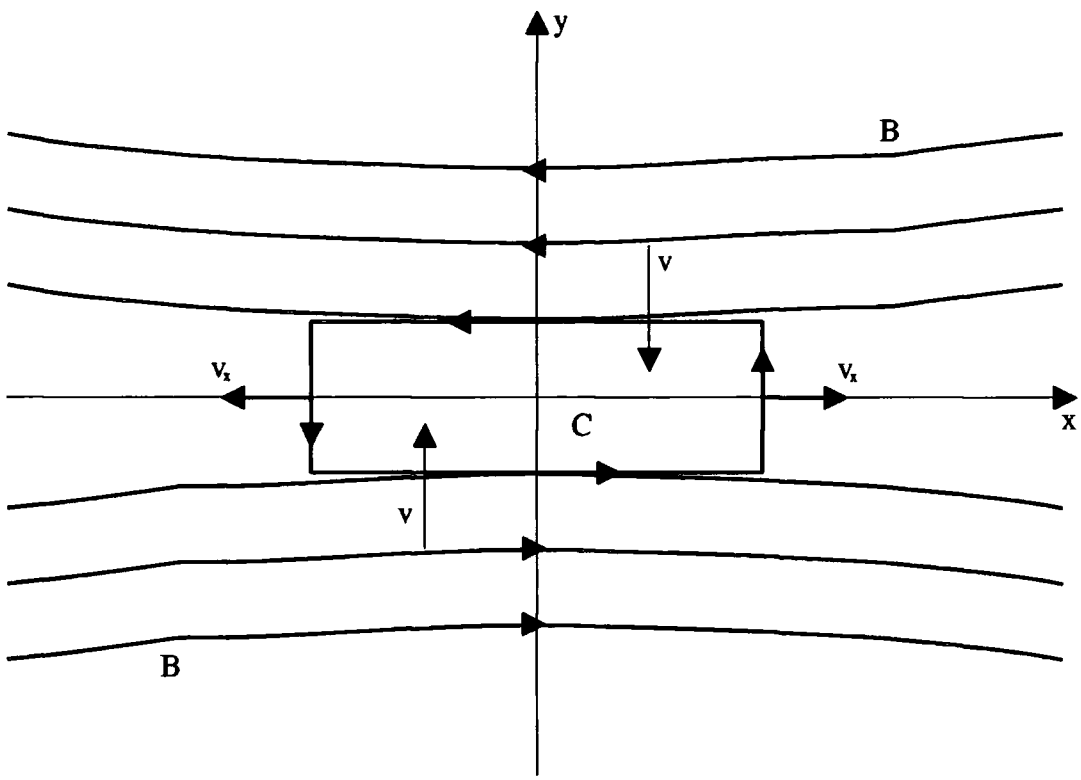

Figure 4.4 Magnetic reconnection occurs in the region C when two magnetic fields (B) of opposite polarity are forced together with a velocity v. An outflow of particles with velocities v_x occurs along the x-axis.

4.2.5 Source models

Any complete model of a compact object system must explain all of the observed features of the radiation across all wavelengths. There are currently no self consistent models which do this; however, models do exist which describe the basic features and allow for TeV gamma ray production.

4.2.5.1 Isolated Pulsar Models

Goldreich and Julian (1969) were the first to point out that a spinning magnetic neutron star will produce a large electric field with a component parallel to the magnetic field. The strength of this electric field is such that charged particles are removed from the surface of the neutron star, creating a plasma filled magnetosphere up to the velocity of light cylinder. This is the surface which, if rotating with the neutron star, would move with a velocity = c. Beyond this point, the magnetic field lines must be open (see Fig 4.5). Sturrock (1971) proposed that currents of highly accelerated charged particles would flow from the magnetic poles along these open field lines and emit curvature radiation. The gamma rays produced in this fashion would pair produce with virtual photons in the strong magnetic field and initiate an electromagnetic cascade, leading to a gamma ray beam. The rotating neutron star will also emit very powerful, low frequency magnetic dipole radiation. Gunn and Ostriker (1969) showed that particles may be accelerated in this radiation field and predicted that protons with energies ~ 10^{16} eV could be produced. However, Rees and Gunn (1974) suggested that the dipole radiation will be unable to propagate through the pulsar magnetosphere and the pulsar's rotational energy is used to power a wind of relativistic electrons and positrons instead.

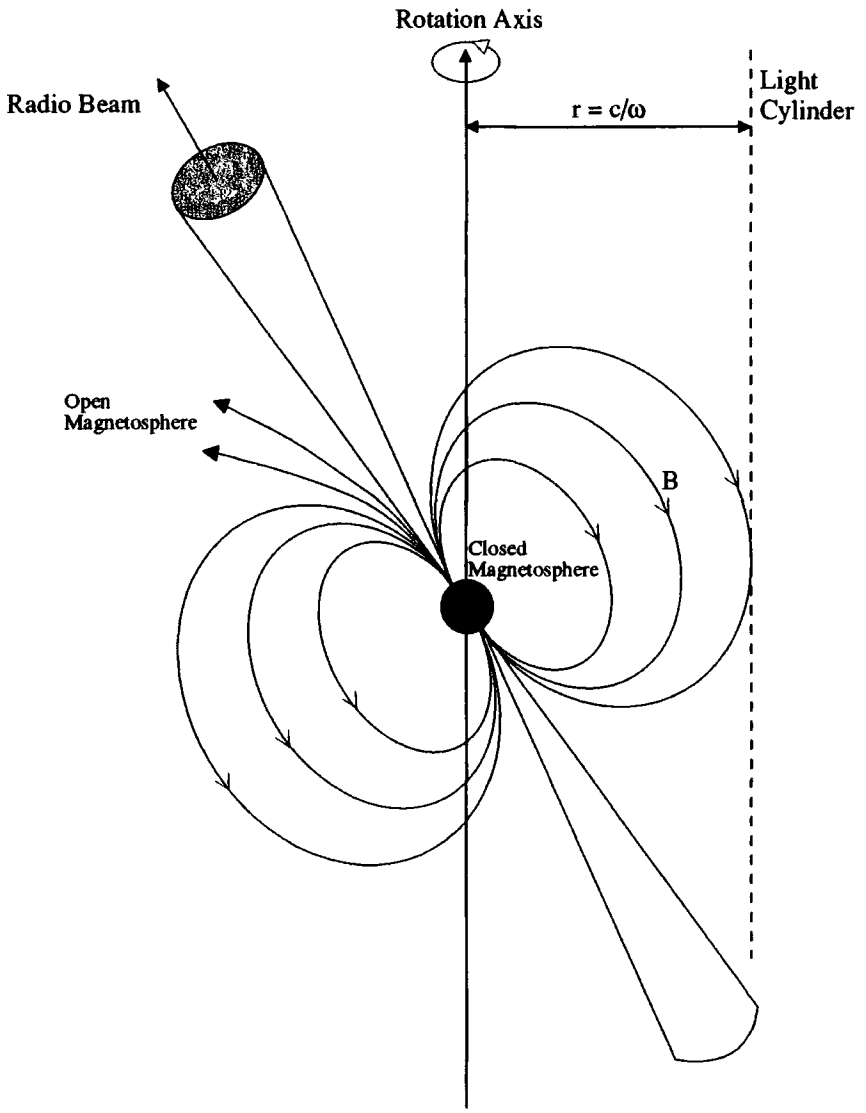

Figure 4.5 A schematic diagram of a pulsar as a rotating magnetised neutron star. (after Longair, 1994)

A further class of pulsar models postulate the existence of vacuum gaps within the magnetosphere of the neutron star, leading to the formation of large electric field potentials in which particle acceleration may occur. Polar cap models (Sturrock, 1970, Ruderman and Sutherland, 1975) postulate the existence of accelerator gaps close to the magnetic poles of the neutron star and have been used to explain the observed radio emission of pulsars (Lyne and Manchester, 1988). Gamma ray emission by this mechanism is harder to explain as high energy photons in the strong magnetic field near the polar cap would interact via pair production (Arons,

1984). The outer gap model of Cheng, et al. (1986, 1986a) predicts the creation of regions of charge depletion near the light cylinder at the last closed field line (Fig. 4.6). Pair production and particle acceleration are sustained by the powerful electric field in the gaps leading to twin gamma ray beams which are observed as they cross the line of sight. Gamma ray production results from two mechanisms. In very young, Crab-type pulsars, accelerated charged particles lose energy primarily by curvature radiation. In older, Vela-type pulsars, the curvature radii of the magnetic field lines is larger and synchrotron losses become more important.

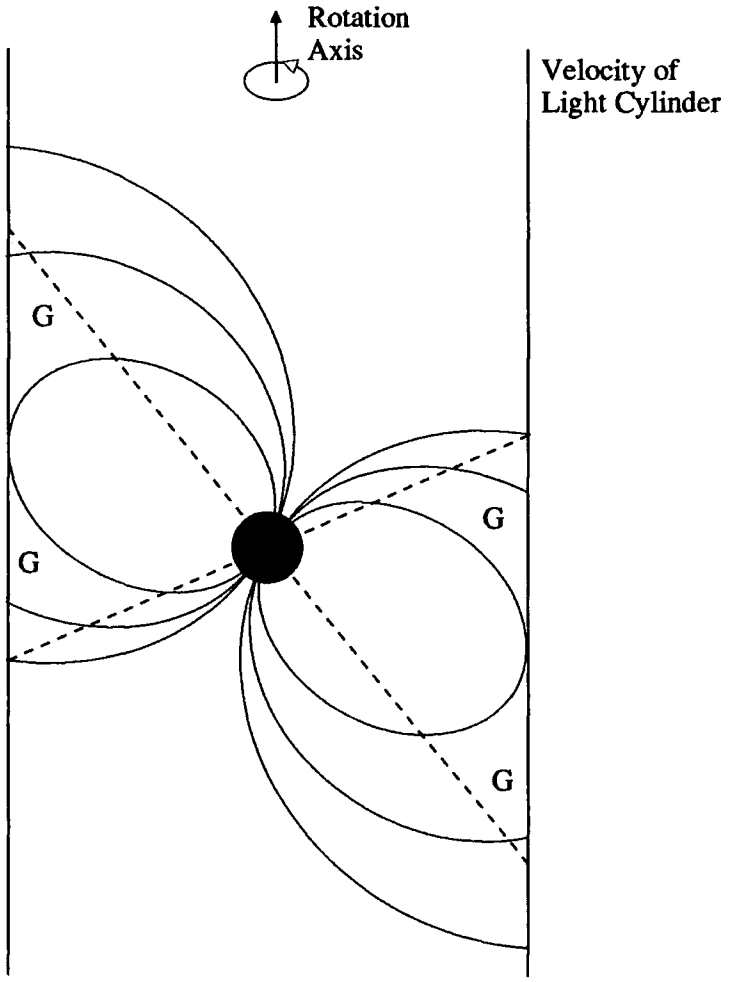

Figure 4.6 A model pulsar magnetosphere. The null surfaces which separate like charges (dashed lines) and the positions of the outer magnetospheric gaps (G) are indicated (after Cheng, et al. 1986).

4.2.5.2 X-Ray Binary System Models

In a situation analogous to the outer gap model, Cheng and Ruderman (1989) have suggested that vacuum gaps may also form in accreting binary systems if an accretion disc is present, the inner region of which rotates faster than the pulsar magnetosphere. The location of the proposed accelerator gap is illustrated in Figure 4.7.

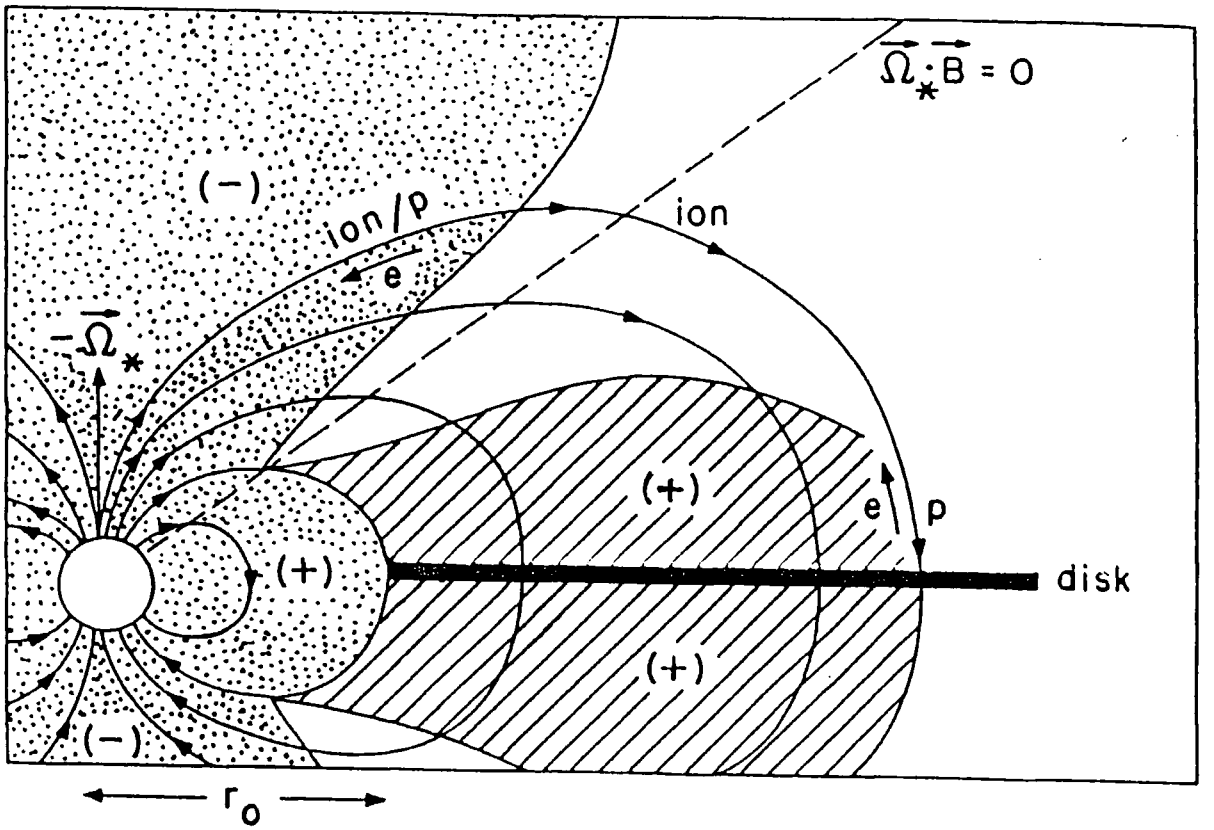

Figure 4.7 The accreting neutron star model of Cheng and Ruderman (1989). The inner (dotted) region corotates with the neutron star while the outer (hatched) region has the same velocity as the accretion disc. The unshaded region illustrates the vacuum gap where a potential drop develops parallel to the magnetic field lines.

Chanmugam & Brecher (1985) have proposed a model, based on a unipolar inductor mechanism, wherein the magnetic field of the neutron star penetrates the accretion disc. Differential rotation within the disc "winds up" and amplifies the field,

setting up a potential across the accretion disc through which particles may be accelerated. VHE gamma rays can then be produced when the particle beam interacts with some target material such as the atmosphere of the primary star. If the magnetic and spin axes of the system are not aligned, pulsed emission can result. A development of this model was suggested by Ruderman, et al. (1989) in which the potential drop is due to a difference in the rotational period of particles in the neutron star magnetosphere and the inner edge of the accretion disc. The maximum energy of particles accelerated by this model is (Gaisser, 1990):

$$E \sim 3.5 \times 10^{14} B_{12}^{-\frac{3}{7}} L_{38}^{\frac{5}{7}} \text{ eV}$$

where B_{12} is the surface field of the neutron star in units of 10^{12} Gauss and L_{38} is the accretion luminosity in units of 10^{38} erg s^{-1}. The stresses built up in the magnetic fields in the disc due to differential rotation and uneven rates of accretion may also be sufficient to cause particle acceleration by magnetic reconnection (e.g. Wang, 1986).

Shock acceleration by the first order Fermi mechanism could occur in the region where matter accretes on to the surface of the compact object. If the shock velocity may be approximated by the freefall velocity at a given distance from the star, then protons may be accelerated up to energies ~ 10^{16} eV. The very strong magnetic fields which exist near the impact point will prevent the escape of charged particles or photons from their production site. To avoid this problem, Kazanas and Ellison (1986a) suggest that neutrons may be stripped from accelerated nuclei by nuclear collisions or photodisintegration and escape the pulsar magnetosphere. The rigidity of the magnetic field in the proposed shock region may also pose a problem for this model (Hillas and Johnson, 1989) as it prevents formation of the magnetic irregularities required to scatter particles across the shock front. Kiraly and Mészáros (1988) have suggested that a relativistic beam of particles may be generated along the magnetic axis of the pulsar as a result of radiation pressure acting on the material

impacting on the surface. Particle acceleration may then occur in a shock formed where the jet interacts with matter accreting in a weaker magnetic field region near the magnetospheric boundary.

Shocks may also form if the Alfvén radius (that distance at which the magnetic pressure about the compact object is great enough to balance the pressure of the accreting matter) is outside of the light cylinder. In this case, the rotational energy of the pulsar can drive a relativistic wind of electrons and positrons (Arons, 1981). A shock forms when this wind interacts with the wind of the companion star, or with the atmosphere of the companion itself (Harding and Gaisser, 1989). This has also been proposed as a method for accelerating particles in pulsars embedded in a supernova remnant (section 6.2.1).

4.3 Pulsed Source Analysis Techniques

Pulsed sources of emission have been among the prime candidates for VHE emission since the birth of gamma ray astronomy. Low gamma ray flux levels and a high rate of background events have led to the development and application of sensitive time series analysis techniques to data from atmospheric Cerenkov experiments. Some of the methods employed are discussed in this section, along with the particular problems involved with searching for pulsed emission from an object in a binary system.

4.3.1 Correcting for Motion Within the Solar System

The calibrated and formatted data files contain an arrival time of the event measured with respect to the reference frame of the telescope. This reference frame is not stationary with respect to the source and so a set of corrections must be applied to allow for the Doppler shifting effects introduced by the relative velocity between source and detector.

The transformation of the event times to the barycentre of the solar system is carried out using the JPL DE200 Earth ephemeris (Standish, 1982). There are three stages involved in the correction. Firstly, the motion of the telescope around the centre of the Earth with respect to the direction of the source is allowed for (<0.021s). The exact geographical locations of the telescopes, necessary for this correction, are given by the GPS system. Next, the detector position is transformed to the barycentre of the solar system to remove the effects of the Earth's orbital motion (<500s). Finally, corrections are made for the relativistic effects introduced by the high velocity of the Earth's motion around the sun, and by the difference in gravitational potential between the true position of the detector and the solar system barycentre (<0.003s) (Mannings, 1990).

4.3.2 Correcting for Motion Within a Binary System

When searching for pulsed emission from a binary system it is incorrect to assume that the emitting region is stationary within the system. The high masses of the compact object and its companion can result in orbital velocities much greater than those found within the solar system, making the corrections for these velocities important. The inherent assumption in these corrections is that the production site for TeV gamma rays is the same as the emission region at other wavelengths.

The accuracy of the correction to the binary system barycentre depends upon the measurement of the parameters of the system's orbital ephemeris by experiments at other wavelengths. These parameters are:

(i) the orbital period of the X-ray source in the binary system, P_b. If available, the first derivative of this period is also used.

(ii) the eccentricity, e, of the orbit.

(iii) a reference epoch T_0 corresponding to the time of passage through a particular point in the orbit (e.g. mid-eclipse of the X-ray source).

(iv) The semi-major axis of the orbit as viewed by the observer: a.sin(i) where a is the

true semi-major axis of the orbit and i, the angle between the pole of the orbit and the line of sight.

A full description of this correction is given by Carraminana (1991).

4.3.3 Phase Sensitive Analysis

The phase sensitive analysis techniques used to investigate VHE gamma ray observations can be divided in to two types, based upon the accuracy to which the period and light curve of emission is known. For objects such as radio pulsars, almost continuous monitoring of the very steady periodic emission is available at other wavelengths and epoch folding methods can be used. Information on the emission from X-ray binary systems is only occasionally available and the emission can be variable in intensity, periodicity and light curve shape (e.g. Charles and Seward, 1995), making more broadly sensitive tests necessary.

4.3.3.1 Epoch Folding

In cases where the period of the emission from the source is well defined by observations at other wavelengths, a simple test for periodicity is given by allocating each event to a relative phase interval based on its measured arrival time. The total number of events in each phase bin is then used to produce an overall light curve which can be tested for evidence of periodicity by comparing it with the expected uniform phase distribution. This comparison can be made by using Pearson's χ^2 test to evaluate the deviation of the number of events in each bin from the expected number (Leahy, et al. 1983). If the shape and precise phase position of the expected light curve is known then the size and position of the phase bins can be determined *a priori* to give the most significant signal. If the light curve is less well measured, then a narrow phase peak may be split between bins and any re-binning will increase the degrees of freedom and incur a statistical penalty.

Gregory and Loredo (1992) have proposed a method for Bayesian analysis of

time series. In this, the expected uniform phase distribution is compared against a series of modelled binned distributions with periodic structure. The model which best fits the phase distribution of the data can then be found and the odds of obtaining such a distribution calculated using Bayesian methods. This method is particularly useful in handling data with gaps in it and in finding the optimum number of phase bins to use. It is also possible to quantify the statistical penalties incurred by invoking a more complex model distribution.

A complementary test for periodicity is to examine the sign of the deviation of the number of events in each bin from the expected number. The run test (Eadie, et al. 1971) can be used for this purpose and will produce a result significantly different from expectation if the deviations are consistently negative or positive. One advantage of this test is that it is independent of Pearson's χ^2 test and can thus be combined with it to produce a more powerful statistic.

4.3.3.2 The Rayleigh Test

Arbitrary binning decisions, which are an unavoidable consequence of epoch folding when the light curve is poorly measured, can be circumvented by the use of circular statistics. Instead of binning the data, the time of arrival of each event is represented by a radial vector on a circle with a phase angle, ϕ, relative to some arbitrary phase (Fig 4.8). These vectors are then tested to see whether they differ significantly from randomness. The criterion for significance used in VHE gamma ray astronomy is normally three standard deviations (3σ). If a significant difference is found then the null hypothesis, H_0: the parent population is uniformly distributed in phase, can be rejected. The Rayleigh test (Rayleigh, 1894) was introduced to VHE gamma ray astronomy by Gibson et al. (1982a) and provides the most commonly used test statistic in this field.

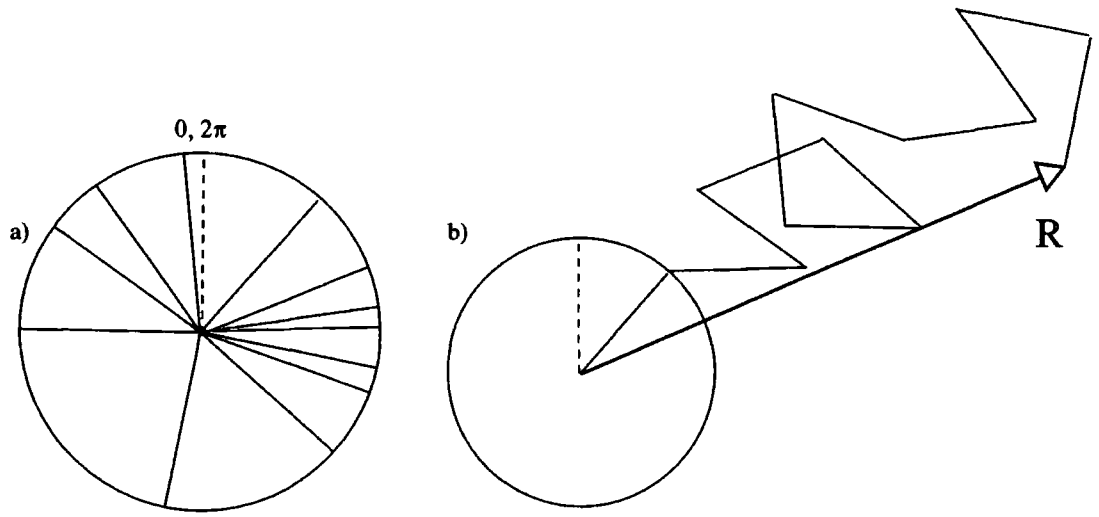

Figure 4.8 Illustration of the Rayleigh test. a) Each time is treated as a unit vector with a phase angle ϕ. b) These are then summed to produce a resultant Rayleigh vector R

The Rayleigh test has been described in some detail by Mardia (1972) and more recently by Batschelet (1981). Briefly, the test is performed by adding the radial vectors for each event in a dataset. The modulus of the resultant vector is divided by the number of events, N, to give a normalised value , R, between 0 and 1 which can then be tested for significance. R is given by:

$$R = \frac{1}{N}\left[\left(\sum_{i=1}^{N}\cos\phi_i\right)^2 + \left(\sum_{i=1}^{N}\sin\phi_i\right)^2\right]^{\frac{1}{2}} \quad (\text{mod } 2\pi)$$

If the number of events is large (N>100), then $2NR^2$ is distributed approximately as a χ^2 distribution with two degrees of freedom. and the probability of obtaining a particular value of $2NR^2$, is:

$$Pr(\geq 2NR^2) = e^{-NR^2}$$

where NR^2 is known as the Rayleigh power. More accurate estimates of the probability for the case where N is small are possible (Greenwood and Durrand, 1955), however, this situation does not arise with the typical datasets necessary to

measure a significant flux of TeV gamma rays with an ACT.

The Rayleigh test is most sensitive to broad sinusoidal light curves. In the case of a source with a double peaked light curve, with the peaks separated by 180° in phase, the phase vectors will cancel each other and give a small resultant R. This problem is often avoided by searching at both the fundamental and the first harmonic of the expected period. Alternatively, the Z^2_m test may be used. The Z^2_m statistic is a modification of the Rayleigh statistic and is equal to twice the sum of the Rayleigh powers for the first m harmonics. If R^2_j is the Rayleigh statistic evaluated at the j^{th} harmonic then:

$$z^2_m = \sum_{j=1}^{m} 2NR^2_j$$

The Z^2_m statistic for large values of N is then distributed approximately as χ^2 with 2m degrees of freedom (Lewis, 1993).

Short exposures and a varying count rate due to zenith angle effects can introduce an artificial enhancement in χ^2 for longer test periods. The first problem can be avoided by truncating the dataset to an integral number of test periods (Poincaré's correction); however, this is difficult if a range of periods are to be tested. Orford (1996) has suggested corrected formulations of χ^2 for datasets of finite length and varying count rate.

4.3.3.3 Period Searching

When searching for periodic emission from a potential gamma ray source using the Rayleigh test it is rarely sufficient to test at a single period. Uncertainties in the period of emission can be caused by unpredictable source behaviour and errors in the orbital parameters. Searching a range of periods, however, leads to an increased chance of finding an apparently significant result and so the search range should be kept as small as possible and all degrees of freedom due to the extra trials fully

accounted for. To determine the number of trials, it is necessary to know the extent of the correlation of the Rayleigh statistic between adjacent test periods. For an estimated period P_1, tested on a dataset of duration T, the phase difference between the first and last events, $\Delta\phi = T/P_1$. If a small increment is added to P_1, the phase difference is decreased slightly. Eventually, such increments lead to a value of the period where the phase difference between the first and last events has slipped by a full cycle. This is the next independent trial period. The number of independent periods, N_P, in the period range P_1 to P_2 is then given by:

$$N_P = \frac{T}{P_1} - \frac{T}{P_2} = \frac{T(P_2 - P_1)}{P_1 P_2}$$

and the distance between independent periods, $(P_2-P_1)/N_P$, known as the Fourier interval:

$$\text{F.I.} = \frac{P_1 P_2}{T}$$

If the period range searched is small compared with T, then $P_1 \sim P_2 \sim P$ and the Fourier interval is simply P^2/T. Standard procedure is to test three times within each Fourier interval (oversampling) to allow for a signal peak falling approximately between two independent test periods. The effect of these extra trials on the true significance of the Rayleigh statistic must be accounted for in the analysis. Monte Carlo studies by De Jager, et al. (1989) and an analytical treatment by Orford (1991) imply that as the Rayleigh power increases, the significance of the effect is overestimated by a factor of ~ 3.

4.3.3.4 Combining Observations

A typical source dataset for an atmospheric Cerenkov experiment will consist of several ($\sim$ 10) observations of a few ($\sim$ 5) hours for each month in which the

source was visible. It is necessary to be able to combine these observations in some fashion to test for periodic emission in the entire dataset. The simplest method available, and that which is most appropriate where the behaviour of the pulse period is poorly known over a timescale of several days, is to combine each of the probabilities of uniformity of phase to produce a new statistic. This does not rely on the phase information being retained between each observation ie. the observations are combined incoherently. If at a test period P, the Rayleigh probability Pr_j is obtained for n observations, then the formula for the combination of these is given by Eadie et al. (1971) as:

$$C = -2 \sum_{j=1}^{n} \ln(Pr_j)$$

which is exactly distributed as χ^2 with 2n degrees of freedom. The Fourier interval for period searches in combined datasets is calculated using the average duration of each independent observation.

In the case of sources where the period and period derivative are extremely well measured, such as with radio pulsars, it is possibly to combine the observations coherently. The datasets are simply treated as one long observation with gaps in it. The period search range must be restricted as far as possible in this case as the Fourier interval is given by P^2/T where T is the time from the start of the first observation to the end of the last.

4.3.3.5 A Software Test

The periodic analyses presented in this chapter have relied upon the use of existing software packages. It is therefore important to test the performance of these packages on a time series with a known periodicity prior to the analysis. This has been done using an EGRET observation of the Vela pulsar. The EGRET data, consisting of 1715 photons, was recorded over three days from the 10^{th} to the 13^{th} of

May, 1991. Figure 4.9 displays the results of the Rayleigh test and the epoch folded light curve at the peak Rayleigh power. The periodicity due to the 89 ms pulsar can be clearly seen.

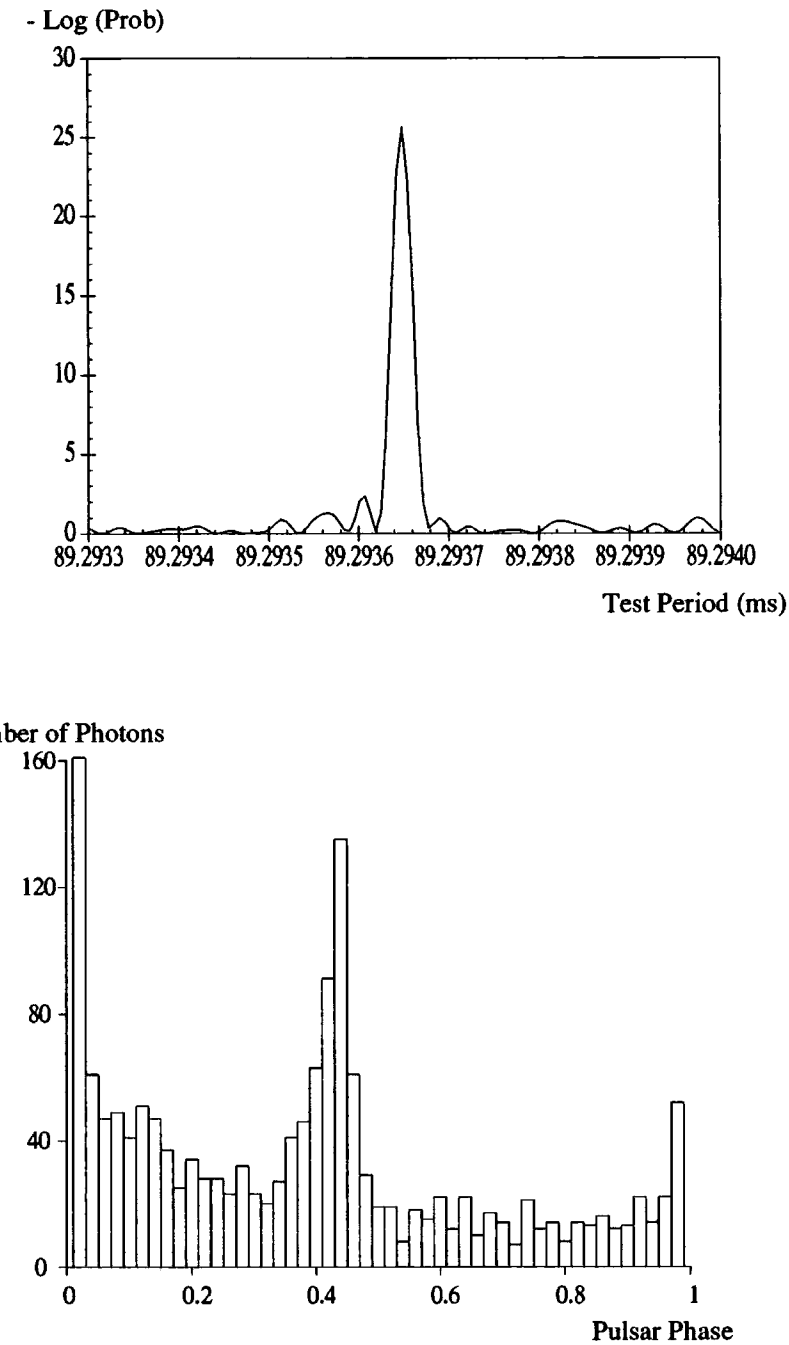

Figure 4.9 The results of the Rayleigh test applied to an EGRET observation of the Vela pulsar. The lower figure shows the light curve at the period of the peak Rayleigh power.

4.4 A Search for Periodic Emission Using the Guard Ring Rejection Technique.

The technique of guard ring rejection has been described in section 3.3.2 and was the method of signal enhancement employed by the University of Durham Mark 3 ACT between its construction in 1986 and the installation of an imaging camera in April 1993. An analysis of all the data recorded by the Mark 3 telescope whilst tracking the X-ray binary source SMC X-1 was presented by Bowden (1993). He concluded that there was no significant evidence for emission at TeV energies, but that a reanalysis of the data using a more accurate orbital ephemeris could prove worthwhile. The results of that analysis are presented here.

4.4.1 SMC X-1

SMC X-1, the first X-ray source discovered in the small Magellanic cloud, was first detected by rocket flight experiments (Price, et al. 1971). Subsequent observations using the UHURU satellite revealed the existence of X-ray eclipses lasting 0.6 days with a period of 3.89 days, establishing the binary nature of the source (Schreier, et al. 1972). A BOI supergiant star, Sk 160, was suggested as the optical counterpart to the X-ray source (Webster, et al. 1972) and this was confirmed by the detection of optical brightness variations in phase with the X-ray eclipse period (Liller, 1973). Optical photometry indicated the presence of an accretion disk which influences the optical light curve (van Paradijs and Zuiderwijk, 1977).

The discovery of X-ray pulsations in SMC X-1, indicating the presence of a pulsar, was reported by Lucke et al. (1976). Between 25% and 35% of the X-ray flux was found to be pulsed at a period of 0.72s with the light curve showing two broad peaks, the interpulse strengthening at higher energies. More recent observations by Kunz et al. (1993) revealed an increase in the pulsed fraction up to >80%, declining to 20% over the course of ~ 200 days. The period, $P_{pulse,}$ of the pulsed emission has

been decreasing since its discovery (Henry and Schreier, 1977) with little variation and no observed spin-down episodes.

SMC X-1 is one of the brightest stellar X-ray sources known, with a maximum inferred X-ray luminosity of ~ 8×10^{38} ergs s^{-1} in the range 1 - 37 keV for an assumed distance of 65 kpc (Levine, et al. 1993). The high accretion rate necessary to generate this X-ray flux is inconsistent with a model powered by stellar wind accretion and can only be explained by Roche lobe overflow from the supergiant. This model also helps to explain the steady pulsar period spin-up. The masses of the two objects in the system have been calculated by van Kerkwijk, et al. (1995) as:

$$15.2^{+2.6}_{-2.1}\ M_{\odot} \text{ for the supergiant}$$

$$1.17^{+0.36}_{-0.32}\ M_{\odot} \text{ for the pulsar.}$$

Variations in luminosity between ~ 10^{37} and 10^{39} ergs s^{-1} have been detected on various timescales. Flaring behaviour is observed over hours and days and the source enters extended low and high states, differing by over an order of magnitude in luminosity and exhibiting a spectral hardening with increased emission (e.g. Tuohy and Rapley, 1975; Bonnet-Bidaud and van der Klis, 1981; Kahabka and Pietsch, 1996).

4.4.2 TeV Gamma Ray Observations of SMC X-1

The first report of TeV observations of SMC X-1, using the University of Durham Mark 3 telescope, was presented by Brazier, et al (1990). 264 hours of data, collected between October 1986 and October 1988 were processed and only those events which triggered the on-source channel alone were accepted for phase sensitive analysis. A contemporaneous X-ray pulse period measurement was used to search for emission in data from July 1987 and provided evidence for a weak signal at the

expected period. The possibility that the VHE gamma ray and the X-ray production sites were not coincident was investigated by correcting event times for orbital motion within the binary system using a small range of values for the semi-major axis and orbital phase. After correction for the number of trials involved in this search, a chance Rayleigh probability of 3×10^{-5} was found for the detection of emission at the pulsar period. This signal was largely confined to the three of the nine observations in the July dataset at orbital phases around 0.25 and 0.75. Some models of X-ray binaries predict that VHE gamma rays may be observed from the decay of neutral pions, produced when an accelerated beam of protons interacts with some target material in the line of sight (e.g. Hillas and Johnson, 1991). This situation could well occur at the nodes of the orbit, with the atmosphere and stellar wind of the primary forming a target for the proton beam. The application of these optimised orbital parameters to the search for pulsed emission in the eight other datasets available gave a chance probability of 10^{-4} for emission at the expected period.

A thorough analysis of all observations of SMC X-1 with the Mark 3 telescope between October 1986 and November 1989 was performed by Mannings (1990). In addition to rejecting events which triggered off-source channels, those events with a response greater than 60% of the on-source channel in any of the guard ring tubes were also removed. A search for emission pulsed at the X-ray period was performed on each of 11 sequences of observations, maintaining phase coherence within each ~ 10 day sequence. Orbital searching techniques were employed and raw chance probabilities of 5×10^{-6} and 5×10^{-5} were noted for the months of July 1987 and September/October 1989 for an assumed emission site co-located with the neutron star position. A series of simulations designed to test the true significance of the Rayleigh statistic after orbital searches of this type indicated that these probabilities were consistent with a random time series. The 20 separate observations within these two sequences were examined individually and the majority of the evidence for emission was found to originate with three datasets, situated about

orbital phases of 0.72, 0.25 and 0.70 and coincident with the neutron star position. Again, the trials involved in this analysis reduced the evidence for emission over this shorter timescale to the level of chance.

A similar analysis method was applied by Bowden (1993) to the Durham SMC X-1 database, including observations up to October 1992. Using a refined relative guard ring response threshold of 45% (Brazier, 1991) and improved pedestal calibration, each observation was tested for pulsed emission over a range of assumed values of semi-major axis and orbital phase. The data were divided into two groups. Observations prior to 1990 were tested for periodicity within one Fourier interval of the expected period, while those after 1990 had the test range broadened to two Fourier intervals, to allow for errors in the expected period caused by the lack of a contemporaneous X-ray measurement. Five single observations were discovered to give a Rayleigh chance probability less than expectation after the large number of trials in this analysis were accounted for. The orbital phases at the time of these observations were 0.25, 0.58, 0.79, 0.81, and 0.86. The most significant of these observations gave a 10% probability of chance occurrence and so conclusive evidence for emission was not obtained.

At higher energies, the South Pole Air Shower Experiment reported the detection of a burst of unpulsed emission from the direction of SMC X-1 lasting one day (18^{th} October 1991) (Vanstekelenborg et al, 1993). The probability of the burst rate occurring by chance was quoted as 0.4% and corresponds to a flux of $1.3 \pm 0.2 \times 10^{-11}$ cm^{-1} s^{-1} above 50 TeV. None of the Durham telescopes were operational during this period.

In 1993 an updated set of orbital parameters for the SMC X-1 binary system were published which included a rate of orbital decay (Levine, et al. 1993). The potential effects of this new information upon any periodic component in the data can be estimated as follows. The maximum Doppler variation in the observed frequency of pulsed emission occurs at the nodes of the orbit. If P' is the pulse period measured

in the rest frame of the observer when the pulsar is moving with velocity, v, at a node, then:

$$P' = P_0 \left(1 \pm \frac{v}{c}\right)$$

and

$$\frac{v}{c} = \frac{2\pi a\sin(i)}{P_{orb}}$$

where P_{orb} is the orbital period and asin(i) is the semi-major axis of the orbit in light seconds. The pulsar frequency shift is then given by:

$$P' - P_0 = \frac{P_0\, 2\pi a\sin(i)}{P_{orb}}$$

For the Levine ephemeris, asin(i) = 53.4876 ± 0.0004 ls whereas previous analyses had used a value of 53.46 ± 0.05 ls. The effect of using these different values of asin(i) will change the correction for pulsar frequency shift by a maximum of $\sim 4 \times 10^{-7}$ s. When retaining phase coherence over 15 days, the Fourier interval can be as short as 3.9×10^{-7} and so inaccuracies in the old orbital parameters may well have been sufficient to destroy any periodicity in the dataset. A re-analysis of the Durham database is presented in the following sections.

4.4.3 Data Selection

There are two reasons for not using all of the recorded events in a phase sensitive analysis. The first is the need to have a "clean" dataset, free from any systematic effects which may introduce biases into the calculated Rayleigh probabilities. Secondly, background discrimination techniques are used to improve the signal to noise ratio within the dataset.

The count rate profiles and observer's comments for all observations of SMC

X-1 with the Mark 3 telescope between 1986 and October 1992 were examined and any effected by frost or condensation on the mirrors, poor weather or by equipment failures were excluded or truncated to eliminate the effect. This selection resulted in 121 observations, taken from 18 different observing periods, with an average duration of 3.3 hours. The full catalogue of these observations is given in Table 4.1.

The first stage of the guard ring background rejection involved rejecting those events which triggered in any coincidence channel except for the central, on-source channel alone. The pedestal offsets for each PMT were then calculated for each night using the cosmic ray response distribution (Bowden, 1993). Following Brazier (1991), events with a signal greater than 45% of the on-source response in any of the guard ring tubes were then removed. The final number of selected events for each observation is also shown in Table 4.1.

Table 4.1: Catalogue of Mark 3 telescope observations of SMC X-1

Observation Date	Duration (hours)	Events Selected	Orbital Phase at Midpoint
24/10/86	2.0	2969	0.79
25/10/86	2.8	3407	0.04
26/10/86	3.4	4073	0.29
27/10/86	3.9	3281	0.55
28/10/86	1.6	2300	0.81
30/10/86	2.1	2685	0.33
01/11/86	3.5	8544	0.83
02/11/86	1.7	6205	0.08
03/11/86	3.3	7573	0.34
04/11/86	2.4	4636	0.61
21/07/87	2.9	1664	0.21
22/07/87	3.5	1485	0.46
23/07/87	4.3	4490	0.72
24/07/87	4.1	4022	0.97
25/07/87	3.3	1004	0.22
26/07/87	1.5	1340	0.49
28/07/87	2.8	2386	0.00
29/07/87	4.3	1503	0.25
31/07/87	4.9	4405	0.77

20/08/87	2.9	2252	0.89
21/08/87	2.8	2805	0.15
22/08/87	2.9	2881	0.41
23/08/87	2.7	3138	0.66
24/08/87	3.2	2629	0.92
25/08/87	3.2	3329	0.18
26/08/87	3.3	3648	0.43
28/08/87	3.3	2721	0.95
14/09/87	2.3	1750	0.30
15/09/87	3.3	3657	0.55
16/09/87	3.3	3072	0.81
17/09/87	2.2	1183	0.07
18/09/87	3.7	3639	0.32
19/09/87	3.8	2652	0.58
20/09/87	3.7	1147	0.84
21/09/87	3.8	2747	0.09
22/09/87	3.8	2883	0.35
23/09/87	2.8	2073	0.61
24/09/87	3.3	1386	0.87
25/09/87	3.2	2131	0.12
26/09/87	2.0	1346	0.40
27/09/87	4.3	2545	0.63
10/10/87	1.7	1303	0.94
11/10/87	2.9	1607	0.21
12/10/87	4.0	1884	0.47
14/10/87	4.3	3017	0.98
16/10/87	5.2	3749	0.53
17/10/87	4.0	3602	0.76
18/10/87	4.0	3460	0.01
19/10/87	4.3	2329	0.29
20/10/87	5.7	6865	0.54
22/10/87	2.9	3516	0.03
23/10/87	3.9	3381	0.30
24/10/87	3.8	2009	0.56
25/10/87	2.1	2874	0.81
13/11/87	1.9	1626	0.69
17/11/87	3.1	1354	0.72
18/11/87	3.1	3079	0.98
19/11/87	3.1	3375	0.23
20/11/87	2.2	1770	0.50
14/07/88	3.3	4809	0.44

16/07/88	3.4	4413	0.96
17/07/88	3.4	5083	0.21
18/07/88	3.4	5379	0.46
20/07/88	3.3	1119	0.98
04/09/88	3.8	1140	0.78
07/09/88	4.0	4062	0.53
09/09/88	4.5	4756	0.04
10/09/88	6.4	7797	0.31
12/09/88	6.0	5616	0.83
13/09/88	5.2	11918	0.07
14/09/88	4.8	8044	0.33
16/09/88	5.2	5748	0.86
01/10/88	2.6	2928	0.68
02/10/88	2.7	4170	0.96
22/09/89	5.3	6811	0.15
23/09/89	3.8	4018	0.41
24/09/89	2.4	3114	0.66
26/09/89	2.6	2705	0.17
28/09/89	4.2	6339	0.69
29/09/89	4.0	6423	0.95
30/09/89	5.1	2117	0.20
01/10/89	4.7	6943	0.46
02/10/89	5.6	7907	0.71
03/10/89	4.3	5320	0.97
04/10/89	2.3	2783	0.24
20/10/89	1.0	1404	0.35
22/10/89	5.8	2870	0.85
23/10/89	2.3	1754	0.09
25/10/89	3.8	3939	0.61
29/10/89	2.8	2923	0.66
30/10/89	2.8	2273	0.92
02/11/89	1.7	1163	0.68
18/11/89	3.3	3963	0.78
19/11/89	4.1	5476	0.04
23/11/89	3.3	3772	0.06
25/11/89	3.4	2771	0.58
29/11/89	3.0	3003	0.61
01/12/89	1.8	2267	0.12
17/09/90	3.4	5693	0.68

18/09/90	2.7	4122	0.93
19/09/90	2.5	3071	0.19
20/09/90	2.5	3031	0.44
11/10/90	2.7	4627	0.82
12/10/90	3.3	5970	0.08
13/10/90	3.9	6294	0.34
16/10/90	2.8	3981	0.10
17/10/90	1.4	1221	0.35
18/10/90	3.6	4402	0.61
20/10/90	1.3	2988	0.13
22/10/90	2.5	5777	0.64
23/10/90	2.5	5311	0.90
10/11/90	2.5	2240	0.50
17/11/90	2.0	2991	0.30
18/11/90	2.0	2828	0.55
10/01/91	2.0	1194	0.17
18/01/91	1.9	1865	0.23
25/08/92	5.2	1952	0.59
20/09/92	2.7	2286	0.25
21/09/92	2.0	1452	0.50
25/09/92	1.5	1563	0.53
26/09/92	3.1	3527	0.79
TOTALS	395.7	421812	

4.4.4 Analysis Procedure

All of the previously mentioned analyses of the Mark 3 SMC X-1 database have involved some degree of searching in orbital parameters. No conclusive evidence for a production site significantly displaced from the X-ray emission region has been obtained. The quoted errors on the values of the semi-major axis and the epoch of eclipse mid-point for the binary system are small for the orbital ephemeris used in this analysis (Table 4.2) and the inclusion of an orbital decay term further increases the accuracy of the ephemeris. These factors, together with the problem of the large number of statistical trials which occur in orbital searching, suggested that a

more powerful test for pulsed emission in the TeV region was to correct event arrival times using the measured ephemeris alone.

Table 4.2: Parameters for the SMC X-1 binary system (Levine, et al. 1993).

Parameter	Value	Uncertainty (1σ)
a.sin(i)	53.4876 lt-sec	0.0004
Eccentricity	<0.00004 (2σ)	0.00001
Pulse period change	-5.30×10^{-4} yr^{-1}	2×10^{-6}
Mid-eclipse epoch	MJED 42836.18277	0.00020
Orbital period	3.89229118 days	4.8×10^{-7}
Orbital period change	-3.36×10^{-6} yr^{-1}	0.02×10^{-6}

The light curve of SMC X-1 at X-ray energies is double peaked, with the interpulse displaced almost exactly 180° in phase from the main pulse. As mentioned in section 4.4.3.2, this type of light curve may produce a deceptively low Rayleigh statistic. To allow for the possibility of a similar shape of light curve in the TeV emission, the data were tested for pulsed emission at both the fundamental and the first harmonic of the pulsar period.

The length of time over which phase coherence can be maintained for time series analyses is dependent upon the accuracy to which the period derivatives are known. If the dataset is of such a length that the period shift between its start and end points is uncertain by a value greater than one Fourier interval, the data must be divided into smaller sections and the chance probabilities combined incoherently. The maximum length of dataset, T_{max}, for a period P is then given by:

$$T_{max} = \frac{P}{\sqrt{\Delta \dot{P}}}$$

where $\Delta \dot{P}$ is the error on the period derivative.

For a period of 355 ms, the half period of SMC X-1, T_{max}~ 20 days. It is therefore reasonable to maintain phase coherence within each 3 week long observing period, but not between them.

The recent published measurements of the X-ray pulse period for SMC X-1

are given in Table 4.3. While the measurement error on each is reasonably small, the RMS deviation of these points from a straight line fit is ~ ±0.03 ms, which may be due to a change in the spin behaviour of the neutron star. To account for this, a search range of ±0.05 ms about the expected period (±0.025 ms in the case of the half period) is used in this analysis.

Table 4.3: X-ray pulse period measurements for SMC X-1.

Epoch (MJED)	Period (ms)	Reference
42836.6823	714.88585±0.0004	Primini, et al. (1977)
43000.1562	714.7337±0.0012	Davison (1977)
43986.407	713.684±0.032	Darbro, et al. (1977)
46941.72954	710.592116±0.00036	Levine, et al. (1993)
47402.52220	710.140672±0.00002	Levine, et al. (1993)
47452	710.0972±0.0022	Gilfanov, et al. (1989)
47591	709.9830±0.0030	Gilfanov, et al. (1989)
47740.35673	709.809901±0.00003	Levine, et al. (1993)

4.4.5 Results

The Rayleigh statistic, R, has been calculated for the data from each observing period, maintaining phase coherence between each observation. The raw probability of the resulting R value occurring by chance at the X-ray period and half-period is shown in Table 4.4, along with the chance probability corrected for the number of trials involved in searching a period range. These trials are conservatively estimated by calculating the number of Fourier intervals involved in searching around the test period, multiplying by three to account for oversampling and by eighteen to allow for the number of different datasets tested.

Table 4.4: Rayleigh test results for all SMC X-1 data by observing period.

Observing Period	Chance probability at full period Raw (corrected)	Chance probability at half period. Raw (corrected)
24/10/86 - 04/11/86	1.8×10^{-2} (1.0)	4.2×10^{-3} (9.9×10^{-1})
21/07/87 - 31/07/87	2.1×10^{-3} (6.6×10^{-1})	4.4×10^{-3} (9.9×10^{-1})
20/08/87 - 28/08/87	5.4×10^{-2} (1.0)	1.0×10^{-2} (1.0)
14/09/87 - 27/09/87	2.1×10^{-3} (7.6×10^{-1})	6.5×10^{-5} (8.3×10^{-2})
10/10/87 - 25/10/87	7.9×10^{-4} (4.6×10^{-1})	1.6×10^{-4} (2.2×10^{-1})
13/11/87 - 20/11/87	1.1×10^{-2} (9.8×10^{-1})	5.1×10^{-3} (9.8×10^{-1})
14/07/88 - 20/07/88	5.3×10^{-4} (1.5×10^{-1})	3.5×10^{-3} (8.9×10^{-1})
04/09/88 - 16/09/88	6.4×10^{-3} (9.8×10^{-1})	3.7×10^{-2} (1.0)
01/10/88 - 02/10/88	2.5×10^{-2} (7.3×10^{-1})	4.2×10^{-2} (9.9×10^{-1})
22/09/89 - 04/10/89	2.9×10^{-4} (1.6×10^{-1})	3.1×10^{-3} (9.8×10^{-1})
20/10/89 - 02/11/89	1.2×10^{-3} (5.5×10^{-1})	5.1×10^{-4} (4.9×10^{-1})
18/11/89 - 01/12/89	2.6×10^{-3} (8.3×10^{-1})	7.1×10^{-4} (6.1×10^{-1})
17/09/90 - 20/09/90	1.0×10^{-1} (1.0)	9.6×10^{-2} (1.0)
11/10/90 - 23/10/90	3.4×10^{-2} (1.0)	6.3×10^{-3} (1.0)
10/11/90 - 18/11/90	8.0×10^{-2} (1.0)	5.8×10^{-2} (1.0)
10/01/91 - 18/01/91	3.6×10^{-2} (1.0)	7.9×10^{-3} (1.0)
25/08/92	4.2×10^{-2} (3.6×10^{-1})	1.2×10^{-2} (2.2×10^{-1})
20/09/92 - 26/09/92	1.5×10^{-1} (1.0)	4.1×10^{-2} (1.0)

These results provide no evidence for VHE gamma ray emission pulsed at the X-ray period or at its first harmonic in any single observing period. Combining the corrected probabilities using the equation given in section 4.4.3.4 indicates a 96.8% probability that the data are uniformly distributed in phase at both the full and the half period over the six year dataset.

Assuming an effective collecting area of 10^8 cm^2 for the Mark 3 telescope based on early experiments with small ACT arrays by the Durham group at the Dugway proving grounds in Utah (e.g. Chadwick, 1987) leads to an average

background count rate of ~ 3.0×10^{-9} cm^{-2} s^{-1}. The Rayleigh statistic is a measure of the fractional pulsed signal strength and by calculating that R which would have produced a 3σ detection (chance probability of 1.348×10^{-3}) using:

$$R^2 = \frac{\ln (1.348 \times 10^{-3})}{N}$$

we can infer a 3σ upper flux limit of ~ 1.2×10^{-11} cm^{-2} s^{-1} above the energy threshold for cosmic rays of ~ 1 TeV.

4.5 A Search for Periodic Emission Using Medium Resolution Image Discrimination.

In April 1993 the Mark 3 telescope was upgraded and the central detector package replaced with a medium resolution imaging camera containing 31 PMT's (see section 3.4.2.3). Background discrimination techniques using the images recorded by this camera have been successfully employed to enhance the gamma ray signal from the X-ray binary Vela X-1 (Chadwick, et al. 1995) and the cataclysmic variable source AE Aquarii (Chadwick, et al. 1995a). The results of a similar analysis of observations of SMC X-1 are presented here.

4.5.1 Data Selection

The 1993 Mark 3 telescope SMC X-1 dataset consists of 12 observations, all taken in the tracking mode, of average duration 3.3 hours. The count rate profiles and observers comments were examined for these and four were discarded due to poor weather conditions and/or equipment problems. The remaining observations are catalogued in Table 4.5, six from July and one from each of September and October. The Mark 5 telescope was also operational for some of these observations but was still under development and subject to various equipment problems. Consequently, these data are not used in this analysis.

The background discrimination techniques which were employed were developed empirically during the analysis of observations of AE Aquarii (Chadwick, et al. 1995a), in which a significant burst of pulsed gamma ray emission was observed. The analysis philosophy was to develop simple parameters which could be used to reject a reasonable fraction of obvious nucleon shower image candidates whilst retaining all of the gamma ray signal.

After formatting and PMT calibration (section 3.5), the data selection proceeds in 5 stages:

(i) The PMT responses are examined and those with a value greater than 5 times the standard deviation of the tube response under sky noise conditions (σ_N) are selected as "image" tubes. Any tubes adjacent to an image PMT and with a response greater than 2.25 σ_N are also selected as "border" tubes. All other PMT responses are deemed to be noise dominated and are set to zero.

(ii) The parameters of the resulting image are calculated. In addition to the standard Hillas parameters described in section 3.3.2, the parameter "*span*" is defined as the angular extent of the image (in radians) subtended at the source position in the camera (Fig. 4.10).

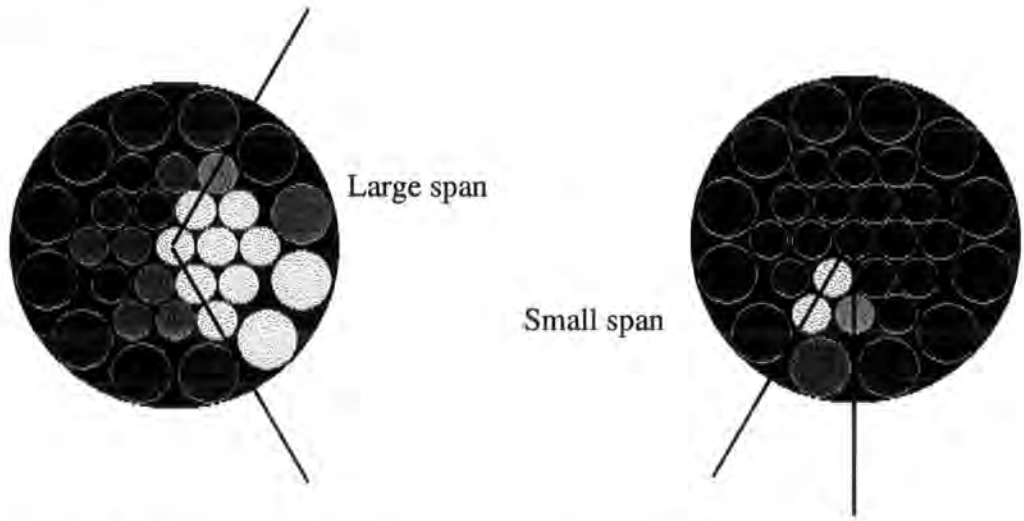

Figure 4.10 An illustration of the definition of the *span* parameter

(iii) The data are then divided into two sets: confined and unconfined events. An event is defined as unconfined if the largest PMT response is in the outer ring of the camera. The image reconstruction for these events is poorer than for the confined events as more of the Cerenkov light was outside the field of view of the camera.

(iv) Selection criteria are applied to both datasets in order to reduce the number of background events. The confined events are cut so that only events with a *span* less than the median value (1.08 radians for this data), an orientation parameter '*alpha*' less than 45° and a mean *distance* greater than 0.4° are selected. The *distance* cut is to ensure that *alpha* is well measured. The unconfined events are selected using only the median *span* cut.

(v) The datasets are recombined prior to time series analysis.

The number of events retained by these selection procedures are also shown in Table 4.5.

Table 4.5: Number of events at each stage of selection

Observation date	Total events	Confined events	Unconfined events	Cut events (total)
16/07/93	10425	8629	1796	1557
18/07/93	10910	8887	2023	1098
20/07/93	12359	10209	2150	1279
21/07/93	12991	10808	2183	1507
22/07/93	11490	9431	2059	1361
23/07/93	11926	9782	2144	1317
11/09/93	17140	13837	3303	4074
12/10/93	15952	12843	3109	3570

4.5.2 Analysis procedure

As mentioned in section 4.3.2, previous analyses and some source models of SMC X-1 predict that VHE gamma ray emission may be more likely to occur around the nodes of the orbit. Three of the eight observations in this dataset have a mid-point within 10% orbital phase of the ascending node. Each observation has therefore been tested for periodicity individually at both the full and half periods. This dataset was recorded more than four years after the most recent X-ray pulse period measurement. To allow for any unpredictable changes in the pulsar spin rate during this time, the

period search range has been widened to ±0.10 ms (~ 5 Fourier intervals) for the full period and ±0.05 ms (~ 10 Fourier intervals) for the half period.

In addition to testing for pulsed emission within each observation, the Rayleigh vector has been calculated for the six July observations, maintaining phase coherence across the month. Again the data have been examined at both the fundamental and the first harmonic of the X-ray pulse period.

4.5.3 Results

The raw chance probabilities for emission on a single night are given in Table 4.6, along with the corrected probabilities after allowing for the degrees of freedom used in the analysis. These consisted of the number of Fourier intervals in the period search range, oversampled by a factor of three and multiplied by the number of nights which were tested (eight). The Rayleigh probabilities for the data prior to the application of the background discrimination are also listed.

Table 4.6: Rayleigh test results for each observation of SMC X-1 in 1993.

Observation date	Chance probability at full period Raw(corrected)		Chance probability at half period Raw(corrected)	
	All data	Cut data	All data	Cut data
16/07/93	1.5×10^{-1} (1.0)	9.9×10^{-2} (1.0)	1.4×10^{-1} (1.0)	6.8×10^{-3} (9.1×10^{-1})
18/07/93	2.2×10^{-2} (9.9×10^{-1})	1.3×10^{-1} (1.0)	4.0×10^{-2} (1.0)	8.0×10^{-3} (9.6×10^{-1})
20/07/93	1.8×10^{-1} (1.0)	3.1×10^{-2} (1.0)	3.1×10^{-2} (1.0)	1.7×10^{-1} (1.0)
21/07/93	2.3×10^{-2} (9.9×10^{-1})	4.7×10^{-2} (1.0)	1.4×10^{-1} (1.0)	4.7×10^{-2} (1.0)
22/07/93	3.7×10^{-2} (1.0)	9.3×10^{-2} (1.0)	7.3×10^{-2} (1.0)	1.7×10^{-1} (1.0)
23/07/93	1.8×10^{-2} (9.8×10^{-1})	8.2×10^{-2} (1.0)	2.5×10^{-2} (1.0)	3.0×10^{-3} (7.1×10^{-1})
11/09/93	3.8×10^{-3} (6.6×10^{-1})	1.6×10^{-4} (4.5×10^{-2})	3.5×10^{-2} (1.0)	1.2×10^{-1} (1.0)
12/10/93	9.5×10^{-2} (1.0)	3.2×10^{-2} (1.0)	5.6×10^{-2} (1.0)	1.3×10^{-3} (6.1×10^{-1})

The most significant of these results, that of 11/09/93 at the full period, constitutes a 1.7 σ fluctuation and so does not exceed the 3 σ detection criterion. However, it is interesting to note that the midpoint orbital phase of this observation is 0.72, closer to an orbital node than any of the other nights examined. The 3 σ flux limit for a single observation is ~ 5.0×10^{-10} cm^{-2} s^{-1} above an energy threshold for cosmic rays (prior to background discrimination) of ~ 500 GeV.

The Rayleigh test result for the six nights in July, retaining phase coherence between observations, gave raw(corrected) chance probabilities of 9.3×10^{-3} (1.0) at the full period and 2.3×10^{-4} (1.0) at the half period. The 3 σ flux limit for this dataset is ~ 2.0×10^{-10} cm^{-2} s^{-1} above an energy threshold for cosmic rays of ~ 500 GeV.

4.6 Conclusions

The results of an analysis of SMC X-1 observations recorded using the Mark 3 telescope have been presented. The guard ring rejection technique was applied to data taken prior to the April 1993 telescope upgrade. No evidence for emission pulsed at the X-ray period was found in any of the 18 datasets analysed after correcting for motion within the binary system using the most recent orbital ephemeris (Levine, et al. 1993). A 3σ upper flux limit has been set at ~ 1.2×10^{-11} cm^{-2} s^{-1} above an energy threshold of ~ 1 TeV for the entire dataset. Eight observations recorded after the installation of a medium resolution imaging camera have also been examined after rejecting some nucleon image candidates. These observations show no evidence for emission. The night by night upper flux limit is ~ 5.0×10^{-10} cm^{-2} s^{-1} and the flux limit for the six July 1993 observations combined is ~ 2.0×10^{-10} cm^{-2} s^{-1} above an energy threshold for cosmic rays, prior to background discrimination, of ~ 500 GeV.

Kunz, et al. (1993) have fitted a power law to the differential spectrum of SMC X-1 at hard X-ray energies (20 - 80 keV) with a spectral index of 3.59±0.17. Extrapolating this spectrum to TeV energies results in a predicted flux many orders of magnitude below the upper limits produced here; however, the mechanisms which have been proposed to account for TeV emission from X-ray binary systems are very different from those producing the X-ray flux, making such comparisons difficult.

These results can only reduce the status of SMC X-1 as a candidate for targeted observations. However, as an extremely luminous, if distant, X-ray binary

object, it remains interesting and should be a part of any X-ray binary observing program of the more sensitive Mark 6 telescope.

CHAPTER FIVE - A NEW TECHNIQUE FOR IMAGE ANALYSIS

5.1 Introduction

The use of an array of photomultiplier tubes to form an imaging camera at the focus of an ACT has led to some highly significant detections of steady emission from VHE gamma ray sources such as the Crab nebula (Weekes, et al. 1989). The measurement of the Cerenkov images by such a camera is limited primarily by the mirror quality, camera size and pixel resolution. Ideally, a large, extremely high resolution camera would be employed; however, this is prohibitively expensive. Because of this, it is important to exploit the information provided by existing cameras as efficiently as possible.

This chapter begins with a description of the standard moment procedure for image parameterisation as suggested by Hillas (1985). Some of the limitations of this procedure are discussed and an alternative technique based upon the fitting of a bivariate Gaussian shape to the Cerenkov photon distribution is proposed. The results of employing the two methods to simulated bivariate gaussian images, simulated hadron and gamma ray EAS images and to real data are then compared.

5.2 The Moment Method of Image Parameterisation

The derivation of the Hillas parameters for Cerenkov images in the camera of an ACT proceeds in three stages. The methods of tube calibration were discussed in section 3.5.2 and the selection of which tubes are included in the parameterisation (the image/border criteria) was described in section 4.4.1. The following sections describe the calculation of the moments of the image as well as some of the problems with this technique.

5.2.1 Calculation of Moments

Suppose that the i^{th} PMT is given coordinates x_i, y_i (in degrees) and registers a signal s_i. The origin of the coordinate system is the centre of the camera. The six moments can then be defined as follows:

$$\text{sum} = \sum s_i \qquad \langle x \rangle = \frac{\sum s_i x_i}{\sum s_i} \qquad \langle y \rangle = \frac{\sum s_i y_i}{\sum s_i}$$

$$\langle x^2 \rangle = \frac{\sum s_i x_i^2}{\sum s_i} \qquad \langle y^2 \rangle = \frac{\sum s_i y_i^2}{\sum s_i} \qquad \langle xy \rangle = \frac{\sum s_i x_i y_i}{\sum s_i}$$

From these we can calculate the variances:

$$V(x) = \langle x^2 \rangle - \langle x \rangle^2 \qquad V(y) = \langle y^2 \rangle - \langle y \rangle^2 \qquad V(xy) = \langle xy \rangle - \langle x \rangle \langle y \rangle$$

These identities can then be used to derive the Hillas parameters of the image. For example, if $d = V(x) - V(y)$ and $z = (d^2 + 4V(xy))^{1/2}$ then:

$$\langle Length \rangle^2 = \frac{V(x) + V(y) + z}{2} \qquad \langle Width \rangle^2 = \frac{V(x) + V(y) - z}{2}$$

The image can then be represented by an ellipse, with its semi-major and semi-minor axes equal to these length and width parameters, respectively. The major axis of this ellipse can be expressed by the equation $y = ax + b$, where:

$$a = \frac{d + z}{2V(xy)} \qquad b = \langle y \rangle - a\langle x \rangle$$

Some of these features are illustrated in Figure 5.1.

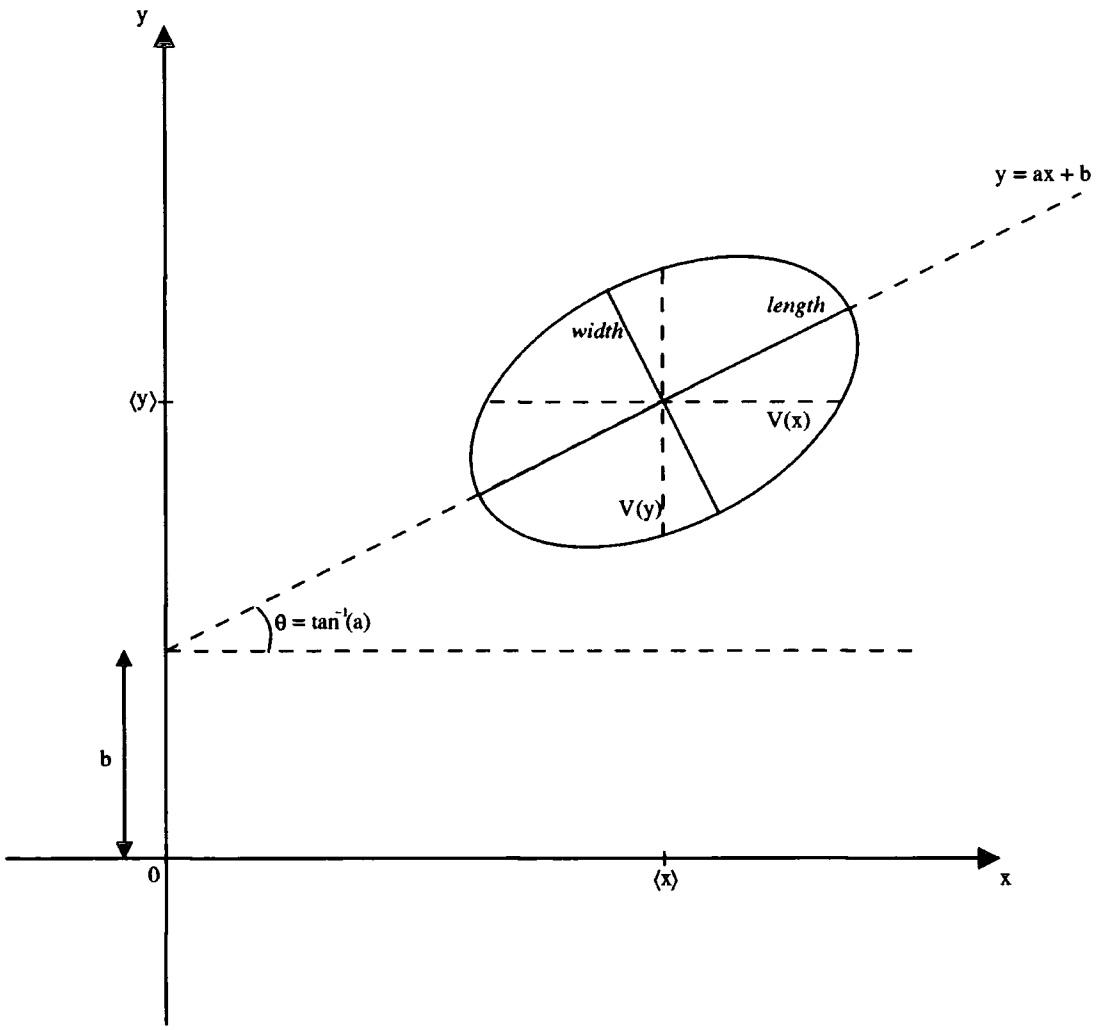

Figure 5.1 Parameterisation of the elliptical image.

5.2.2 Problems With Moment Parameterisation

The moment based analysis which has been described makes certain approximations when calculating the image parameters. The arguments of a moment calculation must be strictly zero or positive, to ensure positive values for $width^2$, etc. We must therefore define in some way which tubes are to be included in the calculation. This requires some arbitrary decision to be made about the extent of the image. The noise-dependent thresholds used in the standard image/border tube selection process result in the loss of any image information which may be present in the noise-dominated pixels not included in the selected tubes.

The other approximation implicit in the moment parameterisation is the

assumption that all of the image falls within the confines of the detector package. This is not the case for images with centroids close to the edge of the camera and so most cut selections include a low upper limit on the *distance* parameter to ensure that the images are not truncated. The possibility exists, however, that the distribution of light within the measured section of the image may allow some reconstruction of the section which is lost.

5.3 The Bivariate Gaussian Fitting Method of Image Parameterisation

Some of the problems inherent in the moment analysis of images may be solved by using optimization methods to fit a smooth function to the signals recorded by all of the tubes in the detector package. A bivariate Gaussian function provides an ideal fitting function as it has no variable moments higher than second order. This allows a simple comparison with the standard second order moment analysis, with the *width* and *length* from the moment calculation being equal to the standard deviation of the bivariate Gaussian function in the *width* and *length* directions.

This section describes how to accomplish such a fit and examines some of the factors involved.

5.3.1 Multivariate Minimization Techniques

The minimization of functions of many variables is problematic due to the large volume of parameter space which needs to be searched. Two classes of optimization techniques exist. Search methods use only function evaluations to determine the direction in which the minimum is expected to lie, whereas gradient methods also require information about the derivatives of the function. The specification for this application was for a method suited to a function with a moderate number of parameters (six), where a reasonably good first estimate of the function shape was available from the moment parameterisation. The downhill simplex method (Nelder and Mead, 1965) was chosen as it is a robust and reasonably

efficient method which is simple to implement and does not require gradient information.

The algorithm used was taken from Press, et al. (1992) which includes a full description of the downhill simplex method. A simplex is the simplest geometrical shape in N dimensions, consisting of N + 1 vertices. For example, in two dimensions, the simplex is a triangle. The minimization method starts by defining an initial simplex with N + 1 vertices, where N is the number of parameters in the function to be fitted. The simplex is then moved by a series of steps (reflections, contractions and expansions) in the direction which produces the best function fit. The process is terminated when the movement of the simplex for a step is smaller than some preset tolerance level.

5.3.2 The Fitting Procedure

The purpose of the procedure is to fit a smooth function to all of the signals recorded by the detector. The moment parameterisation fits a best ellipse, defined as the contour at the constant, 1σ level, to only those signals above a certain threshold using analytical methods. The natural extension of this, which includes all of the signals, is to optimize the fit of a bivariate Gaussian shape to the image, weighting each signal according to the measured noise response of the PMT. The Gaussian fit can then be used instead of the moment fit to calculate the Hillas parameters. The bivariate Gaussian function can be fully described by six parameters, corresponding to the six moments. For speed and ease of computation, the following parameters were used: A, the amplitude, $\langle x \rangle$, $\langle y \rangle$, which define the centroid of the function, $\langle length \rangle^2$, $\langle width \rangle^2$, which define its spread and θ, which defines its orientation. If the origin of the coordinate system is now defined as the centroid of the bivariate Gaussian and the axes chosen such that $\theta = 0$, the function can be expressed as:

$$z = Ae^{\left\{-\frac{x^2}{2\langle length\rangle^2}\right\}} e^{\left\{-\frac{y^2}{2\langle width\rangle^2}\right\}}$$

In order to fit this function to the image, we need a "goodness-of-fit" function which reaches its minimum when the fit is best. Using the same nomenclature as in section 5.2.1, the i^{th} PMT registers a signal s_i and the predicted signal p_i at this position is calculated assuming the bivariate Gaussian shape (after allowance for the telescope point spread function: see section 5.4.2). Some account must be taken of the measured noise on each PMT, σ_i. The minimization function can then be the χ^2 statistic:

$$\chi^2 = \sum \left(\frac{(s_i - p_i)}{\sigma_i} \right)^2$$

The fitting process is best illustrated by a flow diagram (Fig. 5.2).

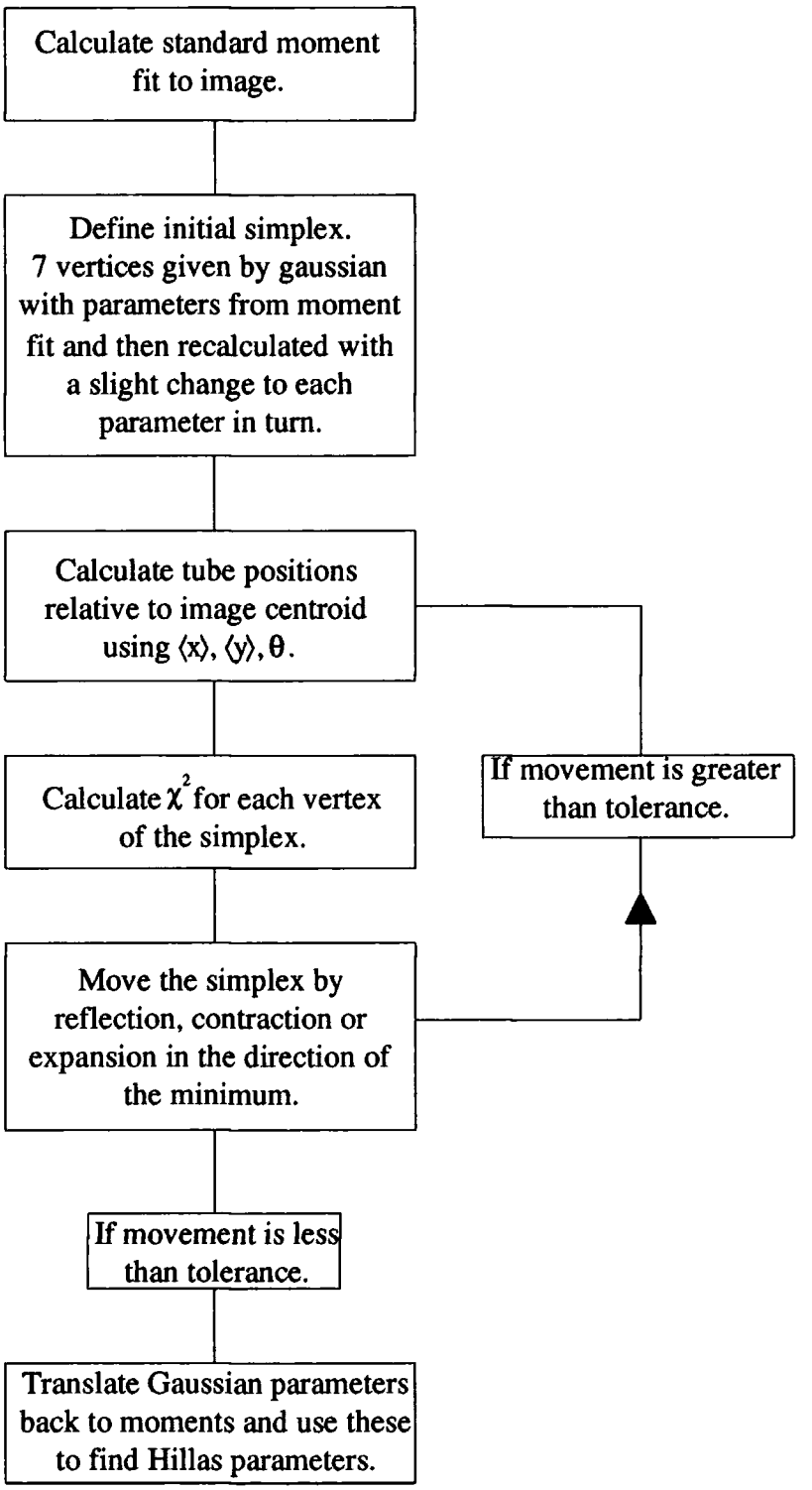

Figure 5.2 Flow diagram showing the bivariate Gaussian fitting procedure.

5.3.3 Other Considerations

When designing the fitting algorithm there are various factors to consider, some which are relevant to all optimization procedures and others which arise from this particular application.

For all optimization methods it is possible that the fit that is reached does not represent the global minimum. There is no sure way to avoid these local minima, but one technique which may help in some cases is to restart the minimization, once the fit has been terminated. The simplex is returned to its initial size, but this time centred on the end point of the first fit. If a local minimum has been found it is possible that the restart may enable the simplex to escape the valley and find its way to the global minimum. Figure 5.3 shows the effect of a restart on the final χ^2 value.

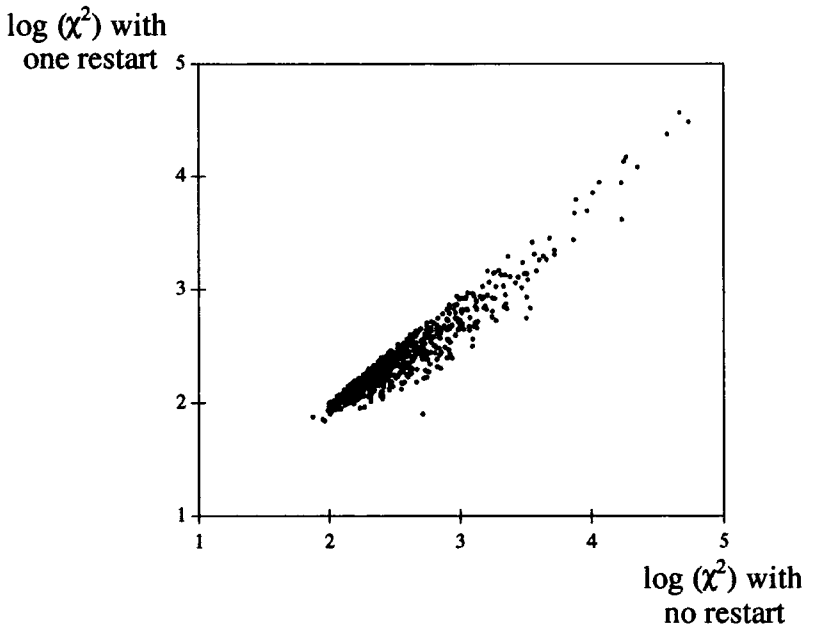

Figure 5.3 Best χ^2 value for the fit with and without a restart at the initial minimum.

The initial function shape should be as good an estimate of the final fit as possible to reduce the number of cycles in the optimization. This is easily achieved in this application by using the ⟨x⟩, ⟨y⟩, ⟨*length*⟩^{2}, ⟨*width*⟩^{2} and θ parameters derived

from the standard analytical moment fit. The exact values of the image/border thresholds used in the moment fit are not critical. The initial value of the amplitude of the bivariate Gaussian is given by the maximum PMT signal.

The χ^2 statistic described in section 5.3.2 uses the measured PMT response to sky noise to weight the accuracy of the fit prediction at each PMT position. In fact, the noise on each signal is made up of two components: the sky noise response and the uncertainty in the Cerenkov signal measurement. The measurement of the Cerenkov signal is affected by intrinsic fluctuations in the photon density across the image (granularity) and a statistical uncertainty $\propto (N_\gamma)^{1/2}$, where N_γ is the number of photons. For gamma ray showers, the granularity is expected to be smaller than for hadronic EAS which will cause the χ^2 statistic to be smaller for gamma rays for the same N_γ (section 5.5). The true uncertainty on the Cerenkov measurement is difficult to measure, but an approximate value can be derived using the calibration laser flashes described in section 3.5.2.3.

Each PMT will measure a distribution of responses to a series of laser flashes. The width of this distribution will be the result of two components: variations in the intensity of the laser flashes and variations in the tube response to a given intensity of flash. Assuming that, for each laser flash, the photon density is the same at all points over the imaging camera, the value of the sum of the signals recorded by the camera over a series of flashes will produce a similar distribution; however, with 109 independent samples of the same light flash, the width of this distribution will be dominated by variations in the intensity of the laser flashes. Assuming that the width of the distribution of sums is caused almost entirely by flash variations, it is possible to remove this component from the distribution of an individual tube's responses and calculate the variance due to errors in the measurement of the light flash alone. This variance and the variance in the the tube response to sky noise, calculated using the randomly triggered events (section 3.5.2.2), give two points on a calibration curve of the variance in the measurement of a given number of photons by each tube.

Assuming that there is a simple linear relationship between the variance and the light intensity, it is possible to redefine the noise, σ_i, as $\sigma_i^2 = \sigma_s^2 + (C.s_i)^2$ where σ_s is the sky noise response measured using random events and C is a constant.

The final consideration when applying the fit is logistical. Is it practical to use such a processor-intensive procedure given the amount of data recorded by an ACT? Running the program on a Hewlett-Packard model 712/80 work station it is possible to produce a fit for ~ 5 events s^{-1}. A reasonably good observing month would produce ~2000000 events from the Mark 6 telescope which could be processed in ~ 4.5 days. Given that the process can be automated and left running overnight and weekends, this is perfectly adequate. Should the data rate increase with future upgrades to the telescope, it may prove necessary to obtain a faster processor.

5.4 A Comparison of the Two Techniques

5.4.1 Results on Artificially Produced Bivariate Gaussian Images

The first test of the Gaussian fitting procedure is to confirm that it reaches the correct fit for images which are Gaussian in form. This also provides a means of testing the effects of measuring a continuous image with a finite, limited resolution camera.

A bivariate Gaussian shape was produced with a randomly generated size, shape, position and orientation. The signal at each PMT position was then calculated assuming a camera geometry identical to that of the Mark 6 telescope. To this signal was added a sample from a noise distribution which mimics the night sky noise distribution. The parameters used to generate the bivariate Gaussian function were noted and then both fitting techniques applied. This was repeated 300 times and the parameter values arrived at by both fitting methods were compared to the true values. Figure 5.4 shows the comparison for the $\langle x \rangle$ parameter. Both methods determine the centroid of the image to a high accuracy, although the moment fit becomes less

accurate near the edge of the camera where images are truncated. Figure 5.5 shows the comparison for the $\langle length \rangle^2$ parameter. The optimization method reproduces this parameter accurately with the exception of a few events where it is likely that the fit has been unable to escape an incorrect local minimum. The moment fit, however, tends to consistently underestimate $\langle length \rangle^2$, particularly at larger values, again due to truncation.

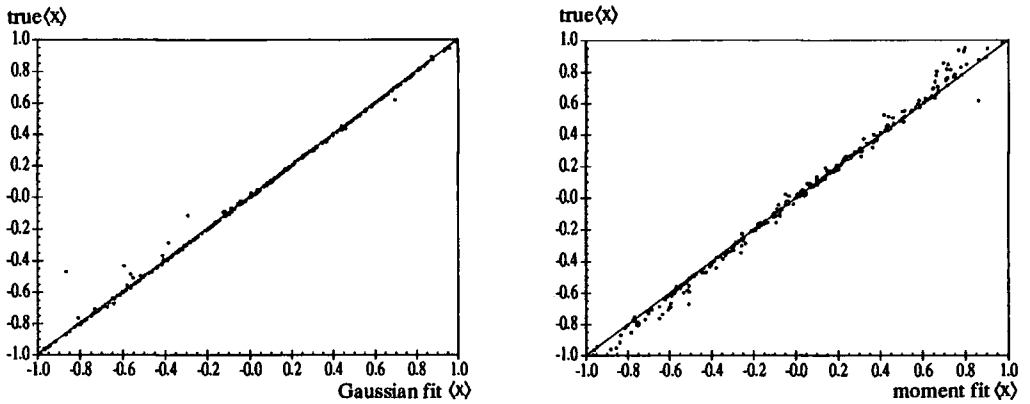

Figure 5.4 Measurement of the ⟨x⟩ parameter for artificial bivariate gaussian shaped images using the gaussian fitting and standard moment parameterisation.

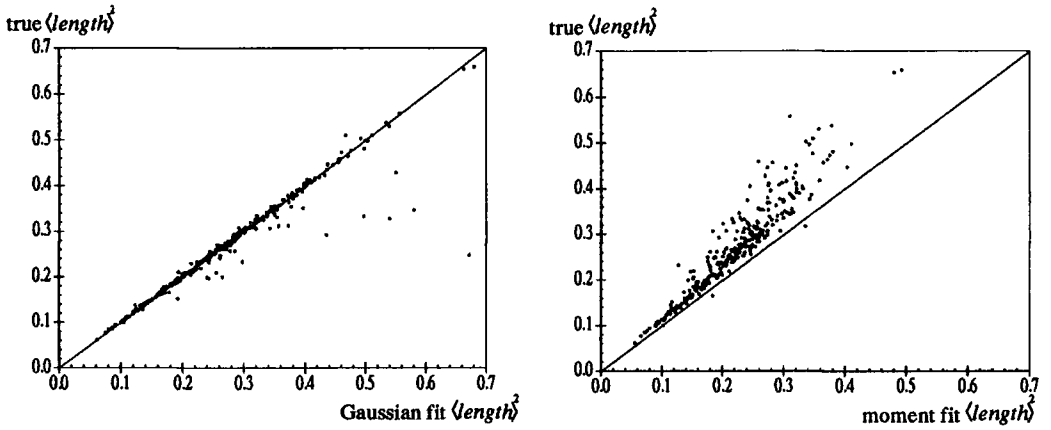

Figure 5.5 Measurement of the $\langle length \rangle^2$ parameter for artificial bivariate gaussian shaped images using the gaussian fitting and standard moment parameterisation.

5.4.2 Results on Simulated Images of EAS

The next stage in the development of the technique is to investigate whether it can provide an improvement in the rejection of hadron initiated EAS from the data.

In the absence of a strong celestial gamma ray source, the only way to test this is by modelling the response of the telescopes to Cerenkov flashes using Monte Carlo simulations. For the Mark 6 telescope, simulated gamma ray and hadron initiated images were produced using the MOCCA Monte Carlo program (Hillas, 1982). The telescope response was modelled for a range of pointing directions from 20° to 35° in zenith and from 180° to 230° in azimuth (where 180° is south), which is the range covered by a typical observation. The composition and spectrum of the primary nucleons were taken from Wiebel-Sooth, et al. (1995). The differential spectral index for the simulated gamma rays was chosen to be -2.2.

Using the simulated hadron and gamma ray initiated events it is possible to derive an estimate of the expected quality factor, Q, for each technique (Fegan, 1992). The parameter distributions for the simulated hadron and gamma ray events calculated using the moment procedure and the gaussian fitting are shown in Figures 5.6 and 5.7 respectively. Also marked on these figures are the event selection criteria which give the best Q factor for each parameter. The distance cut is a lower bound which ensures that the alpha parameter is well measured. Combining these cuts gives 61% gamma ray retention and 97.5% hadron rejection (Q = 3.8) for the moment procedure and 46% gamma ray retention and 99.1% hadron rejection (Q = 4.7) for the gaussian fitting technique.

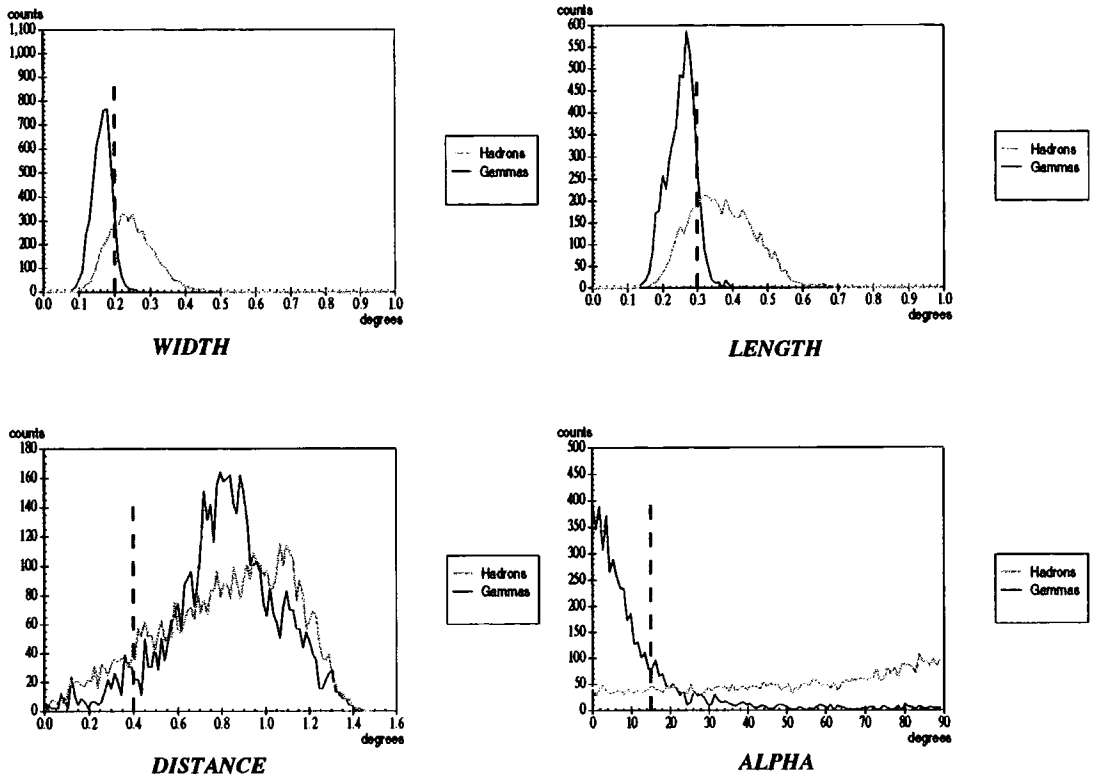

Figure 5.6 Parameter distributions for simulated hadron and gamma ray images calculated using the standard moment procedure.

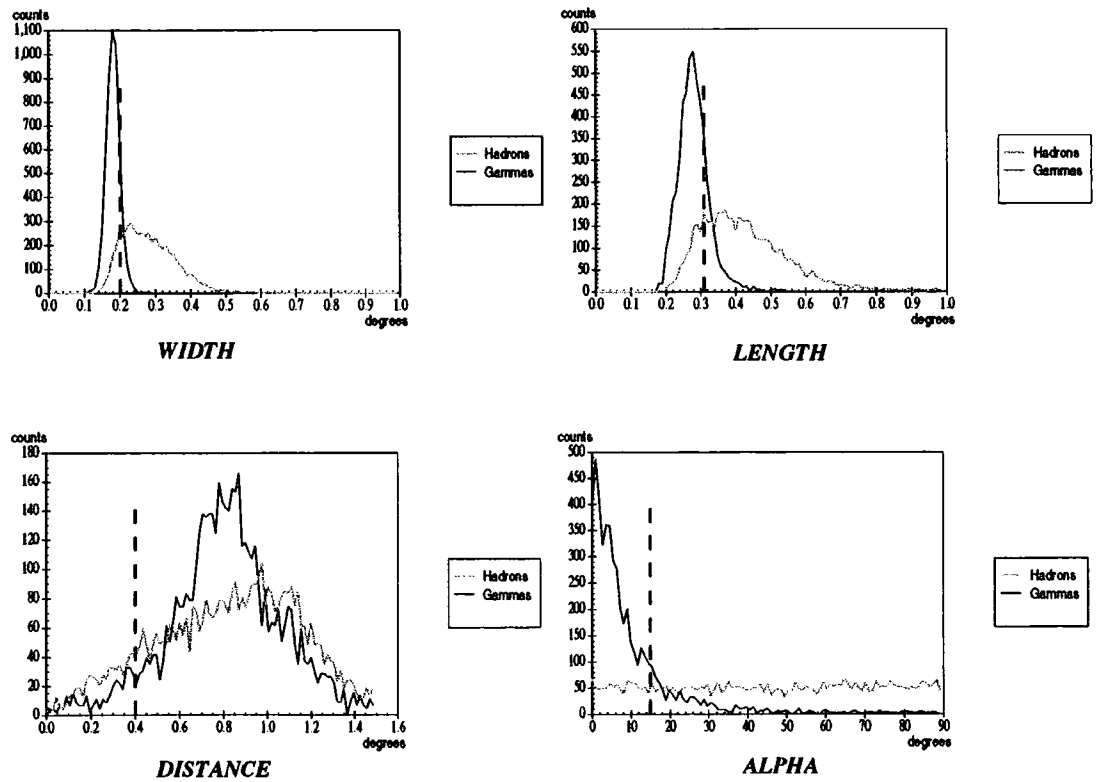

Figure 5.7 Parameter distributions for simulated hadron and gamma ray images calculated using the bivariate gaussian fitting procedure.

The images produced using simulated hadron events compare reasonably well with measured background images when parameterised using the standard moment procedure (Fig. 5.8), although the spread on the *width* and *length* distributions is larger in the real data. The differences between the real and simulated distributions is much more pronounced when the images are parameterised using the bivariate Gaussian fit (Fig. 5.9). The reason for this large discrepancy is not yet entirely clear. The blurring function assumed in the simulations is a gaussian shape with a full width at half maximum taken from measurements of the telescope's point spread function (PSF). One possibility for the difference between real and simulated image parameters is that the true PSF of the telescope mirrors is not composed of a single Gaussian shape but contains a broad, low light-level component which widens the images when all tubes are considered. Recent measurements of the PSF provide some evidence to support this idea.

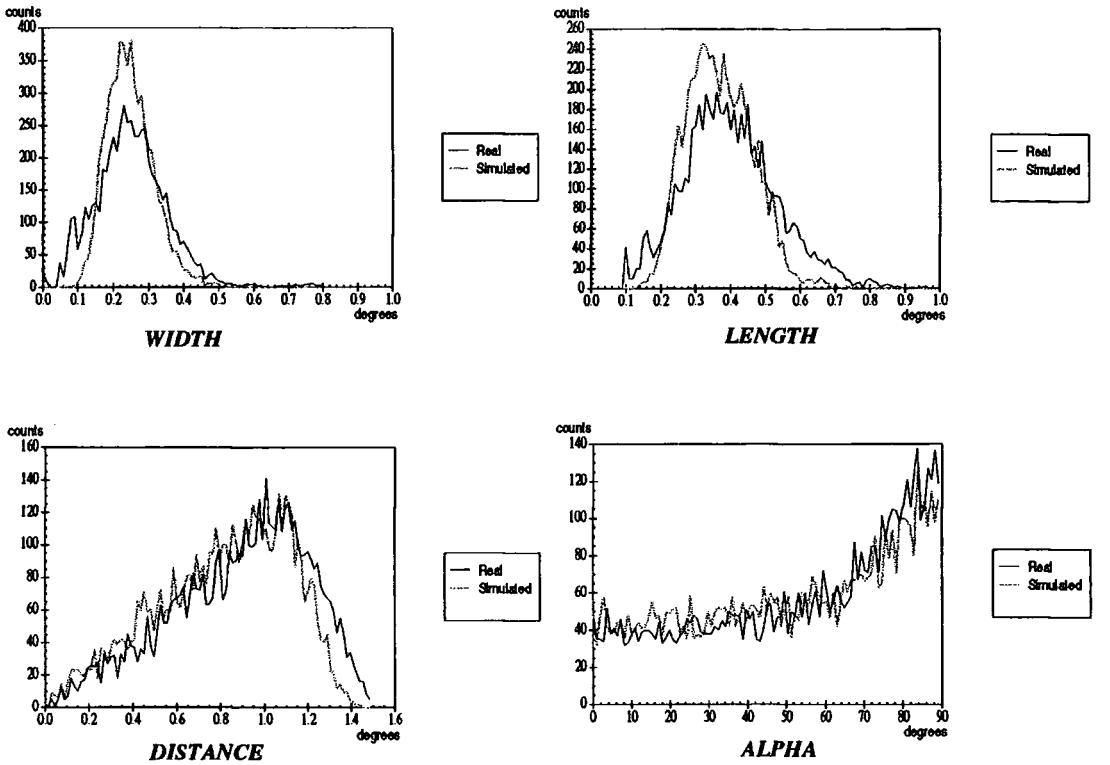

Figure 5.8 Parameter distributions for real and simulated nucleon events calculated using the standard moment procedure. Total event numbers are normalised.

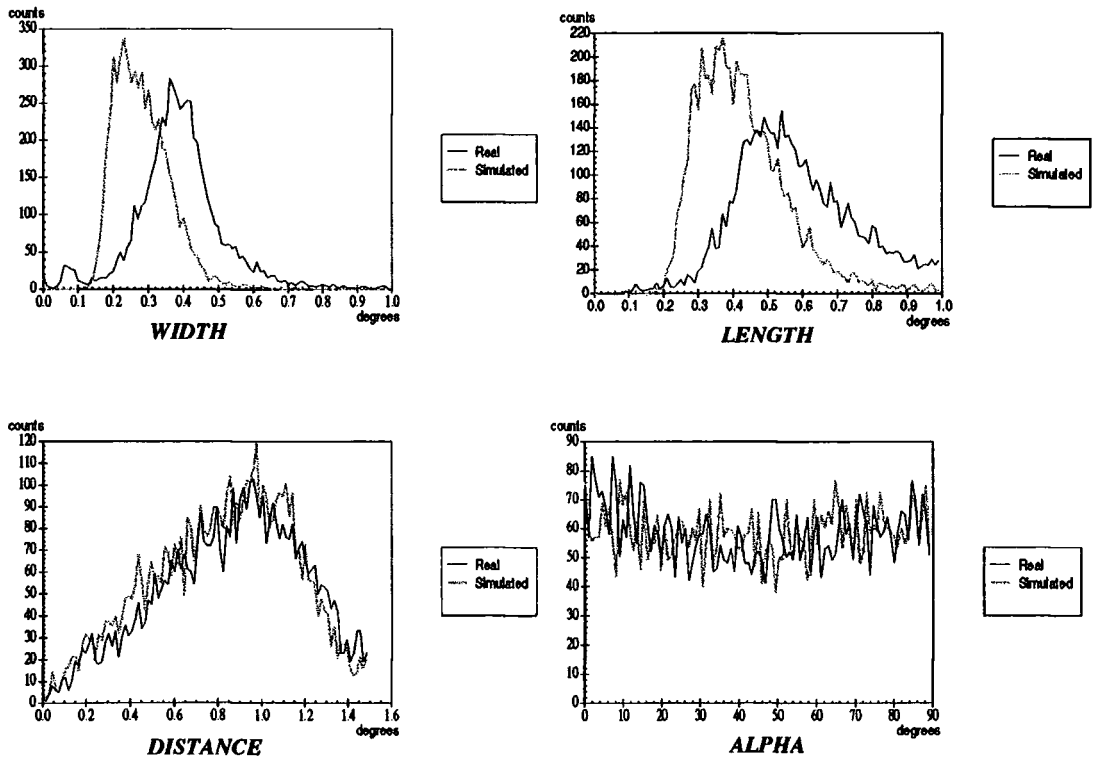

Figure 5.9 Parameter distributions for real and simulated nucleon events calculated using the bivariate Gaussian fitting procedure. Total event numbers are normalised.

Figure 5.10 is a cross section of an image of Jupiter as it would appear in the centre of the field of view. This measurement was made by forming an image of Jupiter on an aiming board which was placed where the detector package is normally positioned. A CCD camera mounted on the telescope frame was then used to record the image. It is clear from this figure that the PSF is not well described by a single gaussian function.

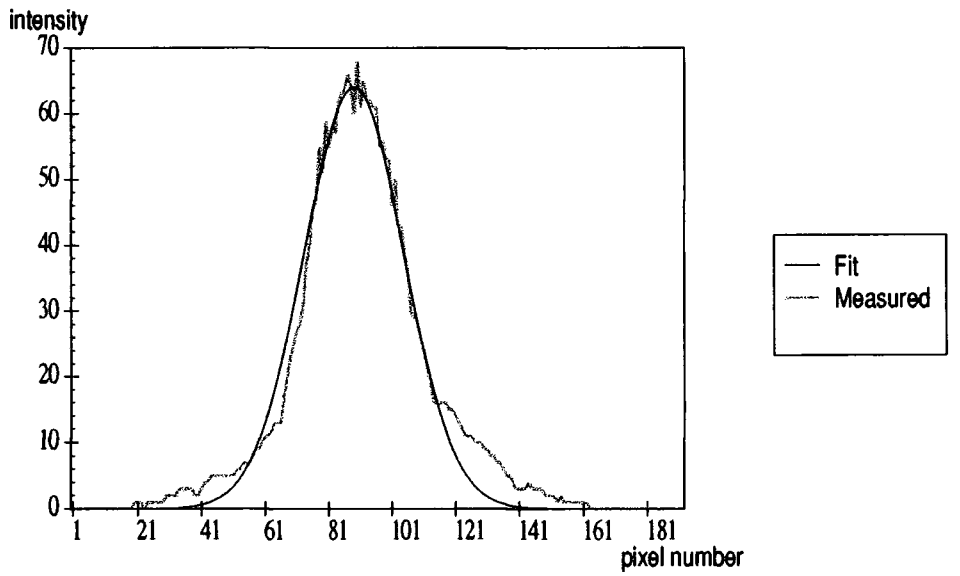

Figure 5.10 Intensity profile of a horizontal cross-section of an image of Jupiter.

In the analysis of data from the Mark 6 telescope, both of the image parameterisation methods have been altered slightly to compensate for this effect. For the moment method, a change has been made to the image/border threshold criteria. Instead of selecting tubes to include in the parameterisation on the basis of their noise response, they are now chosen by examining their recorded signal as a fraction of the peak response in the camera. For example, if the peak tube response in the camera were 50 digital bits, tubes with a response greater than 40% of this (20 bits) are classed as image tubes and those with a signal of 20% (10 bits) are classed as border tubes if adjacent to an image tube. To prevent images with a low peak tube response including many noise dominated tubes, the lowest signal level which a tube can

record and still be included in the parameterisation remains set as a function of its noise response. The effect of this image/border selection method is strongest with large events, whose secondary light component was bright enough to colour those tubes outside of the main image when noise dependent thresholds were used. A comparison of real data parameterised using the fractional peak response criteria and simulated data parameterised using the noise dependent thresholds is shown in Figure 5.11.

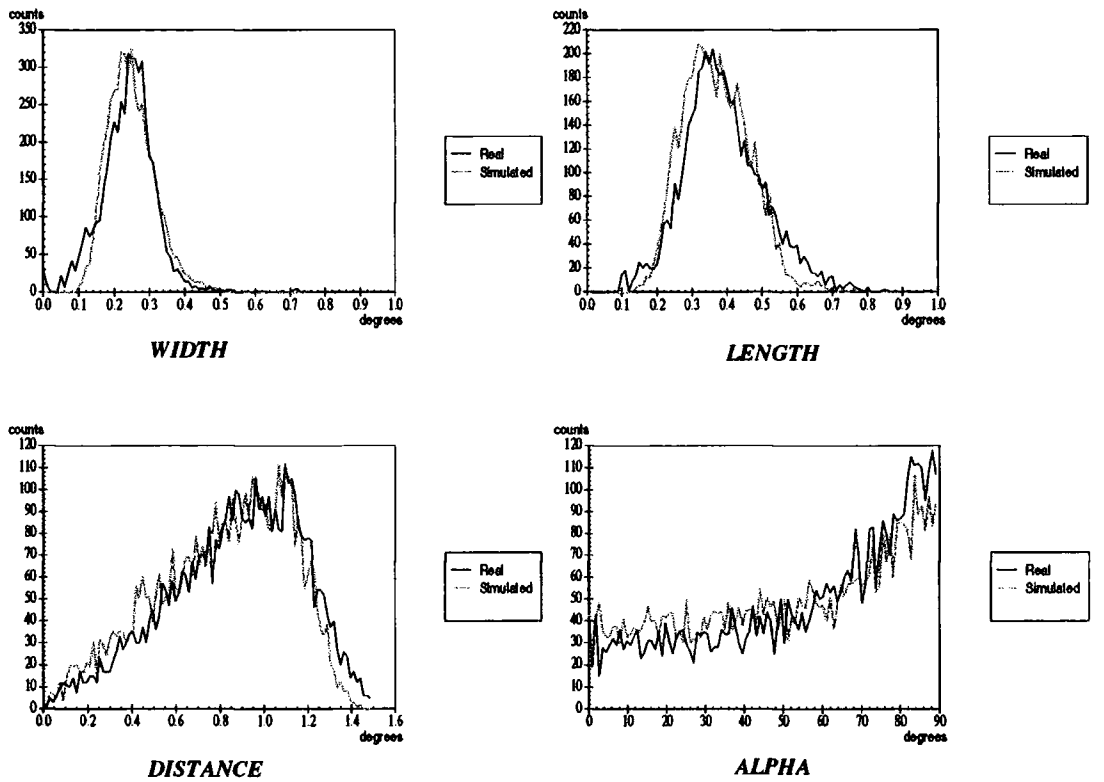

Figure 5.11 Parameter distributions for real and simulated nucleon events calculated using the standard moment procedure. Real events have fractional peak response image/border criteria. Total event numbers are normalised.

A more rigorous modification can be made to the gaussian fitting procedure. First, we parameterise the telescope PSF using a function containing two gaussian components, such that:

$$z = Ae^{-\frac{x^2}{2\sigma_A^2}} + Be^{-\frac{x^2}{2\sigma_B^2}}$$

A an B are the amplitudes of the two gaussian components and σ^2_A and σ^2_B are their corresponding variances. We can then use this function to calculate what fraction of the Cerenkov light observed by each tube would be spread to the other tubes in the camera. This calculation is performed for every tube to construct a PSF matrix. In the minimization routine the predicted signals from the bivariate gaussian test function are then multiplied by the PSF matrix. The modified predicted signals are then compared to the measured signals and the differences used to calculate χ^2 as usual. The final parameters of the best fit bivariate gaussian will then have had the major distortions which resulted from the PSF removed.

The bivariate Gaussian parameters of real data, calculated using the PSF matrix correction, are compared with those of uncorrected simulated events in Figure 5.12. The comparison, while an improvement on that seen when no account was taken of the PSF, is still rather poor. This could indicate that the PSF has been poorly parameterised and that the assumptions of a circularly symmetric function which remains the same over the full field of view of the detector may be inaccurate. Alternatively, the reconstruction of the original image parameters may not be possible to greater accuracy using this technique.

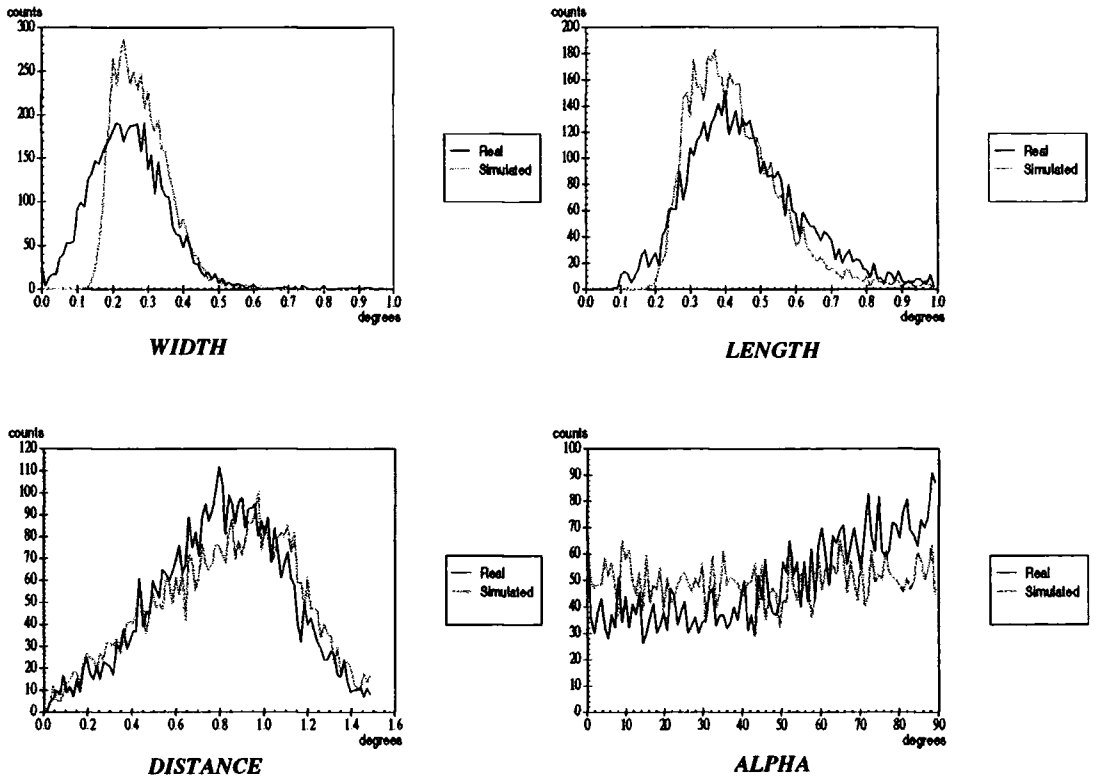

Figure 5.12 Parameter distributions for real and simulated nucleon events calculated using the bivariate Gaussian fitting procedure. Real events have the the PSF matrix correction applied. Total event numbers are normalised.

5.4.3 Camera Boundary Effects

As discussed in chapter three, the major axis of a Cerenkov image indicates the direction from which the shower originated. For an infinite ACT imaging camera observing gamma ray initiated events from the source direction, the distribution of the orientation angles of the major axes relative to the source position in the camera (*alpha)* should be close to 0°. For background, nucleon initiated events, *alpha* should be uniform between 0° and 90°. In a real imaging camera, recorded images are truncated by the camera boundary. As the major axis of the image is shortened, light recorded along the minor axis gains added weight in the moment calculation, causing the *alpha* distribution to be biased towards 90°. The degree of bias will increase as the centre of gravity of the image moves closer to the camera boundary. The Gaussian fitting method should be able to reconstruct the missed part of the image by calculating the best fit for the section which is observed. The *alpha* distributions for

various *distance* bands are shown in Figure 5.13. As expected, the gaussian fitting method results in a more uniform *alpha* distribution at large *distance*, implying that the image orientation is being more accurately reconstructed.

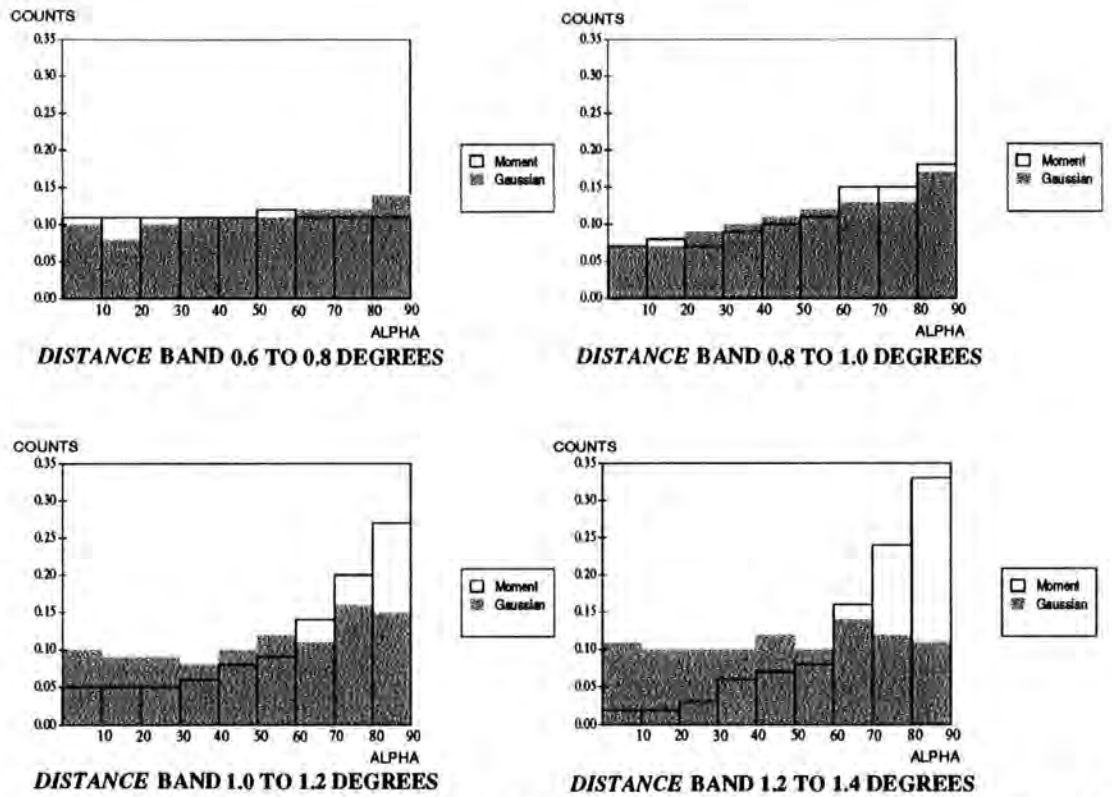

Figure 5.13 Variation of the alpha distribution with *distance* for each parameterisation method. The number of events per distance band are normalised.

5.5 The Goodness-of-fit Parameter

Degrange and Le Bohec (1995) have fitted an analytical model of the photon distribution produced by a gamma ray EAS to simulations of Cerenkov images as they would appear in a 534 pixel imaging camera. They suggest that the final value of the goodness-of-fit function will be significantly smaller for gamma ray initiated showers than for hadron EAS. By selecting events on the basis of a small value of the goodness-of-fit parameter, it should be possible to discriminate the gamma ray showers from the background events.

The Mark 6 telescope camera contains 109 pixels and so does not have the resolution necessary for this type of discrimination; however, it is likely that the more compact photon distribution produced by gamma ray EAS will result a lower final χ^2 value after the gaussian fitting technique has been applied. Figure 5.14 shows the distribution of final χ^2 for simulated hadron and gamma ray showers. While the two distributions are certainly different, effective discrimination between the two is difficult. The maximum quality factor resulting from a final χ^2 selection is only 1.2.

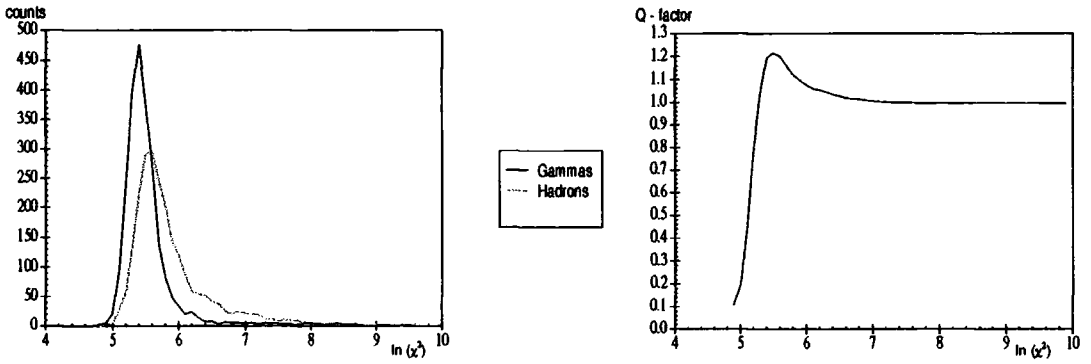

Figure 5.14 The distribution of the goodness-of-fit parameter, χ^2, for simulated gamma ray and hadron images, along with the quality factor possible as a function of the cut value.

Figure 5.15 illustrates the final χ^2 of those events which survive selections using the usual parameters: *length, width, distance* and *alpha* at the values derived in section 5.4.2. The χ^2 distribution of the remaining hadron images falls entirely within the χ^2 distribution of the gamma ray images. From this it would appear that the goodness-of-fit parameter will not be useful either on its own or as an addition to the standard parameter selection values.

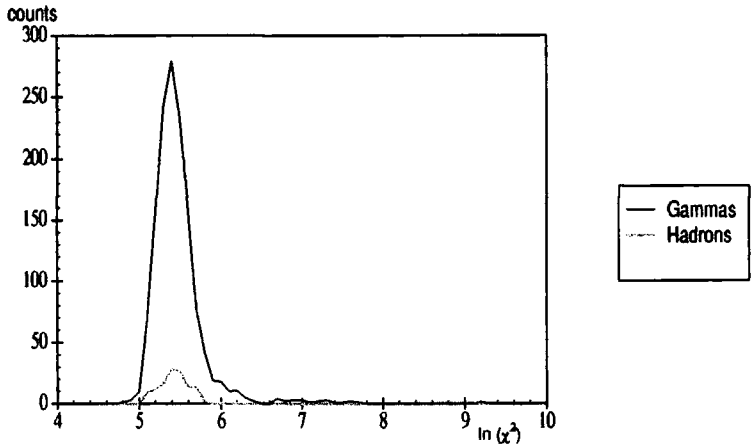

Figure 5.15 The distribution of the goodness-of-fit parameter, χ^2, for simulated gamma ray and hadron images after selecting images on the basis of the *length, width, alpha* and *distance* parameters.

5.6 Conclusions

This chapter has presented a new method for the parameterisation of Cerenkov images of EAS recorded by an ACT imaging camera. This method, based upon the optimisation of a bivariate gaussian fit to the Cerenkov photon distribution, has been compared with the standard moment based method. Results from the application of the two techniques to real data and to artificially created images of bivariate gaussian form suggest that the gaussian fitting method reconstructs the true image shape more accurately than the moment method. Using Monte Carlo simulations to produce Cerenkov images of hadron and gamma ray initiated showers, quality factors have been calculated which suggest that the gaussian fitting technique will provide better background discrimination that the moment method, hence increasing the sensitivity of an ACT to gamma rays. Methods have been proposed to correct for distortions to the parameters of real images, possibly caused by a broad, low-light level component of the telescope's point spread function.

CHAPTER SIX - A SEARCH FOR STEADY EMISSION OF TeV GAMMA RAYS

6.1 Introduction

The highly significant detection of unpulsed TeV gamma rays from the position of the Crab pulsar and nebula by the Whipple collaboration (Weekes, et al. 1989) has highlighted the importance of steady sources of emission in the VHE region. The most probable candidates for steady emission are discussed in this chapter, together with the gamma ray production mechanisms which may be involved.

Observations of the radio pulsar (and possible nebula) PSR 1706-44 were recorded using the University of Durham Mark 6 telescope in May and July of 1996. These observations are examined for evidence of steady emission. The two different image parameterisation techniques outlined in Chapter five are employed in this analysis.

6.2 Sources of Steady Emission: Supernova Remnants and Active Galactic Nuclei

Through the history of ground based gamma ray astronomy there have been many candidates for the steady emission of TeV gamma rays. Nearby galaxies, globular clusters, radio galaxies and diffuse emission from the galactic plane have all featured in observing plans and there have been various claims for emission of low significance (e.g. Weekes, 1988). With the development of the imaging atmospheric Cerenkov technique and in the light of the results from the EGRET experiment aboard the CGRO, attention has been focussed on two classes of object: supernova remnants (SNR) and active galactic nuclei (AGN).

6.2.1 Supernova Remnants

In a supernova explosion, the stellar collapse releases enough energy to eject the outer layers of the star with a velocity ~ 10^4 kms^{-1}. The resulting shell of material is known as a supernova remnant. Two types of SNR exist. The shell-like remnants emit in radio, optical and X-ray wavelengths from an expanding nebula. Filled-centre remnants, or plerions, contain a pulsar which is believed to be the relic of the original star. The fact that these SNR are brightest towards their centre implies that the pulsar's rotational energy is being used to power the emission from the nebula.

Supernova explosions have been used to explain the acceleration of galactic cosmic rays up to energies of ~ 10^{15} eV (Blandford and Ostriker, 1980). Although there is still no direct evidence for this theory, it is widely accepted for two reasons. Firstly, a convincing particle acceleration mechanism exists in the form of the first order Fermi process (section 4.2.4.3; Fermi, 1954) occurring where the supernova blast wave forms a diffusive shock front as it interacts with the interstellar medium. Secondly, the galactic supernovae are almost the only known sources with sufficient energy to generate the observed cosmic ray spectrum up to 10^{15} eV. If such particle acceleration does take place in shell-type supernovae, then the resulting cosmic rays may interact to form neutral pions which decay to VHE gamma rays (section 1.2.1).

Drury, et al. (1994) have modelled the production of gamma rays by SNR and suggest that the most favourable energy range for detection is probably from 1 to 10 TeV (Fig 6.1). No shell-type remnants have been detected in this range using imaging ACT's. Buckley (1994) reports upper flux limits for emission above 250 GeV for a number of SNR using the Whipple telescope. There have been various claims of an association between SNR and some of the 40 unidentified EGRET sources at low galactic latitudes (Sturner and Dermer, 1995, Esposito, et al. 1994). More recently, Dermer, et al. (1996) have suggested an association between these EGRET sources and young pulsars. The pulsars are not, however, positionally

coincident with the gamma ray sources but are believed to be the neutron stars formed after a supernova explosion which have moved away from the remnant at a speed ~ 100 kms^{-1}. This remnant, invisible at other wavelengths, is the proposed gamma ray source.

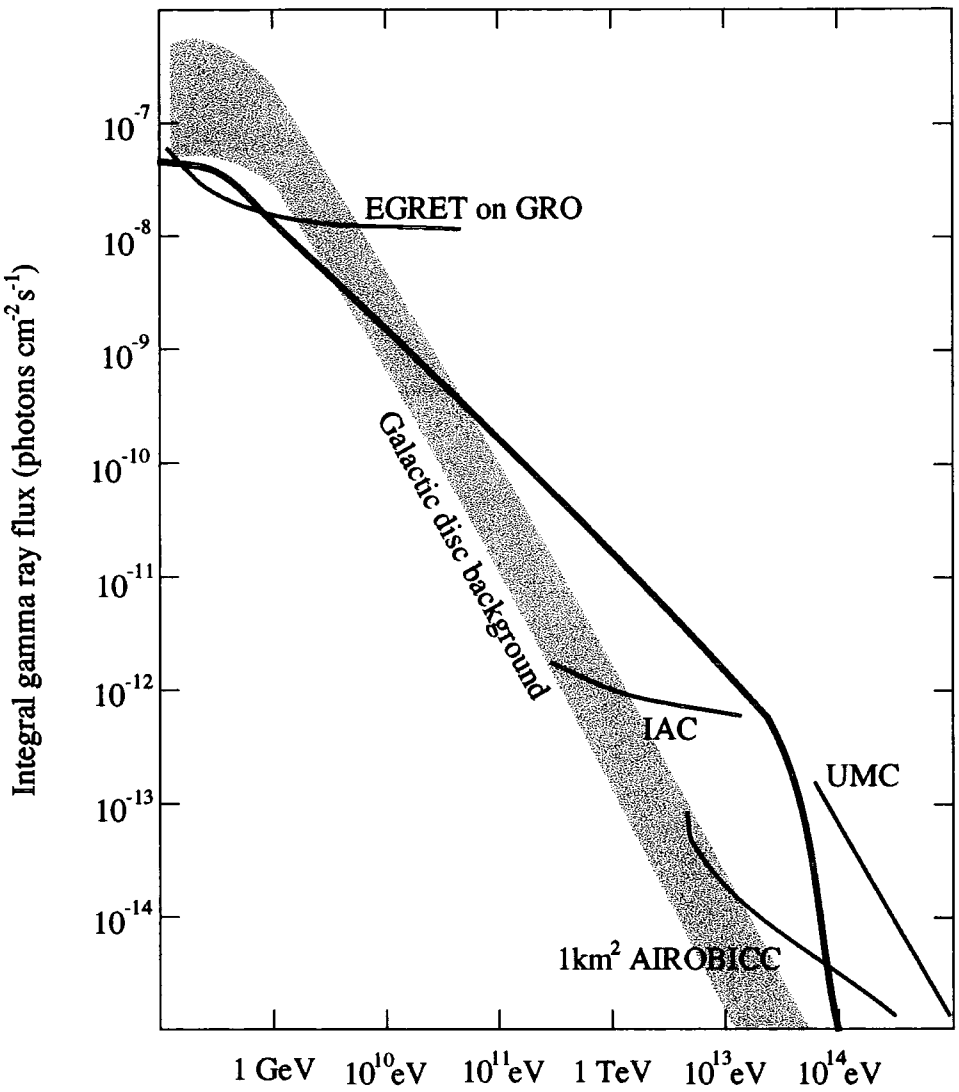

Figure 6.1 The predicted gamma ray flux from a SNR at 1kpc with the canonical energy of 10^{51} ergs expanding into a medium of number density 1 cm^{-3} with a spectral exponent of 2.1. Also indicated is the approximate level of the general galactic disc emission within an acceptance angle of 1°, the sensitivity level of imaging atmospheric Cerenkov telescopes (IAC), of the UMC air shower array, of the 1km^2 AIROBICC detector array and the EGRET instrument on the CGRO (from Drury, 1996).

There are now about 15 clearly identified plerions (Arons, 1996). By far the most well studied of these objects is the Crab pulsar and nebula. The significant detection of unpulsed TeV gamma ray emission from this source by a number of groups (eg. Weekes, et al. 1989; Baillon, et al. 1991; Krennrich, 1994) has established it as the "standard candle" for ground based gamma ray astronomy in the northern hemisphere. At EGRET energies (~ 20 MeV to 30 GeV), the emission from the direction of the Crab pulsar is primarily pulsed, but still contains a significant unpulsed component which possibly exhibits a spectral hardening above ~ 1 GeV (Nolan, et al. 1993). Yoshikoshi (1996) has reported the detection of unpulsed gamma rays at energies above ~ 2.5 TeV from the region of the Vela nebula, possibly removed from the position of the Vela pulsar by ~ 0.14°. This is an initial report of fairly low significance (3.5 σ prior to optimizing the proposed source location) and awaits further confirmation. Steady VHE emission has also been detected from the position of the EGRET pulsar PSR1706-44 (Kifune, et al. 1995) which may also be associated with a surrounding nebula (McAdam, et al. 1993).

Source models for gamma ray emission from plerions tend to be based upon the Crab nebula. The synchrotron-self Compton (SSC) model of De Jager and Harding (1992) provides a particularly good fit to the measured gamma ray spectrum of the Crab (Fig 6.2). In this model, relativistic electrons moving through a magnetic field scatter their own X-ray synchrotron emission up to gamma ray energies.

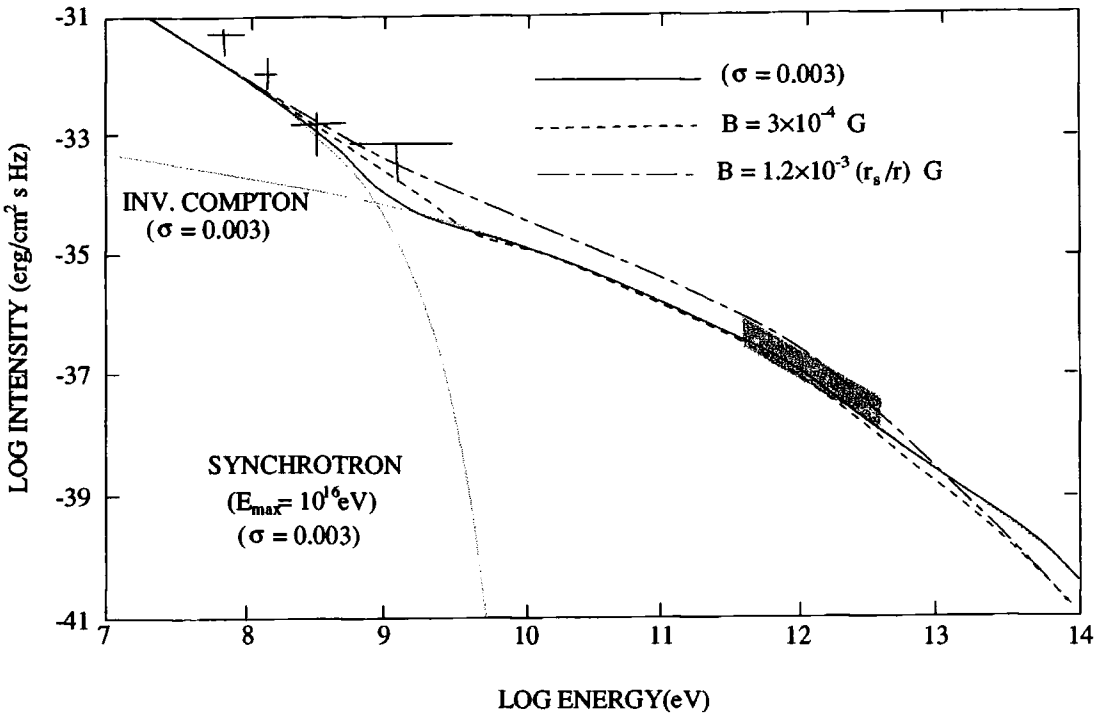

Figure 6.2 The synchrotron-self Compton spectrum of the Crab Nebula as calculated by De Jager and Harding. Crosses indicate COS-B measurements and the hatched area is the Whipple ACT spectrum (from De Jager and Harding, 1992).

The pulsar's rotational energy must be used in some manner in order to accelerate particles up to energies high enough for the SSC mechanism to produce TeV gamma rays. As mentioned in section 4.2.5.1, Rees and Gunn (1974) showed that magnetic dipole radiation will be unable to propagate through a pulsar magnetosphere and suggested that the pulsar's rotational energy must be transported in the form of a relativistic wind of electron-positron pairs. In the case of a plerion, this pulsar wind is confined by the slower moving surrounding nebula and a shock front occurs where the two interact (Fig. 6.3). The radial location of the shock, r_s, can be roughly estimated by balancing the wind ram pressure with the total particle and magnetic field pressure accumulated by the nebula in its lifetime. This gives:

$$r_s = v_{exp}\tau\sqrt{\frac{v_{exp}}{3c}}$$

where v_{exp} is the expansion velocity and τ the age of the nebula. Synchrotron

emission from the position of the shock in towards the pulsar, where the particles have small pitch angles, is expected to be less than elsewhere in the nebula. For the Crab nebula, $r_s \sim 2 \times 10^{15}$ m, which matches the size of an underluminous region in radio (Wilson, 1972), optical (Woltjer, 1987) and X-rays (Aschenbach and Brinkman, 1975). Particles accelerated in this shock by the first order Fermi mechanism will have their pitch angles randomized, causing synchrotron emission and gamma rays by SSC scattering.

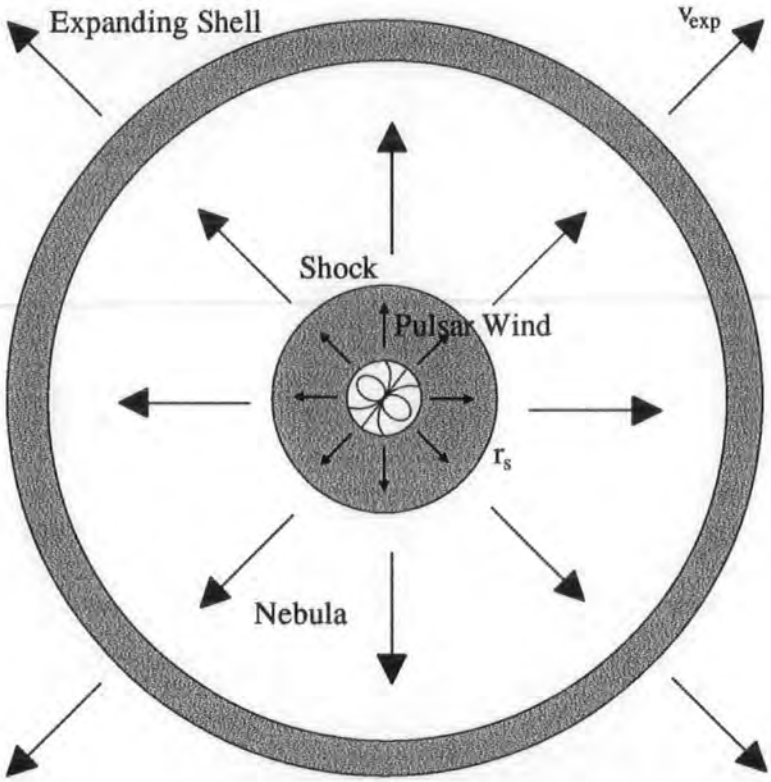

Figure 6.3 Schematic illustration of the pulsar wind model of a plerion (after Harding, 1996)

In order to calculate the inverse Compton gamma ray spectrum of a plerion the energy spectrum of the relativistic particles must be known. This can be derived by inverting the observed synchrotron spectrum, assuming a magnetic field distribution as a function of radius, r, and a nebula geometry. Gould (1965) assumed a spherical nebula and Rieke and Weekes (1969) repeated these calculations for a prolate spheroid. Both used a constant magnetic field strength and a nebula size

independent of frequency. Grindlay and Hoffman (1971) developed the model by assuming a radial dependence for the magnetic field and a frequency dependent nebula size. Kennel and Coroniti (1984) proposed a magnetohydrodynamic (MHD) wind model for the Crab nebula. Their best fit solution for this model suggests that the pulsar wind upstream of the shock is extremely particle dominated, with the ratio of the magnetic field to particle energy density, $\sigma \sim 0.003$. The magnetic field distribution elsewhere in the nebula is heavily dependent upon this ratio. Assuming a value of 0.003, the magnetic field is expected to be a minimum at the shock and to increase roughly as $B(r) \propto r$ until equipartition. This is the point at which the magnetic field and the particle energy density are equal. Beyond this, the field strength decreases as $B(r) \propto 1/r$. De Jager and Harding (1992) have used this model for the magnetic field distribution in their calculation of the electron spectrum which predicts inverse Compton emission from the Crab nebula at TeV energies.

An alternative model for high energy unpulsed emission from plerions was proposed by Kwok, et al. (1991). This is based upon the outer gap model of pulsar emission described in section 4.2.5.1 (Cheng, et al. 1986 and 1986a). They suggest that electrons accelerated in one outer gap may survive in a region beyond the pulsar light cylinder. These electrons may then scatter infra-red photons produced in a second outer gap up to energies of ~ 10 TeV. Pair production between these gamma rays and the same infra-red photons results in relativistic electrons and positrons with large pitch angles. The subsequent VHE synchrotron radiation from these particles will be isotropic and unpulsed.

6.2.2 Active Galactic Nuclei

"Active galaxy" is the term applied to those galaxies with a higher than normal luminosity. More precisely, a galaxy whose observed total luminosity cannot be entirely attributed to starlight. It is generally believed that the power source responsible for the emission from active galaxies is a central, supermassive

($\sim 10^8 M_\odot$) black hole surrounded by an accretion disk (Robson, 1996). These are referred to as active galactic nuclei, or AGNs. Recent observations at X-ray (Tanaka, et al. 1995), optical (Ferrarese, et al. 1996) and radio (Miyoshi, et al. 1995) wavelengths of the motion of material near the nucleus of active galaxies support this theory. Some active galaxies display relativistic jets of material extending out from the galactic nucleus for distances of up to a few megaparsecs. These jets are observed through their synchrotron emission at radio and sometimes optical and X-ray wavelengths. Classifying active galaxies in terms of their observational properties has led to the definition of a variety of different species. Unification schemes suggest that many of the different observational features can be reconciled by assuming they result from the effects of the orientation of the galaxy relative to the observer's line of sight (e.g. Dermer and Schlikeiser, 1992; Antonucci, 1993) (Fig 6.4).

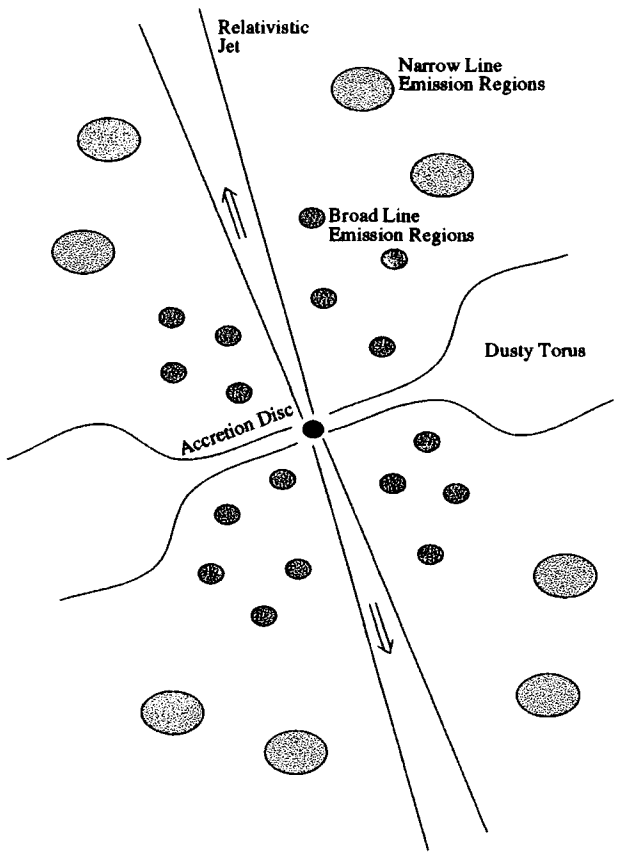

Figure 6.4 A schematic picture of a radio-loud AGN. The observed features depend critically upon the viewing angle. For example, if observed close to the axis of the jet, beamed emission will outshine the host galaxy.

Prior to the launch of the CGRO satellite only one AGN, the radio loud quasar 3C273, had been observed at energies >100 MeV (Swanenburg, et al. 1978). There are now ~ 50 reliably identified AGNs in the EGRET catalogue (Fichtel, 1996; von Montigny, et al. 1995). All of these galaxies belong to the class of AGN known as blazars, which includes optically violent variable quasars and BL Lacertae objects.

In the VHE range, the Whipple collaboration have tracked 36 AGNs, roughly based upon the criteria that they must be at a suitable declination, EGRET detected, a blazar at low redshift or interesting for some other reason (Kerrick, et al. 1995). Two of these candidate sources have now been detected: Markarian 421 (Punch, et al. 1992) and Markarian 501 (Catanese, et al. 1995a; Quinn, et al. 1996). The detection of Markarian 421 has since been confirmed by the HEGRA collaboration (Schubnell, et al. 1996).

Markarian 421 is the closest of the EGRET detected blazars (z = 0.031) but is also one of the faintest, with a reported flux of 0.14×10^{-2} photons m^{-2} s^{-1} above 100 MeV (Michelson, et al. 1992). For this source, the sensitivity of the Whipple ACT is comparable to, if not better than, the EGRET experiment. The non-detection of the 34 other AGNs sampled, 14 of which were EGRET detected blazars, implies that their TeV flux may be being attenuated in some manner. This could be due to an inherent steepening of the particle acceleration spectrum, absorption of TeV gamma rays in the region of the source or absorption by pair production with photons of the intergalactic infra-red (IR) background field (Gould and Schréder, 1967). This last option has been restated more recently by Stecker, et al. (1992), who suggest that measurements of the attenuation of TeV gamma rays from blazars could provide a means of determining the strength of the IR background.

Extragalactic IR radiation could have many sources, but it is believed to be strongly linked to the era of galaxy formation. Measurements of its flux would therefore place useful constraints upon some cosmological models (e.g. Bond, et al.

1986). The IR background flux is difficult to measure directly due to background sources of IR flux such as zodiacal light, instrumental background and the galactic IR field. Using the Whipple and EGRET measurements of Markarian 421, there have been various attempts to obtain values or upper limits for the extragalactic background field (Stecker and De Jager, 1993; De Jager, et al. 1994; Dwek and Slavin, 1994). Biller, et al. (1995) have pointed out some of the problems with these initial attempts and have calculated a conservative upper limit for the infra red photon energy density of 0.04 eV cm^{-3} at the 95% confidence level for IR photons of energy 0.1 to 0.3 eV (Fig 6.5). Salamon, et al. (1994) have noted that, given an independent measure of the intergalactic IR field, it would be possible to use ACT measurements of the absorption of TeV gamma rays from blazars to provide an estimate of their distance. Knowing this, and their velocity from redshift measurements, the Hubble constant can be calculated.

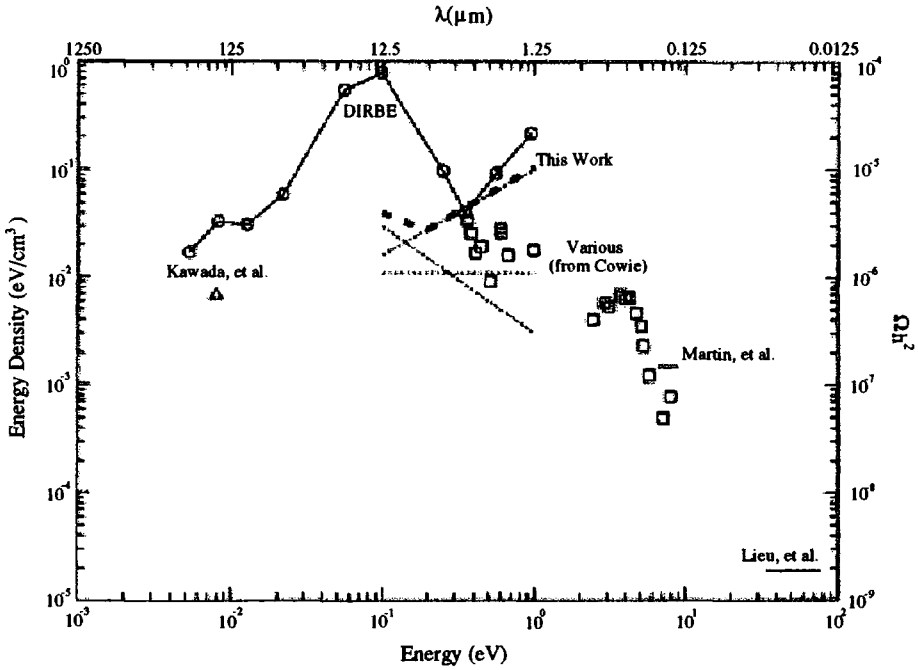

Figure 6.5 Experimental upper limits on the background IR energy density. The energy density is expressed both in units of eV/cm^3 and in terms of the critical density, Ω, times h^2 where the Hubble constant is given by 100h km/s/Mpc. Dotted lines show limits derived for assumed spectral indices of 1.2 (positive slope), 2 (flat) and 3 (negative slope). The bold, dashed line shows the limit derived assuming that this slope is unknown (from Biller, et al. 1995).

The identifying features of blazars are high luminosity ($\sim 10^{45}$ ergs s^{-1}), extreme flux variability, high optical polarization, flat-spectrum radio emission from a compact core and often apparent superluminal motion components. These features are indicative of synchrotron emission from a relativistic jet of particles. In the unified model, blazars are believed to be AGNs observed almost directly along the jet. Relativistic effects due to radiation from a a jet moving at velocity V_{jet} then boost the apparent luminosity, L_{app}, by:

$$L_{app} = \delta^n L, \quad 3 \leq n \leq 4$$

$$\delta = \frac{1}{\gamma(1 - \beta\cos\theta)}, \quad \beta = \frac{V_{jet}}{c}, \quad \gamma = \text{Lorentz factor}$$

where L is the intrinsic luminosity and n is dependent upon the radiation model used (Schlickeiser, 1996). The same relativistic effects can cause apparent bulk motion of material in excess of the speed of light.

Various radiation production mechanisms have been proposed to account for gamma ray emission from blazars. The leptonic production processes can be summarised as follows:

(i) synchrotron self-Compton: the relativistic electrons and positrons in the jet scatter their own synchrotron radiation up to gamma ray energies (e.g. Bloom and Marscher 1993).

(ii) inverse Compton scattering of radiation external to the jet: the relativistic electrons and positrons in the jet scatter external photon fields up to gamma ray energies. The target field could be the result of accretion disc photons (Dermer, et al. 1992), accretion disc photons reflected from emission line clouds (Sikora, et al. 1994) or microwave background and starlight photons.

(iii) pair annihilation radiation: relativistic electrons and positrons in the jet annihilate

to produce gamma ray photons. Considering the spectral broadening caused by the energy distribution of the annihilating particles and the bulk motion in the jet, broad continuum emission might be expected around the MeV range (Henri, et al. 1993). Figure 6.6 shows some of the gamma ray production mechanisms possible from a leptonic jet.

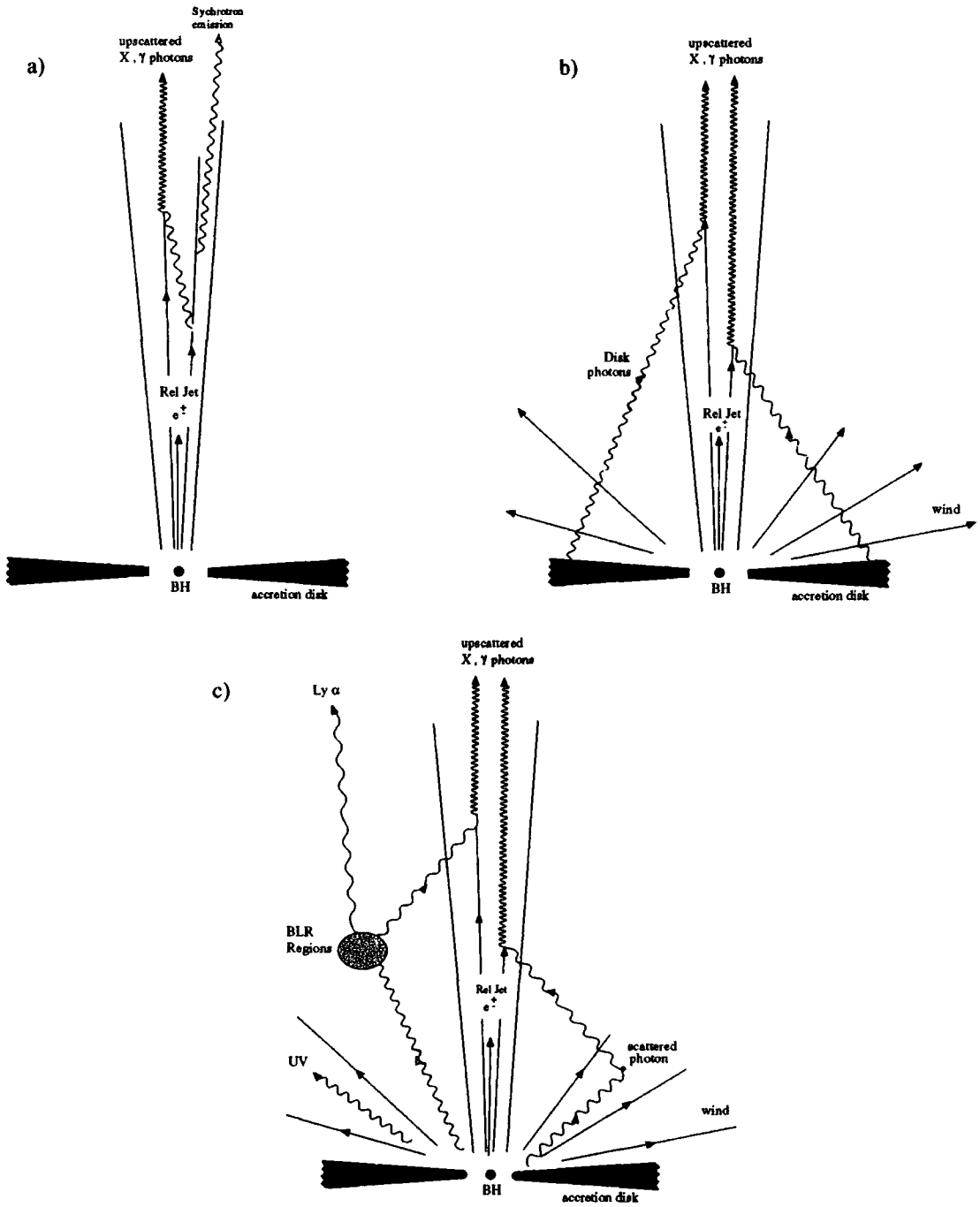

Figure 6.6 Schematic of gamma ray production in a leptonic jet. a) shows the synchrotron self-Compton mechanism . b) and c) show inverse Compton scattering of radiation originating outside of the jet (from Dickinson, M.R.: in preparation)

Hadronic models postulate that efficient proton acceleration is occurring in the cores of AGNs through first order Fermi acceleration at stationary shock fronts in the accretion flow (Kazanas and Ellison, 1986). Subsequent hadron-hadron or

hadron-photon reactions can produce high energy photons or particles. While VHE photons are unable to escape from the optically thick medium close to the core of an AGN, they may initiate an electromagnetic cascade which could be responsible for the relativistic electrons and positrons of the jet (Mannheim, 1995). Alternatively, neutrons produced in hadron collisions may be able to escape the central region of the AGN and produce TeV gamma rays via proton-proton collisions after the neutron has decayed, or directly by hadron-hadron collisions as the neutrons interact with the infalling plasma (Mastichiadis, 1995).

One of the most exciting aspects of the detection of AGNs at TeV energies has been the observation of rapid variability on extremely short timescales. Buckley, et al. (1996) have examined the Whipple telescope observations of Markarian 421 in 1995 and find variability on the scale of ~ 1 day. The emission can be characterized as a succession of rapid flares, consistent with little steady emission. Flares of much greater magnitude have also been observed. In these flare states, the VHE photon flux increases by an order of magnitude over a timescale of 1 - 2 days (Schubnell, et al. 1996; Kerrick, et al. 1995a). An observation of one of the TeV flares has been made with simultaneous observations at other wavelengths (MaComb, et al. 1995). A contemporaneous high state was seen by the X-ray satellite ASCA, but no excess emission was detected by EGRET. This observation lends weight to the SSC model of relativistic electrons compton scattering their own X-ray synchrotron emission up to TeV energies.

The rate of variability of an object can provide some idea of the size of the radiating region by relativistic causality arguments. This in turn can be used to place constraints upon the emission mechanisms at work. In May 1996 the Whipple observatory observed two flares from Markarian 421 separated by eight days (Gaidos, et al. 1996). In the first flare, the flux increased from its quiescent value by more than a factor of 50, with a doubling time of ~ 1 hour. In the second outburst, the emission increased to ~ 25 times the quiescent flux over a period of only ~ 30 minutes

(Fig 6.7). This second flare implies that the emission region may be as small as a few light hours. Existing models for TeV gamma ray emission from blazars are unlikely to provide an explanation for this extraordinary event.

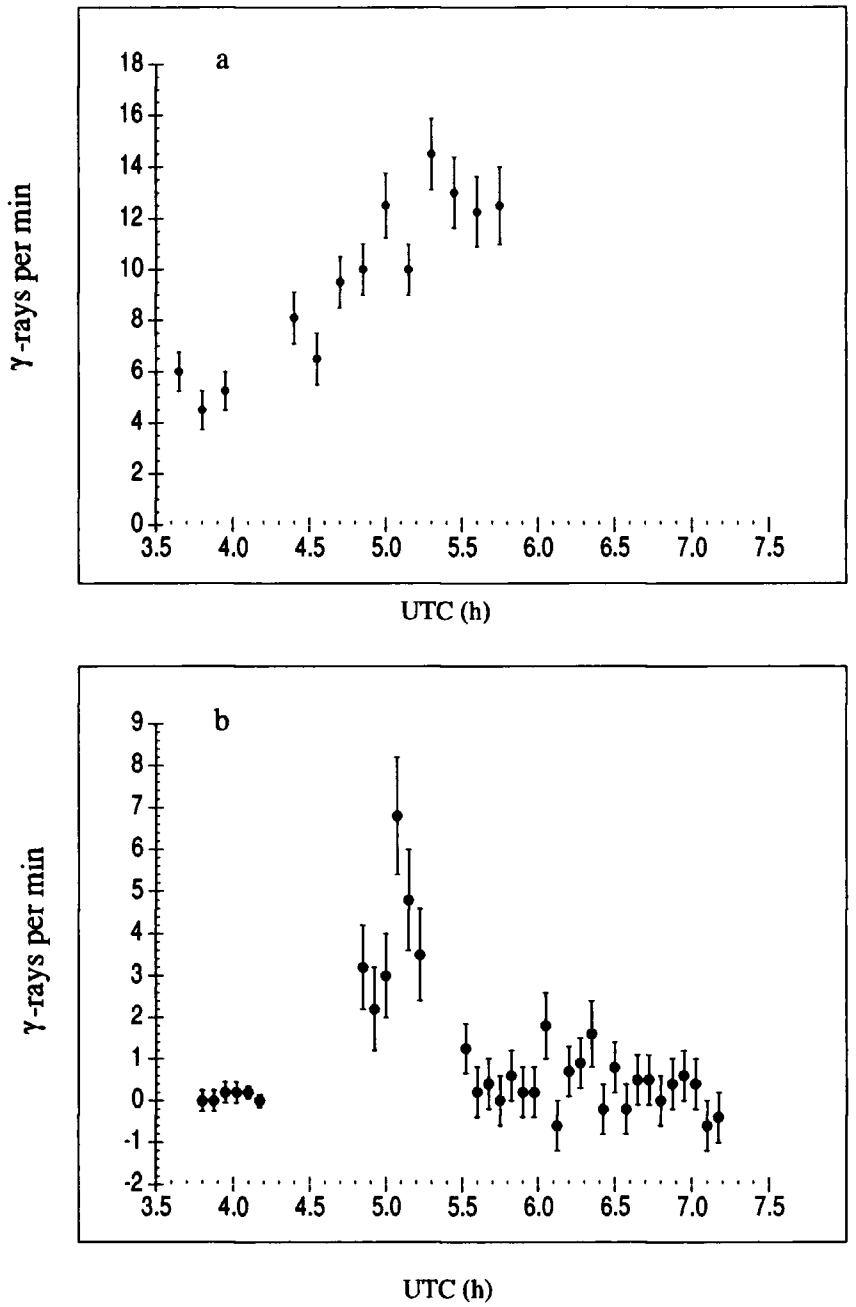

Figure 6.7 Temporal histories of the two flare events. For the first flare (a), each point is a 9 min integration; for the second flare (b), the integration time is 4.5 min. The error bars are statistical standard deviations (from Gaidos, et al. 1996).

Finally, it is worth noting that both Markarian 421 and Markarian 501 are

classed as X-ray selected BL Lacertae objects. That is, their synchrotron emission spectrum peaks in the X-ray region, unlike radio selected BL Lacs whose synchrotron emission peaks in the optical/UV. This indicates that there is a population of extremely high energy electrons and positrons in the jet which may produce TeV photons by Compton mechanisms. Stecker, et al. (1996) have predicted the VHE flux from 23 nearby BL Lacs. Table 6.1 lists those objects which are observable (culminate within 30° of the zenith) with the Durham telescopes from Narrabri.

Table 6.1: Predicted fluxes for southern hemisphere, nearby, X-ray selected BL Lacs. 1ES1101 + 384 (Markarian 421) is given for comparison (from Stecker, et al. 1996).

1ES Name	z	Flux (>0.1GeV) 10^{-7} cm^{-2} s^{-1}	Flux (>0.3TeV) 10^{-11} cm^{-2} s^{-1}	Flux (>1 TeV) 10^{-12} cm^{-2} s^{-1}
1ES0347 - 121	0.188	0.05	0.38	0.08
1ES0548 - 322	0.069	0.56	1.30	1.20
1ES1312 - 423	0.105	0.19	0.24	0.15
1ES2005 - 489	0.071	0.70	0.91	0.84
1ES2155 - 304	0.116	3.90	1.70	0.88
1ES1101 + 384	0.031	1.43	2.30	3.60

6.3 Steady Source Analysis Techniques

6.3.1 Comparison of On Source and Off Source Regions

For observations of a candidate steady source of gamma ray emission, the telescope is operated in the chopping mode which has been described in section 3.2.1. This provides two datasets. The data collected with the telescope directed at the source are known as on source data and those with the telescope pointing at a background region displaced from the source position in right ascension are known as off source data. The same data calibration, preparation and gamma ray event selection

procedures are applied to both datasets. If all systematic effects have been accounted for, any excess of on source counts compared with off source counts will be the result of gamma ray emission from the source region. The significance of the excess is calculated using:

$$\text{significance}(\sigma) = \frac{N_{ON} - N_{OFF}}{\sqrt{N_{TOT}}}$$

where N_{ON} and N_{OFF} are the number of on source and off source counts respectively, $N_{TOT} = N_{ON} + N_{OFF}$, and one standard deviation, $\sigma = (N_{TOT})^{1/2}$.

Possible systematic differences between the on and off source counts due to long term changes in sky conditions or zenith angle effects are removed by the chopping method of operation. A problem may remain, however, due to a difference in sky brightness between the on source and off source fields.

6.3.2 Software Padding

In the standard moment procedure, for a PMT to be designated an image tube, its signal must be larger than ~5σ, where σ is the measured tube response to sky noise. In most cases, the signal will be even larger than this and so the image tubes are dominated by real Cerenkov light signals. Boundary tube thresholds, however, are generally ~ 2σ and the signal always less than ~ 5σ and so these tubes contain an approximately Gaussian sky noise component comparable to the low level power law Cerenkov signal. For a tube with a large sky noise response, and hence a large threshold criterion, the probability increases that a negative noise fluctuation will cancel the Cerenkov component of the signal and result in the tube being removed from the moment calculation (Fig 6.8). The result of this is that for a bright field, fewer boundary tubes will be included in the parameterisation and the images will therefore have smaller *widths* and *lengths*. The inevitable differences in parameter distributions between on source and off source fields of different sky brightness will

cause systematic differences in the number of events selected by any set of cuts, making the identification of a true gamma ray component from the candidate source field more difficult.

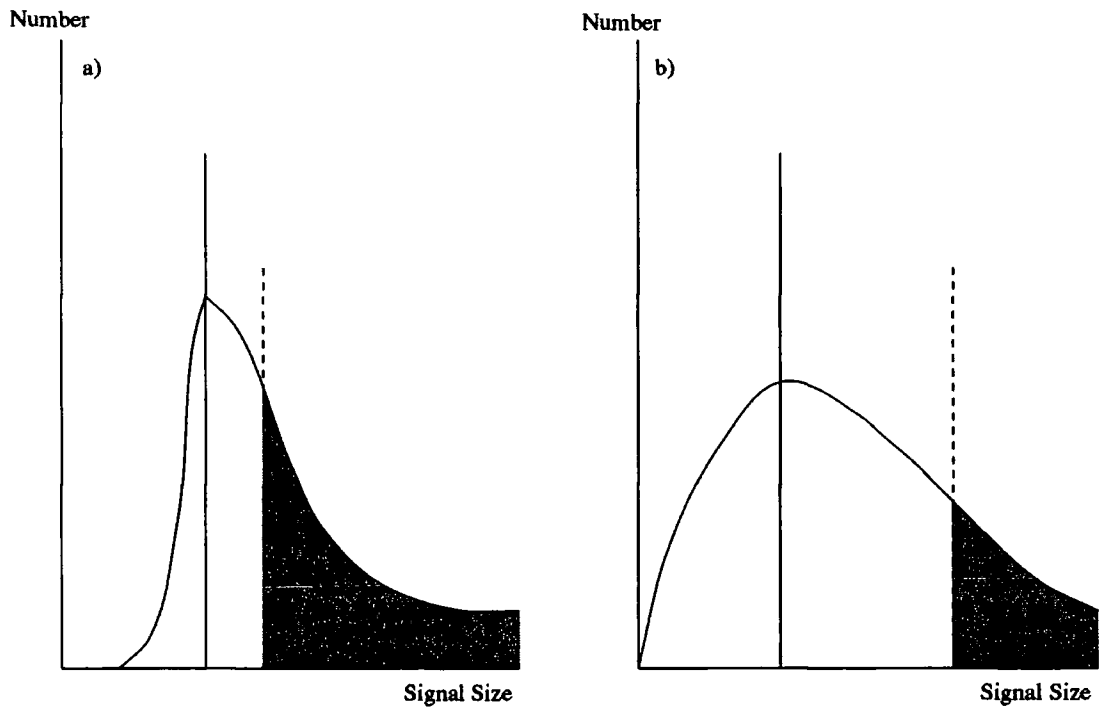

Figure 6.8 Pulse height spectra for boundary tubes (mixture of noise and low-level Cerenkov signal); a) tube with low noise level, b) tube with high noise level. Using a noise dependent boundary threshold, the number of occasions when the tube exceeds this threshold will be less in b) than in a) (shaded area). The distribution shapes have been exaggerated for clarity (after Cawley, 1993).

The starting points for the bivariate Gaussian fitting procedure are calculated using the standard moment procedure. The tube noise responses are also used in the calculation of the χ^2 goodness-of-fit value. The fractional peak response criteria for image/border selection relax to noise dependent thresholds for low values of peak response. In summary, all of the image analysis techniques described in Chapter five depend, to differing extents, upon the measured sky noise response of the PMT's and will therefore be prone to systematic effects caused by differences in sky brightness.

A solution to this problem is to add a randomly generated noise signal to the

signal recorded by the tubes on the darker field in order to equalize the effective noise levels (Cawley, 1993). This technique of "software padding" is analogous to the hardware padding lamps which were used to keep the illumination of PMT's constant in earlier experiments. All of the data analysed for presentation in this chapter were software padded as part of the routine data preparation.

6.4 A Search for Steady Emission From PSR 1706-44

The high resolution camera of the Mark 6 telescope has been used to observe the radio pulsar PSR1706-44 in May and July of 1996. The recorded images have been parameterised using the standard moment procedure and the bivariate Gaussian fitting technique. The results of these analyses are presented here.

6.4.1 PSR 1706-44

PSR 1706-44 was the fourth radio pulsar to be detected by instruments on board the CGRO. It was first identified as a COS-B gamma ray source, 2CG 342-02 (Swanenburg, et al. 1981) but the nature of the source was then unknown. A survey of the southern galactic plane by the Parkes radio telescope at a frequency of 1500 MHz detected 100 pulsars, 46 of which were previously unknown (Johnston, et al. 1992). One of these, PSR 1706-44 was found to have a spin period of 102 ms. EGRET observations of 2CG 342-02 showed that the gamma ray source was positionally coincident with PSR 1706-44. A periodic analysis of the EGRET events with energies greater than 100 MeV revealed highly significant pulsed emission at the same period as the radio pulsar, confirming that the gamma ray and radio sources were the same object (Thompson, et al. 1992).

The radio and gamma ray light curves of PSR 1706-44 are significantly different. The radio emission displays a single narrow pulse with a width of ~ 6% of the period. At gamma ray energies, the pulsar duty cycle is larger, with emission

present over ~ 35% of the pulse period (Fig 6.9). Thompson, et al. (1996) suggest that the light curve consists of two peaks separated by 0.2 in phase, with the possibility of a third peak situated between these two. The spin-down rate of the pulsar implies a characteristic age of only 17,400 years (Johnston, et al. 1995). There is no evidence for unpulsed emission over the EGRET energy range. The spectrum of the pulsed emission is well fitted by a broken power law with a differential spectral index of -1.27 ± 0.09 below 1 GeV and -2.25 ± 0.13 above 1 GeV (Thompson, et al. 1996).

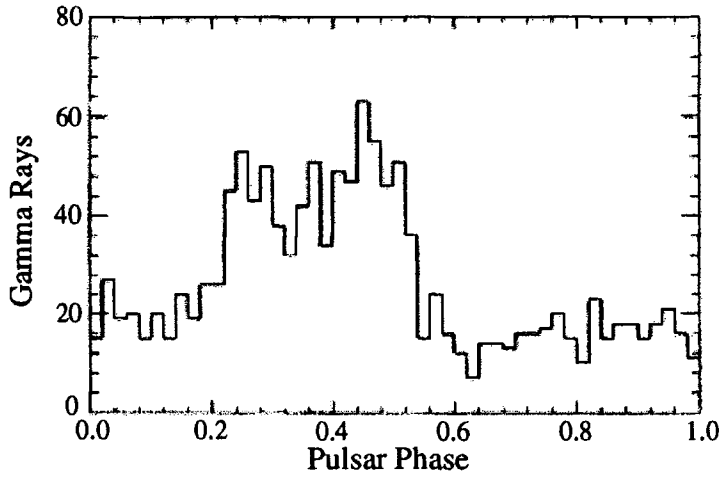

Figure 6.9 High energy (>400 MeV) gamma ray light curve for PSR 1706-44. The 102 ms period is divided into 50 phase bins with the single radio pulse defining the zero phase (from Thompson, et al. 1996).

McAdam, et al. (1993) have suggested that the pulsar may be associated with a shell-like supernova remnant, SNR G343.1-2.3 discovered by its arc-shaped radio emission using the Molongo Observatory Synthesis Telescope. Using three different surface-brightness - diameter relationships to estimate the physical diameter of the SNR they calculate distances to the SNR of 3.5, 4.0 and 3.2 kpc. Using the size - age relationship of Caswell and Lerche (1979) suggests an age of 5600 yrs for the SNR. This is younger than the characteristic pulsar age, but the deduced age is dependent upon the assumed density of the medium into which the SNR is expanding. The distance to the pulsar has been estimated by Johnston, et al. (1995) on the basis of its dispersion measure to be ~ 1.8 kpc. This value is highly dependent upon the model of

the galactic electron energy distribution and hence has a large uncertainty associated with it. Koribalski, et al. (1995) have measured the neutral hydrogen emission and absorption spectra in the direction of PSR 1706-44 and use these to infer a distance to the pulsar of between 2.4 and 3.2 kpc. If the pulsar were associated with the SNR, in order to have travelled from the geometrical centre of the arc to its current position within the pulsar lifetime of 17,400 yrs, it would need to have a transverse velocity ~ 1000 kms^{-1}.

Nicastro, et al. (1996) argue that the high transverse velocity required and the lack of observed interaction of the pulsar with the SNR make the association statistically unlikely. In addition, they have measured the interstellar scintillations caused by electron density fluctuations along the line of sight to the pulsar. As the pulsar moves, the radiation diffraction pattern observed by a radio telescope changes. Measurement of these changes enables an estimate of the pulsar velocity to be derived. Using this method gives a transverse velocity of only 27 kms^{-1} with an error ~ 50%.

PSR 1706-44 has also been detected by the X-ray satellite ROSAT (Becker, et al. 1995). At these energies the emission is unpulsed (Becker and Truemper, 1996). Frail, et al. (1994) report the detection, at a wavelength of 20 cm, of a compact radio nebula surrounding the pulsar. These measurements are indicative of a synchrotron bubble around the pulsar, placing it in the class of filled-centre SNR (plerions).

6.4.2 TeV Gamma Ray Observations of PSR 1706-44

The first reported observations of PSR 1706-44 at TeV energies were performed by Nel, et al (1993). This was a search for pulsed emission only and provided an upper limit of 5.8×10^{-12} photons $cm^{-2}\ s^{-1}$ for gamma rays of energy >2.6 TeV. Kifune, et al. (1995) report the detection of gamma rays of energy > 1 TeV from the direction of PSR 1706-44. The dataset consists of 84 hours of on source data from observations in 1992 and 1993. The significance of the detection is ~ 12 σ and

the gamma ray flux is quoted as 7×10^{-12} photons cm^{-2} s^{-1} with a systematic error of ~ 30%. This corresponds to a flux of ~ 1×10^{-11} ergs cm^{-2} s^{-1} at 1 TeV. Assuming a distance to the pulsar of 1.5 kpc implies a TeV luminosity of ~ 3×10^{33} ergs s^{-1} if the emission is isotropic. This is equivalent to 10^{-3} of the total spin-down energy of the pulsar. Full results of a search for evidence of periodic emission at the 102 ms radio period in this dataset have not been presented, but initial reports suggest that it is unlikely that there is a major pulsed component.

At higher energies, the JANZOS collaboration have observed PSR 1706-44 using a scintillator array and report an upper limit of 1.5×10^{-13} photons cm^{-2} s^{-1} above an energy of ~ 100 TeV (Allen, et al. 1993).

6.4.3 An Analysis Using Moment Parameterisation of Images

The moment method of image parameterisation is the standard technique for the analysis of images from ACT's. It has been described in Chapter five and is applied here to Mark 6 telescope observations of PSR1706 -44.

6.4.3.1 Data Selection

Prior to the application of any background discrimination based on image information, the quality of the dataset must be verified. The count rate profiles for each night of observation are checked for evidence of frost or condensation on the mirrors and removed or truncated if necessary. Any observations involving poor weather or equipment problems are also discarded. The data are then divided into "scans", each consisting of 14 minutes of on source exposure and its corresponding 14 minutes of off source data. One minute of each 15 minute exposure must be discarded as the telescope was steering in to position. The software padding technique described in section 6.3.2 is applied at this stage to equalize the effective sky noise levels of the on and off source regions. Significant differences in the number of events from the on and off source regions are still apparent at this stage.

This is due to different numbers of spurious noise generated triggers. The rate of these is higher for the brighter, on source field as the tube noise fluctuations are larger. Noise triggers are easily recognisable as they contain no Cerenkov light. The first stage of the image selection procedure removes these events.

To begin with, all recorded images are parameterised by the moment method, using the fractional peak response criteria to determine which tubes are include in the parameterisation. This method of tube selection is described in section 5.4.2. The image/border thresholds used in this analysis were 37.5% and 17.5% of the peak response respectively. The dataset is then subjected to an initial, "tidy", selection process. In this, the very faint events (total signal < 300 digital bits) and those near to the camera boundary (*distance* > 1.1°) are rejected. Any single scan which displays a difference in the number of events between the on and off source segments greater than 2σ is removed from the analysis at this stage. The final dataset consists of 9 nights from May and July of 1996 with a total of 574 minutes of on source exposure and the same off source. These observations are catalogued in Table 6.2.

Table 6.2: Catalogue of Mark 6 Telescope observations of PSR 1706-44

Observation Date	On Source Exposure (mins)	On Source Events (Tidy)	Off source Events (Tidy)
11/05/96	42	6917	6819
12/05/96	56	7833	7562
21/05/96	84	15334	15422
22/05/96	28	4244	4116
24/05/96	84	14292	14331
09/07/96	98	15455	15461
11/07/96	56	8923	8867
15/07/96	56	9561	9547
18/07/96	70	12990	12740
TOTALS	574	95549	94865

The next stage of the selection procedure is to start using the shape of the images as a discriminant between the gamma ray and hadron initiated showers. A feature of the parameters of events recorded by the Mark 6 telescope becomes important at this point. Figure 6.10 shows the dependence of the mean *width* parameter as a function of *QTsum*, where *QTsum* is the sum of the signals of all image/border tubes. It is clear that *width* varies quite strongly with the total image brightness. As a result of this, the *width* selection used in this analysis has been applied as a function of *QTsum*. The events are divided into 20 *QTsum* bins and a constant fraction of the smaller width events is selected from each bin. In this analysis, events in the lower 17.5% of the width distribution for each *QTsum* bin have been selected.

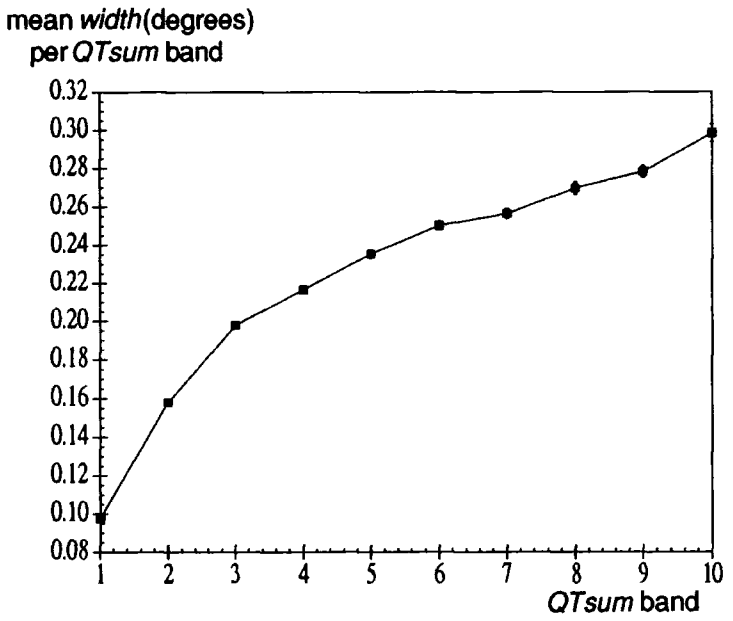

Figure 6.10 Mean *width* as a function of increasing *QTsum* for Mark 6 telescope events. The *QTsum* distribution has been divided into 10 bands, each of which contain the same number of events. The mean *width* is then calculated for each band.

After this *width* selection has been applied, the following additional selection criteria are used: *eccentricity* (=*width*/*length*) < 0.7, 0.60° < *distance* < 0.85°, *ddist* < 0.15°.

The *eccentricity* and *distance* cuts ensure that the images are elliptical and well confined within the camera, whilst being far enough removed from the source position to have their orientation well measured. The other parameter, *ddist*, uses information from the left and right detectors and is a measure of the distance between the image centroids as measured in each. Gamma ray initiated showers are expected to produce a similar image in each three dishes, while the hadron showers will start to show differences over the 14 m baseline. Analysis of the left/right images is in a preliminary stage at present but may well prove to be a powerful discriminatory tool in future (S.E.Shaw, private communication). For this analysis, only the simplest parameter, *ddist*, is used to remove a fraction of the obvious hadron initiated events.

6.4.3.2 Results

Figure 6.11 shows the distribution of the orientation parameter, *alpha*, for the

events remaining after the parameter selections described above. The majority of the on source excess has an *alpha* close to zero as would be expected for a gamma ray signal from the source position. Outside of this region, an overall deficit of low statistical significance may be apparent, especially in the $20° < alpha < 70°$ region. This could indicate some small systematic difference between the on source and off source files, possibly caused by a residual sky noise difference after software padding.

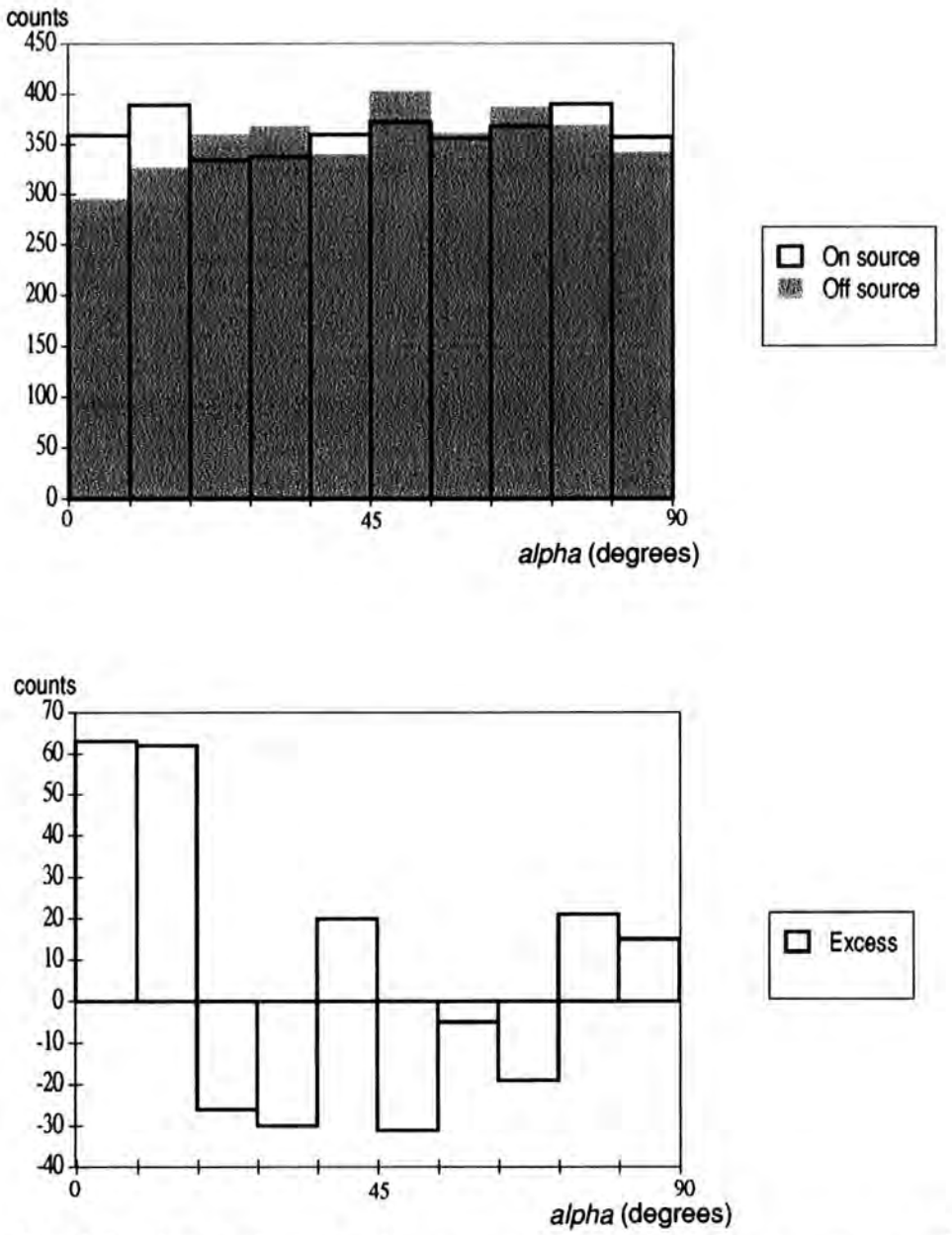

Figure 6.11 *Alpha* distributions for the on source and off source events and the difference between them.

Table 6.3 lists the total on and off source event numbers at each stage of the selection process. The final selection, *alpha* < 20°, produces an excess of 131 events on source, significant at the 3.5 σ level.

Table 6.3: Events remaining after each parameter selection.

Selection Parameters	On Source Total	Off Source Total	Difference
distance<1.10° *QTsum*>300	95549	94865	684 (1.6 σ)
width fraction<17.5%	21528	21122	406 (2.0 σ)
eccentricity<0.7 0.60°<*distance*<0.85° *ddist*<0.15°	3623	3553	70 (0.8 σ)
alpha<18°	787	656	131 (3.5 σ)

6.4.4 An Analysis Using a Bivariate Gaussian Fit to Parameterise Images

The bivariate Gaussian fitting technique has been suggested as an alternative method for parameterising Cerenkov images of EAS. It has been described in Chapter five and is applied here to the Mark 6 telescope observations of PSR 1706-44.

6.4.4.1 Data Selection

The same scans which were selected as free from any weather, condensation or equipment problems in the previous analysis are software padded and then subjected to the bivariate Gaussian fitting procedure. The fit is corrected using the PSF matrix described in section 5.4.2 in an attempt to correct for the point spread function of the telescope mirrors.

The initial "tidy" selection for the fitted events is as follows: *QTsum* > 600, *distance* < 1.5°. For fitted events, the *QTsum* value is in arbitrary units which provide a measure of the volume under the fit prediction. A value of 600 corresponds to an event with a *QTsum* of ~ 250 digital bits when parameterised using the moment method. The purpose of this selection is to remove any noise generated triggers and to remove those events which lie too far out in the camera to be well parameterised. Any scans which show a difference in counts of > 2 σ after this stage are discarded,

resulting in a slightly smaller dataset than in the moment based analysis.

Table 6.4: Catalogue of Mark 6 Telescope observations of PSR 1706-44

Observation Date	On Source Exposure(mins)	On Source Events (Tidy)	Off source Events (Tidy)
11/05/96	28	5453	5318
12/05/96	56	8442	8162
21/05/96	84	16181	16354
22/05/96	14	2092	1974
24/05/96	70	12428	12661
09/07/96	84	12844	12574
11/07/96	56	6844	6857
15/07/96	56	7312	7260
18/07/96	70	10110	10016
TOTALS	518	81706	81176

A *distance* selection of $0.65° < distance < 1.10°$ is then applied and the *QTsum* threshold is also raised to 850 (equivalent to ~ 400 digital bits). This ensures that the events are bright enough to be well parameterised and have centroids far enough from the source position for their orientation to be well defined but are not overly truncated by edge effects. The shape selection used is a fixed *width* cut with an *eccentricity* cut to retain events with reasonable ellipticity. The cut values are $width < 0.36$ and $eccentricity < 0.8$.

6.4.4.2 Results

The *alpha* distributions of the on source, off source, and on source excess events are shown in Figure 6.12. The peak near $alpha = 0$ is even more marked in the excess distribution than was apparent with the moment based analysis, although its

true significance is less due to the larger number of background events remaining.

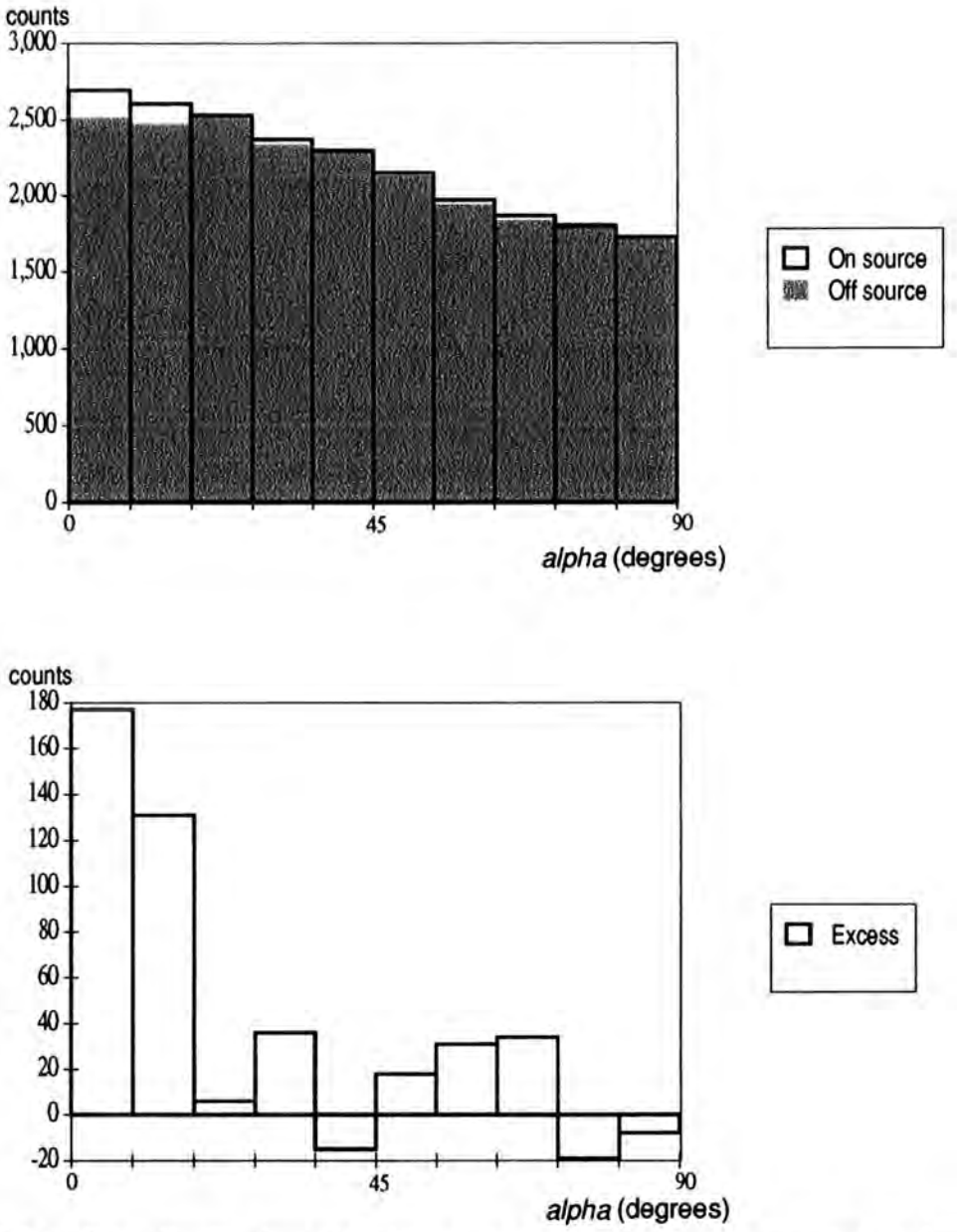

Figure 6.12 *Alpha* distributions for the on source and off source events and the difference between them.

The number of events remaining after each stage of the event selection process are presented in Table 6.5. The final selection, *alpha* < 20°, results in an on source excess of 329 events over a background of 11409 which is significant at the 3.1 σ level.

Table 6.5: Events remaining after each parameter selection.

Selection Parameters	On Source Total	Off Source Total	Difference
distance<1.5° *QTsum*>600	81706	81176	530 (1.3 σ)
0.65°<*distance*<1.10° *QTsum*>*850*	31949	31877	72 (0.3 σ)
width<0.36° *eccentricity*<0.8	22032	21641	391 (1.9 σ)
alpha<20°	5869	5540	329 (3.1 σ)

6.4.5 Discussion

The Mark 6 observations of PSR 1706-44 have been analysed using both the moment and bivariate Gaussian fitting methods for image parameterisation. In both cases, an excess of events from the on source region is apparent after cuts to select gamma ray candidate events have been applied. In particular, the excess events are orientated such that their major axes point towards the position of PSR 1706-44 in the camera.

The moment analysis provides the more significant result (3.5 σ). The raw off source dataset consisted of 259906 events. After all selections, this has been reduced to 656 events, giving 99.7% background rejection and retaining an excess of 131 events on source. The result from the Gaussian fit analysis is marginally less significant (3.1 σ), mainly because the background rejection has not been as efficient. 5540 events remain from a raw off source dataset of 234910, giving 97.6% rejection. However, the excess which is retained is 329 events, appreciably larger than in the moment analysis.

The true significance of these results is difficult to assess, as the selections employed have been guided by the data to some extent. In the absence of more

accurate Monte Carlo simulations, this is the only method available for determining the best selection criteria to improve the signal to noise ratio. If we assume that these results constitute a detection of gamma ray emission from PSR 1706-44, a value of the observed flux can be calculated.

As discussed in section 3.4.6, the energy threshold and effective area for the detection of gamma rays by an ACT depend upon the image selection procedures which have been used to increase the signal/noise ratio. The gamma ray database used in section 3.4.6 has been subjected to the same moment and bivariate Gaussian based analyses as the data in this chapter. The resulting energy dependent effective area and differential flux plots are shown in Figures 6.13 and 6.14.

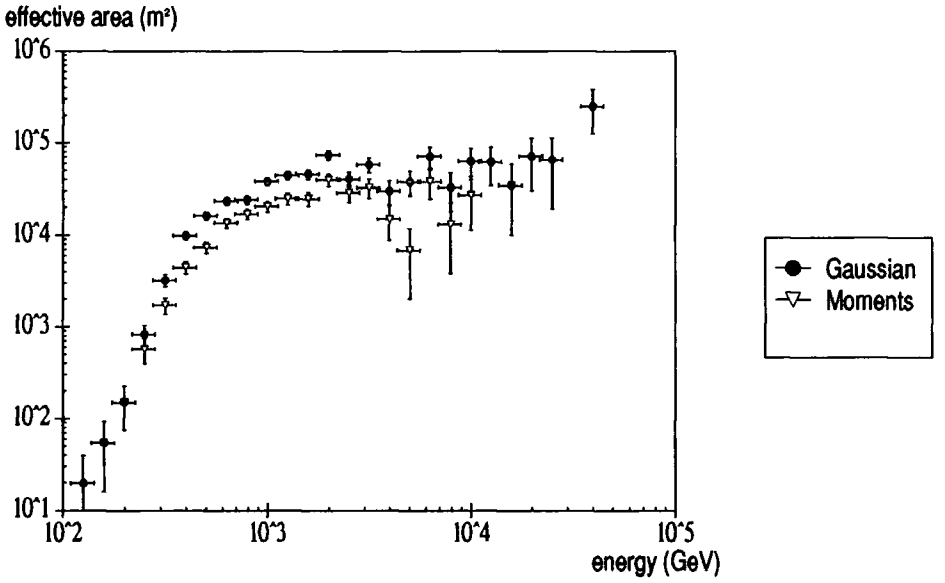

Figure 6.13 Effective area for gamma ray detection, after image selection, of the Mark 6 telescope as a function of primary energy.

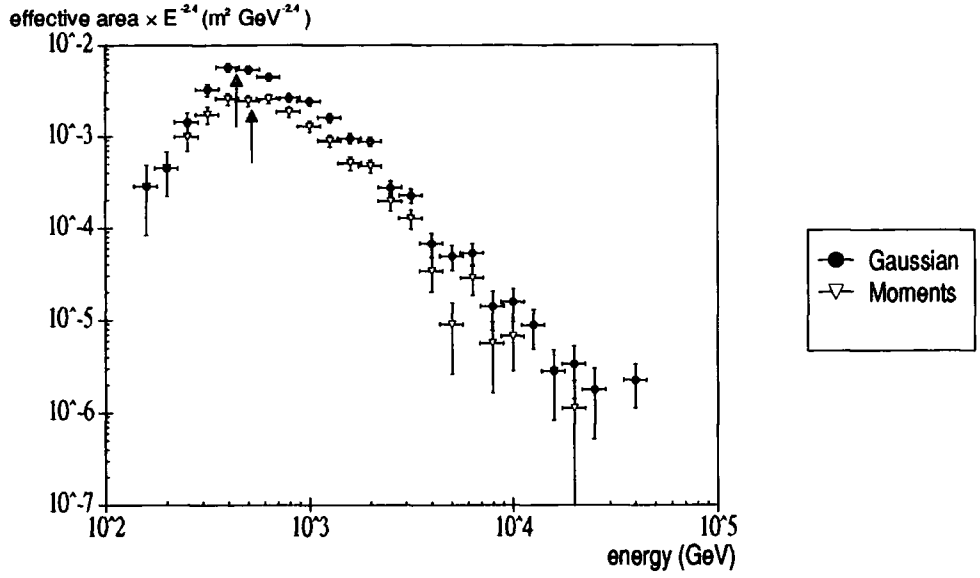

Figure 6.14 Definition of the energy threshold for gamma rays after image selection. The source differential spectrum is assumed to be -2.4. The threshold energy is defined to be the the energy of the maximum differential flux and is approximately 420 GeV for the bivariate Gaussian selection and 500 GeV for the moment selection.

The bivariate Gaussian analysis suggests an energy threshold for gamma rays of ~ 420 GeV. Assuming a conservative systematic error of ± 100 GeV on this threshold, the effective collection area is ~ $(4.1 \pm 0.5)\times10^4$ m^2. Given 329 excess events in 518 minutes implies a gamma ray flux ~ $(2.6 \pm 0.3 \pm 0.1)\times10^{-11}$ cm^{-2} s^{-1} above 420 GeV, where the first and second errors are systematic and statistical respectively. For the moment based analysis, the gamma ray energy threshold is estimated at ~ 500 ± 100 GeV and the effective collection area above this is ~ $(2.2 \pm 0.5)\times10^4$ m^2. The on source excess in this case is 131 events and the dataset is 574 minutes long, leading to a gamma ray flux of ~ $(1.7 \pm 0.4 \pm 0.2)\times10^{-11}$ cm^{-2} s^{-1} above 500 GeV.

Figure 6.15 shows the measured integral energy spectrum of PSR 1706-44, including these points. The pulsed HE gamma ray spectrum from PSR 1706-44 has a spectral break above 1 GeV (Thompson, et al. 1996) and the dashed line in Figure 6.15 is the extrapolation of this (integral spectral index of -1.25). Both the

CANGAROO result and the flux measurements reported here lie below that extrapolation. The EGRET upper limit to unpulsed emission for E > 100 MeV is also shown.

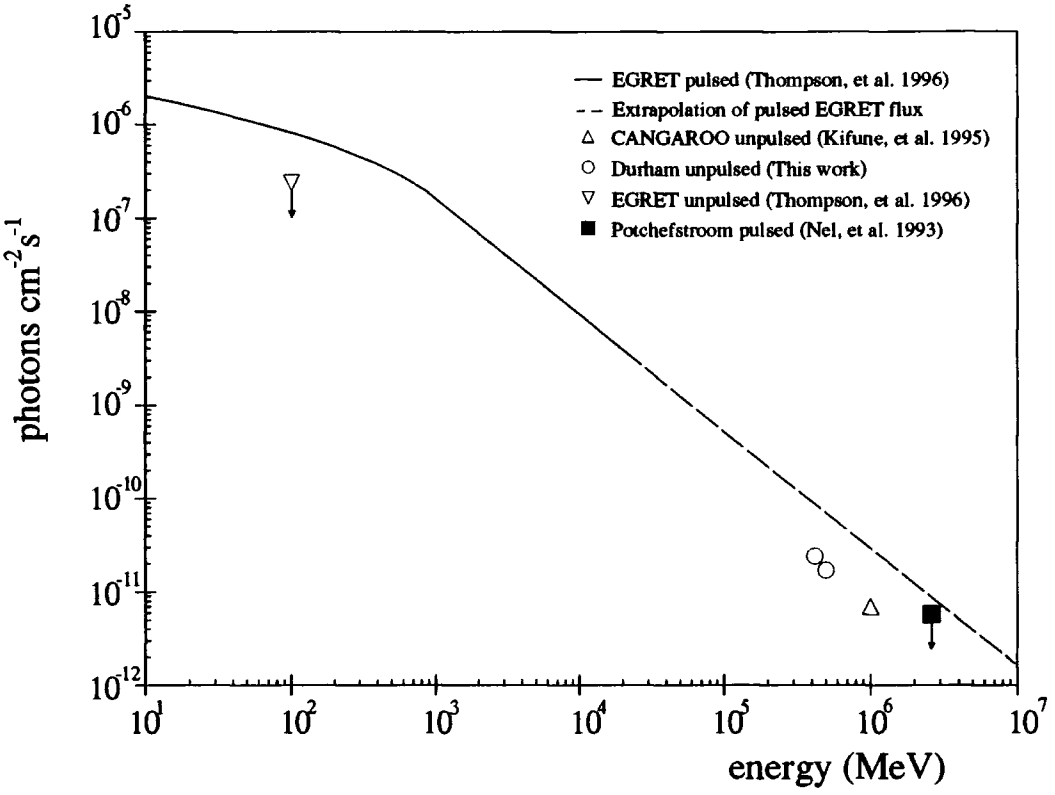

Figure 6.15 Integral spectrum of the gamma ray flux from PSR 1706-44.

If we assume that the VHE gamma ray emission is isotropic, the source luminosity is given by:

$$L = 4\pi D^2.\phi(>E_T).\langle E\rangle$$

where D is the pulsar distance, $\phi(>E_T)$ is the measured integral flux above the energy threshold, E_T, and $\langle E\rangle$ is the average photon energy. Setting D equal to 2.8 ± 0.4 kpc (Nicastro, et al. 1995, Koribalski, et al. 1995), the flux derived from the moment based analysis implies a source luminosity, $L \sim (6.4 \pm 2.4 \pm 0.8)\times10^{34}$ erg s^{-1}. In the

case of the Gaussian analysis, $L \sim (8.2 \pm 2.7 \pm 0.3) \times 10^{34}$ erg s^{-1}. These values are equivalent to ~ 2% of the pulsar's spin-down luminosity of 3.4×10^{36} erg s^{-1}. Table 6.6 shows the luminosity at other wavelengths for the same value of the pulsar distance. The X-ray measurement assumes that the emission is isotropic and characterised by a synchrotron power law spectrum, differential spectral index = 2.4 (Becker, et al. 1995). The EGRET luminosity is calculated assuming that the emission is beamed, with a beaming fraction of $1/4\pi$ (Thompson, et al. 1994).

Table 6.6: The luminosity of PSR1706-44 X-ray energies and above.

Experiment	Energy Range	Luminosity Estimate (D=2.8kpc)
ROSAT	0.1 - 2.4 keV	3.1×10^{33} erg s^{-1}
EGRET	100 MeV - 10 GeV	6.8×10^{34} erg s^{-1}
Durham Mark6	>500 GeV	6.4×10^{34} erg s^{-1}
CANGAROO	>1 TeV	1×10^{34} erg s^{-1}

6.5 Conclusions

The results of an analysis of observations of PSR 1706-44 by the Mark 6 telescope have been presented. The data were analysed using two different methods to parameterise the Cerenkov images. Background discrimination selections applied to images parameterised using a standard moment based method resulted in a 3.5 σ detection of excess events from the on source field. A bivariate Gaussian fit method for parameterising the same images resulted in a 3.1 σ excess from the on source field after background discrimination was applied.

Assuming these excesses are due to gamma ray emission from the pulsar, a flux estimate of $\sim (2.6 \pm 0.3 \pm 0.1) \times 10^{-11}$ cm^{-2} s^{-1} above 420 GeV has been calculated for the bivariate Gaussian analysis. The moment based method results in a gamma ray

flux of $\sim (1.7 \pm 0.4 \pm 0.2) \times 10^{-11}$ cm^{-2} s^{-1} above 500 GeV. These correspond to a source luminosity of $\sim 7 \times 10^{34}$ erg s^{-1}. The detection of TeV gamma ray emission from this object in only 10 hours of on source exposure illustrates the power of the high resolution imaging technique when combined with a telescope of low energy threshold. Various possible future improvements to the analysis techniques may be possible and are discussed in greater detail in chapter 7. The selection criteria which have been developed here will provide a powerful *a priori* analysis method for subsequent datasets, which are likely to be larger than the one used here.

CHAPTER SEVEN - SUMMARY AND FUTURE WORK

7.1 Summary

The status of VHE gamma ray astronomy has been greatly improved over the last decade due largely to the development of Cerenkov image discrimination techniques pioneered by the Whipple collaboration. These methods have led to highly significant and reproducible detections of TeV gamma ray sources. In addition, the success of the CGRO has revealed the rich nature of the gamma ray sky and provided a guide for TeV observations. The discovery of VHE emission from the active galactic nuclei Markarian 421 and Markarian 501 is particularly exciting, as is the observed rapid variability of these sources at TeV energies. Future multi-wavelength studies of these objects promise to provide valuable information about the particle acceleration mechanisms involved. The imaging atmospheric Cerenkov technique has opened up a new window of the electromagnetic spectrum which is beginning to provide insights into very high energy astrophysical environments and the origin of the cosmic rays.

This thesis has presented results from two telescopes using the various imaging detectors which have been developed by the Durham gamma ray astronomy group. Background discrimination has been achieved using the guard ring technique for a seven PMT detector package, medium resolution imaging for a 31 element detector and high resolution imaging for a 109 tube camera. Observations of the high mass X-ray binary SMC X-1, made with the Mark 3 telescope, have been examined for evidence of periodic emission at the X-ray period. No such emission was detected. The processing and calibration routines developed for the Mark 6 telescope have been discussed and its first observations of the EGRET pulsar, PSR 1706-44, have been analysed. The analysis provides some evidence for VHE gamma ray emission from this object.

A new method for exploiting the information provided by a high resolution imaging camera has been developed. This method involves fitting a smooth surface of bivariate Gaussian form to the signals measured by each PMT. Tests using Monte Carlo simulations of the Cerenkov images produced by air showers indicate that this method may provide better background discrimination than the standard, moment based parameterisation. Differences between the simulated and observed images are still significant, making the determination of the best parameter discrimination values difficult. An analysis of the Mark 6 PSR 1706-44 observations using this technique appears to reject fewer background cosmic ray events than the moment method, but retain more of the on source excess.

7.2 Future Work

7.2.1 PSR 1706-44

The analysis of the Mark 6 PSR 1706-44 observations presented in Chapter six is somewhat preliminary. There are various ways in which this small dataset can be exploited further. Firstly, it is unlikely that the parameter selection values used in this thesis represent the optimum background discrimination. Further searching in parameter space will incur more statistical penalties but may result in a more useful set of cuts for *a priori* application to future datasets. Secondly, a relatively high (300 bits) minimum total signal cut has been applied in order to make the image parameter calculations robust. This is a fairly standard technique in VHE gamma ray astronomy and also has the effect of removing any events caused by the Cerenkov radiation from local muons (Catanese, et al. 1995). These events can mimic gamma ray images and comprise a large fraction of the remaining background after image analysis for single dish experiments at low energies. The three-fold spatial coincidence requirement of the Durham telescopes makes them less sensitive to these events. It should therefore be possible to lower the total signal threshold in future and fully exploit the low

energy threshold capabilities of the telescope. Finally, the left and right detectors are expected to provide information about the variability of Cerenkov images over a 14 m baseline which may help to discriminate between hadron and gamma ray initiated EAS.

Once the optimum set of parameter selections have been defined, the existing PSR 1706-44 database should be examined for evidence of periodicity at the EGRET gamma ray and radio period. The radio pulsar is regularly monitored by radio telescopes and so excellent timing information is available (Kaspi, et al. 1995). Optimized cuts and an absence of period searching should then lead to a sensitive measurement of, or stringent upper limit to, the pulsed emission at TeV energies.

7.2.2 Simulations

The Durham approach to celestial gamma ray detection has tended to be empirical and not led by Monte Carlo simulations of EAS. If the telescopes are to become worthwhile astronomical tools, however, it is necessary to know their sensitivities and spectral responses more accurately. This can only be accomplished by the development of realistic simulations of the Cerenkov light from EAS and the response of the telescopes to this light. Various packages exist to simulate the air showers themselves, and cross-checking between these is increasing faith in their veracity. Modelling the telescope response depends upon accurate measurements of its various parameters. One area in which improvements could be made has been highlighted in Chapter five, which examined the point spread function of the Mark 6 telescope central flux collector. Further measurements of this across the entire field of view and with a known background light level may make more accurate simulations possible.

7.2.3 Source Candidates

As one of only two atmospheric Cerenkov installations with high resolution

imaging capabilities in the southern hemisphere, the observations by the Durham group will be extremely important in the development of the field. In particular, the Mark 6 telescope is the only high resolution ACT in the southern hemisphere with a low enough threshold energy to make observations of AGN's. Table 7.1 shows the prime candidates in the observing schedule for the first half of 1997.

Table 7.1: Early 1997 observing schedule for the Durham Gamma Ray Observatory

Date	Source Candidate	Nature of Source Candidate
January	1ES 0548-322	AGN (X-ray BL Lac)
	Vela Pulsar	Gamma ray pulsar/plerion
	Vela X-1	High mass X-ray binary
February	Vela pulsar	Gamma ray pulsar/plerion
	Vela X-1	High mass X-ray binary
	PSR 1055-52	Gamma ray pulsar
March	Vela pulsar	Gamma ray pulsar/plerion
	Vela X-1	High mass X-ray binary
	PSR 1055-52	Gamma ray pulsar
April	PSR 1055-52	Gamma ray pulsar
	PSR 1706-44	Gamma ray pulsar/plerion(?)
May	PSR 1055-52	Gamma ray pulsar
	PSR 1706-44	Gamma ray pulsar/plerion(?)
	1ES 2005-489	AGN (X-ray BL Lac)
June	PSR 1706-44	Gamma ray pulsar/plerion(?)
	1ES 2005-489	AGN (X-ray BL Lac)
July	1ES 2005-489	AGN (X-ray BL Lac)
	AE Aquarii	Cataclysmic Variable
	1ES 2155-304	AGN (X-ray BL Lac)

7.2.4 Future Observing Strategies and Hardware Developments

The Durham observatory in Narrabri now consists of three imaging ACT's of differing capabilities. It is important to determine the best way to exploit these

capabilities in the future. There are various options available when considering how to operate the telescopes. The Mark 3 and Mark 5 telescopes form a stereo pair which are approximately matched in energy threshold and detector resolution. It may be useful to operate these together, independently of the Mark 6. Alternatively, the Mark 5 may provide useful stereo information about the higher energy triggers of the Mark 6, with the Mark 3 operating as an independent burst monitor. Again, this is an area where the results of Monte Carlo simulations could help determine the best course of action.

There are no plans for any major hardware upgrades in the near future. Orford (1995) has proposed an improvement to the telescope trigger system which will provide a lower energy threshold for the same accidental trigger rate currently observed. At present, the telescope triggers and an event is recorded if the analogue signal from all of the PMT's in a coincidence channel crosses a preset discrimination level. In the new system, the PMT signals will be first amplified, squared and then added together before being discriminated. This will allow a reduction in the discriminator level, resulting in more low energy event triggers for the same accidental rate. In the case of a three-fold coincidence system, it may be possible to reduce the energy threshold of the telescope by ~ 40%.

REFERENCES

Aharonian, F., et al., 1995, *J. Phys. G: Nucl. Part. Phys.*, **21**, 419

Allan, H.R., 1971, *Prog. Elem. Part. and Cosmic Ray Physics*, **10**, 170

Allen, W.H., et al., 1993, *Phys. Rev: D.*, **48**, 466

Amenomori, M., et al., 1995, *Proc. 24th Int. Cosmic Ray Conf.*, Rome, **3**, 528

Antonucci, R., 1993, *Ann. Rev. Astron. Astrophys.*, **31**, 473

Arons, J., 1981, *IAU Symp. 94; Origin of Cosmic Rays* (Ed. Setti, G., Spada, G., & Wolfendale, A.W.), D.Reidel, Dordrecht, 175

Arons, J., 1984, *Adv. Space Res.*, **3**, 287

Arons, J., 1996, *Astron. Astrophys. Supp.*, **120**, 49

Aschenbach, N., & Brinkman, W., 1975, *Astron. Astrophys.*, **41**, 147

Baillon, P., 1991, *Proc 21st Int. Cosmic Ray Conf.*, Dublin, **1**, 220

Batschelet, E., 1981, *Circular Statistics in Biology*, Acad. Press, London

Becker, W., & Truemper, J., 1996, *Astron. Astrophys. Supp.*, **120**, 69

Becker, W., et al., 1995, *Astron. Astrophys.*, **298**, 528

de Beer, J.F., et al., 1966, *Proc. Phys. Soc. Lond.*, **89**, 567

Bell, A.R., 1978, *Mon. Not. Roy. Astro. Soc.*, **128**, 147

Bertsch, D.L., et al., 1992, *Nature*, **357**, 306

Bhat, P.N., et al., 1985, *Proc. 19th Int. Cosmic Ray Conf.*, La Jolla, **1**, 159

Bhat, P.N., et al., 1986, *Nature*, **319**, 127

Biller, S.D., et al., 1995, *Ap. J.*, **445**, 277

Blackett, P.M.S., 1948, *Emission Spectra of the Night Sky and Aurora, Rep. Gassiot Comm. of the Roy. Soc.*, 34

Blandford, R.D., & Ostriker, J.P., 1980, *Ap. J.*, **237**, 793

Bloom, S.D. & Marscher, A.P., 1993, *Proc. Compton Symp.* (Ed. Gehrels, N., Friedlander, M.), A.I.P., New York, 533

Boley, F.I., 1964, *Rev. Mod. Phys.*, **36**, 792

Bond, J.R., et al., 1986, *Ap. J.*, **306**, 428

Bondi, H., & Hoyle, F., 1944, *Mon. Not. Roy. Astro. Soc.*, **104**, 273

Bonnet-Bidaud, J.M., & van der Klis, M., 1981, *Astron. Astrophys.*, **97**, 134

Bowden, C.C.G., 1993, *Ph.D. Thesis, University of Durham*

Bowden, C.C.G., et al., 1992, *Astropart. Phys.*, **1**, 47

Bowden, C.C.G., et al., 1992a, *J. Phys. G: Nucl. Part. Phys.*, **118**, 413

Bowden, C.C.G., et al., 1993, *J. Phys. G:Nucl. Part. Phys.*, **19**, L29

Brazier, K.T.S., 1991, *Ph.D. Thesis, University of Durham*

Brazier, K.T.S., et al., 1990, *Proc. 21st Int. Cosmic Ray Conf.*, Adelaide, **2**, 300

Buckley, J.H., 1994, *Bull. American. Astron. Soc.*, **185**, No. 120.07

Buckley, J.H., et al., 1996, *Ap. J.*, **472**, L9

Cameron, R.A., et al., 1992, *The Compton Observatory Science Workshop* (Ed. Schrader, C.R., Gehrels, N., Dennis, B.), NASA, Washington, 3

Carraminana, A., 1991, *Ph.D. Thesis, University of Durham*

Caswell, J.L., & Lerche, I., 1979, *Mon. Not. Roy. Astro. Soc.*, **187**, 201

Catanese, M., et al., 1995, *Towards a Major Atmospheric Cerenkov Detector 4* (Ed. Cresti, M.), Padova, 335

Catanese, M., et al., 1995a, *Towards a Major Atmospheric Cerenkov Detector 4*, (Ed. Cresti, M.), Padova, 348

Cawley, M.F., et al., 1993, *Towards a Major Atmospheric Cerenkov Detector 2*, Calgary, 176

Cerenkov, P.A., 1937, *Phys. Rev.*, **52**, 378

Chadwick, P.M., 1987, *Ph.D. Thesis, University of Durham*

Chadwick, P.M., et al., 1990, *J. Phys. G:Nucl. Part. Phys.*, **16**, 1773

Chadwick, P.M., et al., 1995, *Proc 24th Int. Cosmic Ray Conf.*, Rome, **2**, 374

Chadwick, P.M., et al., 1995a, *Proc. 24th Int. Cosmic Ray Conf.*, Rome, **2**, 88

Chadwick, P.M., et al., 1995b, *Towards a Major Atmospheric Cerenkov Detector 4*, (Ed. Cresti, M.), Padova, 301

Chadwick, P.M., et al., 1996, *Space Sci. Rev.*, **75**, 153

Chanmugam, G., & Brecher, K., 1985, *Nature*, **313**, 767

Charles, P.A., & Seward, F.D., 1995, *Exploring the X-ray Universe*, Cambridge University Press, Cambridge

Cheng, K.S., & Ruderman, M., 1989, *Ap. J.*, **337**, L77

Cheng, K.S., et al., *Ap. J.*, 1986, *Ap. J.*, **300**, 500

Cheng, K.S., et al., *Ap. J.*, 1986a, *Ap. J.*, **300**, 522

Chudakov, A.E., et al., 1962, *J. Phys. Soc. Japan, Supp.*, **A-III**, 106

Cocconi, G., 1960, *Proc. Moscow Cosmic-Ray Conf.*, **2**, 309

Danaher, S., et al., 1993, *Astroparticle Phys.*, **1**, 357

Darbro W., et al., 1981, *Ap. J.*, **246**, 231

Davidson, K., & Ostriker, J.P., 1973, *Ap. J.*, **179**, 585

Davison, P.J.N., 1977, *Mon. Not. Roy. Astro. Soc.*, **179**, 15

Degrange, B., & Le Bohec, S., 1995, *Proc. 24th Int. Cosmic Ray Conf.*, Rome, **3**, 436

Dermer, C.D., & Schlikeiser, R., 1992, *Science*, **257**, 1642

Dermer, C.D., et al., 1992, *Astron. Astrophys.*, **256**, L27

Dermer, C.D., et al., 1996, *Bull. American. Astron. Soc.*, **189**, No. 55.05

Dickinson, J.E., 1995, *Ph.D. Thesis, University of Durham*

Dowthwaite, J.C., et al., 1984, *Ap. J.*, **286**, L35

Drury, L. o'C., 1983, *Rep. Prog. Phys.*, **154**, 973

Drury, L. o'C., et al., 1994, *Astron. Astrophys.*, **287**, 959

Drury, L.o'C., 1996, *Space Sci. Rev.*, **75**, 269

Dwek, E., & Slavin, J., 1994, *Ap. J.*, **436**, 696

Eadie, W.T., et al., 1971, *Statistical Methods in Experimental Physics*, North-Holland, Amsterdam

Esposito, J.A., et al., 1994, *Bull. American. Astron. Soc.*, **184**, No. 66.06

Fegan, D.J., 1992, *Towards a Major Atmospheric Cerenkov Detector* (Ed. Fleury, P., & Vacanti, G.), Editions Frontiers, Gif-sur-Yvette, 3

Fegan, D.J., 1996, *Space Sci. Rev.*, **75**, 137

Fermi, E., 1949, *Phys. Rev.*, **75**, 1169

Fermi, E., 1954, *Ap. J.*, **119**, 1

Ferrarese, L., et al., 1996, *Ap. J.*, **470**, 444

Fichtel, C., 1996, *Astron. Astrophys. Supp.*, **120**, 23

Fierro, J.M., et al., 1993, *Ap. J.*, **413**, L27

Fishman, G.J., et al., 1992, *The Compton Observatory Science Workshop* (Ed. Schrader, C.R., Gehrels, N., Dennis, B.), NASA, Washington, 26

Frail, D.A., et al., 1994, *Ap. J.*, **437**, 781

Frank, I.M., & Tamm, Ig., 1937, *Dokl. Acad. Nauk*, **14**, 109

Fruin, J.H., et al., 1964, *Phys. Letters*, **10**, 176

Gaidos, J.A., et al., 1996, *Nature*, **383**, 319

Gaisser, T.K., 1990, *Cosmic Rays and Particle Physics*, Cambridge University Press, Cambridge

Galbraith, W., & Jelley, J.V., 1953, *Nature*, **171**, 349

Gibson, A.I., et al., 1982, *Nature*, **296**, 883

Gibson, A.I., et al., 1982a, *Proc. Int. Workshop on VHE Gamma Ray Astro.* (Ed. Ramanamurthy, P.V., & Weekes, T.C.), Ootacamund, 97

Gilfanov, M., et al., 1989, *Proc. 23rd ESLAB Symp. on Two Topics in X-ray Astro.*, Bologna, **1**, 71

Gillanders, G.H., et al., 1995, *Proc. 24th Int. Cosmic Ray Conf.*, Rome, **2**, 323

Goeckel, 1910, *Phys. Zeits.*, **11**, 280

Goldreich, P., & Julian, W.H., 1969, *Ap. J.* , **157**, 869

Gould, R.J., & Schréder, G.P., 1966, *Phys. Rev. Lett.*, **16**, 252

Gould, R.J., 1965, *Phys. Rev. Lett.*, **15**, 577

Gould, R.P., & Schréder, G.P., 1967, *Phys. Rev.*, **155**, 1408

Greenwood, J.A., & Durrand, D., 1955, *Annals of Mathematical Statistics*, **26**, 233

Gregory, P.C., & Loredo, T.J., *Ap. J.*, **398**, 146

Greisen, K., 1960, *Ann. Rev. Nucl. Sci.*, **10**, 63

Grindlay, J., et al., 1975, *Ap. J.*, **201**, 82

Grindlay, J.E., & Hoffman, J.A., 1971, *Astrophys. Lett*, **8**, 209

Gunn, J.E., & Ostriker, J.P., 1969, *Phys. Rev. Lett.*, **22**, 728

Harding, A.K., & Gaisser, T.K., 1990, *Ap. J.*, **358**, 561

Harding, A.K., 1996, *Sp. Sci. Rev.*, **75**, 257

Hartman, R.C., et al., 1992, *The Compton Observatory Science Workshop* (Ed. Schrader, C.R., Gehrels, N., Dennis, B.), NASA, Washington, 116

Heaviside, O., 1892, *Electrical Papers*, **2**, 494

Henri, G., et al., 1993, *Ap. J.*, **404**, L41

Henry, P., & Schreier, E., 1977, *Ap J.*, **212**, L13

den Herder, J.W., et al., 1992, *The Compton Observatory Science Workshop* (Ed. Schrader, C.R., Gehrels, N., Dennis, B.), NASA, Washington, 85

Hess, V.F., 1911, *Phys. Zeits.*, **12**, 998

van den Heuvel, E.P.J., 1983, *Accretion-Driven Stellar X-ray Sources* (Ed. Lewin, W.H.G. & van den Heuvel, E.P.J.), Cambridge University Press, Cambridge,

Hewish, A., et al., 1968, *Nature*, **217**, 709

Hill, D.A., & Porter, N.A., 1961, *Nature*, **191**, 690

Hillas, A.M., & Johnson, P.A., 1989, *Proc. Int. Workshop on VHE Gamma Ray Astro.*, Crimea, 96

Hillas, A.M., & Johnson, P.A., 1991, *Proc. 22nd Int. Cosmic Ray Conf.*, Dublin, **2**, 452

Hillas, A.M., & Patterson, J.R., 1987, *Very High Energy Gamma-Ray Astronomy* (Ed. Turver, K.E.), D. Reidel, Dordrecht, 243

Hillas, A.M., 1982, *J. Phys. G: Nucl. Part. Phys.*, **8**, 1475

Hillas, A.M., 1985, *Proc. 19th Int. Cosmic Ray Conf.*, La Jolla, **3**, 445

Hillas, A.M., 1996, *Space Sci. Rev.*, **75**, 17

de Jager, O.C., & Harding, A.K., 1992, *Ap. J.*, **396**, 161

de Jager, O.C., et al., 1989, *Astron. Astrophys.*, **221**,180

de Jager, O.C., et al., 1994, *Nature*, **369**, 294

Jelley, J.V., 1958, *Cerenkov Radiation and its Applications*, Pergamon Press, London

Jelley, J.V., 1966, *Phys. Rev. Lett.*, **16**, 11

Jelley, J.V., 1967, *Progress in Elementary Particle and Cosmic Ray Physics*, (Ed. Wilson, J.G., & Woutheysen), North-Holland, **9**, 41

Johnston, S., et al., 1992, *Mon. Not. Roy. Astro. Soc.*, **255**, 401

Johnston, S., et al., 1995, *Astron. Astrophys.*, **293**, 795

Kahabka, P., & Pietsch, W., 1996, *Astron. Astrophys.*, **312**, 919

Kanbach, G., et al., 1994, *Astron. Astrophys.*, **289**, 855

Kaspi, V.M., et al., 1995, *GRO/Radio Timing Database*, Princeton University

Kazanas, D. & Ellison, D.C., 1986, *Ap. J.*, **304**, 178

Kazanas, D., & Ellison, D.C., 1986a, *Nature*, **319**, 380

Kennel, C.F., & Coroniti, F.V., 1984, *Ap. J.*, **283**, 694

van Kerkwijk, M.H., et al., 1995, *Astron. Astrophys.*, **303**, 497

Kerrick, A.D., et al., 1995, *Ap. J.*, **438**, L59

Kerrick, A.D., et al., 1995a, *Ap. J.*, **452**, 588

Kifune, T., et al., 1993, *Towards a Major Atmospheric Cerenkov Detector 2*, (Ed. Lamb, R.C.), Calgary, 39

Kifune, T., et al., 1995, *Ap. J.*, **438**, L91

Kiraly, P., & Mészáros, P., 1988, *Ap. J.*, **333**, 719

van der Klis, M., 1988, *Scientific American*, **November**, 50

Kohnle, A., et al., 1996, *Astroparticle Phys.*, **5**, 119

Koribalski, B., et al., 1995, *Ap. J.*, **441**, 756

Krennrich, F., 1994, *Towards a Major Atmospheric Cerenkov Telescope 3* (Ed. Kifune, T.), Universal Academy Press, Tokyo, 71

Kunz, M., et al., 1993, *Astron. Atrophys*, **268**, 116

Kwok, P.W., et al., 1991, *Ap. J.*, **379**, 653

Lamb, R.C., 1995, *Towards a Major Atmospheric Cerenkov Detector 4*, (Ed. Cresti, M.), Padova, 386

Lang, K.R., 1986, *Astrophysical Formulae*, Springer-Verlag, New York

Lang, M.J., 1995, *Proc. 24th Int. Cosmic Ray Conf.*, Rome, **3**, 754

Leahy, D.A., et al., 1983, *Ap. J.*, **272**, 256

Levine, A., et al., 1993, *Ap. J.*, **410**, 328

Lewis, D.A., 1993, *Statistical Methods for Physical Science*

Liebert, J., 1980, *Ann. Rev. Astron. Astrophys.*, **18**, 363

Liller, W., 1973, *Ap. J.*, **184**, L37

Longair, M.S., 1992, *High Energy Astrophysics* Vol.1 (2nd Ed), Cambridge University Press, Cambridge

Longair, M.S., 1994, *High Energy Astrophysics* Vol.2 (2nd Ed), Cambridge University Press, Cambridge

Lorenz, E., 1993, *Towards a Major Atmospheric Cerenkov Detector 2*, (Ed. Lamb, R.C.), Calgary, 182

Lucke, R., et al., 1976, *Ap. J.*, **206**, L25

Lyne, A.G., & Manchester, R.N., 1988, *Mon. Not. Roy. Astro. Soc.*, **234**, 477

MaComb, D.J., et al., 1995, *Ap. J.*, **449**, L99

Mallet, L., 1926, *C. R. Acad. Sci. (Paris)*, **183**, 274

Mannheim, K., 1996, *Sp. Sci. Rev.*, **75**, 331

Mannings, V.G., 1990, *Ph.D. Thesis, University of Durham*

Mardia, K.V., 1972, *Statistics of Directional Data*, Acad. Press, London

Mastichiadis, A., 1996, *Sp. Sci. Rev.*, **75**, 317

McAdam, W.B., et al., 1993, *Nature*, **361**, 516

Meintjes, P.J., et al., 1992, *Ap. J.*, **401**, 325

Meintjes, P.J., et al., 1994, *Ap. J.*, **434**, 292

Mészáros, P., 1992, *High-Energy Radiation from Magnetized Neutron Stars*, University of Chicago Press, Chicago

Michelson, P.F., et al., 1992, *I.A.U. Circ.*, **5470**, 1

Miyoshi, M., et al., 1995, *Nature*, **373**, 127

von Montigny, C., 1995, *Ap. J.*, **440**, 525

Morrison, P., 1958, *Nuovo Cimento*, **7**, 858

Moskalenko, I.V., 1995, *Space Sci. Rev.*, **72**, 593

Nel, H. I., et al, 1993, *Ap. J.*, **418**, 836

Nelder, J.A., & Mead, R., 1965, *The Computer Journal*, **7**, 308

Nicastro, L., et al., 1996, *Astron. Astrophys.*, **306**, L49

Nishimura, J., 1994, *Towards a Major Atmospheric Cerenkov Detector 3*, (Ed. Kifune, T.), Universal Academy Press, Tokyo, 1

Nolan, P.L., et al., 1993, *Ap. J.*, **409**, 697

Orford, K.J., 1991, *Experimental Astro.*, **1**, 305

Orford, K.J., 1995, *Experimental Astro.*, **6**, 1

Orford, K.J., 1996, *Astropart. Phys.*, **4**, 235

van Paradijs, J., & Zuiderwijk, E., 1977, *Astron. Astrophys.*, **61**, L19

Patterson, J., et al., 1995, *Towards a Major Atmospheric Cerenkov Detector 4*, (Ed. Cresti, M.), Padova, 116

Porter, N.A., & Long, C.D., 1963, *Contributions to the British Conf. on Nuclear Interactions at Ultra-High Energies*

Press, W.H., et al., 1992, *Numerical Recipes in FORTRAN: The Art of Scientific Computing*, Cambridge University Press, Cambridge

Price, R.E., et al., 1971, *Ap. J.*, **168**, L7

Primini, et al., 1977, *Ap. J.*, **217**, 543

Pringle, J.E., & Rees, M.J., 1972, *Astron. Astrophys.*, **21**, 1

Punch, M., 1993, *Ph.D. Thesis, University College Dublin*

Punch, M., et al, 1992, *Nature*, **358**, 477

Quinn, J., et al., 1996, *Ap. J.*, **456**, L83

Ramanamurthy, P.V., & Wolfendale, A.W., 1986, *Gamma Ray Astronomy*, Cambridge University Press, Cambridge

Ramanamurthy, P.V., et al., 1995, *Ap. J.*, **447**, L109

Ramanamurthy, P.V., et al., 1996, *Ap. J.*, **458**, 755

Rappaport, S.A., & Joss, P.C., 1983, *Accretion-Driven Stellar X-ray Sources* (Ed. Lewin, W.H.G. & van den Heuvel, E.P.J.), Cambridge University Press, Cambridge, 1

Rauterberg, G., et al., 1995, *Proc. 24th Int. Cosmic Ray Conf.*, Rome, **3**, 460

Lord Rayleigh, 1894, *Theory of Sound*, Macmillan, **1**, 35

Rees, M.J., & Gunn, J.E., 1974, *Mon. Not. Roy. Astro. Soc.*, **167**, 1

Reynolds, P.T., 1991, *Proc. 22th Int. Cosmic Ray Conf.*, Dublin, **1**, 496

Rieke, G.H., & Weekes, T.C., 1969, *Ap. J.*, **155**, 429

Roberts, M.D., 1993, *Ph.D. Thesis, University of Adelaide*

Robson, I., 1996, *Active Galactic Nuclei*, Wiley-Praxis, Chichester

Rossi, B., 1964, *Cosmic Rays*, McGraw-Hill

Ruderman, M.A., & Sutherland, P.G., 1975, *Ap. J.*, **196**, 51

Ruderman, M.A., et al., 1989, *Ap. J.*, **336**, 507

Rutherford & Cooke, 1903, *Phys. Rev.*, **16**, 183

Salamon, M.H., et al., 1994, *Ap. J.*, **423**, L1

Schlickeiser, R., 1996, *Sp. Sci. Rev.*, **75**, 299

Schreier, E., et al., 1972, *Ap. J.*, **178**, L71

Schubnell, M.S., et al., 1996, *Ap. J.*, **460**, 644

Sikora, M., et al., 1994, *Ap. J.*, **421**, 153

Standish, E.M., 1982, *Astron. Astrophys.*, **114**, 297

Stecker, F.W., & De Jager, O.C., 1993, *Ap. J.*, **415**, L71

Stecker, F.W., et al., 1992, *Ap. J.*, **390**, L49

Stecker, F.W., et al., 1996, *Ap. J.*, **473**, L75

Sturner, S.J., & Dermer, C.D., 1995, *Astron. Astrophys.*, **293**, L17

Sturrock, P.A., 1970, *Nature*, **227**, 465

Sturrock, P.A., 1971, *Ap. J.*, **164**, 529

Swanenburg, B.N., et al., 1978, *Nature*, **275**, 298

Swanenburg, B.N., et al., 1981, *Ap.J.*, **243**, L69

Tanaka, Y., et al., 1995, *Nature*, **375**, 659

Thompson, D.J., et al., 1992, *Nature*, **359**, 615

Thompson, D.J., et al., 1994, *Ap. J.*, **436**, 229

Thompson, D.J., et al., 1996, *Ap.J.*, **465**, 385

Thornton, G.J., et al., 1995, *Proc. 24th Int. Cosmic Ray Conf.*, Rome, **3**, 476

Toller, G.N., 1990, *The Galactic and Extragalactic Background Radiation* (Ed. Bowyer, S. & Leinert, C.), Kluwer Academic Publishers, Dordrecht, 21

Tumer, O.T., et al., 1990, *Proc. 21st Int. Cosmic Ray Conf.*, Adelaide, **4**, 238

Tuohy, I., & Rapley, C.G., 1975, *Ap. J.*, **198**, L69

Turver, K.E., & Weekes, T.C. 1978, *Nuovo Cimento*, **45B**, 99

Vacanti, G., et al., 1991, *Ap. J.*, **377**, 467

Vanstekelenborg, J., et al., 1993, *Phys. Rev. D*, **48**, 4504

Wang, Y-M., 1986, *Astrophys. Space Sci.*, **121**, 193

Webster, B.L., et al., 1972, *Nature Phys. Sci.*, **240**, 183

Weekes, T.C., & Turver, K.E., 1977, *Proc. 12th ESLAB Symposium*, Frascati, 279

Weekes, T.C., 1988, *Phys. Reports*, **160**, 1

Weekes, T.C., 1996, *Space Sci. Rev.*, **75**, 1

Weekes, T.C., et al., 1989, *Ap. J.*, **342**, 379

Westfall, G.D., et al., 1979, *Phys. Rev. C.*, **19**, 1309

Wiebel-Sooth, B., et al., 1995, *Proc. 24th Int. Cosmic Ray Conf.*, Rome, **2**, 656

Wilson, A.S., 1972, *Mon. Not. Roy. Astro. Soc.*, **157**, 229

Woltjer, L., 1987, *High Energy Phenomena Around Collapsed Objects* (Ed. Pacini, F.), D.Reidel, Dordrecht, **195**, 209

Yoshikoshi, T., 1996, *Ph.D. Thesis, Tokyo Institute of Technology*

Zatsepin, V.I., 1965, *Sov. Phys., JETP*, **20**, 459